

2013-11-13

A Novel Augmented Finite Element Method for Modeling Arbitrary Cracking in Solids

Seyedreza Mohammadizadeh

University of Miami, reza29m@yahoo.com

Follow this and additional works at: https://scholarlyrepository.miami.edu/oa_dissertations

Recommended Citation

Mohammadizadeh, Seyedreza, "A Novel Augmented Finite Element Method for Modeling Arbitrary Cracking in Solids" (2013). *Open Access Dissertations*. 1106.

https://scholarlyrepository.miami.edu/oa_dissertations/1106

This Open access is brought to you for free and open access by the Electronic Theses and Dissertations at Scholarly Repository. It has been accepted for inclusion in Open Access Dissertations by an authorized administrator of Scholarly Repository. For more information, please contact repository.library@miami.edu.

UNIVERSITY OF MIAMI

A NOVEL AUGMENTED FINITE ELEMENT METHOD FOR MODELING
ARBITRARY CRACKING IN SOLIDS

By

Seyedreza Mohammadizadeh

A DISSERTATION

Submitted to the Faculty
of the University of Miami
in partial fulfillment of the requirements for
the degree of Doctor of Philosophy

Coral Gables, Florida

December 2013

©2013

Seyedreza Mohammadzadeh

All Rights Reserved

UNIVERSITY OF MIAMI

A dissertation submitted in partial fulfillment of
the requirements for the degree of
Doctor of Philosophy

A NOVEL AUGMENTED FINITE ELEMENT METHOD FOR MODELING
ARBITRARY CRACKING IN SOLIDS

Seyedreza Mohammadizadeh

Approved:

Qingda Yang, Ph.D.
Associate Professor of Mechanical
and Aerospace Engineering

Weiyong Gu, Ph.D.
Professor of Mechanical
and Aerospace Engineering

Jizhou Song, Ph.D.
Assistant Professor of Mechanical
and Aerospace Engineering

Ali Ghahremaninezhad, Ph.D.
Assistant Professor of Civil,
Architectural, and
Environmental Engineering

James W. Giancaspro, Ph.D.
Associate Professor of Civil,
Architectural and Environmental
Engineering

M. Brian Blake, Ph.D.
Dean of the Graduate School

MOHAMMADIZADEH, SEYEDREZA

(Ph.D., Mechanical Engineering)

(December 2013)

A Novel Augmented Finite Element Method for Modeling Arbitrary Cracking in Solids

Abstract of a dissertation at the University of Miami.

Dissertation supervised by Associate Professor Qingda Yang.

No. of pages in text. (213)

Advanced composite materials are known as important engineering materials in industry. Unlike structural metals which are homogeneous and isotropic, composites are inherently inhomogeneous and anisotropic which leads to further difficulty in damage tolerance design. The predictive capabilities of existing models have met with limited success because they typically cannot account for multiple damage evolution and their coupling. Consequently, current composite design is heavily dependent upon lengthy and costly test programs and empirical design methods. There is an urgent need for efficient numerical tools that are capable of analyzing the progressive failure caused by nonlinearly coupled, multiple damage evolution in composite materials.

This thesis presents a new augmented finite element method (A-FEM) that can account for multiple, intra-elemental discontinuities with a demonstrated improvement in numerical efficiency when compared to the extended finite element method (X-FEM). It has been shown that the new formulation enables the derivation of explicit, fully-condensed elemental equilibrium equations that are mathematically exact within the finite element context. More importantly, it allows for repeated elemental augmentation

to include multiple interactive cracks within a single element without additional external nodes or degrees of freedom (DoFs).

A novel algorithm that can rapidly and accurately solve the nonlinear equilibrium equations at the elemental level has also been developed for cohesive cracks. This new solving algorithm, coupled with mathematically exact elemental equilibrium equations, leads to dramatic improvement in numerical accuracy, efficiency, and stability. The A-FEM's excellent capability in high-fidelity simulation of interactive cracks in solids has been demonstrated through several numerical examples.

Dedicated to:

Mohammad, Soheila, Rahil, Reyhaneh

and my lovely wife, Maryam

Acknowledgement

I would like to thank Dr. Qingda Yang, my supervisor, whose help is one of the most important elements in this study. I thank him for bringing me into this wonderful research area and for his continuous support throughout this program.

I would like to thank the committee members, Dr. Weiyong Gu, Dr. Jizhou Song, Dr. James W. Giancaspro, and Dr. Ali Ghahremaninezhad, for their help in improving the thesis and the useful technical discussions during the course of the study.

I would like to thank my dear colleagues, Dr. Mehdi Naderi, Dr. Wei Liu, Mr. Bao-Chan Dinh Do, and Mr. Derek G. Schesser, whose help and support were tremendous. It has been a great pleasure to work with all of them.

I would like to thank my father, mother and sisters. Although they are too far from me, I always feel their support every moment of my life.

I would like to thank my lovely wife, Maryam, who provided a nice and relaxed atmosphere for me to do my research.

Finally I would like to thank the Department of Mechanical and Aerospace Engineering at the University of Miami for partial financial support. The partial support from National Hypersonic Science Center (NHSC, jointly funded by AFOSR and NASA, AFOSR Contract No. FA9550-09-1-0477) is also acknowledged.

TABLE OF CONTENTS

	PAGE
LIST OF FIGURES.....	viii
LIST OF TABLES	xii
Chapter	
Chapter 1: Introduction.....	1
1.1. What is a composite material?.....	1
1.2. History.....	2
1.3. Area overview.....	6
1.4. A review on damage modeling in composite.....	15
1.4.1. Linear Elastic Fracture Mechanics.....	16
1.4.2. Nonlinear Fracture Mechanics.....	24
1.5. Advances of Numerical methods for Arbitrary Cracking in Solids.....	28
1.5.1. Continuum Damage Mechanics.....	32
1.5.2. Generalized FEM (G-FEM) and eXtended FEM (X-FEM).....	34
1.5.3. Phantom Node Method (PNM) & Augmented FEM (AFEM).....	40
1.6. Research Goal.....	44
Chapter 2: Two-Dimensional A-FEM – Single Crack Formulation.....	46
2.1. Overview.....	46
2.2. Fracture of A Longitudinally Loaded 1D Bar.....	52
2.2.1. Strength of Material Approach.....	52
2.2.2. Standard FEM Approach for Fracture of 1D Bar.....	55
2.3. Problem Statement.....	63
2.4. A-FEM Formulation with Single Intra-Elemental Crack.....	65
2.5. Elemental Condensation Algorithm.....	78
2.6. Numerical Implementation.....	79
2.7. Single Element Validation.....	83
2.7.1. Mode I response.....	83

2.7.2	Mode II response.....	85
2.7.3	Mixed- Mode response.....	87
2.7.4	Mode –I wedge opening response.....	88
2.8	Summary.....	90
Chapter 3: Two- Dimensional A-FEM-Multiple Crack Formulation.....		91
3.1	Overview.....	91
3.2	Elemental Augmentation Formulation – Configuration 1.....	92
3.2.1	General Formulation.....	92
3.2.2	Numerical Treatments for Stress-Free Subdomains.....	98
3.3	Elemental Augmentation Formulation – Configuration 2.....	101
3.3.1	General Formulation.....	101
3.3.2	Numerical Treatments for Stress-Free Subdomains.....	104
3.4	Elemental Augmentation Formulation – Configuration 3.....	106
3.4.1	General Formulation.....	106
3.4.2	Numerical Treatment for Stress-Free Subdomains.....	108
3.5	Elemental Augmentation Formulation – Configuration 4.....	110
3.5.1	General Formulation.....	110
3.5.2	Numerical Treatments for Stress-Free Subdomains.....	116
3.6	Elemental Condensation Algorithm.....	123
3.7	Single Element Validation.....	125
3.7.1	Mode I Response (Configurations 1 & 2).....	126
3.7.2	Mixed Mode (Configuration 1 & 2).....	127
3.7.3	Mode I (configuration 3).....	129
3.7.4	Mode II (Configuration 3).....	131
3.7.5	Wedge Opening (configuration 3).....	132
3.7.6	Mode I (configuration 4).....	134
3.7.7	Mode II (configuration 4).....	136
3.7.8	Wedge opening (configuration 4).....	138
3.7.9	One corner loading (configuration 4).....	139
3.8	Summary.....	141

Chapter 4: Numerical Examples.....	142
4.1 Shear Test of a Precracked Short Beam.....	142
4.1.1 Mesh Sensitivity.....	143
4.1.2 Numerical Efficiency and Stability as Compared to X-FEM.....	146
4.2 Four Point Shear Beam Test.....	149
4.2.1 Mesh sensitivity.....	152
4.2.2 Numerical Efficiency and Stability as Compared to X-FEM in ABAQUS.....	154
4.3 Coupled Fiber- Matrix Interface Debonding and Kinking.....	157
4.4 Axisymmetric Tension Acting on a Fiber-Matrix Interface.....	161
4.5 Three Point Bending Beam Test.....	163
4.6 Multiple Crack Interaction in a Plate.....	165
4.7 Summary.....	168
Chapter 5: Conclusions and Future Study.....	169
5.1 General Conclusions.....	169
5.2 Future Study.....	171
References.....	175
Appendix A: A Piece-Wise Linear Constitutive Law for Cohesive Cracks.....	197
Appendix B: Equilibrium Equations for First 2D Configuration.....	202
Appendix C: Stiffness Matrix for Pentagonal Subdomains.....	204
Appendix D: Integration and Interpolation Matrices for Various Integration Schemes.....	207

LIST OF FIGURES

Figure 1-1 Cross ply laminate subjected to uniaxial loading	9
Figure 1-2 Propagation of a matrix cracking due to fiber-matrix debonding	10
Figure 1-3 Matrix cracking in cross-ply laminate	10
Figure 1-4 Modes of damage in a composite material	11
Figure 1-5 X-ray radiography reveals damage mechanisms viewed through the ply stack in a laminated PMC containing aligned (0°) and transverse (90°) fiber plies loaded in tension	14
Figure 1-6 wide range of applicability of the Engineering Fracture Mechanics	16
Figure 1-7 Elliptical hole in an infinite plate	17
Figure 1-8 A splitting crack and its induced delamination in a composite laminate	38
Figure 2-1 X-ray radiography reveals damage mechanisms viewed through the ply stack in (a) a double-notch tension specimen with symmetric orthogonal ply stack ($[0/90]_s$), and (b) a quasi-isotropic laminate ($[-45/+45/90/0]_s$) with a circular open hole under tensile loading (c) Polarized light micrograph shows distributed damage in a fibrous stitch that has been sheared by a mode II delamination crack(d) Scanning electron micrograph of an echelon cracking between two fibers in a carbon-epoxy composite loaded in off-axis tension.....	47
Figure 2-2 A bar loaded in longitudinal tension under displacement-controlled manner. (a) elastic stage, (b) bridged cohesive cracking stage, (c) rectangular cohesive law.....	52
Figure 2-3 Load- displacement (global response) curve of the bar with cohesive crack following the rectangular law in Figure 2-2.	53
Figure 2-4 (a) A trapezoidal cohesive law, (b) Global load-displacement curve of the 1D bar resulted from the trapezoidal cohesive law.....	54
Figure 2-5 Fracture of a 1D bar with a trapezoidal cohesive law (standard FEM formulation)	57
Figure 2-6 Notation for a body with an arbitrary discontinuity	64
Figure 2-7 Illustration of the element augmentation from (a) a regular element with possible different material domains, to (b) an A-FE with two quadrilateral sub-domains, or to (c) an A-FE with one triangular sub-domain and one pentagonal sub-domain.....	67
Figure 2-8 Flow chart of implementation of the present A-FEM into ABAQUS as a user defined element.....	82
Figure 2-9 Single A-FE response under mode I loading conditions.....	84
Figure 2-10 FBD evaluation of top domain at crack initiation instant	84
Figure 2-11 (a) Deformed shape from A-FEM, (b) from ABAQUS.....	85
Figure 2-12 Single A-FE under mode II loading condition.....	86
Figure 2-13 FBD of the top domain at crack initiation instant	86
Figure 2-14 Deformed shapes from (a) the A-FEM and (b) ABAQUS	86

Figure 2-15 Load-displacement plot for node 3 under mixed mode	87
Figure 2-16 (a) Deformed shape from A-FEM, (b) from ABAQUS	88
Figure 2-17 Load-displacement for wedge opening	89
Figure 2-18 Deformed shape from (a) A-FEM, and (b) ABAQUS	89
Figure 3-1 Four possible cut configurations for a secondary crack from a pentagonal subdomain	91
Figure 3-2 Illustration of a secondary crack in a pentagonal subdomain (3 crack segments I, II, and III).....	92
Figure 3-3 Illustration of a secondary crack in a pentagonal subdomain, second configuration (3 crack segments I, II, and III).....	101
Figure 3-4 Illustration of a secondary crack in a rectangular subdomain (3 crack segments I, II, and III).....	106
Figure 3-5 Illustration of two secondary cracks in cracked quadratic subdomains (4 crack segments I, II, III and IV).....	111
Figure 3-6 Single A-FE response with two cracks under mode I loading conditions for configurations 1 & 2	126
Figure 3-7 (a) Deformed shape from A-FEM, (b) from ABAQUS	127
Figure 3-8 Single A-FE response with two cracks under mixed mode loading conditions for configuration 1& 2	127
Figure 3-9 (a) Deformed shape from A-FEM, (b) from ABAQUS	129
Figure 3-10 Single A-FE response with two cracks under mode I loading for configuration 3	130
Figure 3-11 Deformed shape from A-FEM, (b) Deformed shape from ABAQUS for configuration 3, mode I.....	130
Figure 3-12 Single A-FE response with two cracks under mode II loading conditions for configuration 3	131
Figure 3-13 (a) Deformed shape from A-FEM, (b) Deformed shape from ABAQUS for configuration 3, mode II	132
Figure 3-14 Single A-FE response with two cracks under wedge opening loading conditions for configuration 3.....	133
Figure 3-15 (a) Deformed shape from A-FEM, (b) Deformed shape from ABAQUS for configuration 3, wedge opening.....	134
Figure 3-16 Single A-FE response with three cracks under mode I loading conditions for configuration 4	135
Figure 3-17 (a) Deformed shape from A-FEM, (b) Deformed shape from ABAQUS for configuration 4, mode I.....	135
Figure 3-18 Single A-FE response with three cracks under mode I loading conditions for configuration 4 by displacing two middle nodes on the right edge	136
Figure 3-19 Deformed shape from A-FEM, (b) Deformed shape from ABAQUS for configuration 4, mode I by displacing four nodes in ABAQUS.....	136

Figure 3-20 Single A-FE response with three cracks under mode II loading conditions for configuration 4	137
Figure 3-21 Deformed shape from A-FEM, (b) Deformed shape from ABAQUS for configuration 4 under mode II displacement	137
Figure 3-22 Single A-FE response with three cracks under wedge opening loading conditions for configuration 4.....	138
Figure 3-23 Deformed shape from A-FEM, (b) Deformed shape from ABAQUS for configuration 4 under wedge opening displacement	139
Figure 3-24 Single A-FE response with three cracks under one corner loading conditions for configuration 4	140
Figure 3-25 (a) Deformed shape from A-FEM, (b) Deformed shape from ABAQUS for configuration 4, one corner loading.....	140
Figure 4-1 Precracked short beam	142
Figure 4-2 Simulated load-displacement curves for precracked short beam.....	144
Figure 4-3 Crack trajectories for the shear test with four vastly different meshes.....	144
Figure 4-4 Crack trajectory for each mesh size	145
Figure 4-5 X-FEM predicted load-displacement curves compared with the A-FEM predictions.....	148
Figure 4-6 Comparison of CPU time (right vertical axis) and the numerical error (left axis) as function of mesh sizes.....	149
Figure 4-7 PSB Geometry, boundary and loading.....	150
Figure 4-8 Simulated crack paths for structured 2mm (a), 8mm (b), and 20 mm (c) meshes, and unstructured 8mm (d) and 13 mm (e) meshes.....	151
Figure 4-9 A-FEM simulated load-displacement curves with the five structured meshes as compared to the X-FEM results.....	152
Figure 4-10 Crack trajectories with the five structured meshes as compared to the X-FEM results and experimental results.....	153
Figure 4-11 X-FEM predicted load-displacement curves.....	156
Figure 4-12 Comparison of the CPU time (right vertical axis), and the numerical error (left axis) as function of mesh sizes.....	156
Figure 4-13 A-FEM Simulated nominal stress versus displacement for a single fiber/matrix domain under uniaxial tension. Crack development, including the initial fiber-matrix interface (dashed line), debonding crack and final kinking cracks in matrix are indicated.....	159
Figure 4-14 A-FEM simulated radial surface traction as a function of radial displacement for an axial symmetric single-fiber/matrix unit cell (center plot). The two contour micrographs to its left show the continuous displacement and discontinuous strain (maximum principal) during the elastic stage when the fiber and matrix are rigidly bonded (weak discontinuity). The two right contour graphs show that both the	

displacement and strain are discontinuous after interface debonding occurs (strong discontinuity)	162
Figure 4-15 Three point beam bending specimen, boundary and loading.....	164
Figure 4-16 Simulated normalized load displacement plot for 3-point beam bending test	165
Figure 4-17 Two cracks within the plate	166
Figure 4-18 Load displacement curve for a plate with two far from edge cracks	166
Figure 4-19 Crack propagation stages for a plate with two far from edge cracks	167
Figure 5-1 possible configurations for a tetrahedral element cut by a crack	172
Figure 5-2 Load-displacement curve from A-FEM and ABAQUS for a tetrahedron element.....	173

LIST OF TABLES

Table 4-1: Comparisons of predicted composite properties by mesh (a) and (b)	160
Table C1: Gaussian Quadrature Points and Corresponding Weight Factors.....	206

Chapter 1: Introduction

1.1. What is a composite material?

Nowadays, composites are employed by many industries as structural materials in lieu of traditional materials such as metals and metal alloys. The word *composite* in the term *composite material* indicates the combination of two or more materials on a macroscopic scale, in such a way that the constituents are still distinguishable and not fully blended, to build a useful third material [1]. Composites are regarded as the materials of the future, which revolutionize the industry, help improve environment conditions, provide safer and easier use of different machines, and allow for an expanded design space for alternative engineering applications [2].

If composite materials are designed well, they usually retain the best qualities of their components or constituents and usually have some qualities that neither constituent possesses. This is the main advantage of composites. Some of the properties that can be improved by this way are strength, stiffness, corrosion resistance, wear resistance, weight, fatigue life, thermal insulation and thermal conductivity [1].

Naturally, there is no need to improve all of these properties at the same time and it may be impossible. In fact, some of the properties may be in conflict with one another, e.g., thermal insulation versus thermal conductivity. The objective is merely to create a material that has only the characteristics needed to perform the design task [1]. There are a number of options for matrix and reinforcing materials and they can be mixed in different combinations, ratios, and directions to obtain a composite material with desired

properties. There are many types of composite materials such as metal matrix composites, polymer composites and ceramic matrix composites depending on the type of reinforcing and matrix material but generally four commonly accepted types of composite materials are:

- (1) *Fibrous composite materials* that consist of continuous fibers in a matrix
- (2) *Laminated composite materials* that consist of layers of individual fiber reinforced plies
- (3) *Particulate composite materials* that are composed of particles in a matrix
- (4) Combinations of some or all of the first three types [1]

1.2. History

Composite materials' usage dates back to thousands of years ago. Their exact beginnings are unknown, but all recorded history contains references to some forms of composite materials. A good and simple example of composite system is human body. The muscular system of the human body is a perfect example of how the arrangement of multiple fibrous systems can provide strength, versatility, and efficiency to a mechanical system. Indeed, several examples of composite materials are existed in nature of which the most obvious and beneficial to human society over the history is wood. Wood is made out of an arrangement of cellulose fibers in a matrix of lignin. Tensile strength of the wood is provided by fibers while the lignin matrix is responsible for lateral support to the fibers and compressive resistance [3].

Man-made composite materials appeared first in the beginning of human civilization, when bricks were formed by burning straw and mud together for construction purposes.

The Israelites used this technique in the Middle East for their Egyptian rulers and was described in the Book of Exodus [2]. In the same era, ancient Egyptians stripped the stem of the papyrus plant into thin but long strips to manufacture papyrus sheets for writing. By laying these strips side by side, and laying another layer on the top of these, but with the fibers of the plant in a perpendicular direction to the first layer, several layers were added afterwards to provide enough strength and durability to the papyrus paper for writing. Thus, the first orthotropic laminates were born [2].

After the industrial revolution, the growing need for stronger materials, prompted engineers to look again at combining different materials to obtain better overall mechanical properties. It was in the mid-1800s that the first attempts at creating a new building material capable of withstanding greater stresses began to take place. Joseph Louis Lambot found that the strength of the concrete could be increased by adding thin bars of steel to it in its wet state. This new material quickly achieved high popularity since it brought to architecture and civil engineering the possibility to build higher while reducing material weight and increasing longevity of the constructions [2].

Fiberglass began being manufactured and commercialized first as an insulation material in 1930s [4]. But later it began being applied in the fast growing aeronautic industry, first in reinforced plastic dies for the manufacture of prototype components, and then in jigs and fixtures for forming and holding aircraft sections and assemblies [2].

In 1942, the U.S. Navy replaced all the electrical terminal boards on their ships with fiberglass- melamine composite boards with improved electrical insulation properties [5].

In World War II, many components made of composite materials had been used in the naval and aeronautic industry. A significant knowledge based on polymers reinforced with fiberglass, their manufacture processes and applications had been established. After the War, a lot of companies converted war-oriented applications of composite to commercial applications [4].

There is a common agreement that the pent-up demand for automobiles was a good arena that composites could prove their capabilities. The first fully composite body automobile had been made and tested in 1947. This car was reasonably successful and led to the development of the Corvette in 1953, which was made using fiberglass preforms, which were impregnated with resin and molded in matched metal dies. Compression molding of sheet molding compound (SMC) or bulk molding compound (BMC) was the dominant molding method for automobile parts. The Galstic Corporation developed premix materials of these types as early as 1948.

The beginning of the space age in the 1950s was an important factor for the development of advanced composite materials. Carbon fibers began being commercially available soon after 1961 when the first patent for production of carbon fibers was issued. This allowed for even greater stiffness to weight reductions. New, better, lighter, and stronger components for the aerospace industry began to appear along with new manufacturing processes such as the filament winding technology. Boron and aramid fibers were respectively introduced in the late 1960s and early 1970s [2].

Whereas space and aircraft demands had prompted the quest for new high modulus fibers in the 1960s, composites made with such expensive fibers had to find civil applications in

the 1970s, when space and military demands declined. Thereafter, sport and automobile industries became the most important markets. Graphite tennis rackets and golf clubs replaced the wooden racket heads and steel club shafts [5].

The ceramic matrix composites appeared in the mid-1970s and quickly found many applications such as brakes on aircraft due to their excellent heat resistance and toughness.

In the 1990s, both academic and industrial researchers started to extend the composite paradigm to smaller and smaller scales which led to hybrid materials and nanocomposites. Hybrid materials mix organic and inorganic components at the molecular scale and the main target in that is to mimic the nature process. Remarkably, strategies of hybridization apply to all families of materials, not only to polymers but also to cement and materials for electronics or medical uses.

Since microsynthesis has been successful in making computer components, material scientists have aimed to go beyond the microscale to build up materials atom by atom, which is at the nanoscale. This led to nanocomposites which have better characteristics than regular composites and specialized applications which the regular ones cannot be used [5].

Not only the fibrous reinforcements suffered a significant evolution; new polymers introduced over past years allow the applications of composites to increase tremendously, expanding from aerospace industry to sports equipment, medical apparatus, defense systems, thermally and chemically demanding environments, and electrical/electronic equipment [2]. This magnifies how important role composites play in modern industries.

1.3. Area overview

The use of advanced polymer matrix composites (PMCs) and ceramic matrix composites (CMCs) has been considerably expanded over the last decade to overcome problems and shortages with metals or other traditional materials. Compared to traditional metals, PMCs offer key advantages such as weight savings, better reliability and durability, and lower manufacturing and maintenance costs. One of the major justifications for using advanced composites is the potential for increased structural durability, which facilitates lower maintenance costs. Polymer matrix composites are used in a wide range of applications ranging from commercial aircraft to bath tubs [6].

The problems associated with the conventional technical ceramics like alumina and silicon carbide, such as fracturing easily under mechanical or thermo-mechanical loads because of cracks initiated by small defects or scratches, motivated scientists to develop CMCs. CMC materials overcome the major disadvantages of conventional technical ceramics, namely brittle failure and low fracture toughness, and limited thermal shock resistance. Therefore, their applications are in fields requiring reliability at high-temperatures (beyond the capability of metals) and resistance to corrosion and wear.

These include:

- Heat shield systems for space vehicles, which are needed during the re-entry phase, where high temperatures, thermal shock conditions and heavy vibration loads take place.
- Components for high-temperature gas turbines such as combustion chambers, stator vanes and turbine blades.

- Components for burners, flame holders, and hot gas ducts, where the use of oxide CMCs has found its way.
- Brake disks and brake system components, which experience extreme thermal shock (greater than throwing a glowing part of any material into water).
- Components for slide bearings under heavy loads requiring high corrosion and wear resistance.

In addition to the foregoing, using CMCs instead of conventional ceramics or metal components which have limited lifetimes due to corrosion or high temperatures is a good solution [7].

Despite the increasing usage of structural composites, many mechanical and material issues remain unresolved. Unlike structural metals which are homogeneous and isotropic, composites are inherently inhomogeneous and anisotropic. Microscopic flaws and imperfections are inevitably present due to manufacturing processes. Damage tolerance design has to be an integral part of composite structural design.

Currently, such damage tolerance design relies heavily on experimental testing to establish design limits/tolerance. A component needs to be manufactured and tested—most of the times to complete destruction – in order to determine its elastic and strength properties. The burden of testing to establish design allowable is immense: a typical large airframe, for example, currently requires about 10^4 tests of material specimens, along with tests of components and structures up to entire tails, wing boxes, and fuselages, to achieve safety certification. Such lengthy and costly procedures have been increasingly cited as the bottleneck to fast insertion of composites in new engineering applications [8].

Besides costly and lengthy tests for damage tolerance design in composites, another crucial and important issue is the accurate assessment of in-service damage. For instance, a small flaw in a plane fuselage can grow under several applied mechanical and thermal loads and leads to a tragedy. It is very crucial to guarantee the composite structure safety by knowing the location of such a crack and making sure it does not grow beyond the critical size.

Damage to composites is often hidden to the eye. While a metal structure will show a dent or ding after being damaged. For a composite structure, there may be no visible signs of surface damage, even it has delaminated plies or other damages within. Defects and damages in composites reduce the strength, stiffness and also the service life of the composite structures. Defects may be introduced during manufacture, accidentally in-service or perhaps unavoidably in design because of the requirement to introduce discontinuities such as cutouts, ply drops or structural connections [9]. The defects commonly introduced to composite materials during manufacturing and processing are inclusions, de-bonding, fiber misalignment, voids and residual stresses, which we will have a brief review over them in below:

- a. *Inclusions* – Accidentally included materials during manufacturing like peel paper can have a degrading effect on the mechanical properties.
- b. *De-bonds* –The failure of the interface between the fibers and the matrix material leads to separation between them, called de-bonding. De-bonding can occur because of poor consolidation or as a result of an inclusion.

c. *Fiber misalignment* – This damage is especially prevalent in low fiber volume fraction materials.

d. *Voids* – Voids are due to inclusion of air, solvents or other contamination during mixing of resin.

e. *Residual stresses* – These stresses are mainly caused by the curing process. These affect the mechanical properties and can cause warping, fiber buckling, microcracking of the matrix and delamination. The cause of these stresses is mainly the difference in thermal expansion of the fiber and matrix material in different directions.

The most common damages introduced in composite materials during service loading are matrix cracking, fiber breakage, fiber pullout, delamination, and fiber-matrix de-bonding. As an example, Figure 1-1 shows a composite panel, with 0° plies on the outside and the 90° plies in the inside, uniaxial loaded to a stress of σ_x . The types of damage incurred in the composite laminate due to this uniaxial tensile loading are discussed below.

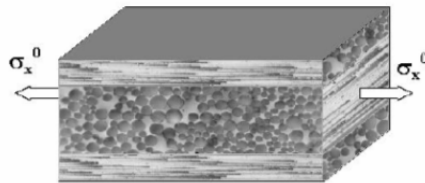


Figure 1-1 Cross ply laminate subjected to uniaxial loading [10]

(a) *Fiber-matrix debonding*: This failure mode occurs in the composite materials due to poor interface bonding between the fibers and the matrix. These debondings join together to form large-scale damage called matrix cracking. Figure 1-2 shows a matrix crack formed from fiber-matrix debonding.

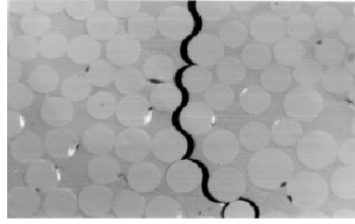


Figure 1-2 Propagation of a matrix cracking due to fiber-matrix debonding [10]

(b) *Transverse ply cracking*: As described by R. Joffe [10], the cracks are initiated from the interface failures. Fiber/matrix debonding cracks often kink into the matrix transverse cracks and join with others which lead to a reduction in load carrying capacity and stiffness of the structure in the direction normal to the cracks. Figure 1-3 shows transverse ply cracking of a cross-ply laminate subjected to uniaxial tension.

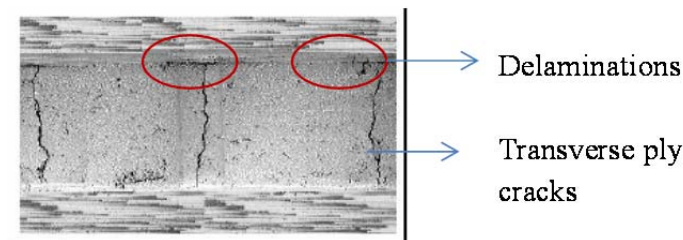


Figure 1-3 Matrix cracking in cross-ply laminate [10]

(c) *Delamination*: Delamination is a form of failure that occurs on a plane between adjacent layers within a laminate. Multiple stress concentration points are introduced by microcracks at the crack tips as the adjacent layers restrain the microcracks. These crack tips exist at the interface between plies of a laminated composite and thus lead to delamination that is large-scale damage. Delamination can increase connectivity of the ply cracks and cause leakage paths to fuel when the structure is used as a pressure vessel.

- (d) *Fiber breaking*: Microcracks in composites are formed because of the poor interfacial bonding when subjected to tensile loading. These microcracks lead to delamination, and fiber breaking would be the next mode of failure after delamination. Since the adjacent layers with no microcracks tend to bear the entire applied load, their fibers tend to crack leading to fiber breakage.
- (e) *Fracture*: This is the final stage of failure and the material breaks and separates out. Fracture might be in the form of complete detachment of the materials or constrained ply cracking. Figure 1-4 shows the various types of damage observed in a composite material when subjected to uniaxial loading [9]. 0° - ply means all fibers are along the loading direction, so in the below figure, the loading direction is in vertical direction, along the fibers.

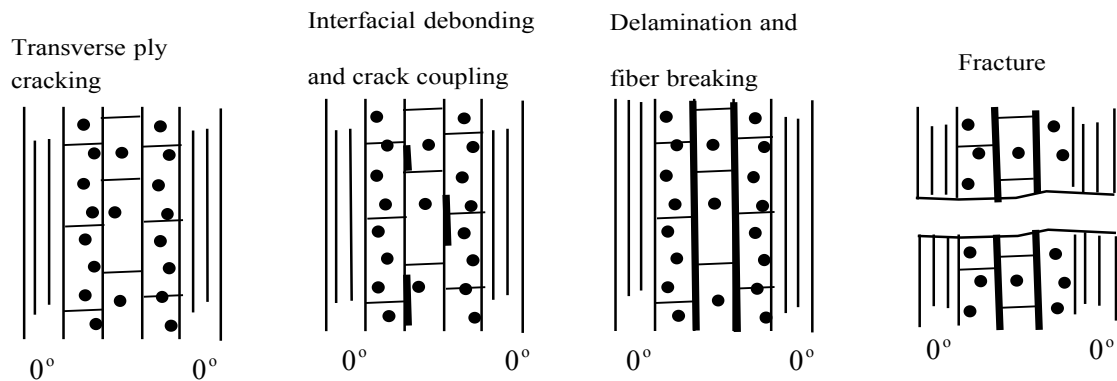


Figure 1-4 Modes of damage in a composite material [9]

As discussed above, many of damage modes are covert and the evolution of such damages imposes a major challenge for damage inspection. Many non-destructive inspection methods tried to identify the damage evolution in composites. These methods include visual inspection, automated tap test, bondmaster, handheld UT camera, phased array UT, thermography and shearography. However, many of these methods are

designed for near surface damage detection and have their own limitations. For instance, tap test, bondmaster, shearography and thermography have some limitations in detecting delamination and disband, but they can detect impact damages very well. Ultrasonic inspections can detect delamination and disband but the level of training for qualified inspectors is very high and the equipment is very expensive [11]. The highly heterogeneous nature of composites leads to large background noises that negate the effectiveness of wave-propagation-based detection methods. Furthermore, different damage modes (ply cracking, matrix/fiber splitting, delamination, microbuckling) in composites exhibit vastly different sensitivities to different inspection methods. Due to these difficulties, no established certification procedures have been established by governmental regulatory authorities. High-fidelity modeling that can accurately predict damage modes and locations is of critical importance [8].

Computational solid mechanics provides a powerful tool for designers and engineers to model parts, components, assemblies, and structures [2]. By assuming the composite to be a homogeneous material with directional material properties, a designer may study stress patterns and stress concentration regions in the assumed component. Several failure criteria have been proposed throughout the years that can be applied at this level of analyses [2].

A more detailed study can be performed with mesomechanical analysis. Although still consider the lamina as a homogeneous material, at this level, the mechanical behavior of a lamina is modeled using constitutive material models. Computational effort is not very high and a more profound study of different damage mechanisms can be investigated [2].

Most recent advances in simulation technology and network computing, have led to a new level of analysis, named micromechanical analysis. This type of model looks upon the behavior of each constituent of the composite, i.e. the composite is seen as a heterogeneous material. Although computationally more expensive, it allows the analyst to have a good overview on the influence of each constituent in the mechanical behavior of the composite. All kinds of damage mechanisms can be recreated at this level of analysis [2]. However, the most challenging task is to correlate the microscopic damage development with large scale structural performance.

Prediction becomes problematic after beginning of damage. The fundamental difficulty is that damage in structural composites involves extremely complicated nonlinear processes acting from the microscale (e.g., microcracking and crazing in polymers), to the scale of the structure itself (e.g., large cracks and global buckling). These multiple damage modes occur in various scales at different load levels and are strongly coupled to each other. This nonlinear coupled damage evolution dominates the macroscopic composite behavior [8].

Figure 1-5 shows the extensive multiple damage that occurred near through-thickness slits or holes in multidirectional laminates [12,13].

Dominant splitting cracks appear as sharply defined horizontal lines (in an H configuration) and eventually span the specimen, tending to isolate the strip containing the slit; wedge-shaped delaminations between the plies appear as areas of shadow around the splitting cracks; and myriad microcracks appear between fibers in the transverse plies.

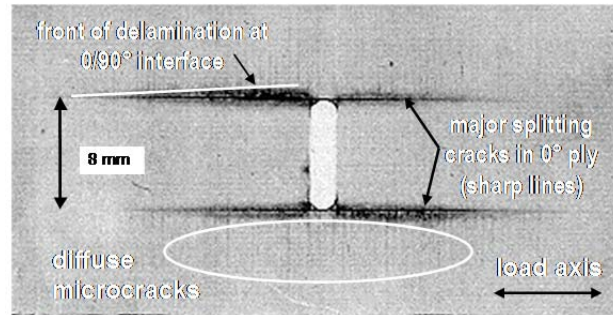


Figure 1-5 X-ray radiography reveals damage mechanisms viewed through the ply stack in a laminated PMC containing aligned (0°) and transverse (90°) fiber plies loaded in tension [13]

Many composite damage studies and predictive methods can work for individual modes, using either continuum theory based models or micromechanics models. For example, continuum damage mechanics (CDM) has been developed to account for the diffuse micro-cracks that occur in off-axial plies [14-16]. Linear elastic fracture mechanics (LEFM) and its computational form of virtual crack closure technique (VCCT) have been used to study delamination cracks in laminated PMCs. However, the requirements of self-similar delamination growth and of a postulated (large) pre-existing crack limit its usefulness to important delamination problems such as free edge crack nucleation and propagation, and delamination in composite panels due to low velocity impact [17]. Several micromechanics models for fiber rupture and fiber/matrix interface cracking have also been developed [17-23]. However, the complex, nonlinear coupling among different damage modes has yet to be fully understood. This is the key to resolving the long-standing question of how to quantify the influence of stacking sequence on the mechanical properties of laminated PMCs [8].

Therefore, there is a high demand from composite engineering communities for a numerical platform that can 1) allow for explicit description of the arbitrary damage

initiation and propagation a priori to final failure; 2) account for the multiscale issues in all major damage processes; 3) include strong nonlinear coupling among all major damage processes that lead to final failure, and 4) offer reliable predictions with high fidelity.

1.4. A review on damage modeling in composite

The ultimate goal in the field of applied solid mechanics is to establish the ability to design structures or components that are capable of safely withstanding static or dynamic service loads for a certain period. In the past, many methods have been developed in an effort to solve the crack initiation and propagation problem. Analytical, semi-analytical and numerical approaches, such as the boundary integral method, the boundary element method, the finite element method and recently a number of meshless methods, have been successfully used for modeling crack aspects of such damage modeling in solids [24].

This is critical in damage tolerance design because to design tolerance, the material or structure is considered to contain flaws and one must decide whether to replace the part or leave it in service under a more tolerable loading for a certain period of time. Such decision making is usually based on the knowledge from fracture mechanics.

Fracture mechanics deals with the mechanical behavior of solids containing cracks or crack-like flaws [25]. The wide range of applicability of the engineering fracture mechanics disciplines is shown in Figure 1-6. In atomic scale which nowadays called Nano-scale, fracture mechanics can be applied to analyze bond breaking between atoms. In experiments such as the tension test for a notched plate, fracture mechanics is needed

to model the problem. In real applications such as ships, aerospace and automation, application of fracture mechanics is crucial to guarantee the safety.

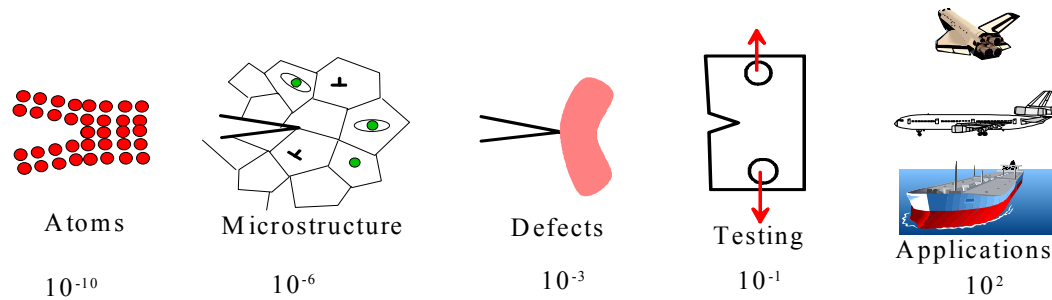


Figure 1-6 wide range of applicability of the Engineering Fracture Mechanics [25]

1.4.1. Linear Elastic Fracture Mechanics

The linear elastic fracture mechanics originated from a seminal study of C. E. Inglis on a flat plate with an elliptical hole, as shown in Figure 1-7. The plate is of infinite dimensions and is loaded far field in tension. He derived that the stress at the tip of the

major axis equals to $\sigma \left(1 + \frac{2a}{b} \right)$. Note that the geometrical parameter in the parenthesis is

the stress concentration factor (SCF), when $a=b$, it is a circular hole, $SCF=3$. A crack-like discontinuity can be modeled by making the minor axis much smaller than the major

axis. In such a case, the radius of curvature, $\rho = \frac{b^2}{a}$, approaches zero and results in an

infinitely large stress at the crack tip.

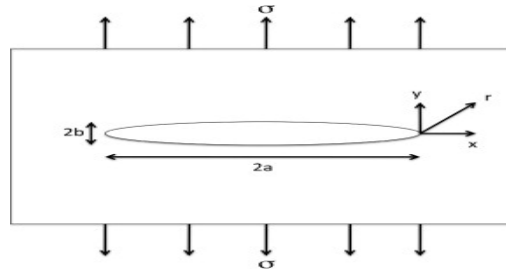


Figure 1-7 Elliptical hole in an infinite plate [25]

A. A. Griffith made use of the Inglis solution by calculating the effect of the crack on the strain energy stored in an infinitely cracked plate. He proposed that this energy, which is a finite quantity, should be taken as a measure for the crack propagation tendency. He also did some tests on cracked glass spheres and showed that the simple elastic analysis could be applied to describe the propagation of different size cracks at different stress levels [25].

Dr. G.R. Irwin extended the Griffith approach to metals by including the energy dissipated by local plastic flow, and later developed the energy release rate (ERR) concept, which was related to the Griffith theory but in a convenient form to solve engineering problems [25].

Later, he used the Westergaard approach to show that the stresses and displacements near the crack tip could be described by a single parameter that was related to the energy release rate. This crack tip characterizing parameter later became known as the stress intensity factor (SIF).

In practice, all this work was largely ignored by engineers as it seemed too mathematical and it was only in the 1970s that fracture mechanics came to be accepted as a useful and even essential tool. Some of the reasons were development of non-destructive examination methods which revealed hidden cracks in structures, the demand of space

industry for high-strength high integrity pressure vessels, the increasing use of welding and the severe conditions of offshore structures, etc.[25]. Hence, most of the practical development of fracture mechanics has occurred in the last forty years.

Generally speaking, there are two types of fracture problems. One is the computation of fracture properties of a given, stationary crack. It involves the calculation of fracture driving force, such as stress intensity factors, J-integral, and energy release rate, on the crack tip, and establish criteria to determine whether crack will propagate or not, and in which direction the crack will propagate. The other one is computation of fracture properties of a moving or dynamic crack.

In linear elastic fracture mechanics (LEFM), an idealized traction-free crack is assumed and all the material resistance to crack advance (the fracture toughness) is assigned to a point process located at the crack tip; the rest of the body is assumed to be linear-elastic. The fracture toughness proves to be a material constant for large cracks [26].

After calibrating, LEFM can be very useful in predicting the external loads at which the crack tip conditions will cause crack propagation for any component geometry. LEFM has been remarkably successful in engineering design, including the design of composites with sufficiently large cracks. Conservative and therefore safe design can be achieved by assuming that a big enough crack, detectable in service inspections, is present, and the load that LEFM predicts for crack propagation exceeds service loads. However, creating realistic damage simulations requires much more than this. The initiation of damage at stress-concentrating sites must be predicted for parts that contain no cracks, and the gradual evolution of initiated damage into large cracks must be modeled. The critical

conceptual limitation of LEFM is representing all the material nonlinearity during crack extension as a point process that will be discussed in more detail later [26].

Using the theoretical achievements, lots of singular shape functions have been built to be implemented into FEM packages and led to development of computational aspects.

Parks presented a technique in determining stress intensity factors based on energy release rate without introducing special singular crack tip elements [27]. The crack is advanced by moving nodal points rather than by removing nodal traction at the crack tip [8]. Some other methods were emerged based on LEFM; virtual crack closure is one of them. The virtual crack closure technique (VCCT), based on the results from a FE stress analysis, has been widely applied to interfacial cracks to compute total and component energy release rates. It shows relative insensitivity to the mesh pattern and mesh density [28].

VCCT was introduced by Rybicki and Kanninen [29] for line cracks and Shivakumar et al., [30] extended that for planar cracks. They used Irwin's assumption to calculate the energy release rate, assuming that the energy released in the process of crack extension is equal to the work required to close the crack to its original state as the crack extends a small amount.

An overview of the VCCT for interfacial cracks with a fixed (self-similar) crack front is provided by Krueger [31]. A two-vector algorithm to trace a crack front was proposed by Xie and Biggers [32], so that the VCCT can be applied to moving delamination problems without using adaptive remeshing.

Slant cracks under mixed mode loading have been studied extensively. In [33], Ishikawa proposed a two-step VCCT approach to separate the strain energy release rate

components through the variation of the stiffness matrix of the crack tip elements. Combining weight function concept and VCCT, Sha and Yang [34] developed procedures to calculate stress intensity factors directly and accurately. Raju [35] developed the explicit expressions for strain energy release rate components for higher order and singular elements in terms of nodal forces and displacements. Shivakumar and Raju [36] presented a general formulation of the equivalent domain integral method for mixed-mode fracture problems in cracked solids. For dynamic fracture mechanics, Nishioka and Atluri [37] introduced a new path independent integral that has the meaning of energy release rate for a propagating crack under mixed mode loading. In [38], Nishioka and Atluri analyzed the dynamic propagation of a slant crack under mixed-mode loading which had been used as a benchmark example in dynamic fracture mechanics.

In crack kinking, the formulations developed for VCCT of a slant crack cannot be used, because it relies on self-similar crack growth while in the kinked one, the crack path changes direction. However, by adopting a different formulation in conjunction with the VCCT, energy release rates can be computed to evaluate the trajectory of kinking cracks and kinking crack fronts [28]. Beam theory can be adopted for simple configurations of adhesively bonded strips, with similar adherends to obtain energy release rates analytically [39]. Procedures to obtain strain energy release rates for planar structures analytically, such as plates, were developed by means of solving a series of integral equations by Hayashi and Nemat-Nasser [40], Azhdari and Nemat-Nasser [41] and He and Hutchinson [42]. Based on Betti's reciprocal theorem, Palaniswamy and Knauss [43] proposed an analytical expression for the total energy release rate, G , which requires a

two-step analyses. Becker et al., [44], implemented a two-step VCCT to calculate the strain energy release rate for crack kinking in functionally graded materials. In the paper by Xie et al., [28], the expression for G given in [43], is partitioned into mode I and mode II components and its equivalent approximation is used to develop a new one-step VCCT for kinking cracks.

As mentioned in previous section, delamination is one of the most common and destructive failure modes in composite structures. Several researchers tried to deal with that by means of different methods [45-47], which VCCT is one of the first ones to consider delamination. The remote loadings applied to composite components are typically resolved into interlaminar tension and shear stresses at discontinuities that create mode I, II and III delaminations. The use of fracture mechanics to characterize the onset and growth of these delaminations has become common practice over the past two decades [48-50]. Calculation of the total strain energy release rate, the mode I component due to interlaminar tension, the mode II component due to interlaminar sliding shear, and the mode III component, due to interlaminar scissoring shear would be necessary [31].

By comparing these calculated energy release rate components to interlaminar fracture toughness properties that measured over a range from pure mode I to pure mode II loading, delamination onset or growth for 2D problems can be predicted [51-55]. Based on results from 2D and 3D finite element analyses, the VCCT [29,35,56] can be used for computing energy release rates to supply the mode separation required when using the mixed-mode fracture criterion [31].

Other than above, the LEFM-based VCCT has been used in conjunction with shell elements for delamination analyses with some success. Yet VCCT has met limitations in

dealing with real composite structures. The oscillatory nature of the singular crack-tip stress field in orthotropic composite laminates introduces numerical instabilities as well as mesh-dependency [57]. This leads to a very restrictive rule for the crack-tip structural element size, it has to be between $1/4$ and $1/2$ of individual ply thickness [58,59]. Moreover, Glaessgen observed that in shell VCCT models of bonded specimens with unequal thicknesses of adherends, the mode mixity did not converge with mesh refinement [60]. This phenomenon is similar to the well-known oscillatory behavior of the in-plane linear elastic stress field surrounding a bimaterial interfacial crack tip [8].

Another shortcoming of the LEFM type methods arises when the crack tip touches an elastically mismatched interface, where the J-integral becomes path-dependent and the energy-based criterion becomes ineffective. In fact, LEFM becomes ineffective even before the crack tip reaches the interface. LEFM predicts that a crack penetrates the interface at either zero or an infinite value of the applied load, depending on the relative stiffness of the bonded materials [61-63]. This implies that a crack cannot extend to a compliant/stiff interface, independent of the material toughness and strength, which is obviously wrong. Cracks may cross a compliant/stiff interface if the tensile strength of the material ahead of the interface is low enough. In such a case, a secondary crack may initiate ahead of the interface before the primary crack reaches the interface. Hence, if only the energy criterion is applied, the behavior of a crack near a compliant/stiff interface may be incorrectly predicted. Therefore, LEFM sometimes fails to predict correctly the behavior of a crack approaching elastically mismatched interface because no LEFM parameter can describe the crack driving force when the crack tip touches the interface. Another more important reason is that the failure of the material ahead of the

interface is not taken into account in LEFM, because it assumes that the failure occurs only at the crack tip [64].

The stress intensity factors or corresponding energy release rates are the only single macroscopic parameters that characterize the details of the local crack tip fields. These global parameters are related to the corresponding material parameters typically the fracture toughness that determine the critical conditions of initiation of crack growth. When the crack tip experiences plastic yielding, the above concepts, based purely on the theory of elasticity, are not valid and have led to the introduction of a path independent J-Integral [65], which is strictly valid for a nonlinear elastic material. If the energy near the crack tip region is converted into significant inelastic energy due to plasticity or when the material locally unloads during the propagation process, the property of path independence is lost. The fracture mechanics analysis presupposes the existence of an infinitely sharp crack leading to the singular crack tip fields. However, in real materials neither the sharpness of the crack nor the stress levels near the crack tip region can be infinite [66]. Further, for cracks along bimaterial interfaces, the crack tip will no longer be embedded in a square-root singular stress field, leading to a condition that stress intensity factor may either be zero or infinity [63,67]. To overcome these limitations in point-wise methods, other approaches are necessary to have more accurate and realistic description of fracture process. This leads to the cohesive zone models.

1.4.2. Nonlinear Fracture Mechanics

As an alternative approach to the singularity driven LEFM approach, Barrenblatt [68,69] and Dugdale [70] proposed the concept of cohesive zone model (CZM). The evolution of CZM as a preferred method to analyze fracture problems in monolithic and composite material systems was not only because it avoids the singularity but also because of its easy implementation in a numerical method of analysis such as in finite element or boundary element method [66].

Cohesive models are able to represent many damage mechanisms such as delamination of plies, large splitting (shear) cracks within plies, multiple matrix cracking within plies, fiber rupture or microbuckling (kink band formation), friction acting between delaminated plies, process zones at crack tips representing crazing or other nonlinearity, and large scale bridging by through-thickness reinforcement or oblique crack-bridging fibers [71].

Cohesive zone models are usually used to model the initiation and propagation of cracks along an interface between two solids, and to model adhesion between two contacting surfaces, by using constitutive laws between separated surfaces.

A “cohesive zone law” relates the relative motion of the two solids adjacent to a surface to the tractions transmitted across that surface. A large number of such constitutive equations have been developed, but there are two general classes:

- (i) Reversible traction-displacement laws, in which the traction is simply a function of the relative distance between the two surfaces, and independent of the history of loading. These are often used to model nucleation and growth of a crack on an interface that is subjected to monotonically increasing loading,

where irreversibility plays no role; and are also used to model interaction between surfaces of nanoscale structures, whose dimensions can be comparable to the distance of action of long-range interatomic forces.

- (ii) Irreversible traction-displacement laws, which model failure processes that lead to the creation of new free surface in the solid. These could include separation of atomic planes due to cleavage, or more complex processes such as rupture by void nucleation and coalescence, or fatigue [72].

Lots of popular CZMs are available in the literature which the main difference between them is in shape and model parameters. Needleman was a pioneer in using polynomial and exponential types of traction-separation equations to simulate particle debonding in metal matrices [73-75]. Xu and Needleman [76,77] further used the above models to study the void nucleation at the interface of particle and matrix material, fast crack growth in brittle materials under dynamic loading, and dynamic crack growth along the interface of bimetals. Tvergaard and Hutchinson [78] used a trapezoidal shape of the traction-separation model to calculate the crack growth resistance in elasto-plastic materials. Yang and Toughless [79,80] and Tvergaard [81] used a quadratic traction-displacement equation to analyze interfaces. Camacho and Ortiz [82] employed a linear cohesive fracture model to propagate multiple cracks along arbitrary paths during impact damage in brittle materials. Geubelle et al., [83] utilized a bilinear CZM to simulate spontaneous initiation and propagation of transverse matrix cracks and delamination fronts in thin composite plates subjected to low-velocity impact.

In all CZMs (except Dugdale's model and Camacho et al.'s model), the traction-separation relations for interfaces are such that with increasing interfacial separation, the

traction across the interface reaches a maximum, then decreases and eventually vanishes, permitting a complete decohesion for a typical variation. It has been well recognized that CZMs can be described by two independent parameters which may be two of the three parameters, namely the cohesive energy, and either of the cohesive strength, or the separation length [84-86]. It should be noted that cohesive energy, surface energy and work of fracture are all expressed as energy per unit area and hence are truly rate quantities.

CZMs have been used to simulate the fracture process in a number of material systems including polymers [84], metallic materials [87], ceramic materials [82], bimaterial systems in polymer matrix composites [76], metal matrix composites [88], and fiber reinforced plastic composites [89]. They have been used to simulate fracture under static [75,77], dynamic [76,82], and cyclic [90] loading conditions. The success in applying to other material systems such as adhesively bonded joints [91,92], and more recently in textile and laminated composites [71,93-101], have also been shown.

A number of different attempts have been made to consider rate effects in a material separation model in recent studies. Knauss and Losi [102] combined a viscoelastic constitutive model with a damage function. Rahulkumar et al., [103] and Allen and Searcy [104] adopted a hereditary integral approach. Bazant and Li [105] formulated a rate-dependent cohesive crack model. Xu et al., [106] had also proposed a rate-dependent CZM, having both rate-independent and rate-dependent material parameters which are determined from experiments and numerical analysis [107].

Yang et al., [108] applied cohesive zone model for efficient and accurate modeling and simulating crack growth in a thin plate under bending. The genuinely 3D crack front is

modeled as a 2D process zone with part-through damage exhibiting residual flexural rigidity and residual strength across the crack line. The model is applicable to a crack with a relatively long crack front compared to the whole crack as well as to the plate thickness. It essentially models the crack growth in two hierarchical steps: (a) through the thickness; and (b) in the in-plane direction. It leads to an efficient and accurate solution to the genuinely 3D crack growth problem in thin plates. Furthermore, the cohesive zone model eliminates the crack-tip singularities appearing in a singularity-based approach [107].

More importantly, CZMs can be used to represent multiple mechanisms acting to supply tractions across delamination, splitting, or other cracks [98,109,110]. The key is that a CZM utilizes a complete traction-separation law to describe a fracture process, rather than using a single energy based parameter (i.e. fracture toughness) as in traditional methods such as in LEFM. This makes CZM very adaptive to any particular fracture processes: simply by varying the traction-separation law a host of different fracture processes can be represented without changing any numerical aspect of the CZM. This attractive feature makes CZMs widely used in composite failure analyses.

It is even possible to devise a cohesive law that can represent multiple mechanisms that are active in a fracture process zone. More recently, cohesive laws with multiple tip processes consideration have been proposed and used successfully in modeling many engineering fracture problems. For example, a bilinear softening law has been used in modeling the fracture process in human cortical bond with distinct mother-daughter cracking pattern [111,112]. Davila et al have also studied the procedure for superposing

linear cohesive laws to represent multiple damage mechanisms in the fracture of composites [97,113].

The model by Xu and Needleman induces artificial compliance due to the elasticity of the intrinsic cohesive law [107]. To alleviate such problems, Geubelle and Baylor [114] and Espinosa and Zavattieri [115] adopted bilinear cohesive zone models to reduce the compliance by providing an adjustable initial slope in the cohesive law.

As discussed above, CZM could alleviate some shortages of point-wise methods such as LEFM by considering fracture process zone and traction separation behavior using constitutive laws. By changing cohesive law's shape and parameters, different problems can be modeled and solved. The required parameters for constitutive law can be found by experiments for different fracture modes.

Although CZM has been widely used in composite fracture analysis, especially in delamination analysis [32,71,98,116-118], the traditional CZM approach carries the major shortcoming that it requires the potential crack path be known a priori, so that CZM elements can be directly implanted along the path. This greatly limits the application of CZM for problems with evolving arbitrary discontinuities and motivates scientists to come up with better methods such as X-FEM and A-FEM.

1.5. Advances of Numerical methods for Arbitrary Cracking in Solids

Due to complexity of the progressive damage processes in composite materials, numerical simulation based tools for full-scale analysis is inevitable. In this regard, finite element method (FEM) based simulation techniques have been powerful tools for thermo-mechanical analysis in solids.

The finite element method (FEM) has become one of the most popular and powerful analytical tools for studying the behavior of a wide range of engineering and physical problems. Quick development of several general-purpose finite element softwares, which were verified and calibrated over the years made them available to almost anyone who asks and pays for them [24].

In applied mathematics, FEM is a general mathematical tool for obtaining approximate solutions to boundary value problems. It uses variational methods (the calculus of variations) to minimize an error function and produce a stable solution. Similar to the idea of approximating a larger circle by many tiny straight lines, FEM also approximates a complex equation on a large domain by many simple equations on smaller subdomains, called finite elements [120].

Although the name of finite element method was given in last few decades, the concept dates back to long times ago. For instance, finding a circumference of a circle by approximating it by the perimeter of polygon by ancient mathematicians was among first FEM applications [120]. The basic ideas of the finite element method as known today were presented in the papers of Turner et al., [121] and Argyris et al., [122].

The name *finite element* was coined by Clough [123]. The development of FEM traces back to the pioneering work by Courant in 1942 who used finite element type of procedure in minimizing the potential energy for the torsion stress using grid values as the unknown parameters [124]. The application of simple finite elements (pin-jointed bar and triangular plate with in plane loads) for the analysis of aircraft structure which is presented in [121] and [125] is considered as one of the great steps in the development of the finite element method.

Several calculations involved in the finite element analysis can be performed in digital computers, so keeping the method practically viable. Application of finite element method was quickened by superfast development of high-speed digital computers. The book by Przemieniecki [126] presents the finite element method as applied to the solution of stress analysis problems. Zienkiewicz et al., [127] presented the broad interpretation of the method and its applicability to any general field problem.

A brief history of the beginning of the finite element was presented by Gupta et al., [128]. With all the progresses, today engineers and applied scientists consider the finite element method one of the well-established and convenient analysis tools [120].

Currently many powerful general purposed FEM packages are available for researchers, students and design engineers (ABAQUS, NASTRAN, ANSYS, ADINA, etc.) While these commercial softwares are increasingly widely used for stress analysis of materials and structures, their capability in analyzing fracture problems, especially coupled multiple cracking problems remains limited [120].

However, traditional finite element methods are based on homogenized continuum theories and usually assume a continuous displacement field within an element (with continuous shape functions). In this section, we briefly review the current state of art in numerical methods for damage modeling [8].

The fundamental difficulty for classic FEM to model fracture problems lies in the fact that the interpolation functions (shape functions), used to approximate elemental displacements from nodal degrees of freedom (DoFs), are typically continuous. However, if an element is cracked, the displacement field in the element becomes discontinuous.

The inability of classic FEM in dealing with discontinuities encouraged researchers to look for alternative methods [8]. Throughout the years many methods have been established to deal with crack or discontinuity in the solid body. Nevertheless, significant challenges remain, many of which relate to the difficulty of developing practicable formulations for dealing with materials containing complex material heterogeneity such as textile composites. Lots of special problems with accurate prediction of local stress and strain fields can be posed by heterogeneity, which can vary strongly with local material features; and with predicting cracks and localized damage bands, which can appear during damage evolution not only on the material boundaries, but also on other surfaces that cannot be specified *a priori*. Such highly heterogeneous materials present unique challenges that cannot be resolved by mainstream formulations of conventional materials/structures modeling. One issue is that the scale of material heterogeneity is on the same scale as that of the features of the structures, which negates the common strategy of homogenizing the material properties in simulations. Another unresolved challenge that is even more critical to composite structural safety and durability is how to accurately account for the damage initiation and propagation and simulate their detrimental effects on structural integrity in a quantifiable way. These challenges call for advanced numerical analysis platforms that can 1) efficiently deal with arbitrary material heterogeneity and the progressive damage/debonding evolution along material interfaces and boundaries; and 2) account for multiple cracks merging into interfaces or bifurcating away from interfaces in a physically consistent manner, without *a priori* knowledge of the crack paths [129]. In the past decades, there have been rapid developments in

advanced numerical methods to cope with such challenges that a brief review over them is provided in next sections.

1.5.1. Continuum Damage Mechanics

The so-called continuum damage mechanics (CDM) is a popular method to seek the use of nonlinear material constitutive law to account for at least the load-bearing loss due to fracture. A CDM theory considers the degradation of material stiffness matrix in the macro-scale by homogenizing the microscopic damage events using the damage mechanics concept [8].

Murzewski [130,131] proposed damage parameter for the first time, and put forward a probabilistic interpretation of the decohesion parameter. Following his work, Kachanov [132] and then Rabotnov [133] formulated the famous equation of damage growth under creep conditions for the uniaxial state of stress. After formulation of theory in the 1950s, Odqvist and Hult [134] published one of the first papers in the Western scientific literature in the early 1960s. Since then, a number of theoretical and experimental investigations have been performed by Chrzanowski [135], Chaboche [136], Krajcinovic [137] and Lemaitre [138]. Damage phenomenon includes different types such as fatigue, cracking, fracture, and creep, etc. Separate researches were done in each field [139].

Dhar et al., [140] proposed a damage mechanics model to study void growth and initiation of cracks. A failure curve was presented for the AISI-1090 steel material and a large deformation finite element analysis was carried out. Fashang and Kuang generalized crack tip stress and strain fields for various plane strain and plane stress fracture specimens [141]. These authors used CDM to quantify the constraints of the

fracture specimens and the effects of specimen configuration on the onset of ductile fracture growth [139].

Based on CDM, Chung et al., [142] simulated damage and crack propagation and meanwhile, they utilized the parallel computing technique for precise analysis with the large-scale structural model. Moyer et al., [143] examined an application of uncoupled CDM to predict stable crack growth in the 2219-T87 aluminum alloy. They presented a formulation of predictive damage methodology and its implementation into a finite element code. Mizuno and Honda [144] used double cantilever beam model to perform an analysis of cracks' growth in piezoelectric ceramics. A damage variable based on CDM used to represent damage within piezoelectric ceramics and its effect on material properties was considered in a constitutive equation of piezoelectric ceramics.

Tavares and King [145] developed a model based on CDM and the Hertzian contact theory to describe fracture by repeated impacts and several tests were done to obtain some experimental data to validate this model. In [146], Leski presented a numerical analysis of a rotor blade damaged in combat. A finite element model of the blade was built and tested and, based on experimental results, four instances of damage were chosen for numerical analyses of stress distributions in a damaged rotor blade.

One of the most important advantages of CDM is that the stress evaluation algorithm is usually explicit; therefore, it does not need to find iterative solutions for nonlinear equations.

However, if a major dominant crack emerges, the method becomes problematic because the major crack leads to high strain gradient and classic FEM is not efficient in dealing with that. More critically for composite materials, because of ill conditioning of the

orthotropic elastic stiffness after crack is introduced, premature convergence difficulties occur [8]. Numerical stress locking may also occur due to lack of discontinuous displacement modes in an element [147]. Introduction of enhanced assumed strain (EAS) has been integrated into the formulation at element level to improve modeling accuracy [148-150], which was an elemental based and thus fully compatible with standard FE program. However, the consistency across boundaries of adjacent elements cannot be guaranteed by element based embedded discontinuities.

Meso-scale averaging along with periodicity assumption is typically used in CDM to obtain homogenized constitutive relations. Several research groups attempted direct coupling of CDM-based in-plane damage modes with various fracture mechanics models for delamination but with only limited success [118,119,151]. Several recent studies have revealed that the homogenization process in CDM leads to loss of key information on multiple damage coupling at the macroscopic scale and results in inaccurate prediction of crack paths [151] and severe stress locking [152].

1.5.2 Generalized FEM (G-FEM) and eXtended FEM (X-FEM)

One of the methods that truly enable explicitly consideration of physical discontinuity in a FE element comes from the seminal work by Babuska and Melenk [153-155]. With this method (which the authors named Generalized Finite Element Method, G-FEM), it has been mathematically proven that any known solutions to boundary value problems can be superposed onto a classic FEM framework by invoking the partition-of-unity property of FE standard shape functions. The Generalized Finite Element Method (G-FEM) uses local spaces consisting of functions, not necessarily polynomials, which reflect the available information on the unknown solution and thus ensure good local approximation.

Then a partition of unity is used to “bond” these spaces together to form the approximating subspace.

A wide variety of shape functions can be used in the G-FEM. This allows the G-FEM to approximate non-smooth solutions of BVPs (boundary value problems) on domains having corners or multiple cracks, or with mixed type of boundary conditions successfully. The G-FEM either does not employ a mesh or uses a mesh only minimally. This allows the G-FEM, without re-meshing or with minimal re-meshing, to be used in problems involving domains with changing boundaries, or with an unknown boundary, as in crack propagation problems or free-boundary problems.

The effectiveness of G-FEM has been shown when applied to problems with domains having complicated boundaries, problems with micro-scales, and problems with boundary layers [156]. Quasi-optimal convergence rates of G-FEM approximation for the general elliptic boundary value problem have been proved [157].

The major cost of the G-FEM, when applied to problems with complex domains, is the numerical integration. In addition, the success of the G-FEM depends on efficient numerical integration based on adaptive procedures.

X-FEM is a special case of G-FEM, when PoU is used to account for cracks [154]. The seminal theory of PoU enables these methods to deal with discrete discontinuities (cracks and shear bands) by adding extra nodal DoFs (as in X-FEM) or phantom nodes (as in PNM) within the finite element framework [129].

The basic ideas and the mathematical foundation of the partition of unity finite element method (PUFEM) were discussed by Melenk and Babuska [155] and Duarte and Oden [158]. Later Belytschko and Black [159] presented a minimal remeshing finite element

method by adding discontinuous enrichment functions to the finite element approximation to account for the presence of a crack. The method was then improved by Moës et al., [160] and Dolbow [161] and called the eXtended Finite Element Method (X-FEM). The new methodology allowed the entire crack to be represented independently of the mesh and constructed the enriched approximation from the interaction of the crack geometry with the mesh.

More contributions from Dolbow et al., [162-164], Daux et al., [165] and Sukumar et al., [166] extended the method for three-dimensional crack modeling and arbitrary branched and intersecting cracks. The use of level set methods to represent the crack location was studied by Stolarska et al., [167], Belytschko et al., [168], Sukumar et al., [169], Moës et al., [170], Gravouil et al., [171], Ventura et al., [172], Zi et al., [173], Budyn et al., [174], Bordas and Moran [175], and Stolarska and Chopp [176].

Besides earlier works that led to progress from LEFM to X-FEM, simulation of localization and fracture has been the main target [24]. Jirásek and Zimmermann [177,178] successfully combined X-FEM with the damage theory and advocated a new concept of a model with transition from a smeared to an embedded discrete crack. Sukumar et al., [179] presented a two-dimensional numerical model of micro-structural effects in brittle fracture, while Dumstorff and Meschke [180] and Patzak and Jirásek [181] proposed an X-FEM for the analysis of brittle materials in the post-cracking regime. In a fundamentally different approach, Ventura et al., [182] proposed a new X-FEM for accurately modeling the displacement and stress fields produced by a dislocation. Simulation of growth of arbitrary cohesive cracks by X-FEM was reported by Moës and Belytschko [183]. The method was further advanced by Zi and Belytschko

[184], Mariani and Perego [185] and Mergheim et al., [186]. A proper representation of the discrete character of cohesive zone formulations by the so-called cohesive crack segments was proposed by de Borst et al., [187-189].

In order to develop a methodology for modeling shear bands as strong discontinuities within a continuum mechanics context, Samaniego and Belytschko [190] and Areias and Belytschko [191] used the enrichment ideas of X-FEM. Later, Song et al., [192] presented a new method for modeling of arbitrary dynamic crack and shear band propagation by a rearrangement of the X-FEM basis and the nodal degrees of freedom, describing the discontinuity superposed elements and the new concept of phantom nodes. The idea of elastic-plastic enrichments was also proposed by Elguedj et al., [193] based on the Ramberg–Osgood power hardening rule and Hutchinson–Rice–Rosengren elastoplastic fields for representing the singularities in elastic plastic fracture mechanics [24].

Fractures of composite materials are also widely studied by X-FEM. Dolbow and Nadeau [194] employed the X-FEM to simulate fracture behavior of micro-structured materials with a focus on functionally graded materials. Then, Dolbow and Gosz [195] described a new interaction energy integral method for the computation of mixed mode stress intensity factors at the tips of arbitrarily oriented cracks in functionally graded materials. In a related contribution, Remmers et al., [196] presented a new formulation for the simulation of delamination growth in thin-layered composite structures. Study of bimaterial interface cracks was performed by Sukumar et al., [197] by developing PoU enrichment techniques. Nagashima et al. [198] and Nagashima and Suemasu [199] described the application of X-FEM to stress analyses of structures containing interface

cracks between dissimilar materials. To include the effects of anisotropy on the enrichment functions, Asadpoure et al., [200], and Asadpoure and Mohammadi [201] developed three independent sets of orthotropic enrichment functions for X-FEM analysis of crack in orthotropic media.

In both G-FEM and X-FEM, special solutions, or at least the functional forms of the solutions, such as crack-tip singular displacement fields and displacement functions, have to be known a priori, so that they can be incorporated into G-FEM or X-FEM as enrichment functions. In laminated or textile composite materials, due to the highly heterogeneous nature, solutions of many cracking systems are not necessarily known [8]. Furthermore, in composite materials, different cracking systems often interact with each other. An example is given in Figure 1-8. This figure shows a splitting crack in the top ply of a laminate and delamination crack induced by the splitting crack. For the location far away from the joint front of the two types of cracks, enrichment functions (f_1 , f_2) may be used. However, at the joint front when the two cracks interact directly, no known solution exists. X-FEM will have difficulty in dealing with this type of problems.

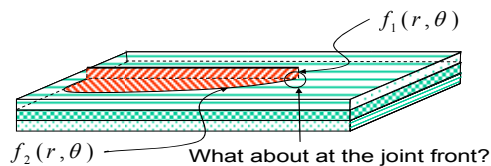


Figure 1-8 A splitting crack and its induced delamination in a composite laminate [8]

Another inconvenience of X-FEM in dealing with arbitrary cracking problems is that it enriches elemental displacement field through adding nodal DoFs, which requires dynamic adjustment of nodal DoFs according to whether a node is completely cut or not.

This not only leads to algorithmic changes of standard FEM, but also leads to incompatibility of X-FEM elements and traditional elements [168]. For example, for an element that encompasses a singular crack-tip, asymptotic displacement functions from fracture mechanics are needed as enrichment functions and the enrichment process leads to the loss of elemental locality in the sense that the blending elements, i.e., the uncracked elements that share the enriched nodes with the crack tip element, have to be treated simultaneously [160,170]. Additional ambiguities for the blending elements can arise and need special treatment [202]. For these reasons, it is difficult to integrate such an element into existing standard finite element programs.

X-FEM has proved its ability to study the crack merging and bifurcation problems due to multiple cracking in homogeneous isotropic or orthotropic materials, wherein the arbitrary intra-element crack merging or bifurcation can be facilitated with properly designated subdomain integration. However, to reach beyond this work, to heterogeneous materials such as laminated or textile composites, accurate modeling of both material interfacial debonding and bulk material cracking, and their nonlinear coupling when they intersect, becomes critical. For example, in laminated composites, intraply cracks tend to spawn local delaminations at interply interfaces and delamination cracks frequently branch into neighboring plies (crack jumping). Exactly where and when such events occur cannot be known *a priori*. While it has been demonstrated that X-FEM can model interface debonding in composites fairly accurately by treating the interfaces as weak discontinuities, the X-FEM will have difficulty in dealing with elements that host both a material interface and coalescing or bifurcating bulk cracks due to the facts that: (1) accurate functional forms of enrichment functions for interface cracks may not be readily

available, especially when the material directions across an interface are not orthogonal; and (2) the enrichment level will be unduly high [203].

1.5.3 Phantom Node Method (PNM) & Augmented FEM (AFEM)

An alternative numerical method that can also treat the arbitrary cracking problems is the phantom node method (PNM), first developed by Belytschko and coworkers [204] based on the initial work of Hansbo and Hansbo [205]. The essence of this method is to use overlapping paired elements to describe a strong or weak discontinuity in a physical element that is bisected by a crack (strong discontinuity) or a material interface (weak discontinuity). One of the advantages of this method is that it uses only standard finite element (FE) shape functions (i.e. more compatible with existing FE programs) and it can conveniently consider both weak and strong discontinuities. Based on this idea, Ling et al., [206] proposed an element with one or multiple copies of element nodes, to account for an arbitrary intra-element crack but otherwise remain a standard FE. This so-called augmented element is fully compatible with existing FE programs and has been implemented into a commercial FE program as a user-defined element [207]. Recent applications of the phantom node or augmented finite element method (A-FEM) include studies on arbitrary cracking in isotropic solids [186,208,209], composite delamination [210,211] and coupled delamination and transply cracking in composite laminates [110,206,212]. Moreover, Belytschko and coworkers have found that this method has some unique advantages in numerical handling of the direction normals associated with plate elements and they have successfully employed this method in analyzing large-scale plate/shell cracking under static and dynamic loads [204]. Fang et al., [203] proposed a new cohesive interface element, named the augmented cohesive zone (A-CZ) element, as

a development of the A-FEM. The new element allows for arbitrary separation of a CZ to conform to the cracking configuration of abutting solid elements. It provides physically consistent interface deformations and accurate stress transfer when arbitrary cracks merge into or branch away from an interface. Ling et al., [99] formulated a model of the phenomenon of delamination jumping across transverse plies by using nonlinear cohesive fracture models in the A-FEM. The nonlinearity of the fracture process zone and the interaction between multiple cracks combine to determine the details of how the delamination jump occurs.

A-FEM and PNM methods are relatively mesh-independent and computationally efficient when dealing with individual (i.e. non-interactive) cracks. However, in these methods each individual crack requires its own additional copy of DoFs or nodes to describe the discontinuous displacement field associated with it. Tracing the evolution of complex fracture surfaces of multiple cracks quickly becomes extremely tedious and numerically burdensome because, in such cases, there are no universal tracking algorithms that can judiciously assign different copies of DoFs or nodes to different cracks for complex crack configurations. Furthermore, the dimensions of local and global stiffness matrices must be dynamically modified in accordance with crack interaction, which makes it very difficult to integrate them into standard FE programs [165,213,214].

Therefore, it is beneficial to seek numerical methods that can account for arbitrary discontinuities with less numerical burden for tracing complex crack surfaces. In this regard, there are mainly two approaches in the literature. One method is the phase-field method [215-217], which introduces an additional nodal DoF to approximate a fracture surface with a highly concentrated yet continuous phase-field, which smoothes the

boundary of the crack over a small region. The major advantage is that the evolution of the fracture surfaces follows from the solution of a coupled system of partial differential equations. Thus, it does not require the fracture surfaces to be tracked algorithmically. This is in contrast to the complexity of many discrete fracture models, and is anticipated to be particularly advantageous when multiple branching and merging cracks are considered in three dimensions.

The phase-field model for quasi-static brittle fracture emanated from the work of Bourdin and coworkers on the variational formulation for Griffith's-type fracture models [218]. The variational formulation for quasi-static brittle fracture leads to an energy functional that closely resembles the potential energy presented by Mumford and Shah [219], which is encountered in image segmentation. A phase-field approximation of the Mumford-Shah potential, based on the theory of Γ -convergence, was presented by Ambrosio and Tortorelli [220]. This approximation was adopted by Bourdin et al., [217] to facilitate the numerical solution of their variational formulation.

Recently, this model has been applied in a dynamic setting by Bourdin et al., [221], Larsen et al., [222]; and Larsen [223]. However, application to structures of engineering interest has not been considered. An alternative quasi-static formulation of this phase-field approximation has been presented in the recent works of Miehe et al., [224,225]. In this formulation, the phase-field approximation follows from continuum mechanics and thermodynamic arguments. Besides the provision of an alternative derivation, Miehe et al., [224] also added various features to the model that are keys to its application to engineering structures. Independently from the phase-field formulation based on

Griffith's theory, dynamic phase-field fracture models have been developed based on Landau- Ginzburg type phase-field evolution equations, e.g., Karma et al., [226].

However, this method is mesh-dependent and it requires an extremely fine mesh to resolve the sharp discontinuity associated with an interface or a crack surface. The computational cost remains extremely high. There are also serious ambiguities regarding the non-zero stresses at crack wake surfaces.

Another approach that does not need additional DoFs when treating intra-element discontinuities is the embedded discontinuity approach. This method follows the earlier work in smeared localization models and enhanced strain methods [148,150,227-230] and it has been extended to account for discrete discontinuities by several research groups [231-238] following Simo and colleagues' seminal approach in treating plastic strain localizations with discrete discontinuous descriptions [239,240]. This approach seeks to enrich the elemental strain field by introducing a crack displacement field with assumed deformation modes (constant and/or linear mode), in addition to the regular continuous displacement field. The intensities associated with the crack deformation modes are considered as internal DoFs, which are either assigned to additional nodes (named enriched nodes) as global DoFs such as in [236], or fully condensed at elemental level as in [234,235,237,239]. It is a common practice to interpolate the discontinuous crack displacements within an element with special (or regularized) shape functions and the strain field resulted from the crack displacements is often taken as the enhanced strain field. The major advantage of this method is that it maintains the standard Galerkin FE structure with standard integration quadrature. The special shape functions, though, have to be carefully constructed so that the resulted enhanced strain field satisfies the

orthogonal principle derived by Simo et al., [240]. Otherwise, spurious deformation modes or serious stress locking may occur [238]. However, this method is less convenient in treating multiple interactive cracks within an element, which is necessary in considering the arbitrary crack coalescence and bifurcation phenomena widely observed in heterogeneous materials.

In any composite material, the issue of material heterogeneity is of paramount importance. The above advanced numerical methods can all deal with arbitrary cracking in homogeneous materials, but their capability in dealing with material heterogeneity remains to be addressed. Because most of them need additional nodes or DoFs, there are some limitations in modeling complicated fracture patterns and the ones that can do are very costly and tedious. This PhD study is dedicated to the development of the new A-FEM that can treat arbitrary cracking phenomena in heterogeneous materials.

1.6. Research Goal

This study is aimed at obtaining a more complete understanding of the multiple damage coupling in solids and its effects on macroscopic mechanical behavior. This will be enabled by the development of an efficient A-FEM based numerical platform that can deal with arbitrary damage evolution and their coupling in homogeneous as well as in heterogeneous materials. The new A-FEM will eliminate the need for additional DoFs or nodes to account for intra-element cracks and it does not need to assume deformation modes *a priori* for discontinuities because they will be natural outcomes from element equilibrium consideration. The anticipated advantages of the new A-FEM over other parallel methods are (1) permitting smooth transition from a weak discontinuity to a strong one, (2) allowing for repeated elemental augmentation to enable multiple,

interactive intra-element discontinuities to account for crack merging (from a bulk material domain into a material interface) or crack bifurcation away from the interface and 3) offering greatly improved numerical accuracy, efficiency and robustness. It will also be shown that the derived augmented element can be easily implemented into any standard FE package, including commercial software package as an add-in to the element library.

Chapter 2: Two-Dimensional A-FEM–Single Crack Formulation

2.1. Overview

Despite extensive research efforts in recent decades on composite materials, predicting the progressive failure of these materials remains a challenging task due to the complicated interactions among multiple damage processes. For laminated composites, the damage processes include transverse matrix cracking, fiber rupture (in tension) or kinking (in compression), splitting between fiber and matrix, and interlaminar delamination [71]. Experimentally it has been widely observed in laminated composites that the intra-ply and inter-ply damages strongly interact with each other to form complex 3D crack networks. Two such examples are given in Figure 2-1.

Figure 2-1 (a) shows the multiple damage modes in a double-notched tension specimen with symmetric $[0/90]_s$ ply stack. Dominant splitting cracks in the 0° -ply appear as sharply defined horizontal lines (in an H configuration) and eventually span the specimen. Many transverse cracks in the 90° -ply occur during the load increase. In addition, the major splitting cracks are accompanied by wedge-shaped delaminations between the plies (areas of shadow around the splitting cracks). Figure 2-1 (b) shows the multiple cracking features in a quasi-isotropic laminate ($[-45/+45/90/0]_s$) with a center open hole. The splitting cracks are shorter and the delaminations are lobe-shaped and transverse cracking occurs predominantly in the $\pm 45^\circ$ -plies. Note that the intra-ply cracks, i.e., the splitting cracks in the 90° -ply and off-axial cracks in $\pm 45^\circ$ plies are distributed differently in space in different plies, but show evidence of coupling via (dark lobed regions) at inter-ply interfaces [207].

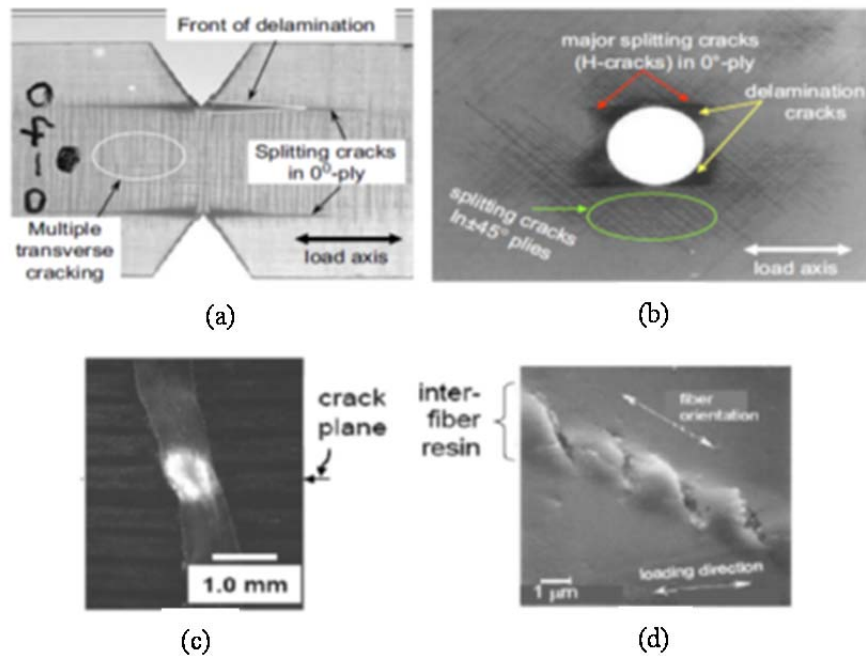


Figure 2-1 X-ray radiography reveals damage mechanisms viewed through the ply stack in (a) a double-notch tension specimen with symmetric orthogonal ply stack $[[0/90]_s) [241]$, and (b) a quasi-isotropic laminate $[-45/+45/90/0]_s$ with a circular open hole under tensile loading [12]. (c) Polarized light micrograph shows distributed damage in a fibrous stitch that has been sheared by a mode II delamination crack [242]. (d) Scanning electron micrograph of an echelon cracking between two fibers in a carbon-epoxy composite loaded in off-axis tension [243]

As well as the crack systems visible in Figure 2-1, microscopic examination shows some fine-scale shear deformation within individual plies. This deformation arises under shear loading. It is continuously distributed, rather than discrete, over spatial scales much smaller than the spacing of any of the crack systems shown in Figure 2-1, and is therefore a distinct mechanism. While not always examined in full detail, the distributed shear deformation is likely to consist at the fiber scale of crazing or arrays of microcracks,

whose length typically span the distance between neighboring fibers, i.e., 1 μm to order of magnitude. Examples appear in old experimental studies: Figure 2-1(c) shows fine-scale damage distributed throughout the section of a fibrous reinforcing stitch that has been sheared by a mode II delamination crack; Figure 2-1(d) shows an array of microcracks between two off-axis fibers in a carbon/epoxy composite loaded in tension. In both cases, shear damage arises from μm -scale phenomena. Several authors have included that shear nonlinearity of the ply material is necessary to achieve good correlation between simulations and experiments, especially for predicting splitting crack growth accurately [98,117,119].

Thus the total damage system in a polymer composite is subject to arbitrary stress states and comprises of multiple crack types and possibly fine-scale distributed shear damage. How to account for these multiple damage mechanisms that have strong interactions in an accurate and computationally efficient scheme remains a difficult task [207].

Traditionally, the intra-ply and inter-ply damage processes were treated separately with different theories: the delamination problems were extensively analyzed using either LEFM methods [59, 60,244] or cohesive interface models [71,100,116,117,241,245]. For the intra-ply damage modes, numerous strength based criteria coupled with CDM for strength degradation have been used [246-248]. Direct coupling of CDM-based in-plane damage modes with various fracture mechanics models for delamination has also been attempted by several research groups but with only limited success [118,119,151,249]. Moreover, several recent studies have shown that the homogenization process at meso-scale in CMD leads to loss of key information on multiple-damage coupling at the macroscopic scale and may result in inaccurate prediction of the crack path [151,250].

Unexpected severe stress locking, (i.e., significant amount of stresses remain although an element has been determined completely failed) may also occur [152].

The inadequacy of CMD has led to the recent trend to integrate explicit representations of all major cracking events into global composite structure models to achieve direct coupling [152,241,251]. Two critical capabilities that enable the direct coupling are: 1) improved cohesive zone models (CZMs) for bulk and interface crack problems to achieve unification of crack initiation and propagation; and 2) improved numerical methods that allow for arbitrary crack initiation and propagation in continua.

Although cohesive zone models (CZMs) have been widely used in composite fracture analysis, especially in delamination analyses, this method suffers from a major shortcoming: it requires the potential crack path to be known *a priori*, so that CZM elements can be directly implanted along the path. This greatly limits the application of CZM for problems with unknown *a priori* cracking paths as frequently observed in composite materials shown in Figure 2-1.

Recently several novel numerical methods have been developed to allow for arbitrary cohesive crack initiation and propagation without continuous remeshing. For example, cohesive models have been integrated into the X-FEM framework and successfully been used to model the fracture in homogeneous quasi-brittle materials [164,168,183,211]. The key feature in X-FEM formulation is the use of enrichment functions for cracked elements locally. This is achieved by enhancing the degrees of freedom (DoFs) of all the nodes employed by the elements with internal discontinuity. One of the advantages of this method is that, for an element that encompasses a singular crack-tip, asymptotic

displacement functions from fracture mechanics can be used as enrichment functions and reasonable numerical solutions can be obtained. One minor problem is that the long-range influence of the crack-tip singular field is truncated by the use of local element shape functions. As a result, ambiguities arise for those blending elements that connect a tip-enriched element to neighboring elements that are not influenced by the crack. These elements have to be treated specially and sometimes the treatment leads to loss of element locality [202, 252].

The X-FEM is very effective for treating cracks or even multiple cracks in homogeneous isotropic materials, for which the enrichment functions are known. However, for complex heterogeneous material systems, such as laminated or textile composites, the enrichment functions are not readily available except for some very special cases (such as a delamination crack at a symmetric plane in which case the bonded plate/beam can be treated as orthotropic materials and the singular stress field is known). Furthermore, in the cases that multiple nonlinear cracking systems co-evolve nonlinearly as shown in Figure 2-1, X-FEM will have difficulty in dealing with the coupling among the multiple cracks.

An alternative numerical method that can also treat the arbitrary cracking problem is the phantom node method (PNM), first developed by Belytschko and coworkers [204] based on the initial work of Hansbo and Hansbo [205]. The essence of this method is to use overlapping paired elements to describe a strong or weak discontinuity in a physical element that is bisected by a crack (strong discontinuity) or a material interface (weak discontinuity). Based on this idea, Ling et al., [206] proposed an element with one or multiple copies of element nodes, to account for an arbitrary intra-element crack.

Otherwise, the element remains a standard FE. This so-called augmented element is fully compatible with existing FE programs and has been implemented into a commercial FE program as a user-defined element [207]. X-FEM and PNM methods are relatively mesh-independent and computationally efficient when dealing with individual (i.e. non-interactive) cracks. However, in these methods each individual crack requires its own additional copy of DoFs or nodes to describe the discontinuous displacement field associated with it. Tracing the evolution of complex fracture surfaces of multiple cracks quickly becomes extremely tedious and numerically burdensome because, in such cases, there are no universal tracking algorithms that can judiciously assign different copies of DoFs or nodes to different cracks for complex crack configurations. Furthermore, the dimensions of local and global stiffness matrices must be dynamically modified in accordance with crack interaction, which makes it very difficult to integrate them into standard FE programs [165,213,214].

A novel augmented finite element method that can treat arbitrary intra-element cracking without additional nodes or DoFs overcomes most of the aforementioned limitations. In this chapter, this novel idea will be presented. The implementation of the A-FEM into a popular commercial code (ABAQUS), as a user subroutine, will also be discussed.

To understand how to deal with arbitrary intra-element discontinuities without the need of additional nodal copies or DoFs, in the next section a simple problem will be used to explain the procedure of accounting for an intra-element discontinuity.

2.2. Fracture of A Longitudinally Loaded 1D Bar

2.2.1. Strength of Material Approach

Assuming a one-dimensional bar with bottom end (point 1) fixed and its top end (point 2) is under displacement-controlled loading (i.e., the displacement at node 2 is monotonically increasing). The bar length dimension is l and has a constant cross-sectional area of A . The bar material behaves like the description that follows. Initially it is elastic with a modulus of E when the stress in the bar (σ) is smaller than a critical stress ($\hat{\sigma}$) (Figure 2-2(a)); however, if the σ reaches $\hat{\sigma}$ (i.e., $\sigma = \hat{\sigma}$), a cohesive crack will be generated within the element as shown in Figure 2-2(b) but the crack will be bridged by the critical stress until the separation between the two crack surface (δ) reaches a critical value, δ_c , at which point the stress abruptly drops to zero, indicating complete fracture. The stress-separation for the discontinuity is shown in Figure 2-2(c).

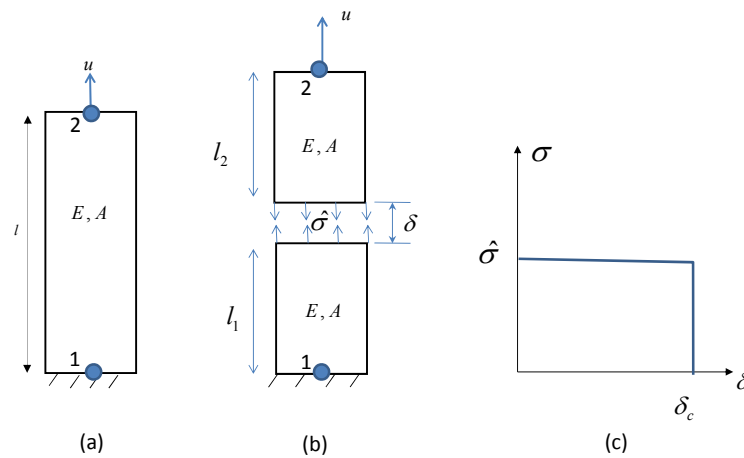


Figure 2-2 A bar loaded in longitudinal tension under displacement-controlled manner. (a) elastic stage, (b) bridged cohesive cracking stage, (c) rectangular cohesive law

The deformation processes can be separated into three stages as below:

- (i) If $u \leq u_1^* = (\hat{\sigma}l/E)$, the bar is in the elastic stage and the displacement is continuous, then the reaction force at node 2 is

$$F_2 = -F_1 = A\sigma = AE\varepsilon = AE(u/l) \quad (2-1)$$

- (ii) If $u_1^* < u \leq u_2^* = (\hat{\sigma}l/E) + \delta_c$, the stress in the bar is $\sigma = \hat{\sigma}$ and the bar has been separated into two parts due to the cohesive crack with top length l_2 and lower part length l_1 . In this case,

$$F_2 = -F_1 = A\hat{\sigma} \quad (2-2)$$

- (iii) If $u > u_2^* = (\hat{\sigma}l/E) + \delta_c$, the stresses in the separated parts are zero both.

$$F_2 = -F_1 = 0 \quad (2-3)$$

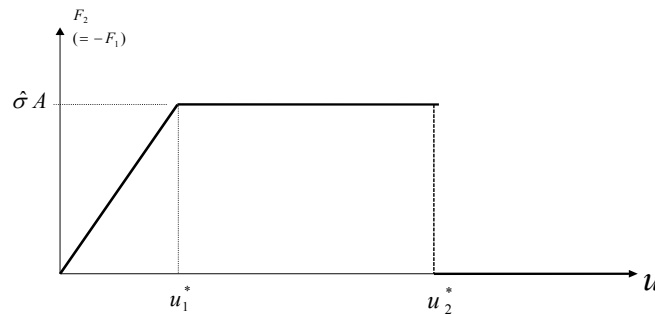


Figure 2-3 Load- displacement (global response) curve of the bar with cohesive crack following the rectangular law in Figure 2-2.

Figure 2-3 depicts the load-displacement curve from the beginning to the complete fracture point. By knowing the nodal displacement, reaction forces are known.

If the material behavior is slightly more complicated as shown in Figure 2-4 (a), we can get the solution similarly as follows. A side note about the trapezoidal cohesive law of

Figure 2-4 (a) is that, the finite initial slope ($\hat{\sigma}/\delta_1$) is often introduced for numerical stability purposes. It may cause unwanted additional structural compliance.

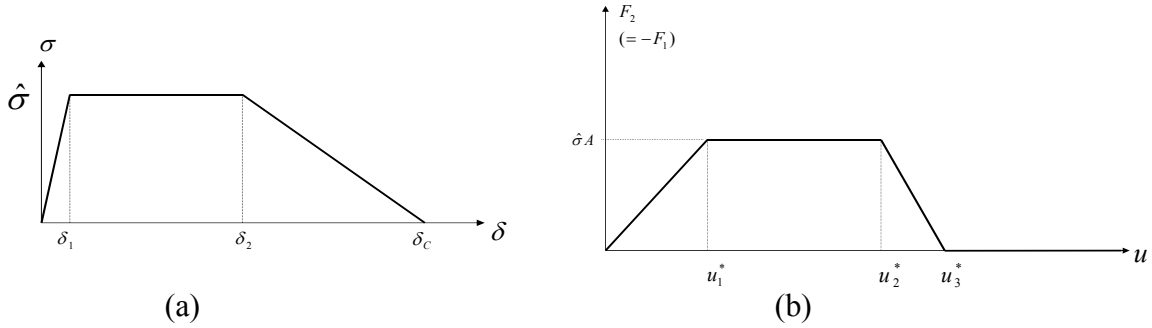


Figure 2-4 (a) A trapezoidal cohesive law, (b) Global load-displacement curve of the 1D bar resulted from the trapezoidal cohesive law.

In practice, the slope is often set to be as large as possible but not adversely impact numerical stability. When dealing with crack initiation in homogeneous materials, whenever possible, such finite slope should be avoided. It is straightforward to derive the solution for this case as follows:

$$F_2 = -F_1 = \begin{cases} \frac{(\hat{\sigma}/\delta_1)AE}{(\hat{\sigma}/\delta_1)l + E} u & u \leq u_1^* \\ \hat{\sigma} A & u_1^* < u \leq u_2^* \\ \frac{\delta_c - u}{\delta_c - (\delta_2 + \hat{\sigma}l/E)} \hat{\sigma} A & u_2^* < u \leq u_3^* \\ 0 & u_3^* < u \end{cases} \quad (2-4)$$

The critical displacements u_1^* , u_2^* , and u_3^* are as follows

$$\begin{aligned}
 u_1^* &= \hat{\sigma}l/E + \delta_1 \\
 u_2^* &= \hat{\sigma}l/E + \delta_2 \\
 u_3^* &= \delta_c
 \end{aligned}
 \tag{2-5}$$

Note that in the 1D bar model we assume the displacement at node 1 is fixed ($u_1=0$). This does not affect the load solution but does affect the absolute displacement at 1 and 2. In a more general case, one can assume displacement at node 1 is u_1 , and that at node 2 is u_2 . Setting $u = u_2 - u_1$ will give exactly the same solution as in Eqn (2-5) which is shown in Figure 2-3 and Figure 2-4.

Clearly, for any material exhibits such a nonlinear behavior, the entire problem becomes nonlinear. Except for a few simple problems such as described above, no easy analytical solutions can be found for most problems. Nonlinear finite element methods are needed to solve such problems. In the following, we shall solve such a problem through standard FEM as an introduction.

2.2.2. Standard FEM Approach for Fracture of 1D Bar

Standard FEM is a displacement based formulation. In other words, an element first assumes nodal displacements are known (albeit symbolically).

Let's assume the nodal displacements at the two nodes 1 and 2 to be u_1 and u_2 as shown in Figure 2-5 (a). We shall again start with the elastic stage (continuous displacement field). With the two nodal displacements known, the displacement at any point x ($0 < x < l$) can be obtained through the following shape functions:

$$u(x) = \{N_1(x) \quad N_2(x)\} \begin{Bmatrix} u_1 \\ u_2 \end{Bmatrix} \quad (2-6)$$

Here the 1-D shape functions are:

$$N_1(x) = \frac{l-x}{l}; \quad N_2(x) = \frac{x}{l} \quad (2-7)$$

The strain in the element is (displacement-strain relation)

$$\varepsilon(x) = \frac{du(x)}{dx} = \{-1/l \quad 1/l\} \begin{Bmatrix} u_1 \\ u_2 \end{Bmatrix} \quad (2-8)$$

The elemental stress is thus (making use of constitutive law)

$$\sigma(x) = E\varepsilon(x) = \{-E/l \quad E/l\} \begin{Bmatrix} u_1 \\ u_2 \end{Bmatrix} \quad (2-9)$$

It is seen that $\sigma(x)$ is independent of position x , which means the equilibrium equation ($d\sigma(x)/dx = 0$) is automatically satisfied. Next we need to consider force equilibrium at nodes 1 and 2. Denote the external (applied) force at nodes 1 and 2 as F_1 and F_2 , respectively. Then

$$F_1 = -\sigma(0)A = \{EA/l \quad -EA/l\} \begin{Bmatrix} u_1 \\ u_2 \end{Bmatrix} \quad (2-10(a))$$

$$F_2 = \sigma(l)A = \{-EA/l \quad EA/l\} \begin{Bmatrix} u_1 \\ u_2 \end{Bmatrix} \quad (2-10(b))$$

Note that the negative sign ahead of $\sigma(0)$ in Eqn (2-10(a)) comes from the fact that the assumed positive F_1 direction creates compression (negative signed stress) at node 1.

Combining Eqns (2-10(a)) and (2-10(b)) into a single matrix form will lead to a standard FE elemental formulation:

$$\begin{Bmatrix} F_1 \\ F_2 \end{Bmatrix} = \begin{bmatrix} EA/l & -EA/l \\ -EA/l & EA/l \end{bmatrix} \begin{Bmatrix} u_1 \\ u_2 \end{Bmatrix} \quad (2-11(a))$$

Let $k_e = EA/l$, then Eqn (2-11(a)) becomes

$$\begin{Bmatrix} F_1 \\ F_2 \end{Bmatrix} = k_e \begin{bmatrix} 1 & -1 \\ -1 & 1 \end{bmatrix} \begin{Bmatrix} u_1 \\ u_2 \end{Bmatrix} \quad (2-11(b))$$

Also, from Eqn (2-9), i.e., $\sigma(x) = (E/l)(u_2 - u_1)$, we know that when $u_2 - u_1 = (\hat{\sigma}/E)l$, the stress in the bar reaches the critical value of $\sigma = \hat{\sigma}$, and the bar will have displacement discontinuity as shown in Figure 2-5(b) according to the cohesive law in Figure 2-5(c).

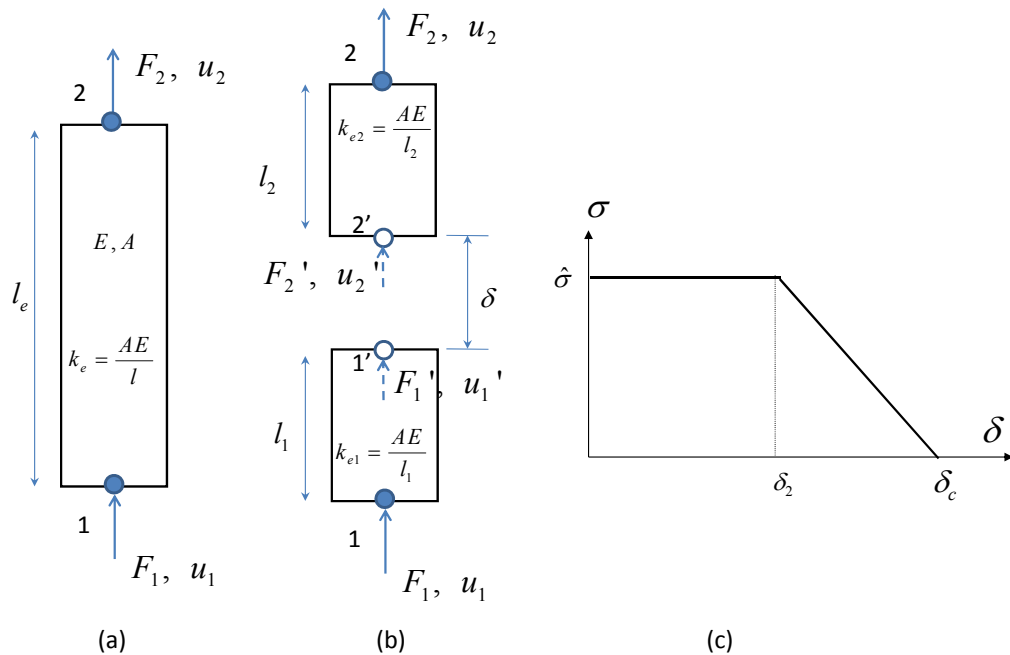


Figure 2-5 Fracture of a 1D bar with a trapezoidal cohesive law (standard FEM formulation)

Now let's consider the nonlinear stage as shown in Figure 2-5(b). As one may see intuitively, now two elements (element 1 with node 1-1', and element 2 with node 2'-2), will be needed to fully account for the problem. However, the trick for arbitrary cracking problems is that one does not know where a crack is going to be before the analysis, hence there is no way to assign nodes 1' and 2'. The X-FEM or PNM resolves this issue by assigning additional nodal DoFs (X-FEM) or by addition extra node copies (PNM). In this study a new approach will be used. This approach seeks to condense these additional DoFs within an element so that the discontinuous displacement can be expressed adequately by the DoFs of the regular nodes.

Consider Figure 2-5(b), since each of the separated domains are elastic, by following the standard FEM formulation we can have two equations as follows:

$$\begin{bmatrix} k_{11} & k_{11'} \\ k_{11'} & k_{11'} \end{bmatrix} \begin{Bmatrix} u_1 \\ u_{1'} \end{Bmatrix} = \begin{Bmatrix} F_1 \\ F_{1'} \end{Bmatrix} \quad (2-12(a))$$

$$\begin{bmatrix} k_{2'2'} & k_{2'2} \\ k_{2'2} & k_{22} \end{bmatrix} \begin{Bmatrix} u_{2'} \\ u_2 \end{Bmatrix} = \begin{Bmatrix} F_{2'} \\ F_2 \end{Bmatrix} \quad (2-12(b))$$

where

$$k_{11} = k_{11'} = EA/l_1 = k_{e1}; \quad k_{22} = k_{2'2'} = EA/l_2 = k_{e2}; \quad k_{11'} = -k_{e1}; \quad k_{2'2} = -k_{e2}.$$

$$1/k_e = 1/k_{e1} + 1/k_{e2} \quad (2-12(c))$$

The crack displacement, i.e., the displacement jump between the two cracked surfaces, is

$$\delta = u_2 - u_1 \quad (2-13)$$

The resultant forces at nodes 1' and 2' are from the cohesive stress as follows:

$$F_1 = -F_2 = \sigma(\delta) = \begin{cases} \hat{\sigma}A & \text{if } \delta = u_2 - u_1 \leq \delta_2 \\ \frac{\delta_c - \delta}{\delta_c - \delta_2} \hat{\sigma}A & \text{if } \delta_2 < \delta = u_2 - u_1 \leq \delta_c \end{cases} \quad (2-14)$$

Assuming first stage in the cohesive law, where $\delta = u_2 - u_1 \leq \delta_2$, Eqn (2-12) becomes,

$$\begin{bmatrix} k_{11} & k_{11'} \\ k_{11'} & k_{11'} \end{bmatrix} \begin{Bmatrix} u_1 \\ u_1' \end{Bmatrix} = \begin{Bmatrix} F_1 \\ \hat{\sigma}A \end{Bmatrix} \quad (2-15(a))$$

$$\begin{bmatrix} k_{2,2'} & k_{2,2} \\ k_{2,2} & k_{22} \end{bmatrix} \begin{Bmatrix} u_2 \\ u_2' \end{Bmatrix} = \begin{Bmatrix} -\hat{\sigma}A \\ F_2 \end{Bmatrix} \quad (2-15(b))$$

Although these two equations can be readily solved, it is beneficial to follow the standard matrix manipulation scheme to gain some insights for more complex problems.

From Eqn (2-15) we have four equations:

$$[k_{11}] \{u_1\} + [k_{11'}] \{u_1'\} = \{F_1\} \quad (2-16(a))$$

$$[k_{11'}] \{u_1\} + [k_{11'}] \{u_1'\} = \{\hat{\sigma}A\} \quad (2-16(b))$$

$$[k_{2,2'}] \{u_2\} + [k_{2,2}] \{u_2'\} = \{-\hat{\sigma}A\} \quad (2-16(c))$$

$$[k_{2,2}] \{u_2\} + [k_{22}] \{u_2'\} = \{F_2\} \quad (2-16(d))$$

Solving $\{u_1'\}$ and $\{u_2'\}$ from Eqn (2-16) one obtains:

$$\{u_1\} = [k_{11}]^{-1} (\{F_1\} - [k_{11}]\{u_1\}) \quad (2-17(a))$$

$$\{u_1\} = [k_{11}]^{-1} (\{\hat{\sigma}A\} - [k_{11}]\{u_1\}) \quad (2-17(b))$$

$$\{u_2\} = [k_{22}]^{-1} (\{-\hat{\sigma}A\} - [k_{22}]\{u_2\}) \quad (2-17(c))$$

$$\{u_2\} = [k_{22}]^{-1} (\{F_2\} - [k_{22}]\{u_2\}) \quad (2-17(d))$$

Canceling $\{u_1\}$ from Eqns (2-17(a)) and (2-17(b)) leads to

$$\{F_1\} = [k_{11}][k_{11}]^{-1}\{\hat{\sigma}A\} + ([k_{11}] - [k_{11}][k_{11}]^{-1}[k_{11}])\{u_1\} \quad (2-18(a))$$

Similarly, canceling $\{u_2\}$ from Eqns (2-17(c)) and (2-17(d)) leads to

$$\{F_2\} = [k_{22}][k_{22}]^{-1}\{-\hat{\sigma}A\} + ([k_{22}] - [k_{22}][k_{22}]^{-1}[k_{22}])\{u_2\} \quad (2-18(b))$$

Further, subtracting Eqn (2-17(b)) from Eqn (2-17(c)) gives the crack displacement,

$$\delta = \{u_2 - u_1\} = -([k_{11}]^{-1} + [k_{22}]^{-1})\{\hat{\sigma}A\} + [k_{11}]^{-1}[k_{11}]\{u_1\} - [k_{22}]^{-1}[k_{22}]\{u_2\} \quad (2-18(c))$$

$$\{u_1\} = [k_{11}]^{-1}\{\hat{\sigma}A\} - [k_{11}]^{-1}[k_{11}]\{u_1\} \quad (2-18(d))$$

$$\{u_2\} = -[k_{22}]^{-1}\{\hat{\sigma}A\} - [k_{22}]^{-1}[k_{22}]\{u_2\} \quad (2-18(e))$$

Thus are solved for all nodal reaction forces (F_1 and F_2) and discontinuous displacements

(u_1 and u_2) as functions of regular nodal displacements (u_1 and u_2), but with the

assumption that $\delta = \{u_2 - u_1\} \leq \delta_2$. From Eqn (2-18(c)), this condition translates to

$$[k_{11}]^{-1}[k_{11}]\{u_1\} - [k_{22}]^{-1}[k_{22}]\{u_2\} \leq \delta_2 + ([k_{11}]^{-1} + [k_{22}]^{-1})\{\hat{\sigma}A\} \quad (2-19)$$

Then, assume the softening stage in cohesive law, where $\delta_2 < u_2, -u_1 \leq \delta_c$, in which case (see Eqn (2-14))

$$F_1 = -F_2 = \frac{\delta_c - \delta}{\delta_c - \delta_2} \hat{\sigma} A = -\alpha \delta_c + \alpha(u_2, -u_1) \quad (2-20)$$

Here $\alpha = -\hat{\sigma}/(\delta_c - \delta_2)$ is the slope of the softening phase of cohesive law (negative).

Further, substituting Eqn (2-20) into Eqn (2-15), one obtains

$$\begin{bmatrix} k_{11} & k_{11'} \\ k_{11'} & k_{11'} \end{bmatrix} \begin{Bmatrix} u_1 \\ u_{1'} \end{Bmatrix} = \begin{Bmatrix} F_1 \\ -\alpha \delta_c A + \alpha(u_2, -u_1) A \end{Bmatrix} \quad (2-21(a))$$

$$\begin{bmatrix} k_{2,2'} & k_{2,2'} \\ k_{2,2'} & k_{22} \end{bmatrix} \begin{Bmatrix} u_2 \\ u_2 \end{Bmatrix} = \begin{Bmatrix} \alpha \delta_c A - \alpha(u_2, -u_1) A \\ F_2 \end{Bmatrix} \quad (2-21(b))$$

Following the same solving procedure, from Eqns (2- (16-18)), one obtains

$$[k_{11}] \{u_1\} + [k_{11'}] \{u_{1'}\} = \{F_1\} \quad (2-22(a))$$

$$[k_{11'}] \{u_1\} + [k_{11'}] \{u_{1'}\} = \{-\alpha \delta_c A + \alpha(u_2, -u_1) A\} \quad (2-22 (b))$$

$$[k_{2,2'}] \{u_2\} + [k_{2,2'}] \{u_2\} = \{\alpha \delta_c A - \alpha(u_2, -u_1) A\} \quad (2-22 (c))$$

$$[k_{2,2'}] \{u_2\} + [k_{22}] \{u_2\} = \{F_2\} \quad (2-22 (d))$$

$$\{u_1\} = [k_{11'}]^{-1} (\{F_1\} - [k_{11}] \{u_1\}) \quad (2-23(a))$$

$$\{u_{1'}\} = [k_{11'}]^{-1} (\{-\alpha \delta_c A + \alpha(u_2, -u_1) A\} - [k_{11'}] \{u_{1'}\}) \quad (2-23 (b))$$

$$\{u_2\} = [k_{2,2'}]^{-1} (\{\alpha \delta_c A - \alpha(u_2, -u_1) A\} - [k_{2,2'}] \{u_2\}) \quad (2-23 (c))$$

$$\{u_{2'}\} = [k_{2,2}]^{-1} (\{F_2\} - [k_{22}] \{u_2\}) \quad (2-23 \text{ (d)})$$

Subtracting Eqn (2-23(b)) from Eqn (2-23(c)), the following can be obtained

$$\{u_2, -u_{1'}\} = ([\mathbf{I}] - [\beta]^{-1}) \{\delta_c\} + [\beta]^{-1} ([k_{11'}]^{-1} [k_{11'}] \{u_1\} - [k_{2,2'}]^{-1} [k_{2,2}] \{u_2\}) \quad (2-24(a))$$

$$\{u_{1'}\} = -\alpha A [k_{11'}]^{-1} [\beta]^{-1} \{\delta_c\} - [k_{11'}]^{-1} ([\mathbf{I}] - \alpha A [\beta]^{-1} [k_{11'}]^{-1}) [k_{11'}] \{u_1\} - \alpha A [k_{11'}]^{-1} [\beta]^{-1} [k_{2,2'}]^{-1} [k_{2,2}] \{u_2\} \quad (2-24(b))$$

$$\{u_2\} = \alpha A [k_{2,2'}]^{-1} [\beta]^{-1} \{\delta_c\} - [k_{2,2'}]^{-1} ([\mathbf{I}] - \alpha A [\beta]^{-1} [k_{2,2'}]^{-1}) [k_{2,2}] \{u_2\} - \alpha A [k_{2,2'}]^{-1} [\beta]^{-1} [k_{11'}]^{-1} [k_{11'}] \{u_1\} \quad (2-24(c))$$

$$\{F_1\} = -\alpha A [k_{11'}] [k_{11'}]^{-1} [\beta]^{-1} \{\delta_c\} + ([k_{11}] - [k_{11'}] [k_{11'}]^{-1} ([\mathbf{I}] - \alpha A [\beta]^{-1} [k_{11'}]^{-1}) [k_{11'}]) \{u_1\} - \alpha A [k_{11'}] [k_{11'}]^{-1} [\beta]^{-1} [k_{2,2'}]^{-1} [k_{2,2}] \{u_2\} \quad (2-24(d))$$

$$\{F_2\} = \alpha A [k_{2,2}] [k_{2,2'}]^{-1} [\beta]^{-1} \{\delta_c\} + ([k_{22}] - [k_{2,2}] [k_{2,2'}]^{-1} ([\mathbf{I}] - \alpha A [\beta]^{-1} [k_{2,2'}]^{-1}) [k_{2,2}]) \{u_2\} - \alpha A [k_{2,2}] [k_{2,2'}]^{-1} [\beta]^{-1} [k_{11'}]^{-1} [k_{11'}] \{u_1\} \quad (2-24(e))$$

With Eqn (2-24(a)), the condition $\delta_2 < u_2, -u_{1'} \leq \delta_c$ can now be recast in terms of nodal

displacement: $\delta_2 < ([\mathbf{I}] - [\beta]^{-1}) \{\delta_c\} + [\beta]^{-1} ([k_{11'}]^{-1} [k_{11'}] \{u_1\} - [k_{2,2'}]^{-1} [k_{2,2}] \{u_2\}) \leq \delta_c$

Full analysis of fracture in a 1D bar shows how to condense the internal nodal displacements and loads, so one can obtain the external nodal forces only as functions of external nodal displacement. The condensation procedure used above shows the main idea behind the new A-FEM method which can be used on other general problems and will be discussed in the following sections.

2.3 Problem Statement

Consider a discontinuous physical domain Ω as shown in Figure 2-6. The domain is composed of two sub-domains of the same or different materials, i. e., $\Omega = \Omega^+ \cup \Omega^-$. The two domains are connected by a discontinuity which could be a cohesive crack or a material boundary, $\Gamma_c = \Gamma_c^+ \cup \Gamma_c^-$.¹ The prescribed tractions \mathbf{F} are imposed on boundary Γ_F and the prescribed displacements $\bar{\mathbf{u}}$ on boundary Γ_u . The stress field inside the domain, $\boldsymbol{\sigma}$, is related to the external loading \mathbf{F} . The strong form of the equilibrium equation and boundary conditions are:

$$\begin{aligned}
 \nabla \cdot \boldsymbol{\sigma}^+ &= 0 \quad (\text{in } \Omega^+); & \nabla \cdot \boldsymbol{\sigma}^- &= 0 \quad (\text{in } \Omega^-); \\
 \boldsymbol{\sigma} \cdot \mathbf{n}^+ &= \mathbf{F}^+ \quad (\text{on } \Gamma_F^+); & \boldsymbol{\sigma} \cdot \mathbf{n}^- &= \mathbf{F}^- \quad (\text{on } \Gamma_F^-); \\
 \mathbf{u}^+ &= \bar{\mathbf{u}}^+ \quad (\text{on } \Gamma_u^+); & \mathbf{u}^- &= \bar{\mathbf{u}}^- \quad (\text{on } \Gamma_u^-); \\
 \mathbf{t}^+ = \boldsymbol{\sigma}^+ \cdot \mathbf{n}^+ &= -\mathbf{t} \quad (\text{on } \Gamma_c^+); & \mathbf{t}^- = \boldsymbol{\sigma}^- \cdot \mathbf{n}^- &= \mathbf{t} \quad (\text{on } \Gamma_c^-);
 \end{aligned} \tag{2-25}$$

Where $\boldsymbol{\sigma}^+$ and $\boldsymbol{\sigma}^-$ are the stresses in the subdomains Ω^+ and Ω^- ; \mathbf{t}^+ and \mathbf{t}^- are the tractions along the discontinuity surfaces Γ_c^+ and Γ_c^- ; \mathbf{n}^+ and \mathbf{n}^- are the out-normal Γ_c^+ and Γ_c^- .

The last two expressions in Eqn (2-25) come from the stress continuity across the discontinuity boundary. The traction, \mathbf{t} , is a function of the relative displacements, $\Delta \mathbf{u}$, between Γ_c^+ and Γ_c^- , i.e.,

¹ For a weak discontinuity $\Gamma_c^+ = \Gamma_c^-$ while for a strong discontinuity Γ_c^+ and Γ_c^- are separated.

$$\begin{aligned} \mathbf{t} &= \mathbf{t}(\Delta \mathbf{u}) && (\text{on } \Gamma_c) \\ \Delta \mathbf{u} &= \mathbf{u}^+ - \mathbf{u}^- && (\text{on } \Gamma_c) \end{aligned} \quad (2-26)$$

where \mathbf{u}^+ and \mathbf{u}^- are the displacement fields in Ω^+ and Ω^- , respectively. Eqn (2-26) serves as the constitutive law and kinematic equation of the discontinuity. In this study, cohesive zone model with piece-wise linear traction separation law is used to describe strong discontinuities. The procedures for piece-wise linearization and setting a proper indexing scheme for cohesive segments, that are critical to the new elemental condensation procedure here, is given in Appendix A in detail.

The domain surrounding the discontinuity is assumed to be elastic. We further assume small strains and displacement condition. Thus the constitutive law and kinematic equations for the two domains can be written as:

$$\begin{aligned} \boldsymbol{\sigma}^+ &= \mathbf{C}^+ : \boldsymbol{\varepsilon}^+ \quad (\text{in } \Omega^+) && \boldsymbol{\sigma}^- = \mathbf{C}^- : \boldsymbol{\varepsilon}^- \quad (\text{in } \Omega^-) \\ \boldsymbol{\varepsilon}^+ &= \boldsymbol{\varepsilon}^+(\mathbf{u}^+) = [\nabla \mathbf{u}^+ + (\nabla \mathbf{u}^+)^T]/2 \quad (\text{in } \Omega^+) && \boldsymbol{\varepsilon}^- = \boldsymbol{\varepsilon}^-(\mathbf{u}^-) = [\nabla \mathbf{u}^- + (\nabla \mathbf{u}^-)^T]/2 \quad (\text{in } \Omega^-) \end{aligned} \quad (2-27)$$

where \mathbf{C}^+ and \mathbf{C}^- being the material stiffness tensors of the two sub-domains traversed by the discontinuity, respectively. They can be identical (for homogeneous materials) or different (for heterogeneous materials). The superscript $(\cdot)^T$ denotes transposition.

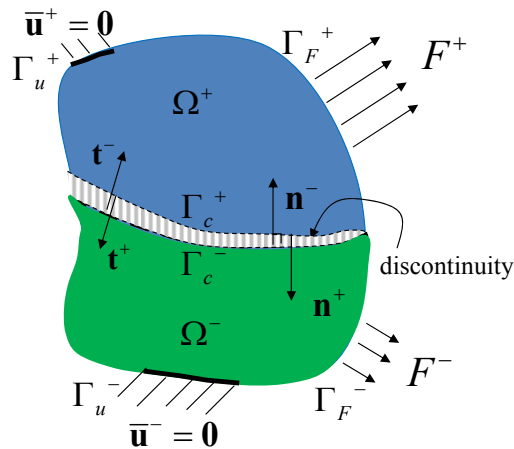


Figure 2-6 Notation for a body with an arbitrary discontinuity

The stated strong form of the problem can be converted into a weak form using the principle of virtual work. The displacement fields (\mathbf{u}^+ and \mathbf{u}^-) must be sub-sets of the kinematically admissible displacement fields, \mathbf{U} :

$$\mathbf{u}^+ \in \mathbf{U} = \{\mathbf{v}^+ \in \mathbf{V} : \mathbf{v}^+ = \mathbf{0} \text{ on } \Gamma_u^+\}; \quad \mathbf{u}^- \in \mathbf{U} = \{\mathbf{v}^- \in \mathbf{V} : \mathbf{v}^- = \mathbf{0} \text{ on } \Gamma_u^-\} \quad (2-28)$$

Applying the principle of virtual work separately to the subdomains, the weak forms can be written as:

$$\begin{aligned} \int_{\Omega^+} \boldsymbol{\sigma}^+ : \boldsymbol{\varepsilon}^+(\mathbf{v}^+) \, d\Omega &= \int_{\Gamma_F^+} \mathbf{F}^+ \cdot \mathbf{v}^+ \, d\Gamma - \int_{\Gamma_c} \mathbf{t}(\Delta\mathbf{v}) \cdot \mathbf{v}^+ \, d\Gamma & \forall (\mathbf{v}^+, \mathbf{v}^-) \in \mathbf{U} \\ \int_{\Omega^-} \boldsymbol{\sigma}^- : \boldsymbol{\varepsilon}^-(\mathbf{v}^-) \, d\Omega &= \int_{\Gamma_F^-} \mathbf{F}^- \cdot \mathbf{v}^- \, d\Gamma + \int_{\Gamma_c} \mathbf{t}(\Delta\mathbf{v}) \cdot \mathbf{v}^- \, d\Gamma \end{aligned} \quad (2-29)$$

where $\Delta\mathbf{v} = \mathbf{v}^+ - \mathbf{v}^-$ (on Γ_c). The left-hand-sides are the internal virtual work and the right-hand-sides are the virtual work done by the external forces and the tractions along the crack surfaces. Note that, if one of the subdomains further cracks, the principle of virtual work can be applied to all three subdomains without any further modifications.

2.4 A-FEM Formulation with Single Intra-Elemental Crack

This section describes how to construct an element with only regular nodes or DoFs that can correctly account for an intra-elemental cohesive crack. Without the loss of generality, consider the 4-node quadratic plane element to illustrate the augmented finite element scheme. The physical element with nodes 1, 2, 3 and 4 is severed by a cohesive crack where the tractions are continuous but displacements are not as shown in Figure 2-7. A common approach is taken by assuming 1) during crack growth, a crack tip always resides at an element boundary during its propagation as in the PNM [210,253]

and the previous A-FEM [206,207], and 2) the existence of a cohesive zone eliminates the crack-tip singularity [71,183].

Before any crack traverses the element, it is elastic and the 4-node bi-linear element formulation using standard shape functions can be used, as shown in Figure 2-7. As the applied load increases, at some stage the element will be separated by a cohesive crack. If the element is cut by a single crack, there are two basic crack configurations: 1) two quadrilateral subdomains as shown in Figure 2-7(b), and (2) one triangular subdomain and one pentagonal subdomain as shown in Figure 2-7(c). Obviously there is a displacement discontinuity across the two separated domains. In such cases, the standard shape functions cannot give accurate results because it only treats continuous displacements. On the other hand, if one can add 4 additional nodes as shown in Figure 2-7 by node numbers 5, 6, 6' and 5', with regular displacement DoFs so that the displacement jumps across the crack are simply the differences in displacements between the respective node-pairs 5-5' and 6-6', the problem can be solved by replacing the original element with three new elements. For example, for the configuration in Figure 2-7 (b), two 4-node bilinear elements (1-2-5-6 and 6'-5'-3-4) and one cohesive element (6-5-5'-6') are sufficient. The two solid elements interact with each other through the cohesive element. This is the basic idea of all sorts of adaptive meshing methods. However, this method is computationally very expensive. In the following paragraphs, we explain how to augment the 2D element by condensing the additional nodes and their associated DoFs.

For each crack, a local coordinate system is defined by the direction along (s) and perpendicular to (n) the crack path, from which the normal (δ_n) and shear (δ_s) crack

displacements can be defined as shown in Figure 2-7. These local crack displacements are related to the global crack displacements, Δu and Δv , by $\{\delta_n, \delta_t\}^T = [\mathbf{R}_1]\{\Delta u, \Delta v\}^T$, where $[\mathbf{R}_1] = \begin{bmatrix} \cos \theta_1 & \sin \theta_1 \\ -\sin \theta_1 & \cos \theta_1 \end{bmatrix}$ is the rotational matrix between the global and local coordinates and θ_1 is the angle between global x -axis and local s -axis (Figure 2-7). As will be seen shortly, introduction of 4 internal nodes allows us to derive accurate elemental equilibrium equations without the need to assume crack deformation modes as commonly done in literature. More importantly, it offers the advantage of permitting multiple, intra-element discontinuities. The DoFs associated with these internal nodes will be condensed at an elemental level. The internal nodes also facilitate independent displacement interpolation and stiffness integration for each subdomain, which leads to a natural consideration of a weak discontinuity if the subdomains are of different materials.

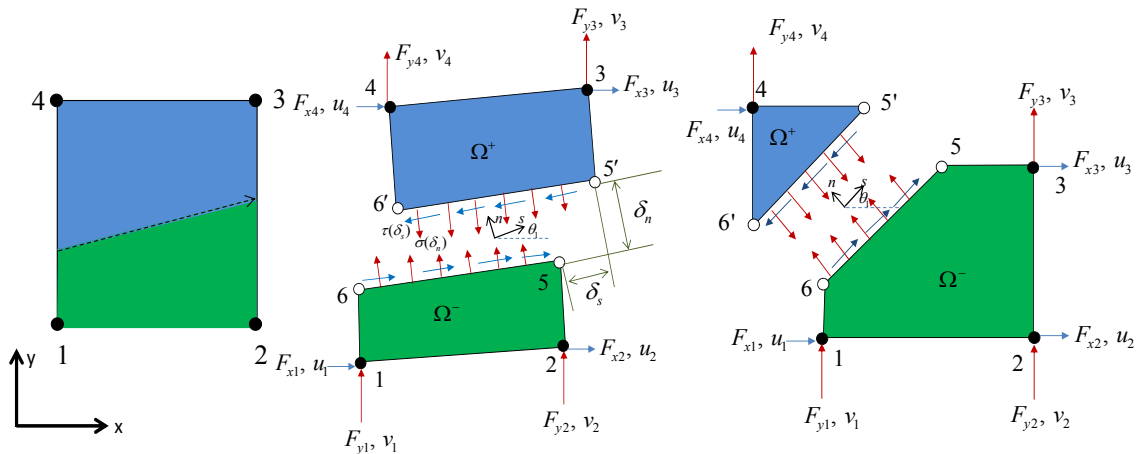


Figure 2-7 Illustration of the element augmentation from (a) a regular element with possible different material domains, to (b) an A-FE with two quadrilateral sub-domains, or to (c) an A-FE with one triangular sub-domain and one pentagonal sub-domain.

First, from Eqn (2-29) the discretized form of element equilibrium equations for the two domains can be expressed in general as follows,

$$\begin{aligned} \left(\int_{\Omega_e^+} (\mathbf{B}^+)^T (\mathbf{D}^+) (\mathbf{B}^+) d\Omega \right) \mathbf{u}^+ &= \int_{\Gamma_{F^+}} (\mathbf{N}^+)^T \mathbf{F}^+ d\Gamma + \int_{\Gamma_c^+} (\mathbf{N}^+)^T \mathbf{t} d\Gamma \\ \left(\int_{\Omega_e^-} (\mathbf{B}^-)^T (\mathbf{D}^-) (\mathbf{B}^-) d\Omega \right) \mathbf{u}^- &= \int_{\Gamma_{F^-}} (\mathbf{N}^-)^T \mathbf{F}^- d\Gamma - \int_{\Gamma_c^-} (\mathbf{N}^-)^T \mathbf{t} d\Gamma \end{aligned} \quad (2-30)$$

where \mathbf{B}^+ and \mathbf{B}^- are the strain matrices, \mathbf{u}^+ and \mathbf{u}^- are nodal DoFs; \mathbf{N}^+ and \mathbf{N}^- are the interpolation matrices composed of shape functions; \mathbf{F}^+ and \mathbf{F}^- are the external force arrays, and $\mathbf{t}(\boldsymbol{\delta}) = \mathbf{R}^T \mathbf{t}'(\boldsymbol{\delta}')$ is the cohesive traction array in the global coordinates (x-o-y). The two stiffness matrices can be obtained independently with shape functions and material properties pertaining to each domain. This allows the current method to model both a strong (discontinuous displacement field) and weak discontinuity (continuous displacement but discontinuous strain field). The two cracking possibilities should be analyzed separately. Following the standard FEM procedure for each sub-domain, the equilibrium equations for each can be written in general form. Because of a large number of DoFs, we will have large matrices (8×8) that make it awkward and tedious to write and proceed. Therefore, we assign some short terms to the large matrices to make the solution and results more convenient to use and modify. The complete equilibrium equation and the method of finding it can be seen in Appendix B.

The displacement field in each subdomain, \mathbf{u}^α ($\alpha = +$ or $-$) can be obtained through standard FE shape function interpolation as indicated,

$$\mathbf{u}^\alpha = \mathbf{N}^\alpha \cdot \mathbf{d}^\alpha \quad (2-31)$$

where \mathbf{d}^α is the nodal displacement array of the subdomain α ($\alpha=+$ or $-$). If the element is cut into 2 quadrilateral sub-domains as shown in Figure 2-7 (b),

$\mathbf{d}^+ = \{u_3, v_3, u_4, v_4, | u_{6'}, v_{6'}, u_{5'}, v_{5'}\}^T$ and $\mathbf{d}^- = \{u_1, v_1, u_2, v_2, | u_6, v_6, u_5, v_5\}^T$. \mathbf{N}^α is the interpolation matrix composed of standard bilinear isoparametric shape functions. The symbol “|” indicates that the displacements ahead of it are regular nodal displacements which are denoted with $\mathbf{d}_{\text{ext}}^+ = \{u_3, v_3, u_4, v_4\}^T$, and those behind it are the internal nodal displacements which are denoted with $\mathbf{d}_{\text{int}}^+ = \{u_{6'}, v_{6'}, u_{5'}, v_{5'}\}^T$.

Similarly, $\mathbf{d}_{\text{ext}}^- = \{u_1, v_1, u_2, v_2\}^T$ and $\mathbf{d}_{\text{int}}^- = \{u_6, v_6, u_5, v_5\}^T$.

If the element is cut into a triangular and a pentagonal subdomain as in Figure 2-7 (c), then one can obtain

$$\mathbf{d}^+ = \begin{Bmatrix} \mathbf{d}_{\text{ext}}^+ \\ \mathbf{d}_{\text{int}}^+ \end{Bmatrix} = \{u_4, v_4, | u_{6'}, v_{6'}, u_{5'}, v_{5'}\}^T \text{ and } \mathbf{d}^- = \begin{Bmatrix} \mathbf{d}_{\text{ext}}^- \\ \mathbf{d}_{\text{int}}^- \end{Bmatrix} = \{u_1, v_1, u_2, v_2, u_3, v_3, | u_6, v_6, u_5, v_5\}^T.$$

The shape functions in the interpolation matrix \mathbf{N}^α are from a polygon FEM with optimized quadrature rules recently developed by Mousavi and colleagues [254]. A brief summary of the shape functions and stiffness integration schemes regarding this method are given in Appendix C. The strain field in each subdomain is:

$$\boldsymbol{\varepsilon}^\alpha = (\partial_L^T \mathbf{N}^\alpha) \cdot \mathbf{d}^\alpha = \mathbf{B}^\alpha \cdot \mathbf{d}^\alpha \quad (2-32)$$

Where ∂_L is the differentiation operator, i. e., $\partial_L = \begin{bmatrix} \partial/\partial x & 0 & \partial/\partial y \\ 0 & \partial/\partial y & \partial/\partial x \end{bmatrix}$, and \mathbf{B}^α is

the so-called strain matrix.

Substituting Eqns (2-31) and (2-32) into Eqn (2-30), one obtains the equilibrium equation for standard elements as follows,

$$\begin{cases} \mathbf{L}^+ \cdot \mathbf{d}^+ = \mathbf{F}_{ext}^+ + \mathbf{F}_{int}^+ \\ \mathbf{L}^- \cdot \mathbf{d}^- = \mathbf{F}_{ext}^- + \mathbf{F}_{int}^- \end{cases} \quad (2-33)$$

where

$\mathbf{L}^\alpha = \iint_{\Omega_e^\alpha} (\mathbf{B}^\alpha)^T \mathbf{D}^\alpha \mathbf{B}^\alpha d\Omega$ is the stiffness matrix corresponding to subdomain α ;

$\mathbf{F}_{ext}^\alpha = \int_{\Gamma_{F^\alpha}} (\mathbf{N}^\alpha)^T \mathbf{f}^\alpha d\Gamma$ is the equivalent external force array on subdomain α ;

$\mathbf{F}_{int}^\alpha = \int_{\Gamma_{c^\alpha}} (\mathbf{N}_{coh}^\alpha)^T \mathbf{t}^\alpha d\Gamma$ is the equivalent internal force array integrated from the cohesive

stresses along the intra-element cohesive crack.

$\mathbf{D}^\alpha = \frac{E^\alpha}{1-(\nu^\alpha)^2} \begin{bmatrix} 1 & \nu^\alpha & 0 \\ \nu^\alpha & 1 & 0 \\ 0 & 0 & (1-\nu^\alpha)/2 \end{bmatrix}$ is the material stiffness matrix of subdomain α .

In the interest of developing an efficient A-FE that can deal with multiple interactive intra-element cracks, here we adopt the non-conforming approach, which basically assumes that the inter-element continuity is enforced only through the regular (or external) nodes and their nodal DoFs (\mathbf{d}_{ext}^+ and \mathbf{d}_{ext}^-); while the conformity of the internal

DoFs associated with the internal nodes (\mathbf{d}_{int}^+ and \mathbf{d}_{int}^-) are not enforced. This simplification leads to the conclusion that \mathbf{F}_{ext}^α is a function of regular nodal DoFs (\mathbf{d}_{ext}^+ and \mathbf{d}_{ext}^-) only, and \mathbf{F}_{int}^α is a function of internal DoFs (\mathbf{d}_{int}^+ and \mathbf{d}_{int}^-) only, which allows us to rewrite Eqn (2-33) as follows,

$$\begin{aligned} \begin{bmatrix} \mathbf{L}_{11}^+ & \mathbf{L}_{12}^+ \\ \mathbf{L}_{21}^+ & \mathbf{L}_{22}^+ \end{bmatrix} \begin{Bmatrix} \mathbf{d}_{ext}^+ \\ \mathbf{d}_{int}^+ \end{Bmatrix} &= \begin{Bmatrix} \mathbf{F}_{ext}^+ \\ \mathbf{F}_{int}^+ \end{Bmatrix} \\ \begin{bmatrix} \mathbf{L}_{11}^- & \mathbf{L}_{12}^- \\ \mathbf{L}_{21}^- & \mathbf{L}_{22}^- \end{bmatrix} \begin{Bmatrix} \mathbf{d}_{ext}^- \\ \mathbf{d}_{int}^- \end{Bmatrix} &= \begin{Bmatrix} \mathbf{F}_{ext}^- \\ \mathbf{F}_{int}^- \end{Bmatrix} \end{aligned} \quad (2-34)$$

where \mathbf{L}_{ij}^α ($i,j=1,2$; $\alpha = +, -$) are the sub-matrices of \mathbf{L}^α , i.e., $\mathbf{L}^\alpha = \begin{bmatrix} \mathbf{L}_{11}^\alpha & \mathbf{L}_{12}^\alpha \\ \mathbf{L}_{21}^\alpha & \mathbf{L}_{22}^\alpha \end{bmatrix}$. Note that

\mathbf{L}_{22}^α is the sub-stiffness matrix related to the two internal nodes of subdomain α .

The condensed elemental equilibrium equations for both of the configurations in Figure 2-7 (b) and Figure 2-7 (c) can be derived in a unified formulation. It is noted that for both configurations, the internal DoFs and equivalent force arrays are the same, i. e.

$$\begin{aligned} \mathbf{d}_{int}^+ = \mathbf{d}_{65'} &= \{u_{6'}, v_{6'}, u_{5'}, v_{5'}\}^T; & \mathbf{d}_{int}^- = \mathbf{d}_{65} &= \{u_6, v_6, u_5, v_5\}^T; \\ \mathbf{F}_{int}^+ = \mathbf{F}_{65'} &= \{F_{x6'}, F_{y6'}, F_{x5'}, F_{y5'}\}^T; & \mathbf{F}_{int}^- = \mathbf{F}_{65} &= \{F_{x6}, F_{y6}, F_{x5}, F_{y5}\}^T; \end{aligned} \quad (2-35(a))$$

The external DoFs and force arrays are specific to a particular crack configuration. For the two quadrilateral subdomain configurations of Figure 2-7 (b), they are

$$\begin{aligned} \mathbf{d}_{ext}^+ = \mathbf{d}_{34} &= \{u_3, v_3, u_4, v_4\}^T; & \mathbf{d}_{ext}^- = \mathbf{d}_{12} &= \{u_1, v_1, u_2, v_2\}^T; \\ \mathbf{F}_{ext}^+ = \mathbf{F}_{34} &= \{F_{x3}, F_{y3}, F_{x4}, F_{y4}\}^T; & \mathbf{F}_{ext}^- = \mathbf{F}_{12} &= \{F_{x1}, F_{y1}, F_{x2}, F_{y2}\}^T; \end{aligned} \quad (2-35(b))$$

For the triangular-pentagonal subdomain configuration of Figure 2-7(c),

$$\begin{aligned} \mathbf{d}_{\text{ext}}^+ &= \mathbf{d}_4 = \{u_4, v_4\}^T; & \mathbf{d}_{\text{ext}}^- &= \mathbf{d}_{123} = \{u_1, v_1, u_2, v_2, u_3, v_3\}^T; \\ \mathbf{F}_{\text{ext}}^+ &= \mathbf{F}_4 = \{F_{x4}, F_{y4}\}^T; & \mathbf{F}_{\text{ext}}^- &= \mathbf{F}_{123} = \{F_{x1}, F_{y1}, F_{x2}, F_{y2}, F_{x3}, F_{y3}\}^T; \end{aligned} \quad (2-35(c))$$

However, for both configurations, the equilibrium equations can be written as:

$$\begin{aligned} \begin{bmatrix} \mathbf{L}_{11}^+ & \mathbf{L}_{12}^+ \\ \mathbf{L}_{21}^+ & \mathbf{L}_{22}^+ \end{bmatrix} \begin{Bmatrix} \mathbf{d}_{\text{ext}}^+ \\ \mathbf{d}_{6'5'} \end{Bmatrix} &= \begin{Bmatrix} \mathbf{F}_{\text{ext}}^+ \\ \mathbf{F}_{6'5'} \end{Bmatrix} \quad (\text{for } \Omega^+) \\ \begin{bmatrix} \mathbf{L}_{11}^- & \mathbf{L}_{12}^- \\ \mathbf{L}_{21}^- & \mathbf{L}_{22}^- \end{bmatrix} \begin{Bmatrix} \mathbf{d}_{\text{ext}}^- \\ \mathbf{d}_{65} \end{Bmatrix} &= \begin{Bmatrix} \mathbf{F}_{\text{ext}}^- \\ \mathbf{F}_{65} \end{Bmatrix} \quad (\text{for } \Omega^-) \end{aligned} \quad (2-36)$$

Also, due to stress continuity across the cohesive crack, $\mathbf{F}_{65} = -\mathbf{F}_{6'5'} = \int_{\Gamma_c} \mathbf{N}_{coh}^T \mathbf{t} d\Gamma$. Eqn (2-36) is valid for both weak and strong discontinuity problems. In the following, it will be demonstrated that the method can handle, in a mathematically rigorous way, the smooth evolution from a weak discontinuity such as rigid bi-material interface to a strong discontinuity such as a cohesive crack.

Weak discontinuity:

If the two subdomains of the element are of two different materials and they are bonded by a rigid interface, the problem is called a weak discontinuity problem because across the interface the normal and tangential displacements are continuous but the strains are not. This type of problems is a bit awkward to handle by the X-FEM or PNM because they have to utilize a large penalty factor to enforce the displacement continuity. The new A-FEM can handle this type of problems very conveniently.

For weak discontinuity problems, $\mathbf{d}_{65'} = \mathbf{d}_{65}$. Together with the condition of $\mathbf{F}_{65'} = -\mathbf{F}_{65}$,

Eqn (2-36) further simplifies to

$$\begin{Bmatrix} \mathbf{F}_{ext}^- \\ \mathbf{F}_{ext}^+ \end{Bmatrix} = \begin{bmatrix} \mathbf{L}_{11}^- - \mathbf{L}_{12}^- \mathbf{\Lambda}^{-1} \mathbf{L}_{21}^- & -\mathbf{L}_{12}^- \mathbf{\Lambda}^{-1} \mathbf{L}_{21}^+ \\ -\mathbf{L}_{12}^+ \mathbf{\Lambda}^{-1} \mathbf{L}_{21}^- & \mathbf{L}_{11}^+ - \mathbf{L}_{12}^+ \mathbf{\Lambda}^{-1} \mathbf{L}_{21}^+ \end{bmatrix} \begin{Bmatrix} \mathbf{d}_{ext}^- \\ \mathbf{d}_{ext}^+ \end{Bmatrix} \quad (2-37)$$

Where $\mathbf{\Lambda} = \mathbf{L}_{22}^- + \mathbf{L}_{22}^+$. Furthermore, the internal forces are determined as:

$$\{\mathbf{F}_{65}\} = \left\{ \left(\mathbf{I} - \mathbf{L}_{22}^- \mathbf{\Lambda}^{-1} \right) \mathbf{L}_{21}^- \quad -\mathbf{L}_{22}^- \mathbf{\Lambda}^{-1} \mathbf{L}_{21}^+ \right\} \begin{Bmatrix} \mathbf{d}_{ext}^- \\ \mathbf{d}_{ext}^+ \end{Bmatrix} \quad (2-38)$$

Thus, for an element containing two material domains with a perfectly bonded interface, once the external nodal displacements are given (which is the case for displacement-based FEs), the resultant forces acting along the interface are immediately known. This solution is mathematically rigorous in the FEM sense. Thus, there is no need to introduce a large but finite stiffness for the interfaces as would be needed in PNM and the earlier version of the A-FEM formulation. The artificially added initial finite stiffness for interfaces may cause problems such as mesh dependence [255] as well as inconsistencies in physical problems [111,112].

With $\{\mathbf{F}_{65}\}$ known, the current tractions acting on the interface are known. For example, the normal and shear stresses averaged along the interface, in local coordinates, are

$$\begin{Bmatrix} \bar{\tau}_{int} \\ \bar{\sigma}_{int} \end{Bmatrix} = [\mathbf{R}_1]^T \begin{Bmatrix} (F_{x5} + F_{x6})/l_{e1} \\ (F_{y5} + F_{y6})/l_{e1} \end{Bmatrix}, \text{ where } l_{e1} \text{ is the interface length (Figure 2-7 (a)). These}$$

stresses can then be used to determine the initiation of interface debonding, which is the

turning point from a weak discontinuity to a strong one. A common initiation criterion used here, is

$$\left(\langle \bar{\sigma}_{\text{int}} \rangle / \hat{\sigma}_1\right)^2 + \left(\bar{\tau}_{\text{int}} / \hat{\tau}_1\right)^2 = 1 \quad (2-39)$$

where the MacAulay bracket $\langle \bullet \rangle$, defined as $\langle \bullet \rangle = (\bullet + |\bullet|) / 2$, is used to reflect the physical observation that compressive normal stresses do not contribute to crack initiation.

If the criterion of Eqn (2-39) is met, the discontinuity becomes a strong one, i. e., $\mathbf{d}_{65'} \neq \mathbf{d}_{65}$, which is addressed next.

Strong discontinuity

If the element is cut by a cohesive crack or the initially rigidly bonded interface crack starts to open, the problem becomes a strong discontinuity one. Following the notation established in Appendix A, the cohesive stresses between two pairs of internal nodes 5-5' and 6-6' can be expressed in its local coordinates as

$$\left\{ \tau_{66'}^{(i)}, \sigma_{66}^{(j)}, \tau_{55'}^{(k)}, \sigma_{55'}^{(l)} \right\}^T = \boldsymbol{\sigma}_0^{(i,j,k,l)} + \mathbf{a}_0^{(i,j,k,l)} \left\{ \delta_{s66'}, \delta_{n66'}, \delta_{s55'}, \delta_{n55'} \right\}^T \quad (i, j, k, l \in [1, 2, 3, 4]) \quad (2-40(a))$$

where

$$\boldsymbol{\sigma}_0^{(i,j,k,l)} = \left\{ \hat{\tau}^{(i-1)} - \alpha_s^{(i)} \delta_s^{(i-1)}, \hat{\sigma}^{(j-1)} - \alpha_n^{(j)} \delta_n^{(j-1)}, \hat{\tau}^{(k-1)} - \alpha_s^{(k)} \delta_s^{(k-1)}, \hat{\sigma}^{(l-1)} - \alpha_n^{(l)} \delta_n^{(l-1)} \right\}^T \quad (2-40(b))$$

is the characteristic stress matrix. The critical stresses, corresponding crack displacements and cohesive slopes have been defined in Appendix A (Eqns (A1-A3) and Figure A1).

$$\boldsymbol{\alpha}_0^{(i,j,k,l)} = \text{Diag}[\alpha_s^{(i)}; \alpha_n^{(j)}; \alpha_s^{(k)}; \alpha_n^{(l)}] = \begin{bmatrix} \alpha_s^{(i)} & 0 & 0 & 0 \\ 0 & \alpha_n^{(j)} & 0 & 0 \\ 0 & 0 & \alpha_s^{(k)} & 0 \\ 0 & 0 & 0 & \alpha_n^{(l)} \end{bmatrix} \quad (2-40(c))$$

is the cohesive stiffness matrix (Appendix A). Here $\text{Diag} [a; b; c; d]$ means a diagonal matrix with non-zero a , b , c and d at the corresponding diagonal places. This notation will be used in the rest of this study.

$\{\delta_{s66'}, \delta_{n66'}, \delta_{s55'}, \delta_{n55'}\}^T$ is the crack displacement array at internal node-pairs 6'-6 and 5'-5 measured in the local coordinate system.

The free indices (i , j , k , and l) can range from 1 to the maximum cohesive segment number, indicating in which segments of the cohesive laws the current cohesive stresses are located (Appendix A). Note, the characteristic stress and stiffness matrices are determined if any particular combination of (i , j , k , and l) is chosen.

\mathbf{F}_{65} and $\mathbf{F}_{65'}$ are obtained by integrating the cohesive stresses in Eqn (2-40(a)) over the crack plane and then converted into global coordinates using the rotation matrix \mathbf{R}_1 , which gives:

$$\mathbf{F}_{65} = -\mathbf{F}_{65'} = l_{el} (\mathbf{S}_o^{(i,j,k,l)} + \boldsymbol{\alpha}^{(i,j,k,l)} \cdot \Delta \mathbf{d}_{\text{int}}) \quad (2-41(a))$$

where $\Delta \mathbf{d}_{\text{int}} = \mathbf{d}_{6'5'} - \mathbf{d}_{65} = \begin{Bmatrix} \mathbf{d}_{6'} - \mathbf{d}_6 \\ \mathbf{d}_{5'} - \mathbf{d}_5 \end{Bmatrix}$ are the crack displacements at node pairs 6'-6 and 5'-5 in global coordinates, i. e.,

$$\Delta \mathbf{d}_{\text{int}} = \mathbf{d}_{6'5'} - \mathbf{d}_{65} = \text{Diag}[\mathbf{R}_1; \mathbf{R}_1] \{\delta_{s66'}, \delta_{n66'}, \delta_{s55'}, \delta_{n55'}\}^T \quad (2-41(b))$$

$\{\mathbf{S}_0\}$ and $[\boldsymbol{\alpha}]$ are related to the characteristic cohesive stress and stiffness matrices in Eqn (2-15) by:

$$\begin{aligned}\mathbf{S}_0 &= \text{Diag}[\mathbf{R}_1^T; \mathbf{R}_1^T] (\mathbf{T}_{coh})^T \boldsymbol{\sigma}_0^{(i,j,k,l)} \\ \boldsymbol{\alpha} &= \text{Diag}[\mathbf{R}_1^T; \mathbf{R}_1^T] (\mathbf{T}_{coh})^T \boldsymbol{\alpha}_0^{(i,j,k,l)} \mathbf{N}_{coh} \text{Diag}[\mathbf{R}_1; \mathbf{R}_1]\end{aligned}\quad (2-41 \text{ (c)})$$

Here \mathbf{T}_{coh} and \mathbf{N}_{coh} are the integration and interpolation matrices associated with the cohesive stress integration and the displacement interpolation along the crack plane, respectively. These matrices are given in Appendix D for several popular interpolation and integration schemes. For the single crack case, we used the standard Gaussian interpolation and integration scheme, i. e.,

$$\mathbf{N}_{coh} = \begin{bmatrix} \text{Diag}[\xi_B; \xi_B] & \text{Diag}[\xi_A; \xi_A] \\ \text{Diag}[\xi_A; \xi_A] & \text{Diag}[\xi_B; \xi_B] \end{bmatrix}; \mathbf{T}_{coh} = \frac{l_{e1}}{2} \begin{bmatrix} \text{Diag}[\xi_B; \xi_B] & \text{Diag}[\xi_A; \xi_A] \\ \text{Diag}[\xi_A; \xi_A] & \text{Diag}[\xi_B; \xi_B] \end{bmatrix} = \frac{l_{e1}}{2} \mathbf{N}_{coh}^T.$$

Where $\xi_A = (1 - 1/\sqrt{3})/2$ and $\xi_B = (1 + 1/\sqrt{3})/2$. The matrices for several other popular interpolation and integration schemes have been summarized in [256].

Substituting Eqn (2-41(a)) into second rows in Eqn (2-36), the following equation is derived:

$$\begin{aligned}(\mathbf{L}_{22}^+ + l_{e1} \boldsymbol{\alpha}) \mathbf{d}_{6'5'} - (l_{e1} \boldsymbol{\alpha}) \mathbf{d}_{65} &= -l_{e1} \mathbf{S}_0 - \mathbf{L}_{21}^+ \mathbf{d}_{\text{ext}}^+ \\ -(l_{e1} \boldsymbol{\alpha}) \mathbf{d}_{6'5'} + (\mathbf{L}_{22}^- + l_{e1} \boldsymbol{\alpha}) \mathbf{d}_{65} &= l_{e1} \mathbf{S}_0 - \mathbf{L}_{21}^- \mathbf{d}_{\text{ext}}^-\end{aligned}\quad (2-42)$$

From Eqn (2-42), the crack displacements at the internal node pairs, $\Delta \mathbf{d}_{\text{int}} = \mathbf{d}_{6'5'} - \mathbf{d}_{65}$, is solved explicitly:

$$\begin{aligned} \Delta \mathbf{d}_{\text{int}} = & -l_{e1} \left(\mathbf{A}^{-1} + \mathbf{B}^{-1} - l_{e1} \mathbf{A}^{-1} \boldsymbol{\alpha} (\boldsymbol{\psi}_{22}^-)^{-1} + l_{e1} \mathbf{B}^{-1} \boldsymbol{\alpha} (\boldsymbol{\psi}_{22}^+)^{-1} \right) \mathbf{S}_0 \\ & + \left(\mathbf{B}^{-1} - l_{e1} \mathbf{A}^{-1} \boldsymbol{\alpha} (\boldsymbol{\psi}_{22}^-)^{-1} \right) \mathbf{L}_{21}^- \mathbf{d}_{\text{ext}}^- + \left(l_{e1} \mathbf{B}^{-1} \boldsymbol{\alpha} (\boldsymbol{\psi}_{22}^+)^{-1} - \mathbf{A}^{-1} \right) \mathbf{L}_{21}^+ \mathbf{d}_{\text{ext}}^+ \end{aligned} \quad (2-43(a))$$

where

$$\boldsymbol{\psi}_{22}^+ = \mathbf{L}_{22}^+ + l_{e1} \boldsymbol{\alpha}; \boldsymbol{\psi}_{22}^- = \mathbf{L}_{22}^- + l_{e1} \boldsymbol{\alpha}; \mathbf{A} = \boldsymbol{\psi}_{22}^+ - l_{e1}^2 \boldsymbol{\alpha} (\boldsymbol{\psi}_{22}^-)^{-1} \boldsymbol{\alpha}; \mathbf{B} = \boldsymbol{\psi}_{22}^- - l_{e1}^2 \boldsymbol{\alpha} (\boldsymbol{\psi}_{22}^+)^{-1} \boldsymbol{\alpha} \quad (2-43(b))$$

The explicit solution to the crack displacements can also be solved as:

$$\begin{aligned} \begin{Bmatrix} \mathbf{d}_{65'} \\ \mathbf{d}_{65} \end{Bmatrix} = & \begin{bmatrix} -l_{e1} \mathbf{A}^{-1} \left(\mathbf{I} - l_{e1} \boldsymbol{\alpha} (\boldsymbol{\psi}_{22}^-)^{-1} \right) & \mathbf{0} \\ \mathbf{0} & l_{e1} \mathbf{B}^{-1} \left(\mathbf{I} - l_{e1} \boldsymbol{\alpha} (\boldsymbol{\psi}_{22}^+)^{-1} \right) \end{bmatrix} \begin{Bmatrix} \mathbf{S}_0 \\ \mathbf{S}_0 \end{Bmatrix} \\ & + \begin{bmatrix} -l_{e1} \mathbf{A}^{-1} \boldsymbol{\alpha} (\boldsymbol{\psi}_{22}^-)^{-1} \mathbf{L}_{12}^- & -\mathbf{A}^{-1} \mathbf{L}_{21}^+ \\ -\mathbf{B}^{-1} \mathbf{L}_{21}^- & -l_{e1} \mathbf{B}^{-1} \boldsymbol{\alpha} (\boldsymbol{\psi}_{22}^+)^{-1} \mathbf{L}_{21}^+ \end{bmatrix} \begin{Bmatrix} \mathbf{d}_{\text{ext}}^- \\ \mathbf{d}_{\text{ext}}^+ \end{Bmatrix} \end{aligned} \quad (2-43(c))$$

The fully condensed equilibrium equation without any internal forces and displacements can be obtained by substituting Eqn (2-43) into first rows in Eqn (2-36) and eliminating \mathbf{F}_{65} and $\mathbf{F}_{65'}$, i.e.,

$$\begin{aligned} \begin{bmatrix} \mathbf{L}_{11}^- - \mathbf{L}_{12}^- \mathbf{B}^{-1} \mathbf{L}_{21}^- & -l_{e1} \mathbf{L}_{12}^- \mathbf{B}^{-1} \boldsymbol{\alpha} (\boldsymbol{\psi}_{22}^+)^{-1} \mathbf{L}_{21}^+ \\ -l_{e1} \mathbf{L}_{12}^+ \mathbf{A}^{-1} \boldsymbol{\alpha} (\boldsymbol{\psi}_{22}^-)^{-1} \mathbf{L}_{21}^- & \mathbf{L}_{11}^+ - \mathbf{L}_{12}^+ \mathbf{A}^{-1} \mathbf{L}_{21}^+ \end{bmatrix} \begin{Bmatrix} \mathbf{d}_{\text{ext}}^- \\ \mathbf{d}_{\text{ext}}^+ \end{Bmatrix} = \\ \begin{Bmatrix} \mathbf{F}_{\text{ext}}^- \\ \mathbf{F}_{\text{ext}}^+ \end{Bmatrix} - \begin{bmatrix} l_{e1} \mathbf{L}_{12}^- \mathbf{B}^{-1} \left(\mathbf{I} - l_{e1} \boldsymbol{\alpha} (\boldsymbol{\psi}_{22}^+)^{-1} \right) & \mathbf{0} \\ \mathbf{0} & -l_{e1} \mathbf{L}_{12}^+ \mathbf{A}^{-1} \left(\mathbf{I} - l_{e1} \boldsymbol{\alpha} (\boldsymbol{\psi}_{22}^-)^{-1} \right) \end{bmatrix} \begin{Bmatrix} \mathbf{S}_0 \\ \mathbf{S}_0 \end{Bmatrix} \end{aligned} \quad (2-44)$$

Eqn (2-44) is highly nonlinear because the matrices \mathbf{S}_0 , \mathbf{A} , \mathbf{B} , $\boldsymbol{\psi}_{22}^+$ and $\boldsymbol{\psi}_{22}^-$, are all nonlinear functions of crack displacements $\Delta \mathbf{d}_{\text{int}}$ (through $\boldsymbol{\alpha}_0$ and $\boldsymbol{\sigma}_0$ - see Eqn (2-41(c)) and Eqn (2-43(b)), which are not known because at this point the only information is the

external displacements $\mathbf{d}_{\text{ext}}^-$ and $\mathbf{d}_{\text{ext}}^+$. We shall defer the discussion of solution procedure to the next section.

2.5 Elemental Condensation Algorithm

In the previous section, the elemental equilibrium equations for a single crack have been derived with details. However, these nonlinear equations have yet to be solved. In literature, Eqn (2-44) is typically re-formulated into an incremental form and then solved with either the direct matrix inversion technique [234, 235,237] or a Newton-Raphson type of iterative solver [233, 257,258]. This is known as the static condensation process.

In this study, the explicit nature of solutions enables a very efficient elemental condensation process that is completely different from what have been used in the literature. Instead of solving the incremental form of the elemental equilibrium of Eqn (2-44), here the internal nodal displacements, Eqn (2-43), is first solved analytically through a simple consistency checking procedure. It will be shown that once these equations are solved, the equilibrium equations, Eqn (2-44), are satisfied with mathematical exactness by substituting the related matrices into them.

It is noted that, once Eqn (2-43(a)) is solved, i.e., \mathbf{S}_0 , \mathbf{A} , \mathbf{B} , $\boldsymbol{\psi}_{22}^+$ and $\boldsymbol{\psi}_{22}^-$ are established, simply substituting these matrices into Eqn (2-44) will guarantee the elemental equilibrium. The global crack displacements in Eqn (2-43(a)) can be converted into local crack displacements using Eqn (2-41(b)), which gives

$$\begin{Bmatrix} \delta_{s66'} \\ \delta_{n66'} \\ \delta_{s55'} \\ \delta_{n55'} \end{Bmatrix}^T = \text{Diag}[\mathbf{R}_1^T; \mathbf{R}_1^T] \begin{pmatrix} -l_{e1} \left(\mathbf{A}^{-1} + \mathbf{B}^{-1} - l_{e1} \mathbf{A}^{-1} \boldsymbol{\alpha}(\boldsymbol{\psi}_{22}^-)^{-1} + l_{e1} \mathbf{B}^{-1} \boldsymbol{\alpha}(\boldsymbol{\psi}_{22}^+)^{-1} \right) \mathbf{S}_0 \\ + \left(\mathbf{B}^{-1} - l_{e1} \mathbf{A}^{-1} \boldsymbol{\alpha}(\boldsymbol{\psi}_{22}^-)^{-1} \right) \mathbf{L}_{21}^- \mathbf{d}_{ext}^- + \left(l_{e1} \mathbf{B}^{-1} \boldsymbol{\alpha}(\boldsymbol{\psi}_{22}^+)^{-1} - \mathbf{A}^{-1} \right) \mathbf{L}_{21}^+ \mathbf{d}_{ext}^+ \end{pmatrix}^{(i,j,k,l)} \quad (2-45)$$

In Eqn (2-45), the superscripts (i, j, k, l) in the right-hand-side are included to emphasize that the matrices \mathbf{S}_0 , \mathbf{A} , \mathbf{B} , $\boldsymbol{\psi}_{22}^+$ and $\boldsymbol{\psi}_{22}^-$ are all functions of the cohesive slope matrix $\boldsymbol{\alpha}_0^{(i,j,k,l)}$ and characteristic stress matrix $\boldsymbol{\sigma}_0^{(i,j,k,l)}$ (Eqns (2-41(c)) & (2-43(b))). Thus, for any trial cohesive segment combination (i, j, k, l) , a set of local crack displacements is immediately solved from Eqn (2-45). The solved local crack displacements are then subjected to a consistency check, and *the true solution is found if the following statement is true:* $\delta_{s66'} \in \Delta \delta_s^{(i)}$ & $\delta_{n66'} \in \Delta \delta_n^{(j)}$ & $\delta_{s55'} \in \Delta \delta_s^{(k)}$ & $\delta_{n55'} \in \Delta \delta_n^{(l)}$

where $\Delta \delta_s^{(i)}, \Delta \delta_n^{(j)}, \Delta \delta_s^{(k)}, \Delta \delta_n^{(l)}$ are the respective crack displacement ranges of the assumed segments (i, j, k, l) (Appendix A).

This is the core idea behind the solving algorithm used in this study. The mathematical exactness (in piece-wise linear sense) of the solution is guaranteed by the unique solution of the local problem (the solution uniqueness for linear material with nonlinear discontinuities has been discussed in [259]).

2.6 Numerical Implementation

The new A-FEM and the solving procedure above can be integrated into any standard FE program as a general purposed element because the elemental locality is completely retained. This section describes how to implement it into an existing FEM program as an

element. For any displacement-based FEM program, the external nodal displacements are passed into the element to establish: 1) instantaneous element stiffness matrix or Jacobian matrix, and 2) the external force array (also called right-hand-side or RHS). Both matrices have been derived and solved explicitly in section 2.4 for single crack case, Eqn (2-44). The local crack displacements were saved as solution-dependent variables (or state variables) and subjected to constant updates so that their maximum values ever experienced were always available for assessing loading or unloading condition (for consistency check). Another minor issue is to guarantee the deformation continuity across the element edge that is shared by a crack-tip element and the element immediately ahead of it, which is a standard continuous element. This was conveniently done in this study by enforcing the internal nodal displacements at the edge to be $\mathbf{d}_5 = \mathbf{d}_{5'} = \mathbf{N}_A \mathbf{d}_A + \mathbf{N}_B \mathbf{d}_B$, where 5 and 5' are the internal nodes at the crack-tip; A and B are the two external nodes of the element edge hosting the crack-tip; and \mathbf{N}_A and \mathbf{N}_B are the standard line shape functions associated with node A and B.

One of the advantages of this method is that it does not need a sophisticated global tracking algorithm such as the level-set functions typically employed in X-FEM for crack propagation. However, it is beneficial to record the crack path so that the inter-element continuity of a crack is reinforced. This was done with a common block accessible to all user elements, within which the geometric information of a crack was constantly updated as it propagated. With this scheme, the global continuity of the crack is ensured with minimal tracking efforts.

As an example, the flowchart for integrating the aforementioned formulation in ABAQUS (V6.10) as a user-defined element is given in Figure 2-8. Integration of the element to other FEM programs should be very similar.

By implementing the 2-D A-FEM formulation into ABAQUS (V6.10), instead of using regular finite elements, by using the augmented finite elements, the ability of considering intra-element weak and strong discontinuities can be obtained.

In next section, we shall verify the A-FEM formulation for simple cases such as a single element which potentially can be cut by a cohesive crack. After testing several cases and comparing to available results for similar problem, the method will be verified for the single discontinuity consideration.

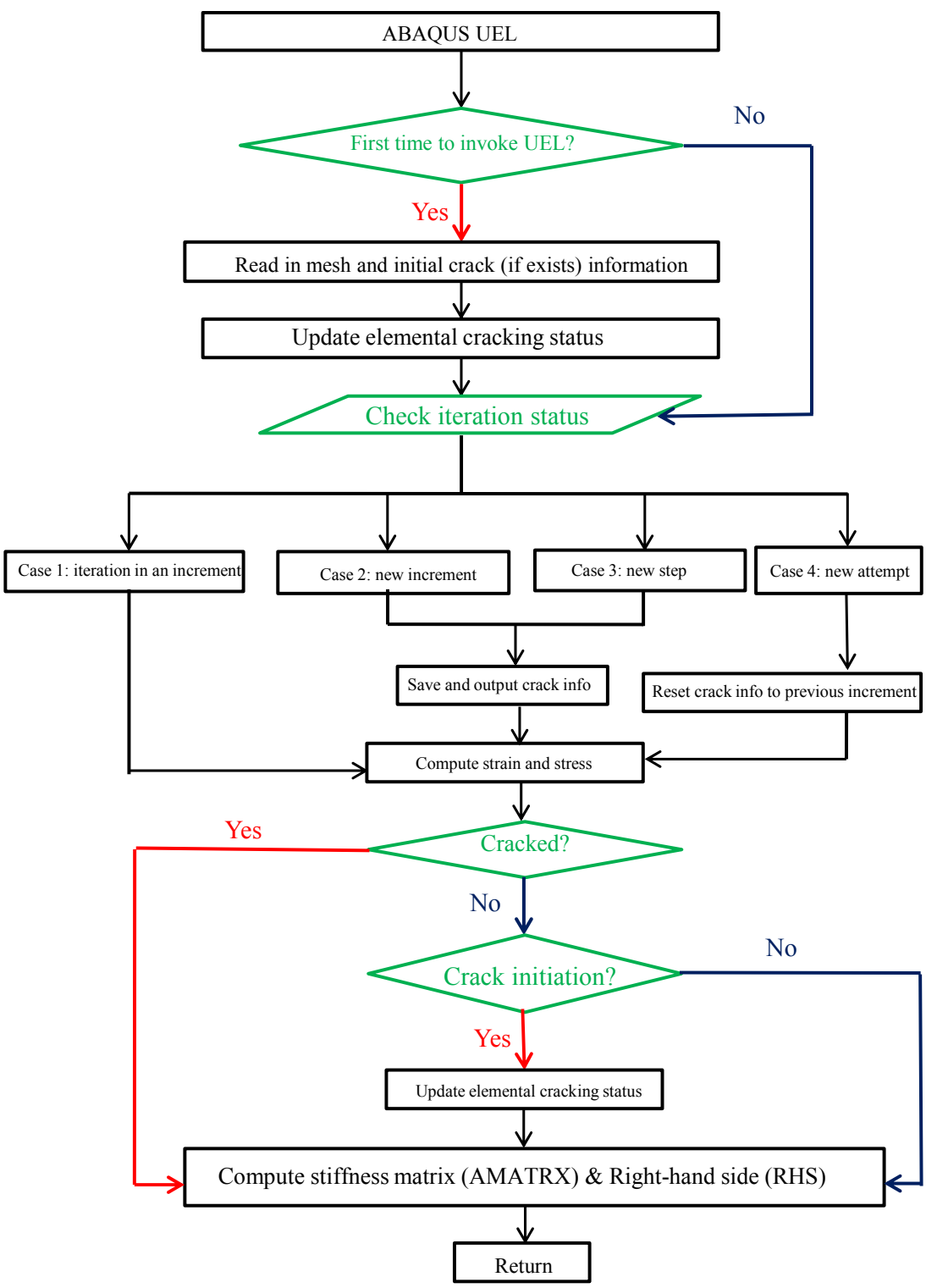


Figure 2-8 Flow chart of implementation of the present A-FEM into ABAQUS as a user defined element

2.7 Single Element Validation

After formulating the A-FEM and defining solution procedure, the first step should be verifying the method by testing the single augmented element under various loading conditions. Displacement –based loading is used to have different modes such as mode I, II and mixed mode loading conditions. The element is assigned a very large modulus so that the responses are mainly from the cohesive law. The element is 2-mm long and 2-mm high, hosting a center horizontal discontinuity. The cohesive law is a triangular one with $\hat{\sigma} = \hat{\tau} = 1$ MPa, $\delta_{nc} = \delta_{sc} = 0.1$ mm. The initial slopes are $\alpha_{n1} = \alpha_{s1} = 10^7$ N/(mm)³, and the slopes at the softening phases are $\alpha_{n2} = \alpha_{s2} = -10$ N/(mm)³. Therefore, the mode I and mode II toughness are $\Gamma_I = \Gamma_{II} = 0.05$ N/mm (50 J/m²).

In each case, the A-FEM results are compared with responses from an FEM model simulated in ABAQUS using a combination of regular elements (CPS4) for top and bottom subdomains, and cohesive elements (COH2D4) with zero thickness to allow separation between two domains. In some cases the A-FEM results are compared to available analytical results.

2.7.1 Mode I response

The mode I loading response is shown in Figure 2-9. In this case, nodes 3 and 4 are displaced just in vertical direction while the other DoFs are fixed, this type of displacement leads to mode I displacement loading. By plotting load-displacement curves for nodes 3 and 4, it is seen that the peak nodal forces at nodes 3 and 4 are 1.0 N/mm and final failure should occur at the critical displacement of 0.1mm. Comparing the results

with ABAQUS results with same geometry and material properties, they are exactly identical.

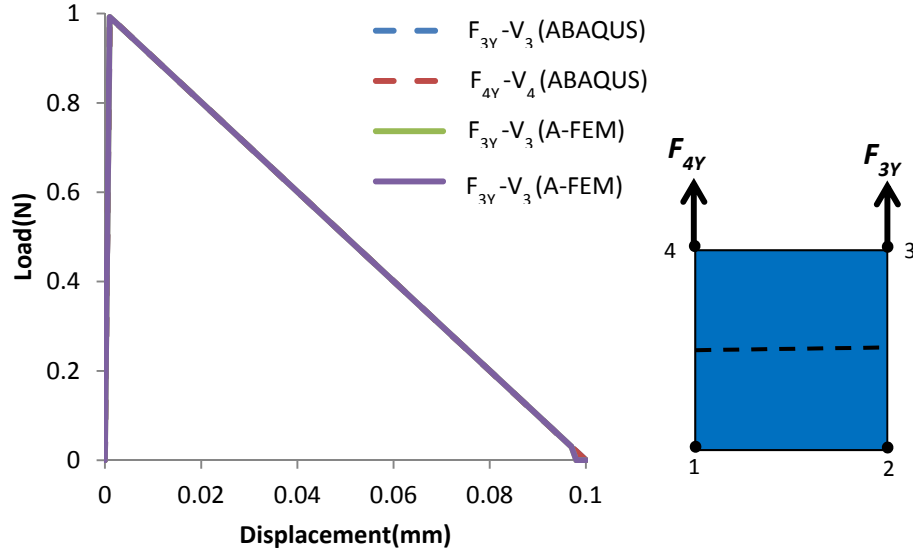


Figure 2-9 Single A-FE response under mode I loading conditions

For this problem the exact solution is available. Through a FBD (free body diagram) analysis of the top domain such as Figure 2-10, the nodal forces at crack initiation are

found as $F_{3y} = F_{4y} = \frac{\hat{\sigma} \cdot 2}{2} = 1$ which are identical to predicted peak loads of the A-FEM.

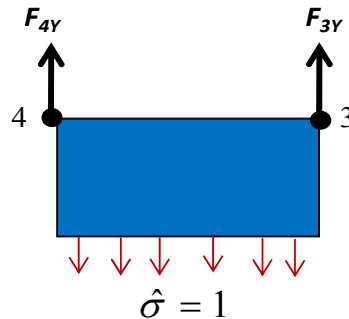


Figure 2-10 FBD evaluation of top domain at crack initiation instant

Comparison of the deformed shapes from the A-FEM and the ABAQUS is shown in Figure 2-11. Both show the same deformation in mode I direction.

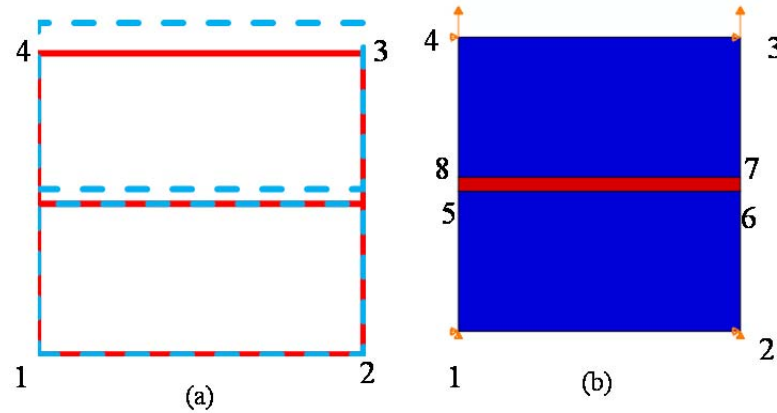


Figure 2-11 (a) Deformed shape from A-FEM, (b) from ABAQUS

It is important to note that although the results are identical from A-FEM and ABAQUS, ABAQUS needs to use three elements, two regular and one cohesive, to model the problem, while the A-FEM solves the problem with only one element.

2.7.2 Mode II response

By displacing nodes 3 and 4 in the horizontal direction and keeping other DoFs fixed, mode II loading condition can be obtained. The nodal force under mode II loading is shown in Figure 2-12 which is identical to the ABAQUS response.

As in the mode I case, considering FBD of top domain in Figure 2-13 and by means of load equilibrium, the equivalent nodal forces can be found as $F_{3x} = F_{4x} = \frac{\hat{\tau} \cdot 2}{2} = 1$. They are identical to the results of the A-FEM and the ABAQUS. The deformed shapes from

the A-FEM and from the ABAQUS as shown in Figure 2-14 are identical. Again, ABAQUS solved this problem by using three elements while the A-FEM solved it just by one element.

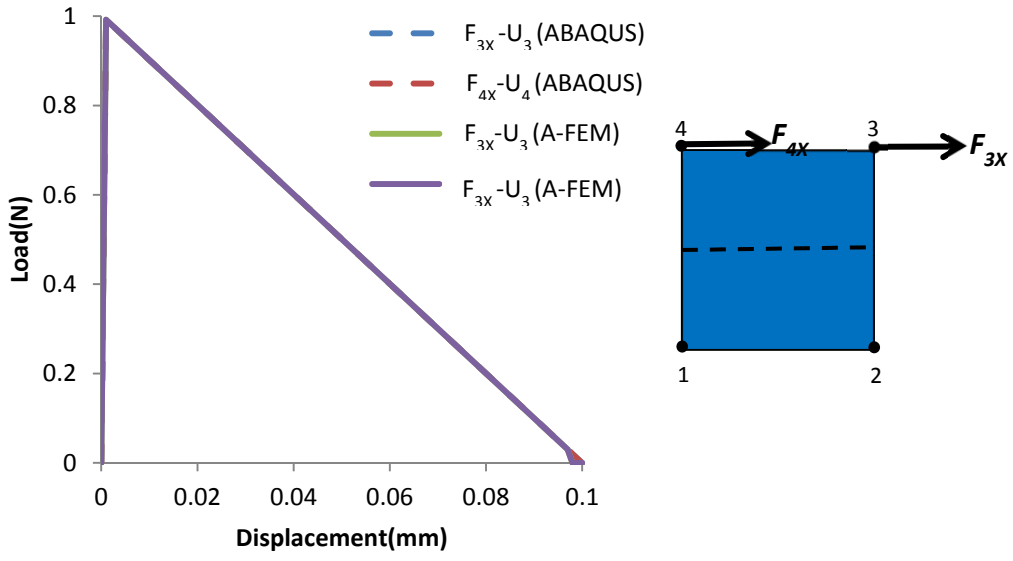


Figure 2-12 Single A-FE under mode II loading condition

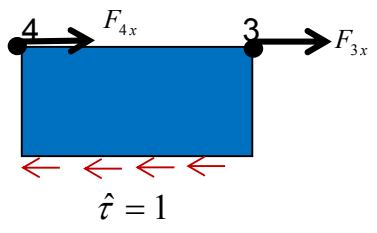


Figure 2-13 FBD of the top domain at crack initiation instant

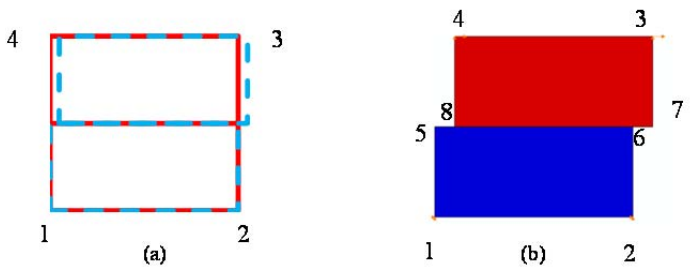


Figure 2-14 Deformed shapes from (a) the A-FEM and (b) ABAQUS

2.7.3 Mixed- Mode response

After verifying pure mode cases, the mixed mode loading case is obtained by combining the previous pure modes as shown in Figure 2-15 which depicts the curves of $F_{3X}-U_3$ and $F_{3Y}-V_3$.

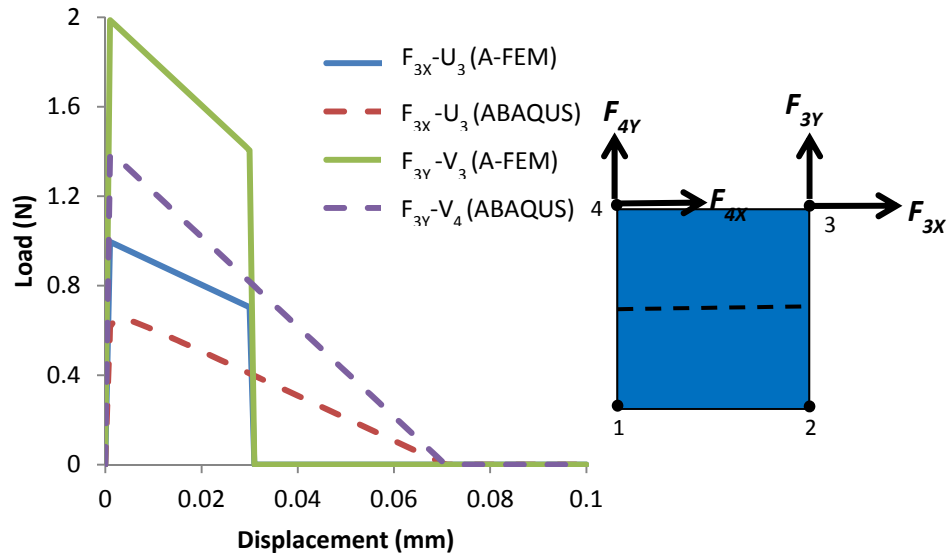


Figure 2-15 Load-displacement plot for node 3 under mixed mode

The curves from ABAQUS and A-FEM look different. Due to the different cohesive law used by ABAQUS, which considered equivalent stress so that stress in each direction can be smaller than the critical stress. But the cohesive law of this study requires that in each direction, the stress state should reach the critical stress before starting to drop. This is the reason that the ABAQUS results shows smaller peak load than the A-FEM results. However the areas under both curves are equal, which means that energy release rates for both methods are identical. This should be always held true because fracture toughness is a type of material property, independent of method or loading. In this case, by moment

equilibrium equation at crack initiation instant it can be found that $F_{3Y} = 2 F_{3X}$, which is held true according to peak loads in these plots.

Comparison of the deformed shapes from two methods shows that the two methods give the identical result.

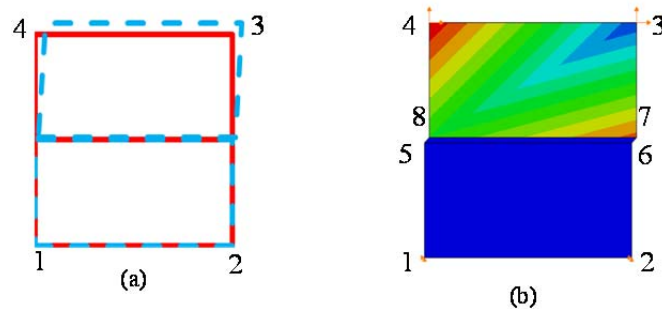


Figure 2-16 (a) Deformed shape from A-FEM, (b) from ABAQUS

2.7.4 Mode –I wedge opening response

The wedge opening mode is an important elemental test to assess the accuracy in the stress state and the energy dissipation in a crack-tip element, where the cohesive stress can be very nonlinear and standard integration schemes may give fairly inaccurate response [260]. In this case, two right nodes (nodes 2 and 3) are pin-constrained while the two left nodes (nodes 1 and 4) are displaced gradually in opposite directions.

The reaction forces versus the nodal displacements are plotted in Figure 2-17 and compared to the ABAQUS results. From Figure 2-17 it is seen that both methods capture fairly well the peak load and the responses before it. However, the post-peak responses are vastly different. In particular, ABAQUS which uses standard Newton-Cotes integration scheme leads to premature failure and energy dissipation is off by 50%. The

A-FEM using improved Gaussian integration scheme, gives a result that is almost identical to the analytical solution [256].

The deformed shapes from two methods are also identical as shown in Figure 2-18.

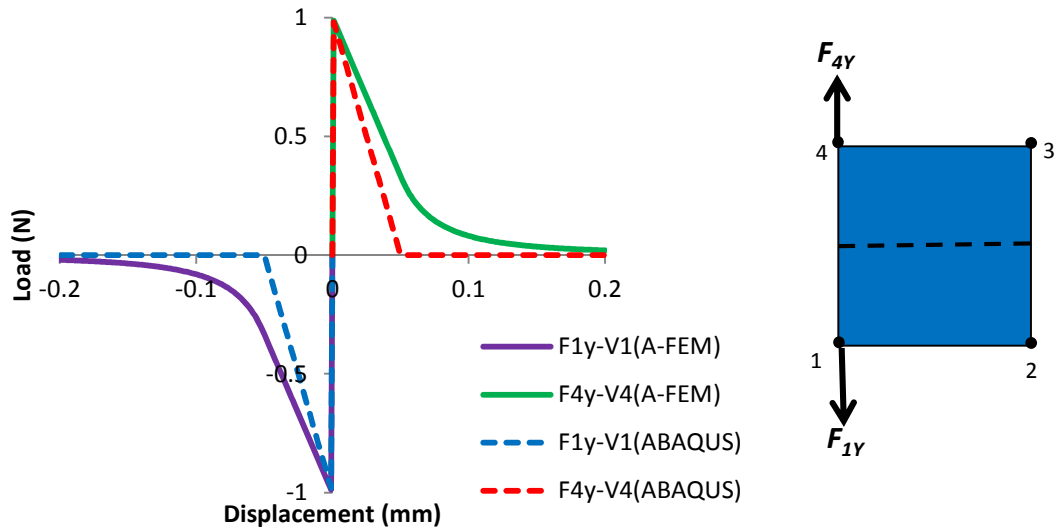


Figure 2-17 Load-displacement for wedge opening

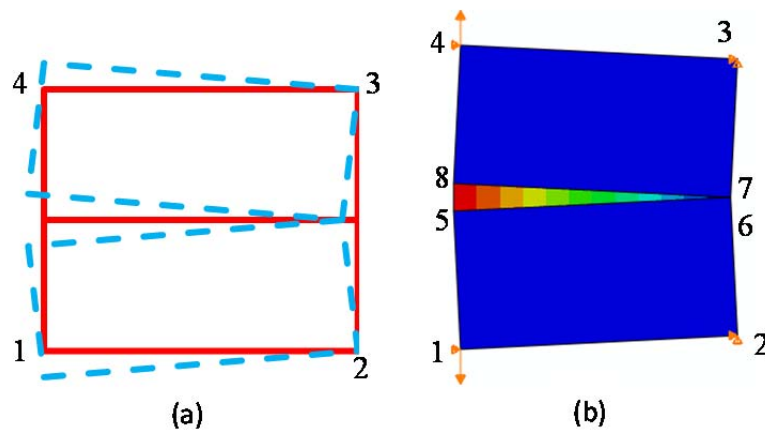


Figure 2-18 Deformed shape from (a) A-FEM, and (b) ABAQUS

2.8 Summary

In this chapter, after a brief review on the exact problem statement, the novel A-FEM was formulated. The solution procedure includes addition of internal nodes at the beginning but using a condensation method, in the final form there were no internal nodes present, means that there is no need to know the crack path *a priori* which is the beauty of the A-FEM. After formulation, implementation process was explained which states how to use this powerful method. At last, some single element validation tests were performed to verify the method for basic cases. All the validations showed that the A-FEM method that needs only one element without any additional DoFs or nodes, can predict the fracture behavior better than FEM in ABAQUS. More elements were needed in ABAQUS to simulate the single element fracture. In large problems this would increase the computational time or may not converge, in which the A-FEM would overcome these limitations.

Chapter 3: Two- Dimensional A-FEM-Multiple Crack Formulation

3.1. Overview

The internal DoFs associated with the four internal nodes, together with the regular nodal DoFs, allow for stress evaluations in each subdomain, making it possible to further augment the element to host more than one cohesive crack. A secondary crack can be introduced to a subdomain as long as it has more than one regular (external) node. In such a case, there are three basic crack configurations if a second crack was introduced and one configuration if third crack was also introduced. The four configurations are shown in Figure 3-1 which l_{e1} is the first crack length, l_{e2} is the second crack length and l_{e3} is the third crack length.

Consider the two crack (a-c) configurations. The second crack intersects and cuts the first crack into two segments with length γl_{e1} (left) and $(1-\gamma)l_{e1}$ (right). To describe the discontinuity induced by the second crack, four more internal nodes, 7, 8, 7' and 8' are introduced and a local coordinate system is defined by the angle between its tangential direction (\mathbf{s}_2) and global x-direction, θ_2 .

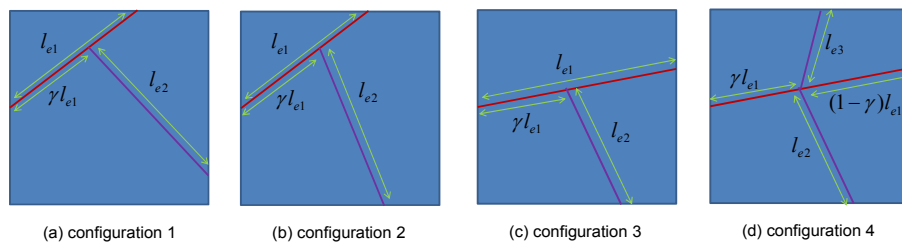


Figure 3-1 Four possible cut configurations for a secondary crack from a pentagonal subdomain

With the 8 internal nodes, it is possible to integrate the subdomain stiffness matrix for each subdomain. The procedure to condense the internal nodal DoFs for all the four configurations will be given in this chapter.

3.2 Elemental Augmentation Formulation – Configuration 1

3.2.1 General Formulation

If the pentagonal subdomain is cut by a second crack of length l_{e2} as shown in Figure 3-1 (a), the exaggerated deformed status of this element along with the regular nodes (filled dots) and internal nodes (open dots), and the active cohesive tractions are illustrated in Figure 3-2. For the second crack, four more internal nodes (7, 8, 7', and 8') can be introduced to account for the discontinuity across the crack surfaces. The three subdomains are noted with Ω^+ , Ω^{I-} and Ω^{II-} .

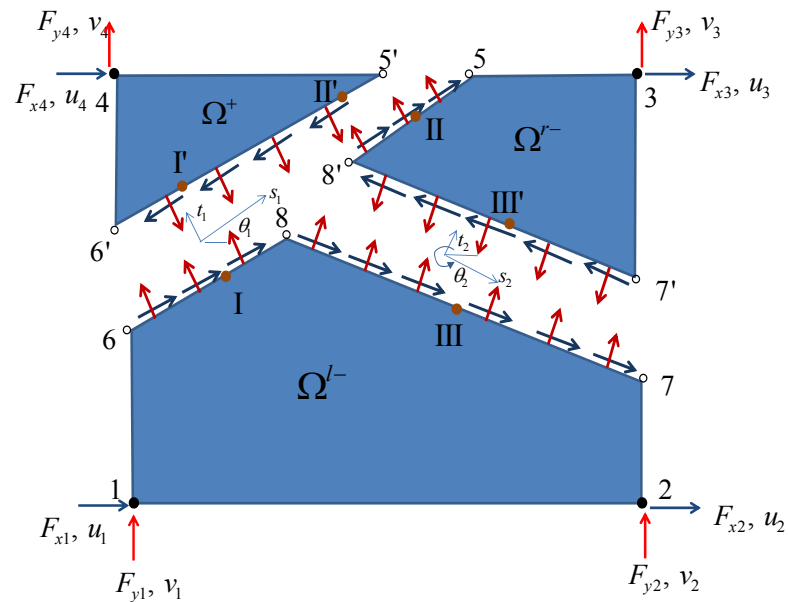


Figure 3-2 Illustration of a secondary crack in a pentagonal subdomain (3 crack segments I, II, and III)

The equilibrium equation for the three sub-domains can be expressed as:

$$\begin{bmatrix} k_{11}^+ & k_{12}^+ & k_{13}^+ & \cdots & \cdots & k_{16}^+ \\ k_{21}^+ & k_{22}^+ & k_{23}^+ & \cdots & \cdots & k_{26}^+ \\ k_{31}^+ & k_{32}^+ & k_{33}^+ & \cdots & \cdots & k_{36}^+ \\ \vdots & \vdots & \vdots & \cdots & \cdots & \vdots \\ \vdots & \vdots & \vdots & \cdots & \cdots & \vdots \\ k_{61}^+ & k_{62}^+ & k_{63}^+ & \cdots & \cdots & k_{66}^+ \end{bmatrix} \begin{Bmatrix} u_4 \\ v_4 \\ u_{6'} \\ v_{6'} \\ u_{5'} \\ v_{5'} \end{Bmatrix} = \begin{Bmatrix} F_{x4} \\ F_{y4} \\ F_{x6'} \\ F_{y6'} \\ F_{x5'} \\ F_{y5'} \end{Bmatrix} \quad (\text{for } \Omega^+) \quad (3-1)$$

$$\begin{bmatrix} k_{11}^{r-} & k_{12}^{r-} & k_{13}^{r-} & \cdots & \cdots & \cdots & \cdots & k_{18}^{r-} \\ k_{21}^{r-} & k_{22}^{r-} & k_{23}^{r-} & \cdots & \cdots & \cdots & \cdots & k_{28}^{r-} \\ k_{31}^{r-} & k_{32}^{r-} & k_{33}^{r-} & \cdots & \cdots & \cdots & \cdots & k_{38}^{r-} \\ \vdots & \vdots & \vdots & \cdots & \cdots & \cdots & \cdots & \vdots \\ \vdots & \vdots & \vdots & \cdots & \cdots & \cdots & \cdots & \vdots \\ \vdots & \vdots & \vdots & \cdots & \cdots & \cdots & \cdots & \vdots \\ \vdots & \vdots & \vdots & \cdots & \cdots & \cdots & \cdots & \vdots \\ k_{81}^{r-} & k_{82}^{r-} & k_{83}^{r-} & \cdots & \cdots & \cdots & \cdots & k_{88}^{r-} \end{bmatrix} \begin{Bmatrix} u_3 \\ v_3 \\ u_5 \\ v_5 \\ u_{8'} \\ v_{8'} \\ u_{7'} \\ v_{7'} \end{Bmatrix} = \begin{Bmatrix} F_{x3} \\ F_{y3} \\ F_{x5} \\ F_{y5} \\ F_{x8'} \\ F_{y8'} \\ F_{x7'} \\ F_{y7'} \end{Bmatrix} \quad (\text{for } \Omega^{r-}) \quad (3-2)$$

$$\begin{bmatrix} k_{11}^{l-} & \cdots & \cdots & k_{14}^{l-} & k_{15}^{l-} & \cdots & \cdots & \cdots & \cdots & k_{1A}^{l-} \\ \vdots & \cdots & \cdots & \vdots & \vdots & \cdots & \cdots & \cdots & \cdots & \vdots \\ \vdots & \cdots & \cdots & \vdots & \vdots & \cdots & \cdots & \cdots & \cdots & \vdots \\ k_{41}^{l-} & \cdots & \cdots & k_{44}^{l-} & k_{45}^{l-} & \cdots & \cdots & \cdots & \cdots & k_{4A}^{l-} \\ k_{51}^{l-} & \cdots & \cdots & k_{54}^{l-} & k_{55}^{l-} & \cdots & \cdots & \cdots & \cdots & k_{5A}^{l-} \\ \vdots & \cdots & \cdots & \vdots & \vdots & \cdots & \cdots & \cdots & \cdots & \vdots \\ \vdots & \cdots & \cdots & \vdots & \vdots & \cdots & \cdots & \cdots & \cdots & \vdots \\ \vdots & \cdots & \cdots & \vdots & \vdots & \cdots & \cdots & \cdots & \cdots & \vdots \\ \vdots & \cdots & \cdots & \vdots & \vdots & \cdots & \cdots & \cdots & \cdots & \vdots \\ k_{A1}^{l-} & \cdots & \cdots & k_{A4}^{l-} & k_{A5}^{l-} & \cdots & \cdots & \cdots & \cdots & k_{AA}^{l-} \end{bmatrix} \begin{Bmatrix} u_1 \\ v_1 \\ u_2 \\ v_2 \\ u_7 \\ v_7 \\ u_8 \\ v_8 \\ u_6 \\ v_6 \end{Bmatrix} = \begin{Bmatrix} F_{x1} \\ F_{y1} \\ F_{x2} \\ F_{y2} \\ F_{x7} \\ F_{y7} \\ F_{x8} \\ F_{y8} \\ F_{x6} \\ F_{y6} \end{Bmatrix} \quad (\text{for } \Omega^{l-}) \quad (3-3)$$

In a more concise form, the above subdomain equilibrium equations can be written as

$$\begin{bmatrix} [\mathbf{L}_{11}^+]_{2 \times 2} & [\mathbf{L}_{12}^+]_{2 \times 4} \\ [\mathbf{L}_{21}^+]_{4 \times 2} & [\mathbf{L}_{22}^+]_{4 \times 4} \end{bmatrix} \begin{Bmatrix} \mathbf{u}_4 \\ \mathbf{u}_{6'5'} \end{Bmatrix} = \begin{Bmatrix} \mathbf{F}_4 \\ \mathbf{F}_{6'5'} \end{Bmatrix} \quad (\text{for } \Omega^+) \quad (3-1)$$

$$\begin{bmatrix} [\mathbf{L}_{11}^{r-}]_{2 \times 2} & [\mathbf{L}_{12}^{r-}]_{2 \times 6} \\ [\mathbf{L}_{21}^{r-}]_{6 \times 2} & [\mathbf{L}_{22}^{r-}]_{6 \times 6} \end{bmatrix} \begin{Bmatrix} \mathbf{u}_3 \\ \mathbf{u}_{58'7'} \end{Bmatrix} = \begin{Bmatrix} \mathbf{F}_3 \\ \mathbf{F}_{58'7'} \end{Bmatrix} \quad (\text{for } \Omega^{r-}) \quad (3-2)$$

$$\begin{bmatrix} [\mathbf{L}_{11}^{l-}]_{4 \times 4} & [\mathbf{L}_{12}^{l-}]_{4 \times 6} \\ [\mathbf{L}_{21}^{l-}]_{6 \times 4} & [\mathbf{L}_{22}^{l-}]_{6 \times 6} \end{bmatrix} \begin{Bmatrix} \mathbf{u}_{12} \\ \mathbf{u}_{786} \end{Bmatrix} = \begin{Bmatrix} \mathbf{F}_{12} \\ \mathbf{F}_{786} \end{Bmatrix} \quad (\text{for } \Omega^{l-}) \quad (3-3)$$

The internal forces ($\mathbf{F}_{6'5'}$, $\mathbf{F}_{58'7'}$, \mathbf{F}_{786}) come from cohesive stress integration from the crack planes. In this case, the crack is composed of three segments, 6'-5', 7-8-6, and 7'-

8'-5. Single-point Gaussian integration within each segment (i.e., constant stress within each segment but the stress can be different at different segment) will be used. The integration points are indicated in Figure 3-2 by the solid dots labeled by I (I'), II (II'), and III (III'). Further, the cohesive stresses at the integration points are denoted as $(\sigma_1^{(m)}, \tau_1^{(n)})$, $(\sigma_{II}^{(k)}, \tau_{II}^{(l)})$, and $(\sigma_{III}^{(p)}, \tau_{III}^{(q)})$, respectively. The superscript (m, n, k, l, p, q) are all free indices that can range from 1 to the maximum cohesive segment number, indicating which segments of the traction-separation laws the current cohesive stresses are located.

The internal forces ($\mathbf{F}_{6'5'}$, $\mathbf{F}_{58'7'}$, \mathbf{F}_{786}) can be easily integrated from the cohesive stresses acting on each crack planes as follows

$$\{\mathbf{F}_{6'5'}\} = [\mathbf{T}_{\mathbf{R}^+}] \left\{ \tau_1^{(m)} \quad \sigma_1^{(n)} \quad \tau_{II}^{(k)} \quad \sigma_{II}^{(l)} \right\} \quad (3-7)$$

$$\{\mathbf{F}_{786}\} = [\mathbf{T}_{\mathbf{R}^{l-}}] \left\{ \tau_1^{(m)} \quad \sigma_1^{(n)} \quad \tau_{III}^{(p)} \quad \sigma_{III}^{(q)} \right\} \quad (3-8)$$

$$\{\mathbf{F}_{58'7'}\} = [\mathbf{T}_{\mathbf{R}^{r-}}] \left\{ \tau_{II}^{(k)} \quad \sigma_{II}^{(l)} \quad \tau_{III}^{(p)} \quad \sigma_{III}^{(q)} \right\} \quad (3-9)$$

$$\text{where } [\mathbf{T}_{\mathbf{R}^+}] = -\frac{1}{2} \begin{bmatrix} \gamma(2-\gamma)l_{e1}[\mathbf{R}_1]^T & (1-\gamma)^2 l_{e1}[\mathbf{R}_1]^T \\ \gamma^2 l_{e1}[\mathbf{R}_1]^T & (1-\gamma^2)l_{e1}[\mathbf{R}_1]^T \end{bmatrix}, [\mathbf{T}_{\mathbf{R}^{l-}}] = \frac{1}{2} \begin{bmatrix} \mathbf{0} & l_{e2}[\mathbf{R}_2]^T \\ \gamma l_{e1}[\mathbf{R}_1]^T & l_{e2}[\mathbf{R}_2]^T \\ \gamma l_{e1}[\mathbf{R}_1]^T & \mathbf{0} \end{bmatrix}$$

$$\text{and } [\mathbf{T}_{\mathbf{R}^{r-}}] = \frac{1}{2} \begin{bmatrix} (1-\gamma)l_{e1}[\mathbf{R}_1]^T & \mathbf{0} \\ (1-\gamma)l_{e1}[\mathbf{R}_1]^T & -l_{e2}[\mathbf{R}_2]^T \\ \mathbf{0} & -l_{e2}[\mathbf{R}_2]^T \end{bmatrix} \text{ are the respective integration matrices for}$$

each crack segment. $[\mathbf{R}_1] = \begin{bmatrix} \cos \theta_1 & \sin \theta_1 \\ -\sin \theta_1 & \cos \theta_1 \end{bmatrix}$ and $[\mathbf{R}_2] = \begin{bmatrix} \cos \theta_2 & \sin \theta_2 \\ -\sin \theta_2 & \cos \theta_2 \end{bmatrix}$ are the two

rotation matrices defined by the two crack directions as shown in Figure 3-2.

The relation between the cohesive stresses and the nodal displacements can be derived as

$$\begin{Bmatrix} \tau_I^{(m)} \\ \sigma_I^{(n)} \end{Bmatrix} = \{\boldsymbol{\sigma}_0\}_I + [\boldsymbol{\alpha}_0]_I [\mathbf{R}_1] \left(\frac{2-\gamma}{2} \begin{Bmatrix} u_{6'} \\ v_{6'} \end{Bmatrix} + \frac{\gamma}{2} \begin{Bmatrix} u_{5'} \\ v_{5'} \end{Bmatrix} \right) - [\boldsymbol{\alpha}_0]_I [\mathbf{R}_1] \left(\frac{1}{2} \begin{Bmatrix} u_6 \\ v_6 \end{Bmatrix} + \frac{1}{2} \begin{Bmatrix} u_8 \\ v_8 \end{Bmatrix} \right) \quad (3-10)$$

$$\begin{Bmatrix} \tau_{II}^{(k)} \\ \sigma_{II}^{(l)} \end{Bmatrix} = \{\boldsymbol{\sigma}_0\}_{II} + [\boldsymbol{\alpha}_0]_{II} [\mathbf{R}_1] \left(\frac{1-\gamma}{2} \begin{Bmatrix} u_{6'} \\ v_{6'} \end{Bmatrix} + \frac{1+\gamma}{2} \begin{Bmatrix} u_{5'} \\ v_{5'} \end{Bmatrix} \right) - [\boldsymbol{\alpha}_0]_{II} [\mathbf{R}_1] \left(\frac{1}{2} \begin{Bmatrix} u_5 \\ v_5 \end{Bmatrix} + \frac{1}{2} \begin{Bmatrix} u_{8'} \\ v_{8'} \end{Bmatrix} \right) \quad (3-11)$$

$$\begin{Bmatrix} \tau_{III}^{(p)} \\ \sigma_{III}^{(q)} \end{Bmatrix} = \{\boldsymbol{\sigma}_0\}_{III} + [\boldsymbol{\alpha}_0]_{III} [\mathbf{R}_2] \left(\frac{1}{2} \begin{Bmatrix} u_{7'} \\ v_{7'} \end{Bmatrix} + \frac{1}{2} \begin{Bmatrix} u_{8'} \\ v_{8'} \end{Bmatrix} \right) - [\boldsymbol{\alpha}_0]_{III} [\mathbf{R}_2] \left(\frac{1}{2} \begin{Bmatrix} u_7 \\ v_7 \end{Bmatrix} + \frac{1}{2} \begin{Bmatrix} u_8 \\ v_8 \end{Bmatrix} \right) \quad (3-12)$$

where

$$[\boldsymbol{\alpha}_0]_I = \text{Diag}[\alpha_s^{(m)}, \alpha_n^{(n)}], [\boldsymbol{\alpha}_0]_{II} = \text{Diag}[\alpha_s^{(k)}, \alpha_n^{(l)}], \text{ and } [\boldsymbol{\alpha}_0]_{III} = \text{Diag}[\alpha_s^{(p)}, \alpha_n^{(q)}]$$

and

$$\{\boldsymbol{\sigma}_0\}_I = \begin{Bmatrix} \hat{\tau}^{(m)} - \alpha_s^{(m)} \delta_s^{(m)} \\ \hat{\sigma}^{(n)} - \alpha_n^{(n)} \delta_n^{(n)} \end{Bmatrix}, \{\boldsymbol{\sigma}_0\}_{II} = \begin{Bmatrix} \hat{\tau}^{(k)} - \alpha_s^{(k)} \delta_s^{(k)} \\ \hat{\sigma}^{(l)} - \alpha_n^{(l)} \delta_n^{(l)} \end{Bmatrix}, \text{ and } \{\boldsymbol{\sigma}_0\}_{III} = \begin{Bmatrix} \hat{\tau}^{(p)} - \alpha_s^{(p)} \delta_s^{(p)} \\ \hat{\sigma}^{(q)} - \alpha_n^{(q)} \delta_n^{(q)} \end{Bmatrix}.$$

Substituting Eqns (3-10)-(3-12) into Eqns (3-7)-(3-9), one can obtain the following

$$\{\mathbf{F}_{6'5'}\} = \{\mathbf{S}_1\} + [\boldsymbol{\alpha}_{11}]\{\mathbf{u}_{6'5'}\} + [\boldsymbol{\alpha}_{12}]\{\mathbf{u}_{786}\} + [\boldsymbol{\alpha}_{13}]\{\mathbf{u}_{58'7'}\} \quad (3-13)$$

$$\{\mathbf{F}_{786}\} = \{\mathbf{S}_2\} + [\boldsymbol{\alpha}_{21}]\{\mathbf{u}_{6'5'}\} + [\boldsymbol{\alpha}_{22}]\{\mathbf{u}_{786}\} + [\boldsymbol{\alpha}_{23}]\{\mathbf{u}_{58'7'}\} \quad (3-14)$$

$$\{\mathbf{F}_{58'7'}\} = \{\mathbf{S}_3\} + [\boldsymbol{\alpha}_{31}]\{\mathbf{u}_{6'5'}\} + [\boldsymbol{\alpha}_{32}]\{\mathbf{u}_{786}\} + [\boldsymbol{\alpha}_{33}]\{\mathbf{u}_{58'7'}\} \quad (3-15)$$

where

$$\{\mathbf{S}_1\} = [\mathbf{T}_R^+] \begin{Bmatrix} \{\boldsymbol{\sigma}_0\}_I \\ \{\boldsymbol{\sigma}_0\}_{II} \end{Bmatrix}, \{\mathbf{S}_2\} = [\mathbf{T}_R^{l-}] \begin{Bmatrix} \{\boldsymbol{\sigma}_0\}_I \\ \{\boldsymbol{\sigma}_0\}_{III} \end{Bmatrix}, \{\mathbf{S}_3\} = [\mathbf{T}_R^{r-}] \begin{Bmatrix} \{\boldsymbol{\sigma}_0\}_{II} \\ \{\boldsymbol{\sigma}_0\}_{III} \end{Bmatrix} \text{ and}$$

$$\begin{aligned}
[\mathbf{a}_{11}] &= \frac{1}{2}[\mathbf{T}_R^+] \begin{bmatrix} (2-\gamma)[\mathbf{a}_0]_{\text{I}}[\mathbf{R}_1] & \gamma[\mathbf{a}_0]_{\text{I}}[\mathbf{R}_1] \\ (1-\gamma)[\mathbf{a}_0]_{\text{II}}[\mathbf{R}_1] & (1+\gamma)[\mathbf{a}_0]_{\text{II}}[\mathbf{R}_1] \end{bmatrix}; & [\mathbf{a}_{12}] &= \frac{1}{2}[\mathbf{T}_R^+] \begin{bmatrix} \mathbf{0} & -[\mathbf{a}_0]_{\text{I}}[\mathbf{R}_1] & -[\mathbf{a}_0]_{\text{I}}[\mathbf{R}_1] \\ \mathbf{0} & \mathbf{0} & \mathbf{0} \end{bmatrix}; \\
[\mathbf{a}_{13}] &= \frac{1}{2}[\mathbf{T}_R^+] \begin{bmatrix} \mathbf{0} & \mathbf{0} & \mathbf{0} \\ -[\mathbf{a}_0]_{\text{II}}[\mathbf{R}_1] & -[\mathbf{a}_0]_{\text{II}}[\mathbf{R}_1] & \mathbf{0} \end{bmatrix}; & [\mathbf{a}_{21}] &= \frac{1}{2}[\mathbf{T}_R^{l-}] \begin{bmatrix} (2-\gamma)[\mathbf{a}_0]_{\text{I}}[\mathbf{R}_1] & \gamma[\mathbf{a}_0]_{\text{I}}[\mathbf{R}_1] \\ \mathbf{0} & \mathbf{0} \end{bmatrix}; \\
[\mathbf{a}_{22}] &= \frac{1}{2}[\mathbf{T}_R^{l-}] \begin{bmatrix} \mathbf{0} & -[\mathbf{a}_0]_{\text{I}}[\mathbf{R}_1] & -[\mathbf{a}_0]_{\text{I}}[\mathbf{R}_1] \\ -[\mathbf{a}_0]_{\text{III}}[\mathbf{R}_2] & -[\mathbf{a}_0]_{\text{III}}[\mathbf{R}_2] & \mathbf{0} \end{bmatrix}; & [\mathbf{a}_{23}] &= \frac{1}{2}[\mathbf{T}_R^{l-}] \begin{bmatrix} \mathbf{0} & \mathbf{0} & \mathbf{0} \\ \mathbf{0} & [\mathbf{a}_0]_{\text{III}}[\mathbf{R}_2] & [\mathbf{a}_0]_{\text{III}}[\mathbf{R}_2] \end{bmatrix}; \\
[\mathbf{a}_{31}] &= \frac{1}{2}[\mathbf{T}_R^{r-}] \begin{bmatrix} (1-\gamma)[\mathbf{a}_0]_{\text{II}}[\mathbf{R}_1] & (1+\gamma)[\mathbf{a}_0]_{\text{II}}[\mathbf{R}_1] \\ \mathbf{0} & \mathbf{0} \end{bmatrix}; & [\mathbf{a}_{32}] &= \frac{1}{2}[\mathbf{T}_R^{r-}] \begin{bmatrix} \mathbf{0} & \mathbf{0} & \mathbf{0} \\ -[\mathbf{a}_0]_{\text{III}}[\mathbf{R}_2] & -[\mathbf{a}_0]_{\text{III}}[\mathbf{R}_2] & \mathbf{0} \end{bmatrix}; \\
[\mathbf{a}_{33}] &= \frac{1}{2}[\mathbf{T}_R^{r-}] \begin{bmatrix} -[\mathbf{a}_0]_{\text{II}}[\mathbf{R}_1] & -[\mathbf{a}_0]_{\text{II}}[\mathbf{R}_1] & \mathbf{0} \\ \mathbf{0} & [\mathbf{a}_0]_{\text{III}}[\mathbf{R}_2] & [\mathbf{a}_0]_{\text{III}}[\mathbf{R}_2] \end{bmatrix}
\end{aligned}$$

Substituting Eqns (3-13)-(3-15) into Eqns (3-2), (3-4) & (3-6), and solving for internal nodal displacements ($\mathbf{u}_{6'5'}$, $\mathbf{u}_{58'7'}$, \mathbf{u}_{786}) as functions of regular nodal displacements (\mathbf{u}_{12} , \mathbf{u}_3 , \mathbf{u}_4), one obtains:

$$\begin{Bmatrix} \mathbf{u}_{6'5'} \\ \mathbf{u}_{786} \\ \mathbf{u}_{58'7'} \end{Bmatrix} = \begin{bmatrix} [\mathbf{Y}_7] & [\mathbf{Y}_8] & [\mathbf{Y}_9] \\ [\mathbf{Y}_4] & [\mathbf{Y}_5] & [\mathbf{Y}_6] \\ [\mathbf{Y}_1] & [\mathbf{Y}_2] & [\mathbf{Y}_3] \end{bmatrix} \begin{Bmatrix} \mathbf{S}_1 \\ \mathbf{S}_2 \\ \mathbf{S}_3 \end{Bmatrix} + \begin{bmatrix} [\mathbf{X}_{13}] & [\mathbf{X}_{14}] & [\mathbf{X}_{15}] \\ [\mathbf{X}_{10}] & [\mathbf{X}_{11}] & [\mathbf{X}_{12}] \\ [\mathbf{X}_7] & [\mathbf{X}_8] & [\mathbf{X}_9] \end{bmatrix} \begin{Bmatrix} \mathbf{u}_{12} \\ \mathbf{u}_3 \\ \mathbf{u}_4 \end{Bmatrix} \quad (3-16)$$

Substituting Eqn (3-16) back into Eqns (3-1), (3-3) & (3-5), the fully condensed elemental equilibrium equation can be obtained as follows

$$\begin{Bmatrix} \mathbf{F}_{12} \\ \mathbf{F}_3 \\ \mathbf{F}_4 \end{Bmatrix} = \begin{bmatrix} [\mathbf{L}'_{12}][\mathbf{Y}_4] & [\mathbf{L}'_{12}][\mathbf{Y}_5] & [\mathbf{L}'_{12}][\mathbf{Y}_6] \\ [\mathbf{L}'_{12}][\mathbf{Y}_1] & [\mathbf{L}'_{12}][\mathbf{Y}_2] & [\mathbf{L}'_{12}][\mathbf{Y}_3] \\ [\mathbf{L}'_{12}][\mathbf{Y}_7] & [\mathbf{L}'_{12}][\mathbf{Y}_8] & [\mathbf{L}'_{12}][\mathbf{Y}_9] \end{bmatrix} \begin{Bmatrix} \mathbf{S}_1 \\ \mathbf{S}_2 \\ \mathbf{S}_3 \end{Bmatrix} + \begin{bmatrix} [\mathbf{L}'_{11}] + [\mathbf{L}'_{12}][\mathbf{X}_{10}] & [\mathbf{L}'_{12}][\mathbf{X}_{11}] & [\mathbf{L}'_{12}][\mathbf{X}_{12}] \\ [\mathbf{L}'_{12}][\mathbf{X}_7] & [\mathbf{L}'_{11}] + [\mathbf{L}'_{12}][\mathbf{X}_8] & [\mathbf{L}'_{12}][\mathbf{X}_9] \\ [\mathbf{L}'_{12}][\mathbf{X}_{13}] & [\mathbf{L}'_{12}][\mathbf{X}_{14}] & [\mathbf{L}'_{11}] + [\mathbf{L}'_{12}][\mathbf{X}_{15}] \end{bmatrix} \begin{Bmatrix} \mathbf{u}_{12} \\ \mathbf{u}_3 \\ \mathbf{u}_4 \end{Bmatrix} \quad (3-17)$$

The matrices in Eqns (3-16) and (3-17) can all be explicitly derived and they are given in the following:

$$\begin{aligned}
[\mathbf{X}_1] &= ([\mathbf{L}_{22}^+] - [\mathbf{a}_{11}]); & [\mathbf{X}_2] &= ([\mathbf{L}_{22}^{\prime-}] - [\mathbf{a}_{22}] - [\mathbf{a}_{21}][\mathbf{X}_1]^{-1}[\mathbf{a}_{12}]); \\
[\mathbf{X}_3] &= (-[\mathbf{a}_{21}][\mathbf{X}_1]^{-1}[\mathbf{a}_{13}] - [\mathbf{a}_{23}]); & [\mathbf{X}_4] &= (-[\mathbf{a}_{31}][\mathbf{X}_1]^{-1}[\mathbf{a}_{12}] - [\mathbf{a}_{32}]); \\
[\mathbf{X}_5] &= ([\mathbf{L}_{22}^{\prime-}] - [\mathbf{a}_{33}] - [\mathbf{a}_{31}][\mathbf{X}_1]^{-1}[\mathbf{a}_{13}]); & [\mathbf{X}_6] &= ([\mathbf{X}_5] - [\mathbf{X}_4][\mathbf{X}_2]^{-1}[\mathbf{X}_3]) \\
[\mathbf{X}_7] &= [\mathbf{X}_6]^{-1}[\mathbf{X}_4][\mathbf{X}_2]^{-1}[\mathbf{L}_{21}^{\prime-}]; & [\mathbf{X}_8] &= -[\mathbf{X}_6]^{-1}[\mathbf{L}_{21}^{\prime-}]; \\
[\mathbf{X}_9] &= [\mathbf{X}_6]^{-1}([\mathbf{X}_4][\mathbf{X}_2]^{-1}[\mathbf{a}_{21}][\mathbf{X}_1]^{-1}[\mathbf{L}_{21}^+] - [\mathbf{a}_{31}][\mathbf{X}_1]^{-1}[\mathbf{L}_{21}^+]) \\
[\mathbf{X}_{10}] &= -[\mathbf{X}_2]^{-1}([\mathbf{X}_3][\mathbf{X}_7] + [\mathbf{L}_{21}^{\prime-}]); & [\mathbf{X}_{11}] &= -[\mathbf{X}_2]^{-1}[\mathbf{X}_3][\mathbf{X}_8]; \\
[\mathbf{X}_{12}] &= -[\mathbf{X}_2]^{-1}([\mathbf{X}_3][\mathbf{X}_9] + [\mathbf{a}_{21}][\mathbf{X}_1]^{-1}[\mathbf{L}_{21}^+]); & [\mathbf{X}_{13}] &= [\mathbf{X}_1]^{-1}([\mathbf{a}_{13}][\mathbf{X}_7] + [\mathbf{a}_{12}][\mathbf{X}_{10}]); \\
[\mathbf{X}_{14}] &= [\mathbf{X}_1]^{-1}([\mathbf{a}_{13}][\mathbf{X}_8] + [\mathbf{a}_{12}][\mathbf{X}_{11}]); & [\mathbf{X}_{15}] &= [\mathbf{X}_1]^{-1}(-[\mathbf{L}_{21}^+] + [\mathbf{a}_{13}][\mathbf{X}_9] + [\mathbf{a}_{12}][\mathbf{X}_{12}])
\end{aligned} \tag{3-18}$$

and

$$\begin{aligned}
[\mathbf{Y}_1] &= [\mathbf{X}_6]^{-1}([\mathbf{a}_{31}][\mathbf{X}_1]^{-1} - [\mathbf{X}_4][\mathbf{X}_2]^{-1}[\mathbf{a}_{21}][\mathbf{X}_1]^{-1}); \\
[\mathbf{Y}_2] &= -[\mathbf{X}_6]^{-1}[\mathbf{X}_4][\mathbf{X}_2]^{-1}; & [\mathbf{Y}_3] &= [\mathbf{X}_6]^{-1} \\
[\mathbf{Y}_4] &= [\mathbf{X}_2]^{-1}([\mathbf{a}_{21}][\mathbf{X}_1]^{-1} - [\mathbf{X}_3][\mathbf{Y}_1]); & [\mathbf{Y}_5] &= [\mathbf{X}_2]^{-1}([\mathbf{I}] - [\mathbf{X}_3][\mathbf{Y}_2]); \\
[\mathbf{Y}_6] &= -[\mathbf{X}_2]^{-1}[\mathbf{X}_3][\mathbf{Y}_3] & [\mathbf{Y}_7] &= [\mathbf{X}_1]^{-1}([\mathbf{I}] + [\mathbf{a}_{13}][\mathbf{Y}_1] + [\mathbf{a}_{12}][\mathbf{Y}_4]); \\
[\mathbf{Y}_8] &= [\mathbf{X}_1]^{-1}([\mathbf{a}_{13}][\mathbf{Y}_2] + [\mathbf{a}_{12}][\mathbf{Y}_5]); & [\mathbf{Y}_9] &= [\mathbf{X}_1]^{-1}([\mathbf{a}_{13}][\mathbf{Y}_3] + [\mathbf{a}_{12}][\mathbf{Y}_6])
\end{aligned} \tag{3-19}$$

The above derivations are based on the assumption that the entire cohesive crack segments are active, i.e., $\{\mathbf{S}_i\}$ and $[\mathbf{a}_{ij}]$ are nonzero so that $[\mathbf{X}_1]$, $[\mathbf{X}_2]$, and $[\mathbf{X}_6]$ are all invertible. However, if one or more segments are completely failed, these matrices may become singular, because, in such conditions the internal nodal displacements become indeterminate. In the following the numerical remedies for such conditions are discussed.

3.2.2 Numerical Treatments for Stress-Free Subdomains

(a) Integration points I and II completely failed:

In this case,

$$\{\mathbf{S}_1\} = \mathbf{0}; [\boldsymbol{\alpha}_{11}] = \mathbf{0}; [\boldsymbol{\alpha}_{12}] = \mathbf{0}; [\boldsymbol{\alpha}_{13}] = \mathbf{0}; [\boldsymbol{\alpha}_{21}] = \mathbf{0}; [\boldsymbol{\alpha}_{31}] = \mathbf{0}.$$

Therefore $[\mathbf{X}_9] = \mathbf{0}$; $[\mathbf{X}_{12}] \sim [\mathbf{X}_{14}] = \mathbf{0}$ and $[\mathbf{Y}_1] = \mathbf{0}$; $[\mathbf{Y}_4] = \mathbf{0}$; $[\mathbf{Y}_8] = \mathbf{0}$; $[\mathbf{Y}_9] = \mathbf{0}$.

The simplified expressions for the displacement and the equilibrium equations are

$$\begin{Bmatrix} \mathbf{u}_{6'5'} \\ \mathbf{u}_{786} \\ \mathbf{u}_{58'7'} \end{Bmatrix} = \begin{bmatrix} [\mathbf{Y}_7] & 0 & 0 \\ 0 & [\mathbf{Y}_5] & [\mathbf{Y}_6] \\ 0 & [\mathbf{Y}_2] & [\mathbf{Y}_3] \end{bmatrix} \begin{Bmatrix} \mathbf{S}_1 \\ \mathbf{S}_2 \\ \mathbf{S}_3 \end{Bmatrix} + \begin{bmatrix} 0 & 0 & [\mathbf{X}_{15}] \\ [\mathbf{X}_{10}] & [\mathbf{X}_{11}] & 0 \\ [\mathbf{X}_7] & [\mathbf{X}_8] & 0 \end{bmatrix} \begin{Bmatrix} \mathbf{u}_{12} \\ \mathbf{u}_3 \\ \mathbf{u}_4 \end{Bmatrix} \quad (3-20)$$

$$\begin{Bmatrix} \mathbf{F}_{12} \\ \mathbf{F}_3 \\ \mathbf{F}_4 \end{Bmatrix} = \begin{bmatrix} 0 & [\mathbf{L}'_{12}][\mathbf{Y}_5] & [\mathbf{L}'_{12}][\mathbf{Y}_6] \\ 0 & [\mathbf{L}'_{12}][\mathbf{Y}_2] & [\mathbf{L}'_{12}][\mathbf{Y}_3] \\ [\mathbf{L}'_{12}][\mathbf{Y}_7] & 0 & 0 \end{bmatrix} \begin{Bmatrix} \mathbf{S}_1 \\ \mathbf{S}_2 \\ \mathbf{S}_3 \end{Bmatrix} + \begin{bmatrix} [\mathbf{L}'_{11}] + [\mathbf{L}'_{12}][\mathbf{X}_{10}] & [\mathbf{L}'_{12}][\mathbf{X}_{11}] & 0 \\ [\mathbf{L}'_{12}][\mathbf{X}_7] & [\mathbf{L}'_{11}] + [\mathbf{L}'_{12}][\mathbf{X}_8] & 0 \\ 0 & 0 & [\mathbf{L}'_{11}] + [\mathbf{L}'_{12}][\mathbf{X}_{15}] \end{bmatrix} \begin{Bmatrix} \mathbf{u}_{12} \\ \mathbf{u}_3 \\ \mathbf{u}_4 \end{Bmatrix} \quad (3-21)$$

In this case, since $[\mathbf{X}_1]^{-1}$ does not exist, $[\mathbf{Y}_7]$ and $[\mathbf{X}_{15}]$ are not defined. However, it is noted that $\{\mathbf{S}_1\} = \mathbf{0}$, thus one can simply set $[\mathbf{Y}_7] = \mathbf{0}$, $[\mathbf{X}_{15}] = \mathbf{0}$, $[\mathbf{L}'_{12}][\mathbf{Y}_7] = \mathbf{0}$, and $[\mathbf{L}'_{11}] + [\mathbf{L}'_{12}][\mathbf{X}_{15}] = \mathbf{0}$. With this numerical treatment, $\{\mathbf{F}_4\} = \mathbf{0}$ is guaranteed. $\{\mathbf{u}_4\}$ is undetermined within this element but will be determined by neighboring elements that share this node.

(b) Integration points II and III completely failed:

In this case, $\{\mathbf{S}\}_3 = \mathbf{0}$; $[\boldsymbol{\alpha}_{13}] = \mathbf{0}$; $[\boldsymbol{\alpha}_{23}] = \mathbf{0}$; $[\boldsymbol{\alpha}_{31}] = \mathbf{0}$; $[\boldsymbol{\alpha}]_{32} = \mathbf{0}$; $[\boldsymbol{\alpha}_{33}] = \mathbf{0}$, which leads to

$$[\mathbf{X}_3] \sim [\mathbf{X}_4] = \mathbf{0}; [\mathbf{X}_7] = \mathbf{0}; [\mathbf{X}_9] = \mathbf{0}; [\mathbf{X}_{11}] = \mathbf{0}; [\mathbf{X}_{14}] = \mathbf{0}, \text{ and}$$

$$[\mathbf{Y}_1] \sim [\mathbf{Y}_2] = \mathbf{0}; [\mathbf{Y}_6] = \mathbf{0}; [\mathbf{Y}_9] = \mathbf{0}.$$

The simplified expressions for the displacement and the equilibrium equations are:

$$\begin{Bmatrix} \mathbf{u}_{6'5'} \\ \mathbf{u}_{786} \\ \mathbf{u}_{58'7'} \end{Bmatrix} = \begin{bmatrix} [\mathbf{Y}_7] & [\mathbf{Y}_8] & 0 \\ [\mathbf{Y}_4] & [\mathbf{Y}_5] & 0 \\ 0 & 0 & \underline{[\mathbf{Y}_3]} \end{bmatrix} \begin{Bmatrix} \mathbf{S}_1 \\ \mathbf{S}_2 \\ \mathbf{S}_3 \end{Bmatrix} + \begin{bmatrix} [\mathbf{X}_{13}] & 0 & [\mathbf{X}_{15}] \\ [\mathbf{X}_{10}] & 0 & [\mathbf{X}_{12}] \\ 0 & \underline{[\mathbf{X}_8]} & 0 \end{bmatrix} \begin{Bmatrix} \mathbf{u}_{12} \\ \mathbf{u}_3 \\ \mathbf{u}_4 \end{Bmatrix} \quad (3-22)$$

$$\begin{Bmatrix} \mathbf{F}_{12} \\ \mathbf{F}_3 \\ \mathbf{F}_4 \end{Bmatrix} = \begin{bmatrix} [\mathbf{L}'_{12}] [\mathbf{Y}_4] & [\mathbf{L}'_{12}] [\mathbf{Y}_5] & 0 \\ 0 & 0 & \underline{[\mathbf{L}'_{12}] [\mathbf{Y}_3]} \\ [\mathbf{L}'_{12}] [\mathbf{Y}_7] & [\mathbf{L}'_{12}] [\mathbf{Y}_8] & 0 \end{bmatrix} \begin{Bmatrix} \mathbf{S}_1 \\ \mathbf{S}_2 \\ \mathbf{S}_3 \end{Bmatrix} + \begin{bmatrix} [\mathbf{L}'_{11}] + [\mathbf{L}'_{12}] [\mathbf{X}_{10}] & 0 & [\mathbf{L}'_{12}] [\mathbf{X}_{12}] \\ 0 & \underline{[\mathbf{L}'_{11}] + [\mathbf{L}'_{12}] [\mathbf{X}_8]} & 0 \\ [\mathbf{L}'_{12}] [\mathbf{X}_{13}] & 0 & [\mathbf{L}'_{11}] + [\mathbf{L}'_{12}] [\mathbf{X}_{15}] \end{bmatrix} \begin{Bmatrix} \mathbf{u}_{12} \\ \mathbf{u}_3 \\ \mathbf{u}_4 \end{Bmatrix} \quad (3-23)$$

In this case, since $[\mathbf{X}_6]^{-1} = [\mathbf{L}'_{22}]^{-1}$ does not exist, $\underline{[\mathbf{Y}_3]}$ and $\underline{[\mathbf{X}_8]}$ are not defined.

However, since $\{\mathbf{S}_3\} = \mathbf{0}$, one can simply set the underlined terms, $\underline{[\mathbf{Y}_3]} = \mathbf{0}$, $\underline{[\mathbf{X}_8]} = \mathbf{0}$,

$\underline{[\mathbf{L}'_{12}] [\mathbf{Y}_3]} = \mathbf{0}$, and $\underline{[\mathbf{L}'_{11}] + [\mathbf{L}'_{12}] [\mathbf{X}_8]} = \mathbf{0}$. In this way, it is guaranteed that

$\{\mathbf{F}_3\} = \mathbf{0}$ but $\{\mathbf{u}_3\}$ cannot be determined by the element. It has to be determined by

neighboring elements that share node 3.

(c) Integration points I and III completely failed:

In this case, $\{\mathbf{S}_2\} = \mathbf{0}$; $[\boldsymbol{\alpha}_{12}] = \mathbf{0}$; $[\boldsymbol{\alpha}_{21}] = \mathbf{0}$; $[\boldsymbol{\alpha}_{22}] = \mathbf{0}$; $[\boldsymbol{\alpha}_{23}] = \mathbf{0}$; $[\boldsymbol{\alpha}_{32}] = \mathbf{0}$, which leads to

$$[\mathbf{X}_3] \sim [\mathbf{X}_4] = \mathbf{0}; [\mathbf{X}_7] = \mathbf{0}; [\mathbf{X}_{11}] \sim [\mathbf{X}_{13}] = \mathbf{0}, \text{ and } [\mathbf{Y}_2] = \mathbf{0}; [\mathbf{Y}_4] = \mathbf{0}; [\mathbf{Y}_6] = \mathbf{0}; [\mathbf{Y}_8] = \mathbf{0}.$$

The simplified expressions for the displacement and the equilibrium equations are:

$$\begin{Bmatrix} \mathbf{u}_{6'5'} \\ \mathbf{u}_{786} \\ \mathbf{u}_{58'7'} \end{Bmatrix} = \begin{bmatrix} [\mathbf{Y}_7] & 0 & [\mathbf{Y}_9] \\ 0 & [\mathbf{Y}_5] & 0 \\ [\mathbf{Y}_1] & 0 & [\mathbf{Y}_3] \end{bmatrix} \begin{Bmatrix} \mathbf{S}_1 \\ \mathbf{S}_2 \\ \mathbf{S}_3 \end{Bmatrix} + \begin{bmatrix} 0 & [\mathbf{X}_{14}] & [\mathbf{X}_{15}] \\ [\mathbf{X}_{10}] & 0 & 0 \\ 0 & [\mathbf{X}_8] & [\mathbf{X}_9] \end{bmatrix} \begin{Bmatrix} \mathbf{u}_{12} \\ \mathbf{u}_3 \\ \mathbf{u}_4 \end{Bmatrix} \quad (3-24)$$

$$\begin{Bmatrix} \mathbf{F}_{12} \\ \mathbf{F}_3 \\ \mathbf{F}_4 \end{Bmatrix} = \begin{bmatrix} 0 & [\mathbf{L}'_{12}][\mathbf{Y}_5] & 0 \\ [\mathbf{L}'_{12}][\mathbf{Y}_1] & 0 & [\mathbf{L}'_{12}][\mathbf{Y}_3] \\ [[\mathbf{L}'_{12}][\mathbf{Y}_7] & 0 & [[\mathbf{L}'_{12}][\mathbf{Y}_9] \end{bmatrix} \begin{Bmatrix} \mathbf{S}_1 \\ \mathbf{S}_2 \\ \mathbf{S}_3 \end{Bmatrix} + \begin{bmatrix} [[\mathbf{L}'_{11}] + [[\mathbf{L}'_{12}][\mathbf{X}_{10}] & 0 & 0 \\ 0 & [[\mathbf{L}'_{11}] + [[\mathbf{L}'_{12}][\mathbf{X}_8] & [[\mathbf{L}'_{12}][\mathbf{X}_9] \\ 0 & [[\mathbf{L}'_{12}][\mathbf{X}_{14}] & [[\mathbf{L}'_{11}] + [[\mathbf{L}'_{12}][\mathbf{X}_{15}] \end{bmatrix} \begin{Bmatrix} \mathbf{u}_{12} \\ \mathbf{u}_3 \\ \mathbf{u}_4 \end{Bmatrix} \quad (3-25)$$

No special treatment is necessary although one can set $[\mathbf{Y}_5] = \mathbf{0}$ without affecting the final solution because $\{\mathbf{S}_2\} = \mathbf{0}$.

(d) All Integration points I, II, and III failed:

In this case, $\{\mathbf{S}_1\} = \{\mathbf{S}_2\} = \{\mathbf{S}_3\} = \mathbf{0}$; and $[\alpha_{ij}] = 0$ ($i, j = 1, 2, 3$), which leads to

$[\mathbf{X}_3] \sim [\mathbf{X}_4] = \mathbf{0}$; $[\mathbf{X}_7] = \mathbf{0}$; $[\mathbf{X}_9] = \mathbf{0}$; $[\mathbf{X}_{11}] \sim [\mathbf{X}_{14}] = \mathbf{0}$, and the simplified expressions for the displacement and the equilibrium equations are:

In this case, $\{\mathbf{F}_3\} = \mathbf{0}$ and $\{\mathbf{F}_4\} = \mathbf{0}$ but $\{\mathbf{u}_3\}$ and $\{\mathbf{u}_4\}$ have to be determined by neighboring elements.

$$\begin{Bmatrix} \mathbf{u}_{6'5'} \\ \mathbf{u}_{786} \\ \mathbf{u}_{58'7'} \end{Bmatrix} = \begin{bmatrix} 0 & 0 & [\mathbf{X}_{15}] \\ [\mathbf{X}_{10}] & 0 & 0 \\ 0 & [\mathbf{X}_8] & 0 \end{bmatrix} \begin{Bmatrix} \mathbf{u}_{12} \\ \mathbf{u}_3 \\ \mathbf{u}_4 \end{Bmatrix} \quad (3-26)$$

$$\begin{Bmatrix} \mathbf{F}_{12} \\ \mathbf{F}_3 \\ \mathbf{F}_4 \end{Bmatrix} = \begin{bmatrix} [L_{11}^-] + [L_{12}^-][\mathbf{X}_{10}] & 0 & 0 \\ 0 & [L_{11}^-] + [L_{12}^-][\mathbf{X}_8] & 0 \\ 0 & 0 & [L_{11}^+] + [L_{12}^+][\mathbf{X}_{15}] \end{bmatrix} \begin{Bmatrix} \mathbf{u}_{12} \\ \mathbf{u}_3 \\ \mathbf{u}_4 \end{Bmatrix} \quad (3-27)$$

In this case, both $[\mathbf{X}_1]^{-1}$ and $[\mathbf{X}_6]^{-1}$ are not defined because $\{\mathbf{u}_3\}$ and $\{\mathbf{u}_4\}$ are indeterminate from this element. Therefore, we can set $[\mathbf{X}_8] = \mathbf{0}$, $[\mathbf{X}_{15}] = \mathbf{0}$, $[L_{11}^-] + [L_{12}^-][\mathbf{X}_8] = \mathbf{0}$ and $[L_{11}^+] + [L_{12}^+][\mathbf{X}_{15}] = \mathbf{0}$.

3.3 Elemental Augmentation Formulation – Configuration 2

3.3.1 General Formulation

If the secondary crack cuts the pentagonal subdomain but against the previous case, the quadrilateral domain is at left and the pentagonal domain is at right.

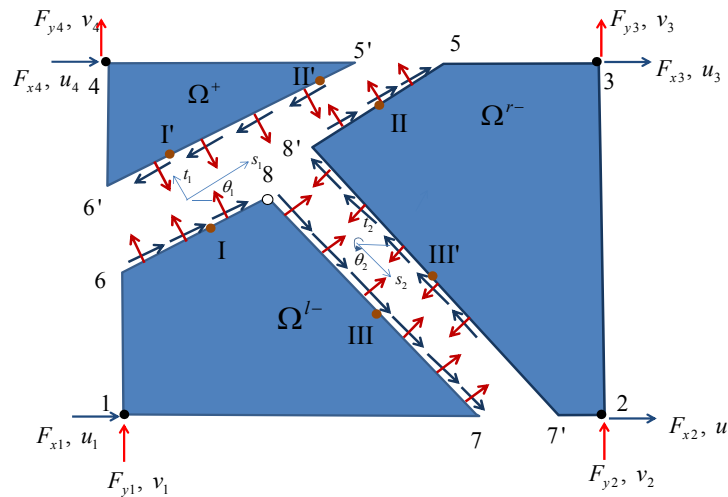


Figure 3-3 Illustration of a secondary crack in a pentagonal subdomain, second configuration (3 crack segments I, II, and III)

The equilibrium equation for the three sub-domains can be expressed as

$$\begin{bmatrix} k_{11}^+ & k_{12}^+ & k_{13}^+ & \cdots & \cdots & k_{16}^+ \\ k_{21}^+ & k_{22}^+ & k_{23}^+ & \cdots & \cdots & k_{26}^+ \\ \hline k_{31}^+ & k_{32}^+ & k_{33}^+ & \cdots & \cdots & k_{36}^+ \\ \vdots & \vdots & \vdots & \cdots & \cdots & \vdots \\ \vdots & \vdots & \vdots & \cdots & \cdots & \vdots \\ k_{61}^+ & k_{62}^+ & k_{63}^+ & \cdots & \cdots & k_{66}^+ \end{bmatrix} \begin{Bmatrix} \mathbf{u}_4 \\ v_4 \\ \mathbf{u}_{6'} \\ v_{6'} \\ \mathbf{u}_{5'} \\ v_{5'} \end{Bmatrix} = \begin{Bmatrix} F_{x4} \\ F_{y4} \\ F_{x6'} \\ F_{y6'} \\ F_{x5'} \\ F_{y5'} \end{Bmatrix} \quad (\text{for } \Omega^+)$$

$$\begin{bmatrix} k_{11}^{r-} & \cdots & \cdots & k_{14}^{r-} & k_{15}^{r-} & \cdots & \cdots & \cdots & \cdots & k_{1A}^{r-} \\ \vdots & \cdots & \cdots & \vdots & \vdots & \cdots & \cdots & \cdots & \cdots & \vdots \\ \vdots & \cdots & \cdots & \vdots & \vdots & \cdots & \cdots & \cdots & \cdots & \vdots \\ \hline k_{41}^{r-} & \cdots & \cdots & k_{44}^{r-} & k_{45}^{r-} & \cdots & \cdots & \cdots & \cdots & k_{4A}^{r-} \\ k_{51}^{r-} & \cdots & \cdots & k_{54}^{r-} & k_{55}^{r-} & \cdots & \cdots & \cdots & \cdots & k_{5A}^{r-} \\ \vdots & \cdots & \cdots & \vdots & \vdots & \cdots & \cdots & \cdots & \cdots & \vdots \\ \vdots & \cdots & \cdots & \vdots & \vdots & \cdots & \cdots & \cdots & \cdots & \vdots \\ \vdots & \cdots & \cdots & \vdots & \vdots & \cdots & \cdots & \cdots & \cdots & \vdots \\ \vdots & \cdots & \cdots & \vdots & \vdots & \cdots & \cdots & \cdots & \cdots & \vdots \\ k_{A1}^{r-} & \cdots & \cdots & k_{A4}^{r-} & k_{A5}^{r-} & \cdots & \cdots & \cdots & \cdots & k_{AA}^{r-} \end{bmatrix} \begin{Bmatrix} \mathbf{u}_2 \\ v_2 \\ \mathbf{u}_3 \\ v_3 \\ \mathbf{u}_5 \\ v_5 \\ \mathbf{u}_{8'} \\ v_{8'} \\ \mathbf{u}_{7'} \\ v_{7'} \end{Bmatrix} = \begin{Bmatrix} F_{x2} \\ F_{y2} \\ F_{x3} \\ F_{y3} \\ F_{x5} \\ F_{y5} \\ F_{x8'} \\ F_{y8'} \\ F_{x7'} \\ F_{y7'} \end{Bmatrix} \quad (\text{for } \Omega^{r-})$$

$$\begin{bmatrix} k_{11}^{l-} & k_{12}^{l-} & k_{13}^{l-} & \cdots & \cdots & \cdots & \cdots & k_{18}^{l-} \\ k_{21}^{l-} & k_{22}^{l-} & k_{23}^{l-} & \cdots & \cdots & \cdots & \cdots & k_{28}^{l-} \\ \hline k_{31}^{l-} & k_{32}^{l-} & k_{33}^{l-} & \cdots & \cdots & \cdots & \cdots & k_{38}^{l-} \\ \vdots & \vdots & \vdots & \cdots & \cdots & \cdots & \cdots & \vdots \\ \vdots & \vdots & \vdots & \cdots & \cdots & \cdots & \cdots & \vdots \\ \vdots & \vdots & \vdots & \cdots & \cdots & \cdots & \cdots & \vdots \\ \vdots & \vdots & \vdots & \cdots & \cdots & \cdots & \cdots & \vdots \\ k_{81}^{l-} & k_{82}^{l-} & k_{83}^{l-} & \cdots & \cdots & \cdots & \cdots & k_{88}^{l-} \end{bmatrix} \begin{Bmatrix} \mathbf{u}_1 \\ v_1 \\ \mathbf{u}_7 \\ v_7 \\ \mathbf{u}_8 \\ v_8 \\ \mathbf{u}_6 \\ v_6 \end{Bmatrix} = \begin{Bmatrix} F_{x1} \\ F_{y1} \\ F_{x7} \\ F_{y7} \\ F_{x8} \\ F_{y8} \\ F_{x6} \\ F_{y6} \end{Bmatrix} \quad (\text{for } \Omega^{l-})$$

$$\begin{bmatrix} [\mathbf{L}_{11}^+]_{2 \times 2} & [\mathbf{L}_{12}^+]_{2 \times 4} \\ [\mathbf{L}_{21}^+]_{4 \times 2} & [\mathbf{L}_{22}^+]_{4 \times 4} \end{bmatrix} \begin{Bmatrix} \mathbf{u}_4 \\ \mathbf{u}_{6'5'} \end{Bmatrix} = \begin{Bmatrix} \mathbf{F}_4 \\ \mathbf{F}_{6'5'} \end{Bmatrix} \quad (\text{for } \Omega^+) \quad (3-28)$$

$$\begin{bmatrix} [\mathbf{L}_{11}^{r-}]_{4 \times 4} & [\mathbf{L}_{12}^{r-}]_{4 \times 6} \\ [\mathbf{L}_{21}^{r-}]_{6 \times 4} & [\mathbf{L}_{22}^{r-}]_{6 \times 6} \end{bmatrix} \begin{Bmatrix} \mathbf{u}_{23} \\ \mathbf{u}_{58'7'} \end{Bmatrix} = \begin{Bmatrix} \mathbf{F}_{23} \\ \mathbf{F}_{58'7'} \end{Bmatrix} \quad (\text{for } \Omega^{r-}) \quad (3-29)$$

$$\begin{bmatrix} [\mathbf{L}_{11}^{l-}]_{2 \times 2} & [\mathbf{L}_{12}^{l-}]_{2 \times 6} \\ [\mathbf{L}_{21}^{l-}]_{6 \times 2} & [\mathbf{L}_{22}^{l-}]_{6 \times 6} \end{bmatrix} \begin{Bmatrix} \mathbf{u}_1 \\ \mathbf{u}_{786} \end{Bmatrix} = \begin{Bmatrix} \mathbf{F}_1 \\ \mathbf{F}_{786} \end{Bmatrix} \quad (\text{for } \Omega^{l-}) \quad (3-30)$$

$$(3-31)$$

$$(3-32)$$

$$(3-33)$$

Compared to Eqns (3-1)-(3-6), the only differences in Eqns (3-28)-(3-33) are the array definitions of the displacements and forces, as well as the associated stiffness submatrices \mathbf{L}_{ij}^{Ω} and $(i, j = 1, 2)$. Similar to the procedure in section 3.2.1, the internal displacements as functions of external displacements, and the condensed equilibrium equation can be obtained as follows.

$$\begin{Bmatrix} \mathbf{u}_{6'5'} \\ \mathbf{u}_{786} \\ \mathbf{u}_{58'7'} \end{Bmatrix} = \begin{bmatrix} [\mathbf{Y}_7] & [\mathbf{Y}_8] & [\mathbf{Y}_9] \\ [\mathbf{Y}_4] & [\mathbf{Y}_5] & [\mathbf{Y}_6] \\ [\mathbf{Y}_1] & [\mathbf{Y}_2] & [\mathbf{Y}_3] \end{bmatrix} \begin{Bmatrix} \mathbf{S}_1 \\ \mathbf{S}_2 \\ \mathbf{S}_3 \end{Bmatrix} + \begin{bmatrix} [\mathbf{X}_{13}] & [\mathbf{X}_{14}] & [\mathbf{X}_{15}] \\ [\mathbf{X}_{10}] & [\mathbf{X}_{11}] & [\mathbf{X}_{12}] \\ [\mathbf{X}_7] & [\mathbf{X}_8] & [\mathbf{X}_9] \end{bmatrix} \begin{Bmatrix} \mathbf{u}_1 \\ \mathbf{u}_{23} \\ \mathbf{u}_4 \end{Bmatrix} \quad (3-34)$$

$$\begin{Bmatrix} \mathbf{F}_1 \\ \mathbf{F}_{23} \\ \mathbf{F}_4 \end{Bmatrix} = \begin{bmatrix} [\mathbf{L}'_{12}][\mathbf{Y}_4] & [\mathbf{L}'_{12}][\mathbf{Y}_5] & [\mathbf{L}'_{12}][\mathbf{Y}_6] \\ [\mathbf{L}'_{12}][\mathbf{Y}_1] & [\mathbf{L}'_{12}][\mathbf{Y}_2] & [\mathbf{L}'_{12}][\mathbf{Y}_3] \\ [\mathbf{L}'_{12}][\mathbf{Y}_7] & [\mathbf{L}'_{12}][\mathbf{Y}_8] & [\mathbf{L}'_{12}][\mathbf{Y}_9] \end{bmatrix} \begin{Bmatrix} \mathbf{S}_1 \\ \mathbf{S}_2 \\ \mathbf{S}_3 \end{Bmatrix} \quad (3-35)$$

$$+ \begin{bmatrix} [\mathbf{L}'_{11}] + [\mathbf{L}'_{12}][\mathbf{X}_{10}] & [\mathbf{L}'_{12}][\mathbf{X}_{11}] & [\mathbf{L}'_{12}][\mathbf{X}_{12}] \\ [\mathbf{L}'_{12}][\mathbf{X}_7] & [\mathbf{L}'_{11}] + [\mathbf{L}'_{12}][\mathbf{X}_8] & [\mathbf{L}'_{12}][\mathbf{X}_9] \\ [\mathbf{L}'_{12}][\mathbf{X}_{13}] & [\mathbf{L}'_{12}][\mathbf{X}_{14}] & [\mathbf{L}'_{11}] + [\mathbf{L}'_{12}][\mathbf{X}_{15}] \end{bmatrix} \begin{Bmatrix} \mathbf{u}_1 \\ \mathbf{u}_{23} \\ \mathbf{u}_4 \end{Bmatrix}$$

where the $[\mathbf{X}_i]$ ($i=1, 2, \dots, 15$) and $[\mathbf{Y}_j]$ ($j = 1, 2, \dots, 9$) are identical to those defined in Eqns (3-18) and (3-19).

3.3.2 Numerical Treatments for Stress-Free Subdomains

(a) Integration points I and II completely failed:

$$\begin{Bmatrix} \mathbf{u}_{6'5'} \\ \mathbf{u}_{786} \\ \mathbf{u}_{58'7'} \end{Bmatrix} = \begin{bmatrix} \underline{[\mathbf{Y}_7]} & 0 & 0 \\ 0 & [\mathbf{Y}_5] & [\mathbf{Y}_6] \\ 0 & [\mathbf{Y}_2] & [\mathbf{Y}_3] \end{bmatrix} \begin{Bmatrix} \mathbf{S}_1 \\ \mathbf{S}_2 \\ \mathbf{S}_3 \end{Bmatrix} + \begin{bmatrix} 0 & 0 & \underline{[\mathbf{X}_{15}]} \\ [\mathbf{X}_{10}] & [\mathbf{X}_{11}] & 0 \\ [\mathbf{X}_7] & [\mathbf{X}_8] & 0 \end{bmatrix} \begin{Bmatrix} \mathbf{u}_1 \\ \mathbf{u}_{23} \\ \mathbf{u}_4 \end{Bmatrix} \quad (3-36)$$

$$\begin{Bmatrix} \mathbf{F}_1 \\ \mathbf{F}_{23} \\ \mathbf{F}_4 \end{Bmatrix} = \begin{bmatrix} 0 & [\mathbf{L}'_{12}][\mathbf{Y}_5] & [\mathbf{L}'_{12}][\mathbf{Y}_6] \\ 0 & [\mathbf{L}'_{12}][\mathbf{Y}_2] & [\mathbf{L}'_{12}][\mathbf{Y}_3] \\ \underline{[\mathbf{L}'_{12}][\mathbf{Y}_7]} & 0 & 0 \end{bmatrix} \begin{Bmatrix} \mathbf{S}_1 \\ \mathbf{S}_2 \\ \mathbf{S}_3 \end{Bmatrix} + \begin{bmatrix} [\mathbf{L}'_{11}] + [\mathbf{L}'_{12}][\mathbf{X}_{10}] & [\mathbf{L}'_{12}][\mathbf{X}_{11}] & 0 \\ [\mathbf{L}'_{12}][\mathbf{X}_7] & [\mathbf{L}'_{11}] + [\mathbf{L}'_{12}][\mathbf{X}_8] & 0 \\ 0 & 0 & \underline{[\mathbf{L}'_{11}] + [\mathbf{L}'_{12}][\mathbf{X}_{15}]} \end{bmatrix} \begin{Bmatrix} \mathbf{u}_1 \\ \mathbf{u}_{23} \\ \mathbf{u}_4 \end{Bmatrix} \quad (3-37)$$

Similar to the numerical treatment in Eqns (3-20) and (3-21), the underlined terms in Eqns (3-36) and (3-37) have to be set to zero because in this case $[\mathbf{X}_1]^{-1}$ does not exist (hence $[\mathbf{Y}_7]$ and $[\mathbf{X}_{15}]$ are not defined). This numerical treatment eliminates numerical singularity without changing the solution and this is made possible by noting $\{\mathbf{S}_1\} = 0$.

(b) Integration points II and III completely failed:

$$\begin{Bmatrix} \mathbf{u}_{6'5'} \\ \mathbf{u}_{786} \\ \mathbf{u}_{58'7'} \end{Bmatrix} = \begin{bmatrix} [\mathbf{Y}_7] & [\mathbf{Y}_8] & 0 \\ [\mathbf{Y}_4] & [\mathbf{Y}_5] & 0 \\ 0 & 0 & \underline{[\mathbf{Y}_3]} \end{bmatrix} \begin{Bmatrix} \mathbf{S}_1 \\ \mathbf{S}_2 \\ \mathbf{S}_3 \end{Bmatrix} + \begin{bmatrix} [\mathbf{X}_{13}] & 0 & [\mathbf{X}_{15}] \\ [\mathbf{X}_{10}] & 0 & [\mathbf{X}_{12}] \\ 0 & [\mathbf{X}_8] & 0 \end{bmatrix} \begin{Bmatrix} \mathbf{u}_1 \\ \mathbf{u}_{23} \\ \mathbf{u}_4 \end{Bmatrix} \quad (3-38)$$

$$\begin{Bmatrix} \mathbf{F}_1 \\ \mathbf{F}_{23} \\ \mathbf{F}_4 \end{Bmatrix} = \begin{bmatrix} [\mathbf{L}'_{12}][\mathbf{Y}_4] & [\mathbf{L}'_{12}][\mathbf{Y}_5] & 0 \\ 0 & 0 & \underline{[\mathbf{L}'_{12}][\mathbf{Y}_3]} \\ [\mathbf{L}'_{12}][\mathbf{Y}_7] & [\mathbf{L}'_{12}][\mathbf{Y}_8] & 0 \end{bmatrix} \begin{Bmatrix} \mathbf{S}_1 \\ \mathbf{S}_2 \\ \mathbf{S}_3 \end{Bmatrix} + \begin{bmatrix} [\mathbf{L}'_{11}] + [\mathbf{L}'_{12}][\mathbf{X}_{10}] & 0 & [\mathbf{L}'_{12}][\mathbf{X}_{12}] \\ 0 & [\mathbf{L}'_{11}] + [\mathbf{L}'_{12}][\mathbf{X}_8] & 0 \\ [\mathbf{L}'_{12}][\mathbf{X}_{13}] & 0 & \underline{[\mathbf{L}'_{11}] + [\mathbf{L}'_{12}][\mathbf{X}_{15}]} \end{bmatrix} \begin{Bmatrix} \mathbf{u}_1 \\ \mathbf{u}_{23} \\ \mathbf{u}_4 \end{Bmatrix} \quad (3-39)$$

In this case both equations are well-defined but one can set $[\mathbf{Y}_3] = \mathbf{0}$ and $[\mathbf{L}'_{12}][\mathbf{Y}_3] = \mathbf{0}$ without effecting the numerical solution because $[\mathbf{S}_2] = \mathbf{0}$.

(c) Integration points I and III completely failed:

$$\begin{Bmatrix} \mathbf{u}_{6'5'} \\ \mathbf{u}_{786} \\ \mathbf{u}_{58'7'} \end{Bmatrix} = \begin{bmatrix} [\mathbf{Y}_7] & 0 & [\mathbf{Y}_9] \\ 0 & \underline{[\mathbf{Y}_5]} & 0 \\ [\mathbf{Y}_1] & 0 & [\mathbf{Y}_3] \end{bmatrix} \begin{Bmatrix} \mathbf{S}_1 \\ \mathbf{S}_2 \\ \mathbf{S}_3 \end{Bmatrix} + \begin{bmatrix} 0 & [\mathbf{X}_{14}] & [\mathbf{X}_{15}] \\ \underline{[\mathbf{X}_{10}]} & 0 & 0 \\ 0 & [\mathbf{X}_8] & [\mathbf{X}_9] \end{bmatrix} \begin{Bmatrix} \mathbf{u}_1 \\ \mathbf{u}_{23} \\ \mathbf{u}_4 \end{Bmatrix} \quad (3-40)$$

$$\begin{Bmatrix} \mathbf{F}_1 \\ \mathbf{F}_{23} \\ \mathbf{F}_4 \end{Bmatrix} = \begin{bmatrix} 0 & \underline{[\mathbf{L}'_{12}][\mathbf{Y}_5]} & 0 \\ [\mathbf{L}'_{12}][\mathbf{Y}_1] & 0 & [\mathbf{L}'_{12}][\mathbf{Y}_3] \\ [\mathbf{L}'_{12}][\mathbf{Y}_7] & 0 & [\mathbf{L}'_{12}][\mathbf{Y}_9] \end{bmatrix} \begin{Bmatrix} \mathbf{S}_1 \\ \mathbf{S}_2 \\ \mathbf{S}_3 \end{Bmatrix} + \begin{bmatrix} \underline{[\mathbf{L}'_{11}] + [\mathbf{L}'_{12}][\mathbf{X}_{10}]} & 0 & 0 \\ 0 & [\mathbf{L}'_{11}] + [\mathbf{L}'_{12}][\mathbf{X}_8] & [\mathbf{L}'_{12}][\mathbf{X}_9] \\ 0 & [\mathbf{L}'_{12}][\mathbf{X}_{14}] & [\mathbf{L}'_{11}] + [\mathbf{L}'_{12}][\mathbf{X}_{15}] \end{bmatrix} \begin{Bmatrix} \mathbf{u}_1 \\ \mathbf{u}_{23} \\ \mathbf{u}_4 \end{Bmatrix} \quad (3-41)$$

In this case, since $[\mathbf{X}_2]^{-1}$ does not exist and $\{\mathbf{S}_2\} = \mathbf{0}$, the underlined terms in the above equations have to be set to zero to avoid numerical singularity.

(d) All Integration points I, II, and III failed:

$$\begin{Bmatrix} \mathbf{u}_{6'5'} \\ \mathbf{u}_{786} \\ \mathbf{u}_{58'7'} \end{Bmatrix} = \begin{bmatrix} 0 & 0 & \underline{[\mathbf{X}_{15}]} \\ \underline{[\mathbf{X}_{10}]} & 0 & 0 \\ 0 & [\mathbf{X}_8] & 0 \end{bmatrix} \begin{Bmatrix} \mathbf{u}_1 \\ \mathbf{u}_{23} \\ \mathbf{u}_4 \end{Bmatrix} \quad (3-42)$$

$$\begin{Bmatrix} \mathbf{F}_1 \\ \mathbf{F}_{23} \\ \mathbf{F}_4 \end{Bmatrix} = \begin{bmatrix} \underline{[\mathbf{L}'_{11}] + [\mathbf{L}'_{12}][\mathbf{X}_{10}]} & 0 & 0 \\ 0 & [\mathbf{L}'_{11}] + [\mathbf{L}'_{12}][\mathbf{X}_8] & 0 \\ 0 & 0 & \underline{[\mathbf{L}'_{11}] + [\mathbf{L}'_{12}][\mathbf{X}_{15}]} \end{bmatrix} \begin{Bmatrix} \mathbf{u}_1 \\ \mathbf{u}_{23} \\ \mathbf{u}_4 \end{Bmatrix} \quad (3-43)$$

In this case, since neither $[X_1]^{-1}$ nor $[X_2]^{-1}$ exists, the underlined terms in the above equations have to be set to zero to avoid numerical singularity.

3.4 Elemental Augmentation Formulation – Configuration 3

3.4.1 General Formulation

If the element is cut into three 4-node quadratic subdomains as shown in Figure 3-4:

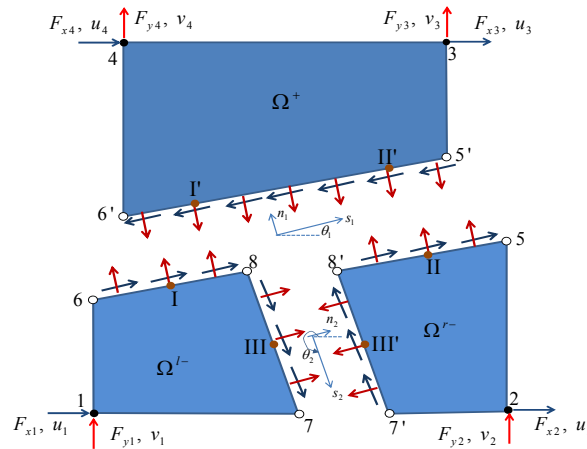


Figure 3-4 Illustration of a secondary crack in a rectangular subdomain (3 crack segments I, II, and III)

The equilibrium equation for each of the subdomains can be written as

$$\begin{bmatrix} k_{11}^+ & \cdots & \cdots & k_{14}^+ & k_{15}^+ & \cdots & \cdots & k_{18}^+ \\ \vdots & \cdots & \cdots & \vdots & \vdots & \cdots & \cdots & \vdots \\ \vdots & \cdots & \cdots & \vdots & \vdots & \cdots & \cdots & \vdots \\ k_{41}^+ & \cdots & \cdots & k_{44}^+ & k_{41}^+ & \cdots & \cdots & k_{48}^+ \\ \hline k_{51}^+ & \cdots & \cdots & k_{54}^+ & k_{55}^+ & \cdots & \cdots & k_{58}^+ \\ \vdots & \cdots & \cdots & \vdots & \vdots & \cdots & \cdots & \vdots \\ \vdots & \cdots & \cdots & \vdots & \vdots & \cdots & \cdots & \vdots \\ k_{81}^+ & \cdots & \cdots & k_{84}^+ & k_{85}^+ & \cdots & \cdots & k_{88}^+ \end{bmatrix} \begin{Bmatrix} u_3 \\ v_3 \\ u_4 \\ v_4 \\ u_{6'} \\ v_{6'} \\ u_{5'} \\ v_{5'} \end{Bmatrix} = \begin{Bmatrix} F_{x3} \\ F_{y3} \\ F_{x4} \\ F_{y4} \\ F_{x6'} \\ F_{y6'} \\ F_{x5'} \\ F_{y5'} \end{Bmatrix} \quad (\text{for } \Omega^+)$$

$$\left[\begin{array}{ccc|ccc} k_{11}^{l-} & k_{12}^{l-} & k_{13}^{l-} & \cdots & \cdots & \cdots & k_{18}^{l-} \\ k_{21}^{l-} & k_{22}^{l-} & k_{23}^{l-} & \cdots & \cdots & \cdots & k_{28}^{l-} \\ k_{31}^{l-} & k_{32}^{l-} & k_{33}^{l-} & \cdots & \cdots & \cdots & k_{38}^{l-} \\ \vdots & \vdots & \vdots & \cdots & \cdots & \cdots & \vdots \\ \vdots & \vdots & \vdots & \cdots & \cdots & \cdots & \vdots \\ \vdots & \vdots & \vdots & \cdots & \cdots & \cdots & \vdots \\ k_{81}^{l-} & k_{82}^{l-} & k_{83}^{l-} & \cdots & \cdots & \cdots & k_{88}^{l-} \end{array} \right] \begin{Bmatrix} u_1 \\ v_1 \\ u_7 \\ v_7 \\ u_8 \\ v_8 \\ u_6 \\ v_6 \end{Bmatrix} = \begin{Bmatrix} F_{x1} \\ F_{y1} \\ F_{x7} \\ F_{y7} \\ F_{x8} \\ F_{y8} \\ F_{x6} \\ F_{y6} \end{Bmatrix} \quad (\text{for } \Omega^{l-})$$

$$\left[\begin{array}{ccc|ccc} k_{11}^{r-} & k_{12}^{r-} & k_{13}^{r-} & \cdots & \cdots & \cdots & k_{18}^{r-} \\ k_{21}^{r-} & k_{22}^{r-} & k_{23}^{r-} & \cdots & \cdots & \cdots & k_{28}^{r-} \\ k_{31}^{r-} & k_{32}^{r-} & k_{33}^{r-} & \cdots & \cdots & \cdots & k_{38}^{r-} \\ \vdots & \vdots & \vdots & \cdots & \cdots & \cdots & \vdots \\ \vdots & \vdots & \vdots & \cdots & \cdots & \cdots & \vdots \\ \vdots & \vdots & \vdots & \cdots & \cdots & \cdots & \vdots \\ k_{81}^{r-} & k_{82}^{r-} & k_{83}^{r-} & \cdots & \cdots & \cdots & k_{88}^{r-} \end{array} \right] \begin{Bmatrix} u_2 \\ v_2 \\ u_5 \\ v_5 \\ u_{8'} \\ v_{8'} \\ u_{7'} \\ v_{7'} \end{Bmatrix} = \begin{Bmatrix} F_{x2} \\ F_{y2} \\ F_{x5} \\ F_{y5} \\ F_{x8'} \\ F_{y8'} \\ F_{x7'} \\ F_{y7'} \end{Bmatrix} \quad (\text{for } \Omega^{r-})$$

Re-write these equations in a more compact form as the following

$$\left[\begin{array}{cc} [\mathbf{L}_{11}^+]_{4 \times 4} & [\mathbf{L}_{12}^+]_{4 \times 4} \\ [\mathbf{L}_{21}^+]_{4 \times 4} & [\mathbf{L}_{22}^+]_{4 \times 4} \end{array} \right] \begin{Bmatrix} \mathbf{u}_{34} \\ \mathbf{u}_{6'5'} \end{Bmatrix} = \begin{Bmatrix} \mathbf{F}_{34} \\ \mathbf{F}_{6'5'} \end{Bmatrix} \quad (\text{for } \Omega^+) \quad (3-44)$$

$$\left[\begin{array}{cc} [\mathbf{L}_{11}^{r-}]_{2 \times 2} & [\mathbf{L}_{12}^{r-}]_{2 \times 6} \\ [\mathbf{L}_{21}^{r-}]_{6 \times 2} & [\mathbf{L}_{22}^{r-}]_{6 \times 6} \end{array} \right] \begin{Bmatrix} \mathbf{u}_2 \\ \mathbf{u}_{58'7'} \end{Bmatrix} = \begin{Bmatrix} \mathbf{F}_2 \\ \mathbf{F}_{58'7'} \end{Bmatrix} \quad (\text{for } \Omega^{r-}) \quad (3-46)$$

$$\left[\begin{array}{cc} [\mathbf{L}_{11}^{l-}]_{2 \times 2} & [\mathbf{L}_{12}^{l-}]_{2 \times 6} \\ [\mathbf{L}_{21}^{l-}]_{6 \times 2} & [\mathbf{L}_{22}^{l-}]_{6 \times 6} \end{array} \right] \begin{Bmatrix} \mathbf{u}_1 \\ \mathbf{u}_{786} \end{Bmatrix} = \begin{Bmatrix} \mathbf{F}_1 \\ \mathbf{F}_{786} \end{Bmatrix} \quad (\text{for } \Omega^{l-}) \quad (3-48)$$

$$(3-49)$$

Following identical solution procedure described in Section 3.2.1, the displacement and equilibrium equations can be derived readily:

$$\begin{Bmatrix} \mathbf{u}_{6'5'} \\ \mathbf{u}_{786} \\ \mathbf{u}_{58'7'} \end{Bmatrix} = \begin{bmatrix} [\mathbf{Y}_7] & [\mathbf{Y}_8] & [\mathbf{Y}_9] \\ [\mathbf{Y}_4] & [\mathbf{Y}_5] & [\mathbf{Y}_6] \\ [\mathbf{Y}_1] & [\mathbf{Y}_2] & [\mathbf{Y}_3] \end{bmatrix} \begin{Bmatrix} \mathbf{S}_1 \\ \mathbf{S}_2 \\ \mathbf{S}_3 \end{Bmatrix} + \begin{bmatrix} [\mathbf{X}_{13}] & [\mathbf{X}_{14}] & [\mathbf{X}_{15}] \\ [\mathbf{X}_{10}] & [\mathbf{X}_{11}] & [\mathbf{X}_{12}] \\ [\mathbf{X}_7] & [\mathbf{X}_8] & [\mathbf{X}_9] \end{bmatrix} \begin{Bmatrix} \mathbf{u}_1 \\ \mathbf{u}_2 \\ \mathbf{u}_{34} \end{Bmatrix} \quad (3-50)$$

$$\begin{aligned}
\begin{Bmatrix} \mathbf{F}_1 \\ \mathbf{F}_2 \\ \mathbf{F}_{34} \end{Bmatrix} &= \begin{bmatrix} [\mathbf{L}'_{12}][\mathbf{Y}_4] & [\mathbf{L}'_{12}][\mathbf{Y}_5] & [\mathbf{L}'_{12}][\mathbf{Y}_6] \\ [\mathbf{L}'_{12}][\mathbf{Y}_1] & [\mathbf{L}'_{12}][\mathbf{Y}_2] & [\mathbf{L}'_{12}][\mathbf{Y}_3] \\ [\mathbf{L}'_{12}][\mathbf{Y}_7] & [\mathbf{L}'_{12}][\mathbf{Y}_8] & [\mathbf{L}'_{12}][\mathbf{Y}_9] \end{bmatrix} \begin{Bmatrix} \mathbf{S}_1 \\ \mathbf{S}_2 \\ \mathbf{S}_3 \end{Bmatrix} \\
&+ \begin{bmatrix} [\mathbf{L}'_{11}] + [\mathbf{L}'_{12}][\mathbf{X}_{10}] & [\mathbf{L}'_{12}][\mathbf{X}_{11}] & [\mathbf{L}'_{12}][\mathbf{X}_{12}] \\ [\mathbf{L}'_{12}][\mathbf{X}_7] & [\mathbf{L}'_{11}] + [\mathbf{L}'_{12}][\mathbf{X}_8] & [\mathbf{L}'_{12}][\mathbf{X}_9] \\ [\mathbf{L}'_{12}][\mathbf{X}_{13}] & [\mathbf{L}'_{12}][\mathbf{X}_{14}] & [\mathbf{L}'_{11}] + [\mathbf{L}'_{12}][\mathbf{X}_{15}] \end{bmatrix} \begin{Bmatrix} \mathbf{u}_1 \\ \mathbf{u}_2 \\ \mathbf{u}_{34} \end{Bmatrix}
\end{aligned} \tag{3-51}$$

Where the $[\mathbf{X}_i]$ ($i=1, 2, \dots, 15$) and $[\mathbf{Y}_j]$ ($j = 1, 2, \dots, 9$) are identical to those defined in Eqns (3-18) and (3-19).

3.4.2 Numerical Treatment for Stress-Free Subdomains

(a) Integration points I and II completely failed:

$$\begin{Bmatrix} \mathbf{u}_{6'5'} \\ \mathbf{u}_{786} \\ \mathbf{u}_{58'7'} \end{Bmatrix} = \begin{bmatrix} [\mathbf{Y}_7] & 0 & 0 \\ 0 & [\mathbf{Y}_5] & [\mathbf{Y}_6] \\ 0 & [\mathbf{Y}_2] & [\mathbf{Y}_3] \end{bmatrix} \begin{Bmatrix} \mathbf{S}_1 \\ \mathbf{S}_2 \\ \mathbf{S}_3 \end{Bmatrix} + \begin{bmatrix} 0 & 0 & [\mathbf{X}_{15}] \\ [\mathbf{X}_{10}] & [\mathbf{X}_{11}] & 0 \\ [\mathbf{X}_7] & [\mathbf{X}_8] & 0 \end{bmatrix} \begin{Bmatrix} \mathbf{u}_{12} \\ \mathbf{u}_3 \\ \mathbf{u}_4 \end{Bmatrix} \tag{3-52}$$

$$\begin{aligned}
\begin{Bmatrix} \mathbf{F}_1 \\ \mathbf{F}_2 \\ \mathbf{F}_{34} \end{Bmatrix} &= \begin{bmatrix} 0 & [\mathbf{L}'_{12}][\mathbf{Y}_5] & [\mathbf{L}'_{12}][\mathbf{Y}_6] \\ 0 & [\mathbf{L}'_{12}][\mathbf{Y}_2] & [\mathbf{L}'_{12}][\mathbf{Y}_3] \\ [\mathbf{L}'_{12}][\mathbf{Y}_7] & 0 & 0 \end{bmatrix} \begin{Bmatrix} \mathbf{S}_1 \\ \mathbf{S}_2 \\ \mathbf{S}_3 \end{Bmatrix} \\
&+ \begin{bmatrix} [\mathbf{L}'_{11}] + [\mathbf{L}'_{12}][\mathbf{X}_{10}] & [\mathbf{L}'_{12}][\mathbf{X}_{11}] & 0 \\ [\mathbf{L}'_{12}][\mathbf{X}_7] & [\mathbf{L}'_{11}] + [\mathbf{L}'_{12}][\mathbf{X}_8] & 0 \\ 0 & 0 & [\mathbf{L}'_{11}] + [\mathbf{L}'_{12}][\mathbf{X}_{15}] \end{bmatrix} \begin{Bmatrix} \mathbf{u}_1 \\ \mathbf{u}_2 \\ \mathbf{u}_{34} \end{Bmatrix}
\end{aligned} \tag{3-53}$$

In this case both equations are well-defined but one can set $[\mathbf{Y}_7] = \mathbf{0}$ and $[\mathbf{L}'_{12}][\mathbf{Y}_7] = \mathbf{0}$ without effecting the numerical solution because $\{\mathbf{S}_1\} = \mathbf{0}$.

(b) Integration points II and III completely failed

$$\begin{Bmatrix} \mathbf{u}_{6'5'} \\ \mathbf{u}_{786} \\ \mathbf{u}_{58'7'} \end{Bmatrix} = \begin{bmatrix} [\mathbf{Y}_7] & [\mathbf{Y}_8] & 0 \\ [\mathbf{Y}_4] & [\mathbf{Y}_5] & 0 \\ 0 & 0 & \underline{[\mathbf{Y}_3]} \end{bmatrix} \begin{Bmatrix} \mathbf{S}_1 \\ \mathbf{S}_2 \\ \mathbf{S}_3 \end{Bmatrix} + \begin{bmatrix} [\mathbf{X}_{13}] & 0 & [\mathbf{X}_{15}] \\ [\mathbf{X}_{10}] & 0 & [\mathbf{X}_{12}] \\ 0 & \underline{[\mathbf{X}_8]} & 0 \end{bmatrix} \begin{Bmatrix} \mathbf{u}_1 \\ \mathbf{u}_2 \\ \mathbf{u}_{34} \end{Bmatrix} \quad (3-54)$$

$$\begin{Bmatrix} \mathbf{F}_1 \\ \mathbf{F}_2 \\ \mathbf{F}_{34} \end{Bmatrix} = \begin{bmatrix} [\mathbf{L}'_{12}][\mathbf{Y}_4] & [\mathbf{L}'_{12}][\mathbf{Y}_5] & 0 \\ 0 & 0 & \underline{[\mathbf{L}'_{12}][\mathbf{Y}_3]} \\ [\mathbf{L}'_{12}][\mathbf{Y}_7] & [\mathbf{L}'_{12}][\mathbf{Y}_8] & 0 \end{bmatrix} \begin{Bmatrix} \mathbf{S}_1 \\ \mathbf{S}_2 \\ \mathbf{S}_3 \end{Bmatrix} + \begin{bmatrix} [\mathbf{L}'_{11}] + [\mathbf{L}'_{12}][\mathbf{X}_{10}] & 0 & [\mathbf{L}'_{12}][\mathbf{X}_{12}] \\ 0 & \underline{[\mathbf{L}'_{11}] + [\mathbf{L}'_{12}][\mathbf{X}_8]} & 0 \\ [\mathbf{L}'_{12}][\mathbf{X}_{13}] & 0 & [\mathbf{L}'_{11}] + [\mathbf{L}'_{12}][\mathbf{X}_{15}] \end{bmatrix} \begin{Bmatrix} \mathbf{u}_1 \\ \mathbf{u}_2 \\ \mathbf{u}_{34} \end{Bmatrix} \quad (3-55)$$

In this case, since $[\mathbf{X}_6]^{-1}$ does not exist and we have $\{\mathbf{S}_3\} = \mathbf{0}$, the underlined terms in the above equations have to be set to zero to avoid numerical singularity. This numerical treatment guarantees $\{\mathbf{F}_2\} = \mathbf{0}$ but $\{\mathbf{u}_2\}$ is indeterminate and has to be decided by neighboring elements.

(c) Integration points I and III completely failed

$$\begin{Bmatrix} \mathbf{u}_{6'5'} \\ \mathbf{u}_{786} \\ \mathbf{u}_{58'7'} \end{Bmatrix} = \begin{bmatrix} [\mathbf{Y}_7] & 0 & [\mathbf{Y}_9] \\ 0 & \underline{[\mathbf{Y}_5]} & 0 \\ [\mathbf{Y}_1] & 0 & [\mathbf{Y}_3] \end{bmatrix} \begin{Bmatrix} \mathbf{S}_1 \\ \mathbf{S}_2 \\ \mathbf{S}_3 \end{Bmatrix} + \begin{bmatrix} 0 & [\mathbf{X}_{14}] & [\mathbf{X}_{15}] \\ \underline{[\mathbf{X}_{10}]} & 0 & 0 \\ 0 & [\mathbf{X}_8] & [\mathbf{X}_9] \end{bmatrix} \begin{Bmatrix} \mathbf{u}_1 \\ \mathbf{u}_2 \\ \mathbf{u}_{34} \end{Bmatrix} \quad (3-56)$$

$$\begin{Bmatrix} \mathbf{F}_1 \\ \mathbf{F}_2 \\ \mathbf{F}_{34} \end{Bmatrix} = \begin{bmatrix} 0 & \underline{[\mathbf{L}'_{12}][\mathbf{Y}_5]} & 0 \\ [\mathbf{L}'_{12}][\mathbf{Y}_1] & 0 & [\mathbf{L}'_{12}][\mathbf{Y}_3] \\ [\mathbf{L}'_{12}][\mathbf{Y}_7] & 0 & [\mathbf{L}'_{12}][\mathbf{Y}_9] \end{bmatrix} \begin{Bmatrix} \mathbf{S}_1 \\ \mathbf{S}_2 \\ \mathbf{S}_3 \end{Bmatrix} + \begin{bmatrix} \underline{[\mathbf{L}'_{11}] + [\mathbf{L}'_{12}][\mathbf{X}_{10}]} & 0 & 0 \\ 0 & [\mathbf{L}'_{11}] + [\mathbf{L}'_{12}][\mathbf{X}_8] & [\mathbf{L}'_{12}][\mathbf{X}_9] \\ 0 & [\mathbf{L}'_{12}][\mathbf{X}_{14}] & [\mathbf{L}'_{11}] + [\mathbf{L}'_{12}][\mathbf{X}_{15}] \end{bmatrix} \begin{Bmatrix} \mathbf{u}_1 \\ \mathbf{u}_2 \\ \mathbf{u}_{34} \end{Bmatrix} \quad (3-57)$$

In this case, since $[\mathbf{X}_2]^{-1}$ does not exist and we have $\{\mathbf{S}_2\} = \mathbf{0}$, the underlined terms in the above equations must be set to zero to avoid numerical singularity. This numerical

treatment guarantees $\{\mathbf{F}_1\} = \mathbf{0}$. $\{\mathbf{u}_1\}$ is indeterminate and has to be decided by neighboring elements.

(d) all integration points I, II, and III failed

$$\begin{Bmatrix} \mathbf{u}_{6'5'} \\ \mathbf{u}_{786} \\ \mathbf{u}_{58'7'} \end{Bmatrix} = \begin{bmatrix} 0 & 0 & [\mathbf{X}_{15}] \\ \underline{[\mathbf{X}_{10}]} & 0 & 0 \\ 0 & \underline{[\mathbf{X}_8]} & 0 \end{bmatrix} \begin{Bmatrix} \mathbf{u}_1 \\ \mathbf{u}_2 \\ \mathbf{u}_{34} \end{Bmatrix} \quad (3-58)$$

$$\begin{Bmatrix} \mathbf{F}_1 \\ \mathbf{F}_2 \\ \mathbf{F}_{34} \end{Bmatrix} = \begin{bmatrix} \underline{[\mathbf{L}'_{11}]} + \underline{[\mathbf{L}'_{12}][\mathbf{X}_{10}]} & 0 & 0 \\ 0 & \underline{[\mathbf{L}'_{11}]} + \underline{[\mathbf{L}'_{12}][\mathbf{X}_8]} & 0 \\ 0 & 0 & [\mathbf{L}'_{11}] + [\mathbf{L}'_{12}][\mathbf{X}_{15}] \end{bmatrix} \begin{Bmatrix} \mathbf{u}_1 \\ \mathbf{u}_2 \\ \mathbf{u}_{34} \end{Bmatrix} \quad (3-59)$$

In this case, since either $[\mathbf{X}_2]^{-1}$ nor $[\mathbf{X}_6]^{-1}$ exist; the underlined terms in the above equations must be set to zero to avoid numerical singularity. This numerical treatment guarantees $\{\mathbf{F}_1\} = \{\mathbf{F}_2\} = \mathbf{0}$. $\{\mathbf{u}_1\}$ and $\{\mathbf{u}_2\}$ are indeterminate and have to be decided by neighboring elements.

3.5 Elemental Augmentation Formulation - Configuration 4

3.5.1 General Formulation

If another crack cuts the top subdomain in previous configuration, the three cracks cut the element into four quadrilateral elements as in Figure 3-5. In this case more additional internal nodes are required to consider the third crack behavior and stresses. Denote these four nodes as 9, 9', A and A', which are added to previous open dots to show internal nodes. The additional crack also requires another integration point which is showed by IV and its counterpart IV'.

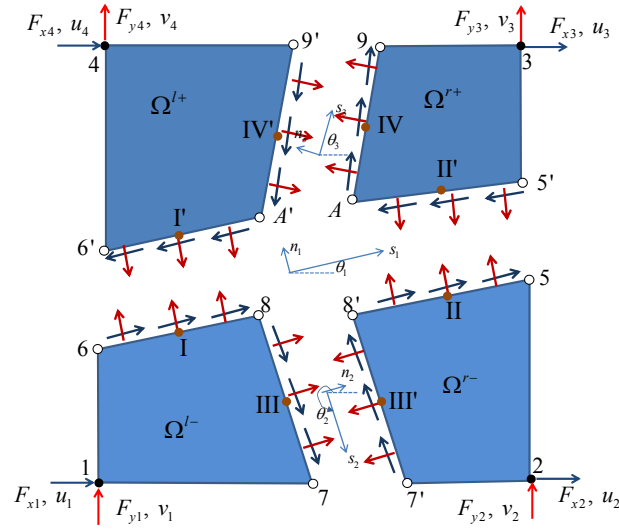


Figure 3-5 Illustration of two secondary cracks in cracked quadratic subdomains (4 crack segments I, II, III and IV)

The equilibrium equation for four subdomains can be expressed as

$$\begin{bmatrix} k_{11}^{l+} & k_{12}^{l+} & k_{13}^{l+} & \cdots & \cdots & \cdots & \cdots & k_{18}^{l+} \\ k_{21}^{l+} & k_{22}^{l+} & k_{23}^{l+} & \cdots & \cdots & \cdots & \cdots & k_{28}^{l+} \\ \hline k_{31}^{l+} & k_{32}^{l+} & k_{33}^{l+} & \cdots & \cdots & \cdots & \cdots & k_{38}^{l+} \\ \vdots & \vdots & \vdots & \cdots & \cdots & \cdots & \cdots & \vdots \\ \vdots & \vdots & \vdots & \cdots & \cdots & \cdots & \cdots & \vdots \\ \vdots & \vdots & \vdots & \cdots & \cdots & \cdots & \cdots & \vdots \\ \vdots & \vdots & \vdots & \cdots & \cdots & \cdots & \cdots & \vdots \\ k_{81}^{l+} & k_{82}^{l+} & k_{83}^{l+} & \cdots & \cdots & \cdots & \cdots & k_{88}^{l+} \end{bmatrix} \begin{Bmatrix} u_4 \\ v_4 \\ u_{6'} \\ v_{6'} \\ u_{A'} \\ v_{A'} \\ u_{9'} \\ v_{9'} \end{Bmatrix} = \begin{Bmatrix} F_{x4} \\ F_{y4} \\ F_{x6'} \\ F_{y6'} \\ F_{xA'} \\ F_{yA'} \\ F_{x9'} \\ F_{y9'} \end{Bmatrix} \quad (\text{for } \Omega^{l+})$$

$$\begin{bmatrix} k_{11}^{r+} & k_{12}^{r+} & k_{13}^{r+} & \cdots & \cdots & \cdots & \cdots & k_{18}^{r+} \\ k_{21}^{r+} & k_{22}^{r+} & k_{23}^{r+} & \cdots & \cdots & \cdots & \cdots & k_{28}^{r+} \\ \hline k_{31}^{r+} & k_{32}^{r+} & k_{33}^{r+} & \cdots & \cdots & \cdots & \cdots & k_{38}^{r+} \\ \vdots & \vdots & \vdots & \cdots & \cdots & \cdots & \cdots & \vdots \\ \vdots & \vdots & \vdots & \cdots & \cdots & \cdots & \cdots & \vdots \\ \vdots & \vdots & \vdots & \cdots & \cdots & \cdots & \cdots & \vdots \\ \vdots & \vdots & \vdots & \cdots & \cdots & \cdots & \cdots & \vdots \\ k_{81}^{r+} & k_{82}^{r+} & k_{83}^{r+} & \cdots & \cdots & \cdots & \cdots & k_{88}^{r+} \end{bmatrix} \begin{Bmatrix} u_3 \\ v_3 \\ u_9 \\ v_9 \\ u_A \\ v_A \\ u_{5'} \\ v_{5'} \end{Bmatrix} = \begin{Bmatrix} F_{x3} \\ F_{y3} \\ F_{x9} \\ F_{y9} \\ F_{xA} \\ F_{yA} \\ F_{x5'} \\ F_{y5'} \end{Bmatrix} \quad (\text{for } \Omega^{r+})$$

$$\begin{bmatrix} k_{11}^{l-} & k_{12}^{l-} & k_{13}^{l-} & \cdots & \cdots & \cdots & \cdots & k_{18}^{l-} \\ k_{21}^{l-} & k_{22}^{l-} & k_{23}^{l-} & \cdots & \cdots & \cdots & \cdots & k_{28}^{l-} \\ \hline k_{31}^{l-} & k_{32}^{l-} & k_{33}^{l-} & \cdots & \cdots & \cdots & \cdots & k_{38}^{l-} \\ \vdots & \vdots & \vdots & \cdots & \cdots & \cdots & \cdots & \vdots \\ \vdots & \vdots & \vdots & \cdots & \cdots & \cdots & \cdots & \vdots \\ \vdots & \vdots & \vdots & \cdots & \cdots & \cdots & \cdots & \vdots \\ \vdots & \vdots & \vdots & \cdots & \cdots & \cdots & \cdots & \vdots \\ k_{81}^{l-} & k_{82}^{l-} & k_{83}^{l-} & \cdots & \cdots & \cdots & \cdots & k_{88}^{l-} \end{bmatrix} \begin{Bmatrix} \mathbf{u}_1 \\ v_1 \\ \mathbf{u}_7 \\ v_7 \\ \mathbf{u}_8 \\ v_8 \\ \mathbf{u}_6 \\ v_6 \end{Bmatrix} = \begin{Bmatrix} F_{x1} \\ F_{y1} \\ F_{x7} \\ F_{y7} \\ F_{x8} \\ F_{y8} \\ F_{x6} \\ F_{y6} \end{Bmatrix} \quad (\text{for } \Omega^{l-})$$

$$\begin{bmatrix} k_{11}^{r-} & k_{12}^{r-} & k_{13}^{r-} & \cdots & \cdots & \cdots & \cdots & k_{18}^{r-} \\ k_{21}^{r-} & k_{22}^{r-} & k_{23}^{r-} & \cdots & \cdots & \cdots & \cdots & k_{28}^{r-} \\ \hline k_{31}^{r-} & k_{32}^{r-} & k_{33}^{r-} & \cdots & \cdots & \cdots & \cdots & k_{38}^{r-} \\ \vdots & \vdots & \vdots & \cdots & \cdots & \cdots & \cdots & \vdots \\ \vdots & \vdots & \vdots & \cdots & \cdots & \cdots & \cdots & \vdots \\ \vdots & \vdots & \vdots & \cdots & \cdots & \cdots & \cdots & \vdots \\ \vdots & \vdots & \vdots & \cdots & \cdots & \cdots & \cdots & \vdots \\ k_{81}^{r-} & k_{82}^{r-} & k_{83}^{r-} & \cdots & \cdots & \cdots & \cdots & k_{88}^{r-} \end{bmatrix} \begin{Bmatrix} \mathbf{u}_2 \\ v_2 \\ \mathbf{u}_5 \\ v_5 \\ \mathbf{u}_{8'} \\ v_{8'} \\ \mathbf{u}_{7'} \\ v_{7'} \end{Bmatrix} = \begin{Bmatrix} F_{x2} \\ F_{y2} \\ F_{x5} \\ F_{y5} \\ F_{x8'} \\ F_{y8'} \\ F_{x7'} \\ F_{y7'} \end{Bmatrix} \quad (\text{for } \Omega^{r-})$$

Rewriting the equations in a more compact form as the following one obtains:

$$[\mathbf{L}_{11}^{l-}]\{\mathbf{u}_1\} + [\mathbf{L}_{12}^{l-}]\{\mathbf{u}_{786}\} = \{\mathbf{F}_1\} \quad (3-60)$$

$$[\mathbf{L}_{21}^{l-}]\{\mathbf{u}_1\} + [\mathbf{L}_{22}^{l-}]\{\mathbf{u}_{786}\} = \{\mathbf{F}_{786}\} \quad (3-61)$$

$$[\mathbf{L}_{11}^{r-}]\{\mathbf{u}_2\} + [\mathbf{L}_{12}^{r-}]\{\mathbf{u}_{587}\} = \{\mathbf{F}_2\} \quad (3-62)$$

$$[\mathbf{L}_{21}^{r-}]\{\mathbf{u}_2\} + [\mathbf{L}_{22}^{r-}]\{\mathbf{u}_{587}\} = \{\mathbf{F}_{587}\} \quad (3-63)$$

$$[\mathbf{L}_{11}^{r+}]\{\mathbf{u}_3\} + [\mathbf{L}_{12}^{r+}]\{\mathbf{u}_{9A5'}\} = \{\mathbf{F}_3\} \quad (3-64)$$

$$[\mathbf{L}_{21}^{r+}]\{\mathbf{u}_3\} + [\mathbf{L}_{22}^{r+}]\{\mathbf{u}_{9A5'}\} = \{\mathbf{F}_{9A5'}\} \quad (3-65)$$

$$[\mathbf{L}_{11}^{l+}]\{\mathbf{u}_4\} + [\mathbf{L}_{12}^{l+}]\{\mathbf{u}_{6'A9'}\} = \{\mathbf{F}_4\} \quad (3-66)$$

$$[\mathbf{L}_{21}^{l+}]\{\mathbf{u}_4\} + [\mathbf{L}_{22}^{l+}]\{\mathbf{u}_{6'A9'}\} = \{\mathbf{F}_{6'A9'}\} \quad (3-67)$$

The internal forces (\mathbf{F}_{786} , $\mathbf{F}_{58'7'}$, $\mathbf{F}_{9,45'}$, and $\mathbf{F}_{6',A'9'}$) can be easily integrated from the cohesive stresses acting on each crack planes as follows

$$\{\mathbf{F}_{786}\} = [\mathbf{T}_{\mathbf{R}}^{l-}] \{\mathbf{S}_1\} = \frac{1}{2} \begin{bmatrix} \mathbf{0} & l_{e2} [\mathbf{R}_2]^T \\ \gamma l_{e1} [\mathbf{R}_1]^T & l_{e2} [\mathbf{R}_2]^T \\ \gamma l_{e1} [\mathbf{R}_1]^T & \mathbf{0} \end{bmatrix} \begin{Bmatrix} \tau_I^{(m)} \\ \sigma_I^{(n)} \\ \tau_{III}^{(p)} \\ \sigma_{III}^{(q)} \end{Bmatrix} \quad (3-68)$$

$$\{\mathbf{F}_{58'7'}\} = [\mathbf{T}_{\mathbf{R}}^{r-}] \{\mathbf{S}_2\} = \frac{1}{2} \begin{bmatrix} (1-\gamma)l_{e1} [\mathbf{R}_1]^T & \mathbf{0} \\ (1-\gamma)l_{e1} [\mathbf{R}_1]^T & -l_{e2} [\mathbf{R}_2]^T \\ \mathbf{0} & -l_{e2} [\mathbf{R}_2]^T \end{bmatrix} \begin{Bmatrix} \tau_{II}^{(k)} \\ \sigma_{II}^{(l)} \\ \tau_{III}^{(p)} \\ \sigma_{III}^{(q)} \end{Bmatrix} \quad (3-69)$$

$$\{\mathbf{F}_{9,45'}\} = [\mathbf{T}_{\mathbf{R}}^{r+}] \{\mathbf{S}_3\} = \frac{1}{2} \begin{bmatrix} \mathbf{0} & l_{e3} [\mathbf{R}_3]^T \\ -(1-\gamma)l_{e1} [\mathbf{R}_1]^T & l_{e3} [\mathbf{R}_3]^T \\ -(1-\gamma)l_{e1} [\mathbf{R}_1]^T & \mathbf{0} \end{bmatrix} \begin{Bmatrix} \tau_{II}^{(k)} \\ \sigma_{II}^{(l)} \\ \tau_{IV}^{(r)} \\ \sigma_{IV}^{(s)} \end{Bmatrix} \quad (3-70)$$

$$\{\mathbf{F}_{6',A'9'}\} = [\mathbf{T}_{\mathbf{R}}^{l+}] \{\mathbf{S}_4\} = \frac{1}{2} \begin{bmatrix} -\gamma l_{e1} [\mathbf{R}_1]^T & \mathbf{0} \\ -\gamma l_{e1} [\mathbf{R}_1]^T & -l_{e3} [\mathbf{R}_3]^T \\ \mathbf{0} & -l_{e3} [\mathbf{R}_3]^T \end{bmatrix} \begin{Bmatrix} \tau_I^{(m)} \\ \sigma_I^{(n)} \\ \tau_{IV}^{(r)} \\ \sigma_{IV}^{(s)} \end{Bmatrix} \quad (3-71)$$

Where $[\mathbf{R}_1]$, $[\mathbf{R}_2]$ and $[\mathbf{R}_3]$ are the rotation matrices defined by the crack orientation defined in Figure 3-5. With the assumed single-point Gaussian integration, the cohesive stresses as functions of nodal displacements can be easily established as

$$\begin{Bmatrix} \tau_I^{(m)} \\ \sigma_I^{(n)} \end{Bmatrix} = \{\boldsymbol{\sigma}_0\}_I + [\boldsymbol{\alpha}_0]_I [\mathbf{R}_1] \left(\frac{1}{2} \begin{Bmatrix} u_6 \\ v_6 \end{Bmatrix} + \frac{1}{2} \begin{Bmatrix} u_{A'} \\ v_{A'} \end{Bmatrix} \right) - [\boldsymbol{\alpha}_0]_I [\mathbf{R}_1] \left(\frac{1}{2} \begin{Bmatrix} u_6 \\ v_6 \end{Bmatrix} + \frac{1}{2} \begin{Bmatrix} u_8 \\ v_8 \end{Bmatrix} \right) \quad (3-72)$$

$$\begin{Bmatrix} \tau_{II}^{(k)} \\ \sigma_{II}^{(l)} \end{Bmatrix} = \{\boldsymbol{\sigma}_0\}_{II} + [\boldsymbol{\alpha}_0]_{II} [\mathbf{R}_1] \left(\frac{1}{2} \begin{Bmatrix} u_A \\ v_A \end{Bmatrix} + \frac{1}{2} \begin{Bmatrix} u_{5'} \\ v_{5'} \end{Bmatrix} \right) - [\boldsymbol{\alpha}_0]_{II} [\mathbf{R}_1] \left(\frac{1}{2} \begin{Bmatrix} u_5 \\ v_5 \end{Bmatrix} + \frac{1}{2} \begin{Bmatrix} u_{8'} \\ v_{8'} \end{Bmatrix} \right) \quad (3-73)$$

$$\begin{Bmatrix} \tau_{III}^{(p)} \\ \sigma_{III}^{(q)} \end{Bmatrix} = \{\boldsymbol{\sigma}_0\}_{III} + [\boldsymbol{\alpha}_0]_{III} [\mathbf{R}_2] \left(\frac{1}{2} \begin{Bmatrix} u_7 \\ v_7 \end{Bmatrix} + \frac{1}{2} \begin{Bmatrix} u_8 \\ v_8 \end{Bmatrix} \right) - [\boldsymbol{\alpha}_0]_{III} [\mathbf{R}_2] \left(\frac{1}{2} \begin{Bmatrix} u_7 \\ v_7 \end{Bmatrix} + \frac{1}{2} \begin{Bmatrix} u_8 \\ v_8 \end{Bmatrix} \right) \quad (3-74)$$

$$\begin{Bmatrix} \tau_{IV}^{(r)} \\ \sigma_{IV}^{(s)} \end{Bmatrix} = \{\boldsymbol{\sigma}_0\}_{IV} + [\boldsymbol{\alpha}_0]_{IV} [\mathbf{R}_3] \left(\frac{1}{2} \begin{Bmatrix} u_9 \\ v_9 \end{Bmatrix} + \frac{1}{2} \begin{Bmatrix} u_A \\ v_A \end{Bmatrix} \right) - [\boldsymbol{\alpha}_0]_{IV} [\mathbf{R}_3] \left(\frac{1}{2} \begin{Bmatrix} u_9 \\ v_9 \end{Bmatrix} + \frac{1}{2} \begin{Bmatrix} u_A \\ v_A \end{Bmatrix} \right) \quad (3-75)$$

Substituting Eqns (3-72) - (3-75) into Eqns (3-68)- (3-71), one has:

$$\{\mathbf{F}_{786}\} = \{\mathbf{S}_1\} + [\boldsymbol{\alpha}_{11}] \{\mathbf{u}_{786}\} + [\boldsymbol{\alpha}_{12}] \{\mathbf{u}_{58'7'}\} + [\boldsymbol{\alpha}_{13}] \{\mathbf{u}_{6'A'9'}\} \quad (3-76)$$

$$\{\mathbf{F}_{58'7'}\} = \{\mathbf{S}_2\} + [\boldsymbol{\alpha}_{21}] \{\mathbf{u}_{786}\} + [\boldsymbol{\alpha}_{22}] \{\mathbf{u}_{58'7'}\} + [\boldsymbol{\alpha}_{23}] \{\mathbf{u}_{9A5'}\} \quad (3-77)$$

$$\{\mathbf{F}_{9A5'}\} = \{\mathbf{S}_3\} + [\boldsymbol{\alpha}_{31}] \{\mathbf{u}_{58'7'}\} + [\boldsymbol{\alpha}_{32}] \{\mathbf{u}_{9A5'}\} + [\boldsymbol{\alpha}_{33}] \{\mathbf{u}_{6'A'9'}\} \quad (3-78)$$

$$\{\mathbf{F}_{6'A'9'}\} = \{\mathbf{S}_4\} + [\boldsymbol{\alpha}_{41}] \{\mathbf{u}_{786}\} + [\boldsymbol{\alpha}_{42}] \{\mathbf{u}_{9A5'}\} + [\boldsymbol{\alpha}_{43}] \{\mathbf{u}_{6'A'9'}\} \quad (3-79)$$

where,

$$\begin{aligned} [\boldsymbol{\alpha}_{11}] &= \frac{1}{2} [\mathbf{T}_R^{l-}] \begin{bmatrix} \mathbf{0} & -[\boldsymbol{\alpha}_0]_I [\mathbf{R}_1] & -[\boldsymbol{\alpha}_0]_I [\mathbf{R}_1] \\ -[\boldsymbol{\alpha}_0]_{III} [\mathbf{R}_2] & -[\boldsymbol{\alpha}_0]_{III} [\mathbf{R}_2] & \mathbf{0} \end{bmatrix}; \quad [\boldsymbol{\alpha}_{12}] = \frac{1}{2} [\mathbf{T}_R^{l-}] \begin{bmatrix} \mathbf{0} & \mathbf{0} & \mathbf{0} \\ \mathbf{0} & [\boldsymbol{\alpha}_0]_{III} [\mathbf{R}_2] & [\boldsymbol{\alpha}_0]_{III} [\mathbf{R}_2] \end{bmatrix}; \\ [\boldsymbol{\alpha}_{13}] &= \frac{1}{2} [\mathbf{T}_R^{l-}] \begin{bmatrix} [\boldsymbol{\alpha}_0]_I [\mathbf{R}_1] & [\boldsymbol{\alpha}_0]_I [\mathbf{R}_1] & \mathbf{0} \\ \mathbf{0} & \mathbf{0} & \mathbf{0} \end{bmatrix}; \quad [\boldsymbol{\alpha}_{21}] = \frac{1}{2} [\mathbf{T}_R^{r-}] \begin{bmatrix} \mathbf{0} & \mathbf{0} & \mathbf{0} \\ -[\boldsymbol{\alpha}_0]_{III} [\mathbf{R}_2] & -[\boldsymbol{\alpha}_0]_{III} [\mathbf{R}_2] & \mathbf{0} \end{bmatrix}; \\ [\boldsymbol{\alpha}_{22}] &= \frac{1}{2} [\mathbf{T}_R^{r-}] \begin{bmatrix} -[\boldsymbol{\alpha}_0]_{III} [\mathbf{R}_1] & -[\boldsymbol{\alpha}_0]_{III} [\mathbf{R}_1] & \mathbf{0} \\ \mathbf{0} & [\boldsymbol{\alpha}_0]_{III} [\mathbf{R}_2] & [\boldsymbol{\alpha}_0]_{III} [\mathbf{R}_2] \end{bmatrix}; \quad [\boldsymbol{\alpha}_{23}] = \frac{1}{2} [\mathbf{T}_R^{r-}] \begin{bmatrix} \mathbf{0} & [\boldsymbol{\alpha}_0]_{III} [\mathbf{R}_1] & [\boldsymbol{\alpha}_0]_{III} [\mathbf{R}_1] \\ \mathbf{0} & \mathbf{0} & \mathbf{0} \end{bmatrix} \quad (3-80) \\ [\boldsymbol{\alpha}_{31}] &= \frac{1}{2} [\mathbf{T}_R^{r+}] \begin{bmatrix} -[\boldsymbol{\alpha}_0]_{III} [\mathbf{R}_1] & -[\boldsymbol{\alpha}_0]_{III} [\mathbf{R}_1] & \mathbf{0} \\ \mathbf{0} & \mathbf{0} & \mathbf{0} \end{bmatrix}; \quad [\boldsymbol{\alpha}_{32}] = \frac{1}{2} [\mathbf{T}_R^{r+}] \begin{bmatrix} \mathbf{0} & [\boldsymbol{\alpha}_0]_{III} [\mathbf{R}_1] & [\boldsymbol{\alpha}_0]_{III} [\mathbf{R}_1] \\ -[\boldsymbol{\alpha}_0]_{IV} [\mathbf{R}_3] & -[\boldsymbol{\alpha}_0]_{IV} [\mathbf{R}_3] & \mathbf{0} \end{bmatrix}; \\ [\boldsymbol{\alpha}_{33}] &= \frac{1}{2} [\mathbf{T}_R^{r+}] \begin{bmatrix} \mathbf{0} & \mathbf{0} & \mathbf{0} \\ \mathbf{0} & [\boldsymbol{\alpha}_0]_{IV} [\mathbf{R}_3] & [\boldsymbol{\alpha}_0]_{IV} [\mathbf{R}_3] \end{bmatrix}; \quad [\boldsymbol{\alpha}_{41}] = \frac{1}{2} [\mathbf{T}_R^{l+}] \begin{bmatrix} \mathbf{0} & -[\boldsymbol{\alpha}_0]_I [\mathbf{R}_1] & -[\boldsymbol{\alpha}_0]_I [\mathbf{R}_1] \\ \mathbf{0} & \mathbf{0} & \mathbf{0} \end{bmatrix}; \\ [\boldsymbol{\alpha}_{42}] &= \frac{1}{2} [\mathbf{T}_R^{l+}] \begin{bmatrix} \mathbf{0} & \mathbf{0} & \mathbf{0} \\ -[\boldsymbol{\alpha}_0]_{IV} [\mathbf{R}_3] & -[\boldsymbol{\alpha}_0]_{IV} [\mathbf{R}_3] & \mathbf{0} \end{bmatrix}; \quad [\boldsymbol{\alpha}_{43}] = \frac{1}{2} [\mathbf{T}_R^{l+}] \begin{bmatrix} [\boldsymbol{\alpha}_0]_I [\mathbf{R}_1] & [\boldsymbol{\alpha}_0]_I [\mathbf{R}_1] & \mathbf{0} \\ \mathbf{0} & [\boldsymbol{\alpha}_0]_{IV} [\mathbf{R}_3] & [\boldsymbol{\alpha}_0]_{IV} [\mathbf{R}_3] \end{bmatrix} \end{aligned}$$

Using this information and solving internal displacements as functions of external displacements gives:

$$\begin{Bmatrix} \mathbf{u}_{786} \\ \mathbf{u}_{587'} \\ \mathbf{u}_{9A5'} \\ \mathbf{u}_{6'A9'} \end{Bmatrix} = \begin{bmatrix} [\mathbf{Y}_{13}] & [\mathbf{Y}_{14}] & [\mathbf{Y}_{15}] & [\mathbf{Y}_{16}] \\ [\mathbf{Y}_5] & [\mathbf{Y}_6] & [\mathbf{Y}_7] & [\mathbf{Y}_8] \\ [\mathbf{Y}_9] & [\mathbf{Y}_{10}] & [\mathbf{Y}_{11}] & [\mathbf{Y}_{12}] \\ [\mathbf{Y}_1] & [\mathbf{Y}_2] & [\mathbf{Y}_3] & [\mathbf{Y}_4] \end{bmatrix} \begin{Bmatrix} \mathbf{S}_1 \\ \mathbf{S}_2 \\ \mathbf{S}_3 \\ \mathbf{S}_4 \end{Bmatrix} + \begin{bmatrix} [\mathbf{X}_{20}] & [\mathbf{X}_{21}] & [\mathbf{X}_{22}] & [\mathbf{X}_{23}] \\ [\mathbf{X}_{12}] & [\mathbf{X}_{13}] & [\mathbf{X}_{14}] & [\mathbf{X}_{15}] \\ [\mathbf{X}_{16}] & [\mathbf{X}_{17}] & [\mathbf{X}_{18}] & [\mathbf{X}_{19}] \\ [\mathbf{X}_8] & [\mathbf{X}_9] & [\mathbf{X}_{10}] & [\mathbf{X}_{11}] \end{bmatrix} \begin{Bmatrix} \mathbf{u}_1 \\ \mathbf{u}_2 \\ \mathbf{u}_3 \\ \mathbf{u}_4 \end{Bmatrix} \quad (3-81)$$

Substituting Eqn (3-81) into Eqns (3-60), (3-62), (3-64) and (3-66), one has

$$\begin{Bmatrix} \mathbf{F}_1 \\ \mathbf{F}_2 \\ \mathbf{F}_3 \\ \mathbf{F}_4 \end{Bmatrix} = \begin{bmatrix} [\mathbf{L}'_{12}][\mathbf{Y}_{13}] & [\mathbf{L}'_{12}][\mathbf{Y}_{14}] & [\mathbf{L}'_{12}][\mathbf{Y}_{15}] & [\mathbf{L}'_{12}][\mathbf{Y}_{16}] \\ [\mathbf{L}'_{12}][\mathbf{Y}_5] & [\mathbf{L}'_{12}][\mathbf{Y}_6] & [\mathbf{L}'_{12}][\mathbf{Y}_7] & [\mathbf{L}'_{12}][\mathbf{Y}_8] \\ [\mathbf{L}'_{12}][\mathbf{Y}_9] & [\mathbf{L}'_{12}][\mathbf{Y}_{10}] & [\mathbf{L}'_{12}][\mathbf{Y}_{11}] & [\mathbf{L}'_{12}][\mathbf{Y}_{12}] \\ [\mathbf{L}'_{12}][\mathbf{Y}_1] & [\mathbf{L}'_{12}][\mathbf{Y}_2] & [\mathbf{L}'_{12}][\mathbf{Y}_3] & [\mathbf{L}'_{12}][\mathbf{Y}_4] \end{bmatrix} \begin{Bmatrix} \mathbf{S}_1 \\ \mathbf{S}_2 \\ \mathbf{S}_3 \\ \mathbf{S}_4 \end{Bmatrix} + \begin{bmatrix} ([\mathbf{L}'_{11}] + [\mathbf{L}'_{12}][\mathbf{X}_{20}]) & [\mathbf{L}'_{12}][\mathbf{X}_{21}] & [\mathbf{L}'_{12}][\mathbf{X}_{22}] & [\mathbf{L}'_{12}][\mathbf{X}_{23}] \\ [\mathbf{L}'_{12}][\mathbf{X}_{12}] & ([\mathbf{L}'_{11}] + [\mathbf{L}'_{12}][\mathbf{X}_{13}]) & [\mathbf{L}'_{12}][\mathbf{X}_{14}] & [\mathbf{L}'_{12}][\mathbf{X}_{15}] \\ [\mathbf{L}'_{12}][\mathbf{X}_{16}] & [\mathbf{L}'_{12}][\mathbf{X}_{17}] & ([\mathbf{L}'_{11}] + [\mathbf{L}'_{12}][\mathbf{X}_{18}]) & [\mathbf{L}'_{12}][\mathbf{X}_{19}] \\ [\mathbf{L}'_{12}][\mathbf{X}_8] & [\mathbf{L}'_{12}][\mathbf{X}_9] & [\mathbf{L}'_{12}][\mathbf{X}_{10}] & ([\mathbf{L}'_{11}] + [\mathbf{L}'_{12}][\mathbf{X}_{11}]) \end{bmatrix} \begin{Bmatrix} \mathbf{u}_1 \\ \mathbf{u}_2 \\ \mathbf{u}_3 \\ \mathbf{u}_4 \end{Bmatrix} \quad (3-82)$$

The matrices in Eqns (3-81) and (3-82) are defined as below.

$$\begin{aligned} [\mathbf{X}_1] &= ([\mathbf{L}'_{22}] - [\mathbf{a}_{11}]); & [\mathbf{X}_3] &= ([\mathbf{L}'_{22}] - [\mathbf{a}_{22}] - [\mathbf{a}_{21}][\mathbf{X}_1]^{-1}[\mathbf{a}_{12}] - [\mathbf{a}_{23}][\mathbf{X}_2]^{-1}[\mathbf{a}_{31}]); \\ [\mathbf{X}_2] &= ([\mathbf{L}'_{22}] - [\mathbf{a}_{32}]); & [\mathbf{X}_4] &= (-[\mathbf{a}_{21}][\mathbf{X}_1]^{-1}[\mathbf{a}_{13}] - [\mathbf{a}_{23}][\mathbf{X}_2]^{-1}[\mathbf{a}_{33}]); \\ [\mathbf{X}_5] &= (-[\mathbf{a}_{41}][\mathbf{X}_1]^{-1}[\mathbf{a}_{12}] - [\mathbf{a}_{42}][\mathbf{X}_2]^{-1}[\mathbf{a}_{31}]); & [\mathbf{X}_6] &= ([\mathbf{L}'_{22}] - [\mathbf{a}_{43}] - [\mathbf{a}_{41}][\mathbf{X}_1]^{-1}[\mathbf{a}_{13}] - [\mathbf{a}_{42}][\mathbf{X}_2]^{-1}[\mathbf{a}_{33}]); \\ [\mathbf{X}_7] &= ([\mathbf{X}_6] - [\mathbf{X}_5][\mathbf{X}_3]^{-1}[\mathbf{X}_4]); & [\mathbf{X}_8] &= [\mathbf{X}_7]^{-1}([\mathbf{X}_5][\mathbf{X}_3]^{-1}[\mathbf{a}_{21}][\mathbf{X}_1]^{-1}[\mathbf{L}'_{21}] - [\mathbf{a}_{41}][\mathbf{X}_1]^{-1}[\mathbf{L}'_{21}]); \\ [\mathbf{X}_9] &= [\mathbf{X}_7]^{-1}[\mathbf{X}_5][\mathbf{X}_3]^{-1}[\mathbf{L}'_{21}], & [\mathbf{X}_{10}] &= [\mathbf{X}_7]^{-1}([\mathbf{X}_5][\mathbf{X}_3]^{-1}[\mathbf{a}_{23}][\mathbf{X}_2]^{-1}[\mathbf{L}'_{21}] - [\mathbf{a}_{42}][\mathbf{X}_2]^{-1}[\mathbf{L}'_{21}]); \\ [\mathbf{X}_{11}] &= -[\mathbf{X}_7]^{-1}[\mathbf{L}'_{21}] & [\mathbf{X}_{12}] &= [\mathbf{X}_3]^{-1}(-[\mathbf{a}_{21}][\mathbf{X}_1]^{-1}[\mathbf{L}'_{21}] - [\mathbf{X}_4][\mathbf{X}_8]), \\ [\mathbf{X}_{13}] &= [\mathbf{X}_3]^{-1}(-[\mathbf{L}'_{21}] - [\mathbf{X}_4][\mathbf{X}_9]), & [\mathbf{X}_{14}] &= [\mathbf{X}_3]^{-1}(-[\mathbf{a}_{23}][\mathbf{X}_2]^{-1}[\mathbf{L}'_{21}] - [\mathbf{X}_4][\mathbf{X}_{10}]), \\ [\mathbf{X}_{15}] &= -[\mathbf{X}_3]^{-1}[\mathbf{X}_4][\mathbf{X}_{11}] & [\mathbf{X}_{16}] &= [\mathbf{X}_2]^{-1}([\mathbf{a}_{31}][\mathbf{X}_{12}] + [\mathbf{a}_{33}][\mathbf{X}_8]) \\ [\mathbf{X}_{17}] &= [\mathbf{X}_2]^{-1}([\mathbf{a}_{31}][\mathbf{X}_{13}] + [\mathbf{a}_{33}][\mathbf{X}_9]) & [\mathbf{X}_{18}] &= [\mathbf{X}_2]^{-1}([\mathbf{a}_{31}][\mathbf{X}_{14}] + [\mathbf{a}_{33}][\mathbf{X}_{10}] - [\mathbf{L}'_{21}]) \\ [\mathbf{X}_{19}] &= [\mathbf{X}_2]^{-1}([\mathbf{a}_{31}][\mathbf{X}_{15}] + [\mathbf{a}_{33}][\mathbf{X}_{11}]) & [\mathbf{X}_{20}] &= [\mathbf{X}_1]^{-1}([\mathbf{a}_{12}][\mathbf{X}_{12}] + [\mathbf{a}_{13}][\mathbf{X}_8] - [\mathbf{L}'_{21}]) \\ [\mathbf{X}_{21}] &= [\mathbf{X}_1]^{-1}([\mathbf{a}_{12}][\mathbf{X}_{13}] + [\mathbf{a}_{13}][\mathbf{X}_9]) & [\mathbf{X}_{22}] &= [\mathbf{X}_1]^{-1}([\mathbf{a}_{12}][\mathbf{X}_{14}] + [\mathbf{a}_{13}][\mathbf{X}_{10}]) \\ [\mathbf{X}_{23}] &= [\mathbf{X}_1]^{-1}([\mathbf{a}_{12}][\mathbf{X}_{15}] + [\mathbf{a}_{13}][\mathbf{X}_{11}]) \end{aligned} \quad (3-83)$$

$$\begin{aligned}
[\mathbf{Y}_1] &= [\mathbf{X}_7]^{-1}([\mathbf{a}_{41}] - [\mathbf{X}_5][\mathbf{X}_3]^{-1}[\mathbf{a}_{21}])([\mathbf{X}_1]^{-1}; & [\mathbf{Y}_2] &= -[\mathbf{X}_7]^{-1}[\mathbf{X}_5][\mathbf{X}_3]^{-1}; \\
[\mathbf{Y}_3] &= [\mathbf{X}_7]^{-1}([\mathbf{a}_{42}] - [\mathbf{X}_5][\mathbf{X}_3]^{-1}[\mathbf{a}_{23}])([\mathbf{X}_2]^{-1}; & [\mathbf{Y}_4] &= [\mathbf{X}_7]^{-1}; \\
[\mathbf{Y}_5] &= [\mathbf{X}_3]^{-1}([\mathbf{a}_{21}][\mathbf{X}_1]^{-1} - [\mathbf{X}_4][\mathbf{Y}_1]); & [\mathbf{Y}_6] &= [\mathbf{X}_3]^{-1}([\mathbf{I}] - [\mathbf{X}_4][\mathbf{Y}_2]); \\
[\mathbf{Y}_7] &= [\mathbf{X}_3]^{-1}([\mathbf{a}_{23}][\mathbf{X}_2]^{-1} - [\mathbf{X}_4][\mathbf{Y}_3]); & [\mathbf{Y}_8] &= -[\mathbf{X}_3]^{-1}[\mathbf{X}_4][\mathbf{Y}_4]; \\
[\mathbf{Y}_9] &= [\mathbf{X}_2]^{-1}([\mathbf{a}_{31}][\mathbf{Y}_5] + [\mathbf{a}_{33}][\mathbf{Y}_1]); & [\mathbf{Y}_{10}] &= [\mathbf{X}_2]^{-1}([\mathbf{a}_{31}][\mathbf{Y}_6] + [\mathbf{a}_{33}][\mathbf{Y}_2]); \\
[\mathbf{Y}_{11}] &= [\mathbf{X}_2]^{-1}([\mathbf{I}] + [\mathbf{a}_{31}][\mathbf{Y}_7] + [\mathbf{a}_{33}][\mathbf{Y}_3]); & [\mathbf{Y}_{12}] &= [\mathbf{X}_2]^{-1}([\mathbf{a}_{31}][\mathbf{Y}_8] + [\mathbf{a}_{33}][\mathbf{Y}_4]); \\
[\mathbf{Y}_{13}] &= [\mathbf{X}_1]^{-1}([\mathbf{I}] + [\mathbf{a}_{12}][\mathbf{Y}_5] + [\mathbf{a}_{13}][\mathbf{Y}_1]); & [\mathbf{Y}_{14}] &= [\mathbf{X}_1]^{-1}([\mathbf{a}_{12}][\mathbf{Y}_6] + [\mathbf{a}_{13}][\mathbf{Y}_2]); \\
[\mathbf{Y}_{15}] &= [\mathbf{X}_1]^{-1}([\mathbf{a}_{12}][\mathbf{Y}_7] + [\mathbf{a}_{13}][\mathbf{Y}_3]); & [\mathbf{Y}_{16}] &= [\mathbf{X}_1]^{-1}([\mathbf{a}_{12}][\mathbf{Y}_8] + [\mathbf{a}_{13}][\mathbf{Y}_4]).
\end{aligned} \tag{3-84}$$

3.5.2 Numerical Treatments for Stress-Free Subdomains

(a) Integration points I and II completely failed:

In this case, the displacement and equilibrium equations simplify to

$$\begin{Bmatrix} \mathbf{u}_{786} \\ \mathbf{u}_{587'} \\ \mathbf{u}_{9A5'} \\ \mathbf{u}_{6'A9'} \end{Bmatrix} = \begin{bmatrix} [\mathbf{Y}_{13}] & [\mathbf{Y}_{14}] & 0 & 0 \\ [\mathbf{Y}_5] & [\mathbf{Y}_6] & 0 & 0 \\ 0 & 0 & [\mathbf{Y}_{11}] & [\mathbf{Y}_{12}] \\ 0 & 0 & [\mathbf{Y}_3] & [\mathbf{Y}_4] \end{bmatrix} \begin{Bmatrix} \mathbf{S}_1 \\ \mathbf{S}_2 \\ \mathbf{S}_3 \\ \mathbf{S}_4 \end{Bmatrix} + \begin{bmatrix} [\mathbf{X}_{20}] & [\mathbf{X}_{21}] & 0 & 0 \\ [\mathbf{X}_{12}] & [\mathbf{X}_{13}] & 0 & 0 \\ 0 & 0 & [\mathbf{X}_{18}] & [\mathbf{X}_{19}] \\ 0 & 0 & [\mathbf{X}_{10}] & [\mathbf{X}_{11}] \end{bmatrix} \begin{Bmatrix} \mathbf{u}_1 \\ \mathbf{u}_2 \\ \mathbf{u}_3 \\ \mathbf{u}_4 \end{Bmatrix} \tag{3-85}$$

$$\begin{Bmatrix} \mathbf{F}_1 \\ \mathbf{F}_2 \\ \mathbf{F}_3 \\ \mathbf{F}_4 \end{Bmatrix} = \begin{bmatrix} [\mathbf{L}'_{12}][\mathbf{Y}_{13}] & [\mathbf{L}'_{12}][\mathbf{Y}_{14}] & 0 & 0 \\ [\mathbf{L}'_{12}][\mathbf{Y}_5] & [\mathbf{L}'_{12}][\mathbf{Y}_6] & 0 & 0 \\ 0 & 0 & [\mathbf{L}'_{12}][\mathbf{Y}_{11}] & [\mathbf{L}'_{12}][\mathbf{Y}_{12}] \\ 0 & 0 & [\mathbf{L}'_{12}][\mathbf{Y}_3] & [\mathbf{L}'_{12}][\mathbf{Y}_4] \end{bmatrix} \begin{Bmatrix} \mathbf{S}_1 \\ \mathbf{S}_2 \\ \mathbf{S}_3 \\ \mathbf{S}_4 \end{Bmatrix} \\
+ \begin{bmatrix} ([\mathbf{L}'_{11}] + [\mathbf{L}'_{12}][\mathbf{X}_{20}]) & [\mathbf{L}'_{12}][\mathbf{X}_{21}] & 0 & 0 \\ [\mathbf{L}'_{12}][\mathbf{X}_{12}] & ([\mathbf{L}'_{11}] + [\mathbf{L}'_{12}][\mathbf{X}_{13}]) & 0 & 0 \\ 0 & 0 & ([\mathbf{L}'_{11}] + [\mathbf{L}'_{12}][\mathbf{X}_{18}]) & [\mathbf{L}'_{12}][\mathbf{X}_{19}] \\ 0 & 0 & [\mathbf{L}'_{12}][\mathbf{X}_{10}] & ([\mathbf{L}'_{11}] + [\mathbf{L}'_{12}][\mathbf{X}_{11}]) \end{bmatrix} \begin{Bmatrix} \mathbf{u}_1 \\ \mathbf{u}_2 \\ \mathbf{u}_3 \\ \mathbf{u}_4 \end{Bmatrix} \tag{3-86}$$

Both equations are well-defined and there is no need for special treatment in this case.

(b) Integration points I and III completely failed:

In this case, the displacement and equilibrium equations simplify to

$$\begin{Bmatrix} \mathbf{u}_{786} \\ \mathbf{u}_{58'7} \\ \mathbf{u}_{9A5'} \\ \mathbf{u}_{6'A'9} \end{Bmatrix} = \begin{bmatrix} \underline{[\mathbf{Y}_{13}]} & 0 & 0 & 0 \\ 0 & [\mathbf{Y}_6] & [\mathbf{Y}_7] & [\mathbf{Y}_8] \\ 0 & [\mathbf{Y}_{10}] & [\mathbf{Y}_{11}] & [\mathbf{Y}_{12}] \\ 0 & [\mathbf{Y}_2] & [\mathbf{Y}_3] & [\mathbf{Y}_4] \end{bmatrix} \begin{Bmatrix} \mathbf{S}_1 \\ \mathbf{S}_2 \\ \mathbf{S}_3 \\ \mathbf{S}_4 \end{Bmatrix} + \begin{bmatrix} \underline{[\mathbf{X}_{20}]} & 0 & 0 & 0 \\ 0 & [\mathbf{X}_{13}] & [\mathbf{X}_{14}] & [\mathbf{X}_{15}] \\ 0 & [\mathbf{X}_{17}] & [\mathbf{X}_{18}] & [\mathbf{X}_{19}] \\ 0 & [\mathbf{X}_9] & [\mathbf{X}_{10}] & [\mathbf{X}_{11}] \end{bmatrix} \begin{Bmatrix} \mathbf{u}_1 \\ \mathbf{u}_2 \\ \mathbf{u}_3 \\ \mathbf{u}_4 \end{Bmatrix} \quad (3-87)$$

$$\begin{Bmatrix} \mathbf{F}_1 \\ \mathbf{F}_2 \\ \mathbf{F}_3 \\ \mathbf{F}_4 \end{Bmatrix} = \begin{bmatrix} \underline{[\mathbf{L}'_{12}][\mathbf{Y}_{13}]} & 0 & 0 & 0 \\ 0 & [\mathbf{L}'_{12}][\mathbf{Y}_6] & [\mathbf{L}'_{12}][\mathbf{Y}_7] & [\mathbf{L}'_{12}][\mathbf{Y}_8] \\ 0 & [\mathbf{L}'_{12}][\mathbf{Y}_{10}] & [\mathbf{L}'_{12}][\mathbf{Y}_{11}] & [\mathbf{L}'_{12}][\mathbf{Y}_{12}] \\ 0 & [\mathbf{L}'_{12}][\mathbf{Y}_2] & [\mathbf{L}'_{12}][\mathbf{Y}_3] & [\mathbf{L}'_{12}][\mathbf{Y}_4] \end{bmatrix} \begin{Bmatrix} \mathbf{S}_1 \\ \mathbf{S}_2 \\ \mathbf{S}_3 \\ \mathbf{S}_4 \end{Bmatrix} + \begin{bmatrix} \underline{([\mathbf{L}'_{11}] + [\mathbf{L}'_{12}][\mathbf{X}_{20}])} & 0 & 0 & 0 \\ 0 & ([\mathbf{L}'_{11}] + [\mathbf{L}'_{12}][\mathbf{X}_{13}]) & [\mathbf{L}'_{12}][\mathbf{X}_{14}] & [\mathbf{L}'_{12}][\mathbf{X}_{15}] \\ 0 & [\mathbf{L}'_{12}][\mathbf{X}_{17}] & ([\mathbf{L}'_{11}] + [\mathbf{L}'_{12}][\mathbf{X}_{18}]) & [\mathbf{L}'_{12}][\mathbf{X}_{19}] \\ 0 & [\mathbf{L}'_{12}][\mathbf{X}_9] & [\mathbf{L}'_{12}][\mathbf{X}_{10}] & ([\mathbf{L}'_{11}] + [\mathbf{L}'_{12}][\mathbf{X}_{11}]) \end{bmatrix} \begin{Bmatrix} \mathbf{u}_1 \\ \mathbf{u}_2 \\ \mathbf{u}_3 \\ \mathbf{u}_4 \end{Bmatrix} \quad (3-88)$$

Since in this case $[\mathbf{X}_1]^{-1}$ does not exist, $[\mathbf{Y}_{13}]$ and $[\mathbf{X}_{20}]$ are not defined. A simple treatment is to set all the underlined terms to be zero.

(c) Integration points I and IV completely failed:

In this case, the displacement and equilibrium equations simplify to

$$\begin{Bmatrix} \mathbf{u}_{786} \\ \mathbf{u}_{58'7} \\ \mathbf{u}_{9A5'} \\ \mathbf{u}_{6'A'9} \end{Bmatrix} = \begin{bmatrix} [\mathbf{Y}_{13}] & [\mathbf{Y}_{14}] & [\mathbf{Y}_{15}] & 0 \\ [\mathbf{Y}_5] & [\mathbf{Y}_6] & [\mathbf{Y}_7] & 0 \\ [\mathbf{Y}_9] & [\mathbf{Y}_{10}] & [\mathbf{Y}_{11}] & 0 \\ 0 & 0 & 0 & \underline{[\mathbf{Y}_4]} \end{bmatrix} \begin{Bmatrix} \mathbf{S}_1 \\ \mathbf{S}_2 \\ \mathbf{S}_3 \\ \mathbf{S}_4 \end{Bmatrix} + \begin{bmatrix} [\mathbf{X}_{20}] & [\mathbf{X}_{21}] & [\mathbf{X}_{22}] & 0 \\ [\mathbf{X}_{12}] & [\mathbf{X}_{13}] & [\mathbf{X}_{14}] & 0 \\ [\mathbf{X}_{16}] & [\mathbf{X}_{17}] & [\mathbf{X}_{18}] & 0 \\ 0 & 0 & 0 & \underline{[\mathbf{X}_{11}]} \end{bmatrix} \begin{Bmatrix} \mathbf{u}_1 \\ \mathbf{u}_2 \\ \mathbf{u}_3 \\ \mathbf{u}_4 \end{Bmatrix} \quad (3-89)$$

$$\begin{aligned}
\begin{Bmatrix} \mathbf{F}_1 \\ \mathbf{F}_2 \\ \mathbf{F}_3 \\ \mathbf{F}_4 \end{Bmatrix} &= \begin{bmatrix} [\mathbf{L}'_{12}][\mathbf{Y}_{13}] & [\mathbf{L}'_{12}][\mathbf{Y}_{14}] & [\mathbf{L}'_{12}][\mathbf{Y}_{15}] & 0 \\ [\mathbf{L}'_{12}][\mathbf{Y}_5] & [\mathbf{L}'_{12}][\mathbf{Y}_6] & [\mathbf{L}'_{12}][\mathbf{Y}_7] & 0 \\ [\mathbf{L}'_{12}][\mathbf{Y}_9] & [\mathbf{L}'_{12}][\mathbf{Y}_{10}] & [\mathbf{L}'_{12}][\mathbf{Y}_{11}] & 0 \\ 0 & 0 & 0 & \underline{[\mathbf{L}'_{12}][\mathbf{Y}_4]} \end{bmatrix} \begin{Bmatrix} \mathbf{S}_1 \\ \mathbf{S}_2 \\ \mathbf{S}_3 \\ \mathbf{S}_4 \end{Bmatrix} \\
+ &\begin{bmatrix} ([\mathbf{L}'_{11}] + [\mathbf{L}'_{12}][\mathbf{X}_{20}]) & [\mathbf{L}'_{12}][\mathbf{X}_{21}] & [\mathbf{L}'_{12}][\mathbf{X}_{22}] & 0 \\ [\mathbf{L}'_{12}][\mathbf{X}_{12}] & ([\mathbf{L}'_{11}] + [\mathbf{L}'_{12}][\mathbf{X}_{13}]) & [\mathbf{L}'_{12}][\mathbf{X}_{14}] & 0 \\ [\mathbf{L}'_{12}][\mathbf{X}_{16}] & [\mathbf{L}'_{12}][\mathbf{X}_{17}] & ([\mathbf{L}'_{11}] + [\mathbf{L}'_{12}][\mathbf{X}_{18}]) & 0 \\ 0 & 0 & 0 & \underline{([\mathbf{L}'_{11}] + [\mathbf{L}'_{12}][\mathbf{X}_{11}])} \end{bmatrix} \begin{Bmatrix} \mathbf{u}_1 \\ \mathbf{u}_2 \\ \mathbf{u}_3 \\ \mathbf{u}_4 \end{Bmatrix}
\end{aligned} \tag{3-90}$$

Since in this case $[\mathbf{X}_7]^{-1} (= [\mathbf{L}'_{22}]^{-1})$ does not exist, $[\mathbf{Y}_4]$ and $[\mathbf{X}_{11}]$ are not defined. A simple treatment is to set all the underlined terms to be zero.

(d) Integration points II and III completely failed:

In this case, the displacement and equilibrium equations simplify to

$$\begin{Bmatrix} \mathbf{u}_{786} \\ \mathbf{u}_{58'7} \\ \mathbf{u}_{9A5'} \\ \mathbf{u}_{6'A9'} \end{Bmatrix} = \begin{bmatrix} [\mathbf{Y}_{13}] & 0 & [\mathbf{Y}_{15}] & [\mathbf{Y}_{16}] \\ 0 & \underline{[\mathbf{Y}_6]} & 0 & 0 \\ [\mathbf{Y}_9] & 0 & [\mathbf{Y}_{11}] & [\mathbf{Y}_{12}] \\ [\mathbf{Y}_1] & 0 & [\mathbf{Y}_3] & [\mathbf{Y}_4] \end{bmatrix} \begin{Bmatrix} \mathbf{S}_1 \\ \mathbf{S}_2 \\ \mathbf{S}_3 \\ \mathbf{S}_4 \end{Bmatrix} + \begin{bmatrix} [\mathbf{X}_{20}] & 0 & [\mathbf{X}_{22}] & [\mathbf{X}_{23}] \\ 0 & \underline{[\mathbf{X}_{13}]} & 0 & 0 \\ [\mathbf{X}_{16}] & 0 & [\mathbf{X}_{18}] & [\mathbf{X}_{19}] \\ [\mathbf{X}_8] & 0 & [\mathbf{X}_{10}] & [\mathbf{X}_{11}] \end{bmatrix} \begin{Bmatrix} \mathbf{u}_1 \\ \mathbf{u}_2 \\ \mathbf{u}_3 \\ \mathbf{u}_4 \end{Bmatrix} \tag{3-91}$$

$$\begin{aligned}
\begin{Bmatrix} \mathbf{F}_1 \\ \mathbf{F}_2 \\ \mathbf{F}_3 \\ \mathbf{F}_4 \end{Bmatrix} &= \begin{bmatrix} [\mathbf{L}'_{12}][\mathbf{Y}_{13}] & 0 & [\mathbf{L}'_{12}][\mathbf{Y}_{15}] & [\mathbf{L}'_{12}][\mathbf{Y}_{16}] \\ 0 & \underline{[\mathbf{L}'_{12}][\mathbf{Y}_6]} & 0 & 0 \\ [\mathbf{L}'_{12}][\mathbf{Y}_9] & 0 & [\mathbf{L}'_{12}][\mathbf{Y}_{11}] & [\mathbf{L}'_{12}][\mathbf{Y}_{12}] \\ [\mathbf{L}'_{12}][\mathbf{Y}_1] & 0 & [\mathbf{L}'_{12}][\mathbf{Y}_3] & [\mathbf{L}'_{12}][\mathbf{Y}_4] \end{bmatrix} \begin{Bmatrix} \mathbf{S}_1 \\ \mathbf{S}_2 \\ \mathbf{S}_3 \\ \mathbf{S}_4 \end{Bmatrix} \\
+ &\begin{bmatrix} ([\mathbf{L}'_{11}] + [\mathbf{L}'_{12}][\mathbf{X}_{20}]) & 0 & [\mathbf{L}'_{12}][\mathbf{X}_{22}] & [\mathbf{L}'_{12}][\mathbf{X}_{23}] \\ 0 & \underline{([\mathbf{L}'_{11}] + [\mathbf{L}'_{12}][\mathbf{X}_{13}])} & 0 & 0 \\ [\mathbf{L}'_{12}][\mathbf{X}_{16}] & 0 & ([\mathbf{L}'_{11}] + [\mathbf{L}'_{12}][\mathbf{X}_{18}]) & [\mathbf{L}'_{12}][\mathbf{X}_{19}] \\ [\mathbf{L}'_{12}][\mathbf{X}_8] & 0 & [\mathbf{L}'_{12}][\mathbf{X}_{10}] & \underline{([\mathbf{L}'_{11}] + [\mathbf{L}'_{12}][\mathbf{X}_{11}])} \end{bmatrix} \begin{Bmatrix} \mathbf{u}_1 \\ \mathbf{u}_2 \\ \mathbf{u}_3 \\ \mathbf{u}_4 \end{Bmatrix}
\end{aligned} \tag{3-92}$$

Since in this case $[\mathbf{X}_3]^{-1} (= [\mathbf{L}'_{22}]^{-1})$ does not exist, $[\mathbf{Y}_6]$ and $[\mathbf{X}_{13}]$ are not defined. A simple treatment is to set all the underlined terms to be zero.

(e) Integration points II and IV completely failed:

In this case, the displacement and equilibrium equations simplify to

$$\begin{Bmatrix} \mathbf{u}_{786} \\ \mathbf{u}_{58'7'} \\ \mathbf{u}_{9A5'} \\ \mathbf{u}_{6'A9'} \end{Bmatrix} = \begin{bmatrix} [\mathbf{Y}_{13}] & [\mathbf{Y}_{14}] & 0 & [\mathbf{Y}_{16}] \\ [\mathbf{Y}_5] & [\mathbf{Y}_6] & 0 & [\mathbf{Y}_8] \\ 0 & 0 & \underline{[\mathbf{Y}_{11}]} & 0 \\ [\mathbf{Y}_1] & [\mathbf{Y}_2] & 0 & [\mathbf{Y}_4] \end{bmatrix} \begin{Bmatrix} \mathbf{S}_1 \\ \mathbf{S}_2 \\ \mathbf{S}_3 \\ \mathbf{S}_4 \end{Bmatrix} + \begin{bmatrix} [\mathbf{X}_{20}] & [\mathbf{X}_{21}] & 0 & [\mathbf{X}_{23}] \\ [\mathbf{X}_{12}] & [\mathbf{X}_{13}] & 0 & [\mathbf{X}_{15}] \\ 0 & 0 & \underline{[\mathbf{X}_{18}]} & 0 \\ [\mathbf{X}_8] & [\mathbf{X}_9] & 0 & [\mathbf{X}_{11}] \end{bmatrix} \begin{Bmatrix} \mathbf{u}_1 \\ \mathbf{u}_2 \\ \mathbf{u}_3 \\ \mathbf{u}_4 \end{Bmatrix} \quad (3-93)$$

$$\begin{Bmatrix} \mathbf{F}_1 \\ \mathbf{F}_2 \\ \mathbf{F}_3 \\ \mathbf{F}_4 \end{Bmatrix} = \begin{bmatrix} [\mathbf{L}'_{12}][\mathbf{Y}_{13}] & [\mathbf{L}'_{12}][\mathbf{Y}_{14}] & 0 & [\mathbf{L}'_{12}][\mathbf{Y}_{16}] \\ [\mathbf{L}'_{12}][\mathbf{Y}_5] & [\mathbf{L}'_{12}][\mathbf{Y}_6] & 0 & [\mathbf{L}'_{12}][\mathbf{Y}_8] \\ 0 & 0 & \underline{[\mathbf{L}'_{12}][\mathbf{Y}_{11}]} & 0 \\ [\mathbf{L}'_{12}][\mathbf{Y}_1] & [\mathbf{L}'_{12}][\mathbf{Y}_2] & 0 & [\mathbf{L}'_{12}][\mathbf{Y}_4] \end{bmatrix} \begin{Bmatrix} \mathbf{S}_1 \\ \mathbf{S}_2 \\ \mathbf{S}_3 \\ \mathbf{S}_4 \end{Bmatrix} + \begin{bmatrix} ([\mathbf{L}'_{11}] + [\mathbf{L}'_{12}][\mathbf{X}_{20}]) & [\mathbf{L}'_{12}][\mathbf{X}_{21}] & 0 & [\mathbf{L}'_{12}][\mathbf{X}_{23}] \\ [\mathbf{L}'_{12}][\mathbf{X}_{12}] & ([\mathbf{L}'_{11}] + [\mathbf{L}'_{12}][\mathbf{X}_{13}]) & 0 & [\mathbf{L}'_{12}][\mathbf{X}_{15}] \\ 0 & 0 & \underline{([\mathbf{L}'_{11}] + [\mathbf{L}'_{12}][\mathbf{X}_{18}])} & 0 \\ [\mathbf{L}'_{12}][\mathbf{X}_8] & [\mathbf{L}'_{12}][\mathbf{X}_9] & 0 & ([\mathbf{L}'_{11}] + [\mathbf{L}'_{12}][\mathbf{X}_{11}]) \end{bmatrix} \begin{Bmatrix} \mathbf{u}_1 \\ \mathbf{u}_2 \\ \mathbf{u}_3 \\ \mathbf{u}_4 \end{Bmatrix} \quad (3-94)$$

Since in this case $[\mathbf{X}_2]^{-1} (= [\mathbf{L}'_{22}]^{-1})$ does not exist, $[\mathbf{Y}_6]$ and $[\mathbf{X}_{13}]$ are not defined. A

simple treatment is to set all the underlined terms to be zero.

(f) Integration points III and IV completely failed:

In this case, the displacement and equilibrium equations simplify to

$$\begin{Bmatrix} \mathbf{u}_{786} \\ \mathbf{u}_{58'7'} \\ \mathbf{u}_{9A5'} \\ \mathbf{u}_{6'A9'} \end{Bmatrix} = \begin{bmatrix} [\mathbf{Y}_{13}] & 0 & 0 & [\mathbf{Y}_{16}] \\ 0 & [\mathbf{Y}_6] & [\mathbf{Y}_7] & 0 \\ 0 & [\mathbf{Y}_{10}] & [\mathbf{Y}_{11}] & 0 \\ [\mathbf{Y}_1] & 0 & 0 & [\mathbf{Y}_4] \end{bmatrix} \begin{Bmatrix} \mathbf{S}_1 \\ \mathbf{S}_2 \\ \mathbf{S}_3 \\ \mathbf{S}_4 \end{Bmatrix} + \begin{bmatrix} [\mathbf{X}_{20}] & 0 & 0 & [\mathbf{X}_{23}] \\ 0 & [\mathbf{X}_{13}] & [\mathbf{X}_{14}] & 0 \\ 0 & [\mathbf{X}_{17}] & [\mathbf{X}_{18}] & 0 \\ [\mathbf{X}_8] & 0 & 0 & [\mathbf{X}_{11}] \end{bmatrix} \begin{Bmatrix} \mathbf{u}_1 \\ \mathbf{u}_2 \\ \mathbf{u}_3 \\ \mathbf{u}_4 \end{Bmatrix} \quad (3-95)$$

$$\begin{Bmatrix} \mathbf{F}_1 \\ \mathbf{F}_2 \\ \mathbf{F}_3 \\ \mathbf{F}_4 \end{Bmatrix} = \begin{bmatrix} [\mathbf{L}'_{12}][\mathbf{Y}_{13}] & 0 & 0 & [\mathbf{L}'_{12}][\mathbf{Y}_{16}] \\ 0 & [\mathbf{L}'_{12}][\mathbf{Y}_6] & [\mathbf{L}'_{12}][\mathbf{Y}_7] & 0 \\ 0 & [\mathbf{L}'_{12}][\mathbf{Y}_{10}] & [\mathbf{L}'_{12}][\mathbf{Y}_{11}] & 0 \\ [\mathbf{L}'_{12}][\mathbf{Y}_1] & 0 & 0 & [\mathbf{L}'_{12}][\mathbf{Y}_4] \end{bmatrix} \begin{Bmatrix} \mathbf{S}_1 \\ \mathbf{S}_2 \\ \mathbf{S}_3 \\ \mathbf{S}_4 \end{Bmatrix} \quad (3-96)$$

$$+ \begin{bmatrix} ([\mathbf{L}'_{11}] + [\mathbf{L}'_{12}][\mathbf{X}_{20}]) & 0 & 0 & [\mathbf{L}'_{12}][\mathbf{X}_{23}] \\ 0 & ([\mathbf{L}'_{11}] + [\mathbf{L}'_{12}][\mathbf{X}_{13}]) & [\mathbf{L}'_{12}][\mathbf{X}_{14}] & 0 \\ 0 & [\mathbf{L}'_{12}][\mathbf{X}_{17}] & ([\mathbf{L}'_{11}] + [\mathbf{L}'_{12}][\mathbf{X}_{18}]) & 0 \\ [\mathbf{L}'_{12}][\mathbf{X}_8] & 0 & 0 & ([\mathbf{L}'_{11}] + [\mathbf{L}'_{12}][\mathbf{X}_{11}]) \end{bmatrix} \begin{Bmatrix} \mathbf{u}_1 \\ \mathbf{u}_2 \\ \mathbf{u}_3 \\ \mathbf{u}_4 \end{Bmatrix}$$

Both equations are well-defined and there is no need for special treatment in this case.

(g) Integration points I, II, III completely failed:

In this case, the displacement and equilibrium equations simplify to

$$\begin{Bmatrix} \mathbf{u}_{786} \\ \mathbf{u}_{587'} \\ \mathbf{u}_{9A5'} \\ \mathbf{u}_{6'A9'} \end{Bmatrix} = \begin{bmatrix} \underline{[\mathbf{Y}_{13}]} & 0 & 0 & 0 \\ 0 & \underline{[\mathbf{Y}_6]} & 0 & 0 \\ 0 & 0 & [\mathbf{Y}_{11}] & [\mathbf{Y}_{12}] \\ 0 & 0 & [\mathbf{Y}_3] & [\mathbf{Y}_4] \end{bmatrix} \begin{Bmatrix} \mathbf{S}_1 \\ \mathbf{S}_2 \\ \mathbf{S}_3 \\ \mathbf{S}_4 \end{Bmatrix} + \begin{bmatrix} \underline{[\mathbf{X}_{20}]} & 0 & 0 & 0 \\ 0 & \underline{[\mathbf{X}_{13}]} & 0 & 0 \\ 0 & 0 & [\mathbf{X}_{18}] & [\mathbf{X}_{19}] \\ 0 & 0 & [\mathbf{X}_{10}] & [\mathbf{X}_{11}] \end{bmatrix} \begin{Bmatrix} \mathbf{u}_1 \\ \mathbf{u}_2 \\ \mathbf{u}_3 \\ \mathbf{u}_4 \end{Bmatrix} \quad (3-97)$$

$$\begin{Bmatrix} \mathbf{F}_1 \\ \mathbf{F}_2 \\ \mathbf{F}_3 \\ \mathbf{F}_4 \end{Bmatrix} = \begin{bmatrix} \underline{[\mathbf{L}'_{12}][\mathbf{Y}_{13}]} & 0 & 0 & 0 \\ 0 & \underline{[\mathbf{L}'_{12}][\mathbf{Y}_6]} & 0 & 0 \\ 0 & 0 & [\mathbf{L}'_{12}][\mathbf{Y}_{11}] & [\mathbf{L}'_{12}][\mathbf{Y}_{12}] \\ 0 & 0 & [\mathbf{L}'_{12}][\mathbf{Y}_3] & [\mathbf{L}'_{12}][\mathbf{Y}_4] \end{bmatrix} \begin{Bmatrix} \mathbf{S}_1 \\ \mathbf{S}_2 \\ \mathbf{S}_3 \\ \mathbf{S}_4 \end{Bmatrix} \quad (3-98)$$

$$+ \begin{bmatrix} \underline{([\mathbf{L}'_{11}] + [\mathbf{L}'_{12}][\mathbf{X}_{20}])} & 0 & 0 & 0 \\ 0 & \underline{([\mathbf{L}'_{11}] + [\mathbf{L}'_{12}][\mathbf{X}_{13}])} & 0 & 0 \\ 0 & 0 & ([\mathbf{L}'_{11}] + [\mathbf{L}'_{12}][\mathbf{X}_{18}]) & [\mathbf{L}'_{12}][\mathbf{X}_{19}] \\ 0 & 0 & [\mathbf{L}'_{12}][\mathbf{X}_{10}] & \underline{([\mathbf{L}'_{11}] + [\mathbf{L}'_{12}][\mathbf{X}_{11}])} \end{bmatrix} \begin{Bmatrix} \mathbf{u}_1 \\ \mathbf{u}_2 \\ \mathbf{u}_3 \\ \mathbf{u}_4 \end{Bmatrix}$$

Since in this case both $[\mathbf{X}_1]^{-1} (= [\mathbf{L}'_{22}]^{-1})$ and $[\mathbf{X}_3]^{-1} (= [\mathbf{L}'_{22}]^{-1})$ do not exist, $[\mathbf{Y}_6]$, $[\mathbf{Y}_{13}]$,

$[\mathbf{X}_{13}]$, and $[\mathbf{X}_{20}]$ are not defined. A simple treatment is to set all the underlined terms to

be zero.

(h) Integration points II, III, IV completely failed:

In this case, the displacement and equilibrium equations simplify to

$$\begin{Bmatrix} \mathbf{u}_{786} \\ \mathbf{u}_{58'7} \\ \mathbf{u}_{9A5'} \\ \mathbf{u}_{6'A'9} \end{Bmatrix} = \begin{bmatrix} [\mathbf{Y}_{13}] & 0 & 0 & [\mathbf{Y}_{16}] \\ 0 & \underline{[\mathbf{Y}_6]} & 0 & 0 \\ 0 & 0 & \underline{[\mathbf{Y}_{11}]} & 0 \\ [\mathbf{Y}_1] & 0 & 0 & [\mathbf{Y}_4] \end{bmatrix} \begin{Bmatrix} \mathbf{S}_1 \\ \mathbf{S}_2 \\ \mathbf{S}_3 \\ \mathbf{S}_4 \end{Bmatrix} + \begin{bmatrix} [\mathbf{X}_{20}] & 0 & 0 & [\mathbf{X}_{23}] \\ 0 & \underline{[\mathbf{X}_{13}]} & 0 & 0 \\ 0 & 0 & \underline{[\mathbf{X}_{18}]} & 0 \\ [\mathbf{X}_8] & 0 & 0 & [\mathbf{X}_{11}] \end{bmatrix} \begin{Bmatrix} \mathbf{u}_1 \\ \mathbf{u}_2 \\ \mathbf{u}_3 \\ \mathbf{u}_4 \end{Bmatrix} \quad (3-99)$$

$$\begin{Bmatrix} \mathbf{F}_1 \\ \mathbf{F}_2 \\ \mathbf{F}_3 \\ \mathbf{F}_4 \end{Bmatrix} = \begin{bmatrix} [\mathbf{L}'_{12}][\mathbf{Y}_{13}] & 0 & 0 & [\mathbf{L}'_{12}][\mathbf{Y}_{16}] \\ 0 & \underline{[\mathbf{L}'_{12}][\mathbf{Y}_6]} & 0 & 0 \\ 0 & 0 & \underline{[\mathbf{L}'_{12}][\mathbf{Y}_{11}]} & 0 \\ [\mathbf{L}'_{12}][\mathbf{Y}_1] & 0 & 0 & [\mathbf{L}'_{12}][\mathbf{Y}_4] \end{bmatrix} \begin{Bmatrix} \mathbf{S}_1 \\ \mathbf{S}_2 \\ \mathbf{S}_3 \\ \mathbf{S}_4 \end{Bmatrix} + \begin{bmatrix} ([\mathbf{L}'_{11}] + [\mathbf{L}'_{12}][\mathbf{X}_{20}]) & 0 & 0 & [\mathbf{L}'_{12}][\mathbf{X}_{23}] \\ 0 & \underline{([\mathbf{L}'_{11}] + [\mathbf{L}'_{12}][\mathbf{X}_{13}])} & 0 & 0 \\ 0 & 0 & \underline{([\mathbf{L}'_{11}] + [\mathbf{L}'_{12}][\mathbf{X}_{18}])} & 0 \\ [\mathbf{L}'_{12}][\mathbf{X}_8] & 0 & 0 & \underline{([\mathbf{L}'_{11}] + [\mathbf{L}'_{12}][\mathbf{X}_{11}])} \end{bmatrix} \begin{Bmatrix} \mathbf{u}_1 \\ \mathbf{u}_2 \\ \mathbf{u}_3 \\ \mathbf{u}_4 \end{Bmatrix} \quad (3-100)$$

Since in this case both $[\mathbf{X}_2]^{-1} (= [\mathbf{L}'_{22}]^{-1})$ and $[\mathbf{X}_3]^{-1} (= [\mathbf{L}'_{22}]^{-1})$ do not exist, $[\mathbf{Y}_6]$, $[\mathbf{Y}_{11}]$, $[\mathbf{X}_{13}]$, and $[\mathbf{X}_{18}]$ are not defined. A simple treatment is to set all the underlined terms to be zero.

(i) Integration points III, IV, I completely failed:

In this case, the displacement and equilibrium equations simplify to

$$\begin{Bmatrix} \mathbf{u}_{786} \\ \mathbf{u}_{58'7} \\ \mathbf{u}_{9A5'} \\ \mathbf{u}_{6'A'9} \end{Bmatrix} = \begin{bmatrix} \underline{[\mathbf{Y}_{13}]} & 0 & 0 & 0 \\ 0 & [\mathbf{Y}_6] & [\mathbf{Y}_7] & 0 \\ 0 & [\mathbf{Y}_{10}] & [\mathbf{Y}_{11}] & 0 \\ 0 & 0 & 0 & \underline{[\mathbf{Y}_4]} \end{bmatrix} \begin{Bmatrix} \mathbf{S}_1 \\ \mathbf{S}_2 \\ \mathbf{S}_3 \\ \mathbf{S}_4 \end{Bmatrix} + \begin{bmatrix} \underline{[\mathbf{X}_{20}]} & 0 & 0 & 0 \\ 0 & [\mathbf{X}_{13}] & [\mathbf{X}_{14}] & 0 \\ 0 & [\mathbf{X}_{17}] & [\mathbf{X}_{18}] & 0 \\ 0 & 0 & 0 & \underline{[\mathbf{X}_{11}]} \end{bmatrix} \begin{Bmatrix} \mathbf{u}_1 \\ \mathbf{u}_2 \\ \mathbf{u}_3 \\ \mathbf{u}_4 \end{Bmatrix} \quad (3-101)$$

$$\begin{Bmatrix} \mathbf{F}_1 \\ \mathbf{F}_2 \\ \mathbf{F}_3 \\ \mathbf{F}_4 \end{Bmatrix} = \begin{bmatrix} \underline{[\mathbf{L}'_{12}][\mathbf{Y}_{13}]} & 0 & 0 & 0 \\ 0 & \underline{[\mathbf{L}'_{12}][\mathbf{Y}_6]} & \underline{[\mathbf{L}'_{12}][\mathbf{Y}_7]} & 0 \\ 0 & \underline{[\mathbf{L}'_{12}][\mathbf{Y}_{10}]} & \underline{[\mathbf{L}'_{12}][\mathbf{Y}_{11}]} & 0 \\ 0 & 0 & 0 & \underline{[\mathbf{L}'_{12}][\mathbf{Y}_4]} \end{bmatrix} \begin{Bmatrix} \mathbf{S}_1 \\ \mathbf{S}_2 \\ \mathbf{S}_3 \\ \mathbf{S}_4 \end{Bmatrix} + \begin{bmatrix} \underline{([\mathbf{L}'_{11}] + [\mathbf{L}'_{12}][\mathbf{X}_{20}])} & 0 & 0 & 0 \\ 0 & \underline{([\mathbf{L}'_{11}] + [\mathbf{L}'_{12}][\mathbf{X}_{13}])} & \underline{[\mathbf{L}'_{12}][\mathbf{X}_{14}]} & 0 \\ 0 & \underline{[\mathbf{L}'_{12}][\mathbf{X}_{17}]} & \underline{([\mathbf{L}'_{11}] + [\mathbf{L}'_{12}][\mathbf{X}_{18}])} & 0 \\ 0 & 0 & 0 & \underline{([\mathbf{L}'_{11}] + [\mathbf{L}'_{12}][\mathbf{X}_{11}])} \end{bmatrix} \begin{Bmatrix} \mathbf{u}_1 \\ \mathbf{u}_2 \\ \mathbf{u}_3 \\ \mathbf{u}_4 \end{Bmatrix} \quad (3-102)$$

Since in this case both $[\mathbf{X}_1]^{-1} (= [\mathbf{L}'_{22}]^{-1})$ and $[\mathbf{X}_7]^{-1} (= [\mathbf{L}'_{22}]^{-1})$ do not exist, $[\mathbf{Y}_4]$, $[\mathbf{Y}_{13}]$, $[\mathbf{X}_{11}]$, and $[\mathbf{X}_{20}]$ are not defined. A simple treatment is to set all the underline terms to be zero.

(j) Integration points IV, I, II completely failed:

In this case, the displacement and equilibrium equations simplify to

$$\begin{Bmatrix} \mathbf{u}_{786} \\ \mathbf{u}_{58'7} \\ \mathbf{u}_{9A5'} \\ \mathbf{u}_{6'A'9'} \end{Bmatrix} = \begin{bmatrix} [\mathbf{Y}_{13}] & [\mathbf{Y}_{14}] & 0 & 0 \\ [\mathbf{Y}_5] & [\mathbf{Y}_6] & 0 & 0 \\ 0 & 0 & \underline{[\mathbf{Y}_{11}]} & 0 \\ 0 & 0 & 0 & \underline{[\mathbf{Y}_4]} \end{bmatrix} \begin{Bmatrix} \mathbf{S}_1 \\ \mathbf{S}_2 \\ \mathbf{S}_3 \\ \mathbf{S}_4 \end{Bmatrix} + \begin{bmatrix} [\mathbf{X}_{20}] & [\mathbf{X}_{21}] & 0 & 0 \\ [\mathbf{X}_{12}] & [\mathbf{X}_{13}] & 0 & 0 \\ 0 & 0 & \underline{[\mathbf{X}_{18}]} & 0 \\ 0 & 0 & 0 & \underline{[\mathbf{X}_{11}]} \end{bmatrix} \begin{Bmatrix} \mathbf{u}_1 \\ \mathbf{u}_2 \\ \mathbf{u}_3 \\ \mathbf{u}_4 \end{Bmatrix} \quad (3-103)$$

$$\begin{Bmatrix} \mathbf{F}_1 \\ \mathbf{F}_2 \\ \mathbf{F}_3 \\ \mathbf{F}_4 \end{Bmatrix} = \begin{bmatrix} \underline{[\mathbf{L}'_{12}][\mathbf{Y}_{13}]} & \underline{[\mathbf{L}'_{12}][\mathbf{Y}_{14}]} & 0 & 0 \\ \underline{[\mathbf{L}'_{12}][\mathbf{Y}_5]} & \underline{[\mathbf{L}'_{12}][\mathbf{Y}_6]} & 0 & 0 \\ 0 & 0 & \underline{[\mathbf{L}'_{12}][\mathbf{Y}_{11}]} & 0 \\ 0 & 0 & 0 & \underline{[\mathbf{L}'_{12}][\mathbf{Y}_4]} \end{bmatrix} \begin{Bmatrix} \mathbf{S}_1 \\ \mathbf{S}_2 \\ \mathbf{S}_3 \\ \mathbf{S}_4 \end{Bmatrix} + \begin{bmatrix} \underline{([\mathbf{L}'_{11}] + [\mathbf{L}'_{12}][\mathbf{X}_{20}])} & \underline{[\mathbf{L}'_{12}][\mathbf{X}_{21}]} & 0 & 0 \\ \underline{[\mathbf{L}'_{12}][\mathbf{X}_{12}]} & \underline{([\mathbf{L}'_{11}] + [\mathbf{L}'_{12}][\mathbf{X}_{13}])} & 0 & 0 \\ 0 & 0 & \underline{([\mathbf{L}'_{11}] + [\mathbf{L}'_{12}][\mathbf{X}_{18}])} & 0 \\ 0 & 0 & 0 & \underline{([\mathbf{L}'_{11}] + [\mathbf{L}'_{12}][\mathbf{X}_{11}])} \end{bmatrix} \begin{Bmatrix} \mathbf{u}_1 \\ \mathbf{u}_2 \\ \mathbf{u}_3 \\ \mathbf{u}_4 \end{Bmatrix} \quad (3-104)$$

Since in this case both $[\mathbf{X}_2]^{-1}(=[\mathbf{L}'_{22}]^{-1})$ and $[\mathbf{X}_7]^{-1}(=[\mathbf{L}'_{22}]^{-1})$ do not exist, $[\mathbf{Y}_4]$, $[\mathbf{Y}_{11}]$, $[\mathbf{X}_{11}]$, and $[\mathbf{X}_{18}]$ are not defined. A simple treatment is to set all the underlined terms to be zero.

(k) Integration points I, II, III, IV completely failed:

In this case, all $\{\mathbf{S}_i\} = 0$ ($i = 1, 2, 3, 4$) are zero and all the external displacements are indeterminate at elemental level. The equations reduce to

$$\begin{Bmatrix} \mathbf{u}_{786} \\ \mathbf{u}_{587'} \\ \mathbf{u}_{9A5'} \\ \mathbf{u}_{6'A9'} \end{Bmatrix} = \begin{bmatrix} \underline{[\mathbf{X}_{20}]} & 0 & 0 & 0 \\ 0 & \underline{[\mathbf{X}_{13}]} & 0 & 0 \\ 0 & 0 & \underline{[\mathbf{X}_{18}]} & 0 \\ 0 & 0 & 0 & \underline{[\mathbf{X}_{11}]} \end{bmatrix} \begin{Bmatrix} \mathbf{u}_1 \\ \mathbf{u}_2 \\ \mathbf{u}_3 \\ \mathbf{u}_4 \end{Bmatrix} \quad (3-105)$$

$$\begin{Bmatrix} \mathbf{F}_1 \\ \mathbf{F}_2 \\ \mathbf{F}_3 \\ \mathbf{F}_4 \end{Bmatrix} = \begin{bmatrix} (\underline{[\mathbf{L}'_{11}]} + \underline{[\mathbf{L}'_{12}]}[\underline{[\mathbf{X}_{20}]}]) & 0 & 0 & 0 \\ 0 & (\underline{[\mathbf{L}'_{11}]} + \underline{[\mathbf{L}'_{12}]}[\underline{[\mathbf{X}_{13}]}]) & 0 & 0 \\ 0 & 0 & (\underline{[\mathbf{L}'_{11}]} + \underline{[\mathbf{L}'_{12}]}[\underline{[\mathbf{X}_{18}]}]) & 0 \\ 0 & 0 & 0 & (\underline{[\mathbf{L}'_{11}]} + \underline{[\mathbf{L}'_{12}]}[\underline{[\mathbf{X}_{11}]}]) \end{bmatrix} \begin{Bmatrix} \mathbf{u}_1 \\ \mathbf{u}_2 \\ \mathbf{u}_3 \\ \mathbf{u}_4 \end{Bmatrix} \quad (3-106)$$

The numerical singularity can be avoided by setting all the underlined terms to be zero.

3.6 Elemental Condensation Algorithm

In previous sections, the elemental equilibrium equations for multi-crack configurations have been derived in detail. However, as discussed in chapter 2 for single-crack case, these nonlinear equations have yet to be solved. Such as the single-crack case, the crack displacements as explicit functions of external displacements are not readily available. However, the solving procedure presented for single crack case, remains applicable in solving the multi-crack problems. For instance, consider Eqn (3-16) which expresses

crack displacements in terms of external displacements for configuration 1. The equation is repeated below with superscripts added to emphasize the dependence of \mathbf{X}_p ($p=1,2,\dots,15$), \mathbf{Y}_q ($q=1,2,\dots,9$) and \mathbf{S}_r ($r=1,2,3$) on the cohesive segment combination (i, j, k, l, m, n).

$$\begin{Bmatrix} \mathbf{u}_{6'5'} \\ \mathbf{u}_{786} \\ \mathbf{u}_{58'7'} \end{Bmatrix} = \left(\begin{bmatrix} [\mathbf{Y}_7] & [\mathbf{Y}_8] & [\mathbf{Y}_9] \\ [\mathbf{Y}_4] & [\mathbf{Y}_5] & [\mathbf{Y}_6] \\ [\mathbf{Y}_1] & [\mathbf{Y}_2] & [\mathbf{Y}_3] \end{bmatrix} \begin{Bmatrix} \mathbf{S}_1 \\ \mathbf{S}_2 \\ \mathbf{S}_3 \end{Bmatrix} \right)^{(i,j,k,l,m,n)} + \begin{bmatrix} [\mathbf{X}_{13}] & [\mathbf{X}_{14}] & [\mathbf{X}_{15}] \\ [\mathbf{X}_{10}] & [\mathbf{X}_{11}] & [\mathbf{X}_{12}] \\ [\mathbf{X}_7] & [\mathbf{X}_8] & [\mathbf{X}_9] \end{bmatrix}^{(i,j,k,l,m,n)} \begin{Bmatrix} \mathbf{u}_{12} \\ \mathbf{u}_3 \\ \mathbf{u}_4 \end{Bmatrix} \quad (3-107)$$

For the trial cohesive segment combination (i, j, k, l, m, n) and given external nodal displacements, a set of solution to the internal nodal displacements $\mathbf{u}_{6'5'} = \{\mathbf{u}_{6'}, \mathbf{u}_{5'}\}^T$, $\mathbf{u}_{786} = \{\mathbf{u}_7, \mathbf{u}_8, \mathbf{u}_6\}^T$ and $\mathbf{u}_{58'7'} = \{\mathbf{u}_5, \mathbf{u}_{8'}, \mathbf{u}_{7'}\}^T$, is immediately solved from Eqn (3-107).

Then, the crack displacements at the integration points of each segment (points I, II and III in Figure 3-2) are computed and converted to local coordinates, i. e.,

$$\begin{aligned} \{\delta_{sI}, \delta_{nI}\}^T &= \mathbf{R}_1^T \left((1-\gamma/2)\mathbf{u}_{6'} + (\gamma/2)\mathbf{u}_{5'} - (\mathbf{u}_6 + \mathbf{u}_8)/2 \right)^{(i,j,k,l,m,n)} \\ \{\delta_{sII}, \delta_{nII}\}^T &= \mathbf{R}_1^T \left((1-\gamma/2)\mathbf{u}_{6'} + (1+\gamma)/2\mathbf{u}_{5'} - (\mathbf{u}_5 + \mathbf{u}_{8'})/2 \right)^{(i,j,k,l,m,n)} \\ \{\delta_{sIII}, \delta_{nIII}\}^T &= \mathbf{R}_2^T \left((\mathbf{u}_{7'} + \mathbf{u}_{8'})/2 - (\mathbf{u}_7 + \mathbf{u}_8)/2 \right)^{(i,j,k,l,m,n)} \end{aligned} \quad (3-108)$$

The local crack displacements are then subjected to a consistency check similar to the single-crack case and the exact solution is found when the following statement is true:

$$\begin{aligned} & \left(\delta_{sI} \in \Delta\delta_s^{(i)} \text{ true} \right) \& \& \left(\delta_{nI} \in \Delta\delta_n^{(j)} \text{ true} \right) \& \& \left(\delta_{sII} \in \Delta\delta_s^{(k)} \text{ true} \right) \& \& \left(\delta_{nII} \in \Delta\delta_n^{(l)} \text{ true} \right) \\ & \& \& \left(\delta_{sIII} \in \Delta\delta_s^{(m)} \text{ true} \right) \& \& \left(\delta_{nIII} \in \Delta\delta_n^{(n)} \text{ true} \right) \end{aligned}$$

Once the solution is found, \mathbf{X}_p ($p=1,2,\dots,15$), \mathbf{Y}_q ($q=1,2,\dots,9$) and \mathbf{S}_r ($r=1,2,3$) are all established with determined (i, j, k, l, m, n). Substituting them into Eqn (3-17), the fully

condensed elemental equilibrium is then satisfied with mathematical exactness (in piecewise linear sense and within the limit of FE discretization accuracy).

Following the flowchart in Figure 2-8, the A-FEM and solving procedure for multi-crack cases can be integrated into any standard FE programs as a general purposed element because the elemental locality is completely retained.

3.7 Single Element Validation

After formulating the A-FEM method for multi-crack configurations, this section is to verify the formulation by testing a single augmented element under various loading conditions. Displacement-controlled loading is used here to achieve mode I, II and mixed mode loading conditions. The element is assigned a very large modulus so that the responses are primarily from the cohesive law. The element is 2-mm long and 2-mm high and, based on desired configurations, two or three discontinuities are assigned. The cohesive law is triangular with $\hat{\sigma} = \hat{\tau} = 1$ MPa, $\delta_{nc} = \delta_{sc} = 0.1$ mm. The initial slopes are $\alpha_{n1} = \alpha_{s1} = 10^7$ N/(mm)³, and the slopes in the softening phases are $\alpha_{n2} = \alpha_{s2} = -10$ N/(mm)³. Therefore, the mode I and mode II toughnesses are $\Gamma_I = \Gamma_{II} = 0.05$ N/mm (50 J/m²).

In each case, the single A-FEM results are compared with ABAQUS results obtained using a combination of regular elements (CPS4) for subdomains, and cohesive elements (COH2D4) with zero thickness to consider the cracks between different domains. In some cases the predicted peak loads are compared with analytical results to verify the A-FEM results.

3.7.1 Mode I Response (Configurations 1 & 2)

As a first verification test, consider an element which is cut into a triangular, a rectangular and a pentagonal domain as shown in Figure 3-6. By displacing node 4 vertically one can have mode I loading. The load-displacement curve in Figure 3-6 shows how the element with two cracks behaves and the results from the A-FEM and ABAQUS are identical. Similar to single crack case, the peak load can be obtained by considering FBD analysis. The horizontal crack length is 1 mm, so the peak load is 1N, which is predicted correctly by the A-FEM and the ABAQUS. The predicted deformed shapes by the A-FEM and ABAQUS are shown in Figure 3-7.

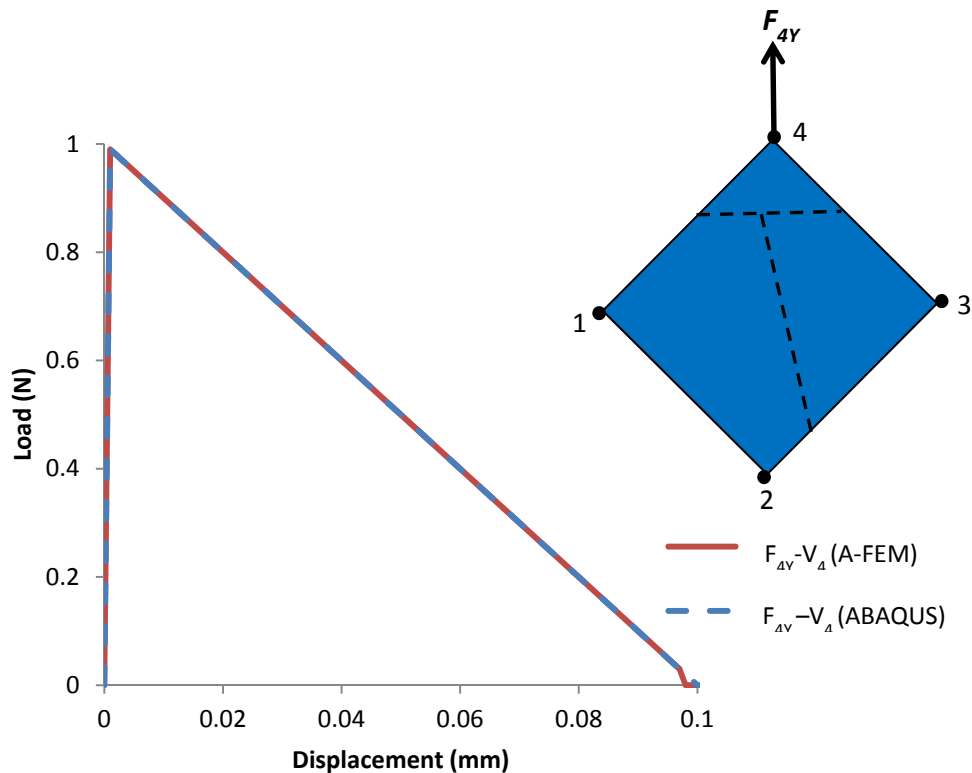


Figure 3-6 Single A-FE response with two cracks under mode I loading conditions for configurations 1 & 2

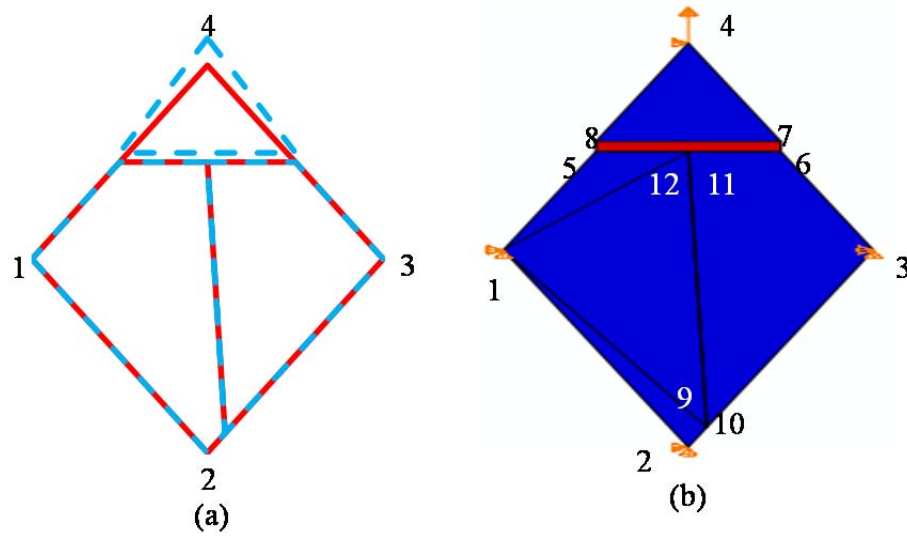


Figure 3-7 (a) Deformed shape from A-FEM, (b) from ABAQUS

Although the load-displacement curves and the deformed shapes are identical from two methods, it should be noticed that ABAQUS used 7 elements to obtain the same results as obtained by the single A-FEM. Other than using three cohesive elements, ABAQUS computes the stiffness matrix of pentagon by the traditional triangulization method. In the A-FEM method, the direct integration method of polygonal FEM as explained in Appendix C is used to compute the stiffness matrix for the pentagon.

3.7.2 Mixed Mode (Configuration 1 & 2)

In the previous configuration, by displacing node 4 vertically, pure mode I can occur because displacement is in the opening mode. However, because of the cracking geometry, pure mode II is not achievable because by imposing F_{4X} the triangular domain rotates, leading to mixed mode loading.

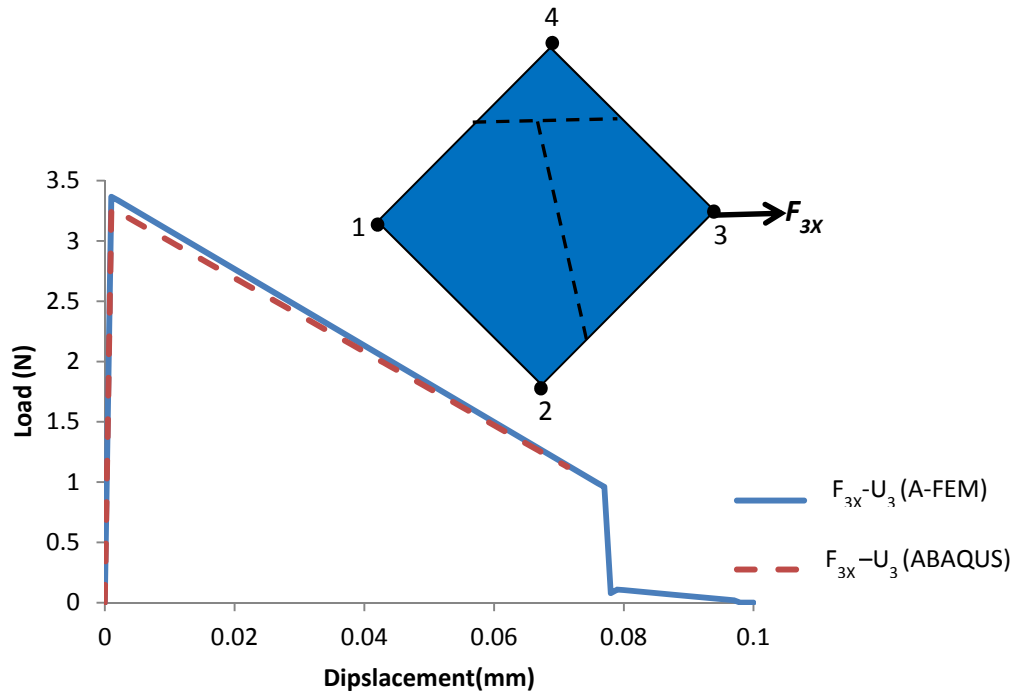


Figure 3-8 Single A-FE response with two cracks under mixed mode loading conditions for configurations 1 & 2

So in this case by displacing node 3 in the horizontal direction, we study the behavior. The load-displacement results for displaced node 3 from A-FEM and ABAQUS are compared together in Figure 3-8. They show similar behavior initially but ABAQUS could not finish the job and stopped before complete failure. Similar to previous case, the peak load predicted from ABAQUS and A-FEM are consistent with the analytical results of $F_{3X} = 3.3$ N.

The deformed shapes from two methods as shown in Figure 3-9 are consistent.

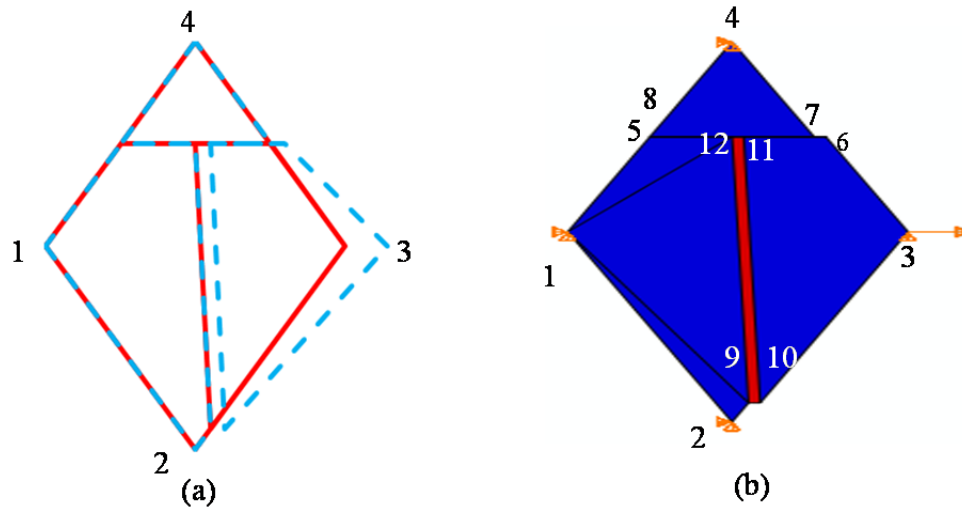


Figure 3-9 (a) Deformed shape from A-FEM, (b) from ABAQUS

Note that in this case, ABAQUS with 7 elements was not able to finish the job but A-FEM did it with only one element smoothly. The kink in the load-displacement curve is due to failure of one of the integration points, after that it continues to complete failure.

3.7.3 Mode I (configuration 3)

To verify the A-FEM for configuration 3, the numerical model in the inset of Figure 3-10 was used. Assume that two cracks cut a rectangular element to three rectangular domains. By displacing nodes 3 and 4 vertically, mode I loading can be achieved. The load-displacement in Figure 3-10 shows identical results from the A-FEM and ABAQUS. The predicted peak load also agrees well with the FBD analysis.

The predicted deformed shapes from the two methods agree with each other as shown in Figure 3-11.

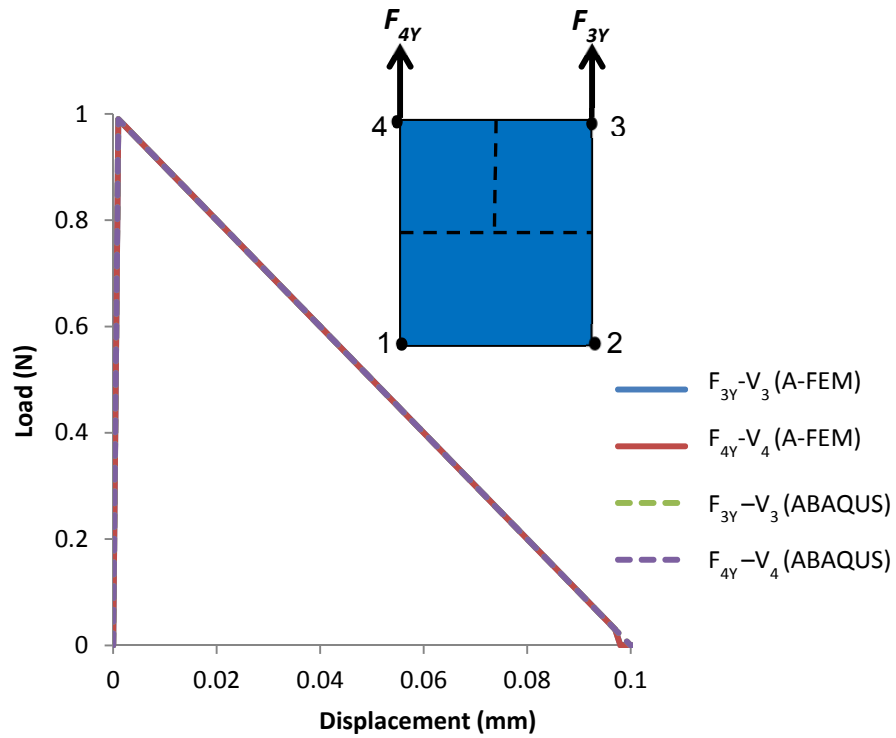


Figure 3-10 Single A-FE response with two cracks under mode I loading for configuration 3

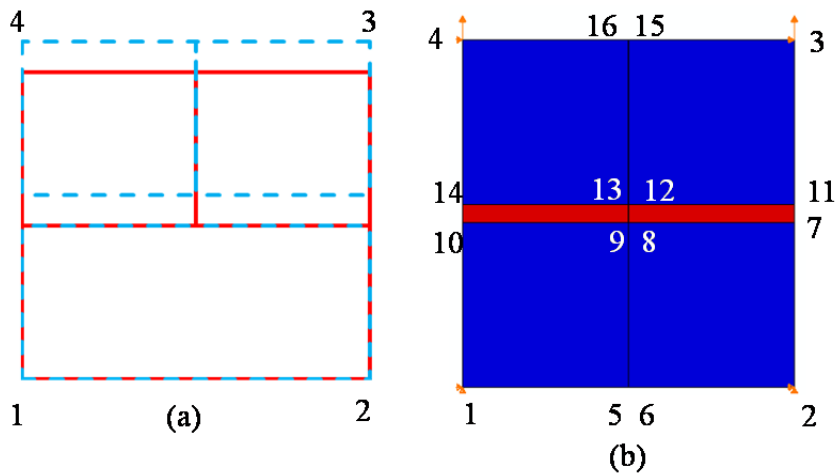


Figure 3-11 Deformed shape from A-FEM, (b) Deformed shape from ABAQUS for configuration 3, mode I

Although ABAQUS gives the same results as A-FEM, it requires 7 elements to obtain the results but A-FEM solves the problem with just one element.

3.7.4 Mode II (Configuration 3)

By displacing nodes 3 and 4 in horizontal direction, the mode II response can be evaluated. For this configuration, one can plot total load as a function of total displacement on the top edge from ABAQUS and A-FEM. It can be seen from Figure 3-12 that the A-FEM and ABAQUS results are identical but ABAQUS needs 7 elements to solve the problem, while the A-FEM needs only one element. The predicted deformed shape from the A-FEM and ABAQUS are also similar as seen in Figure 3-13.

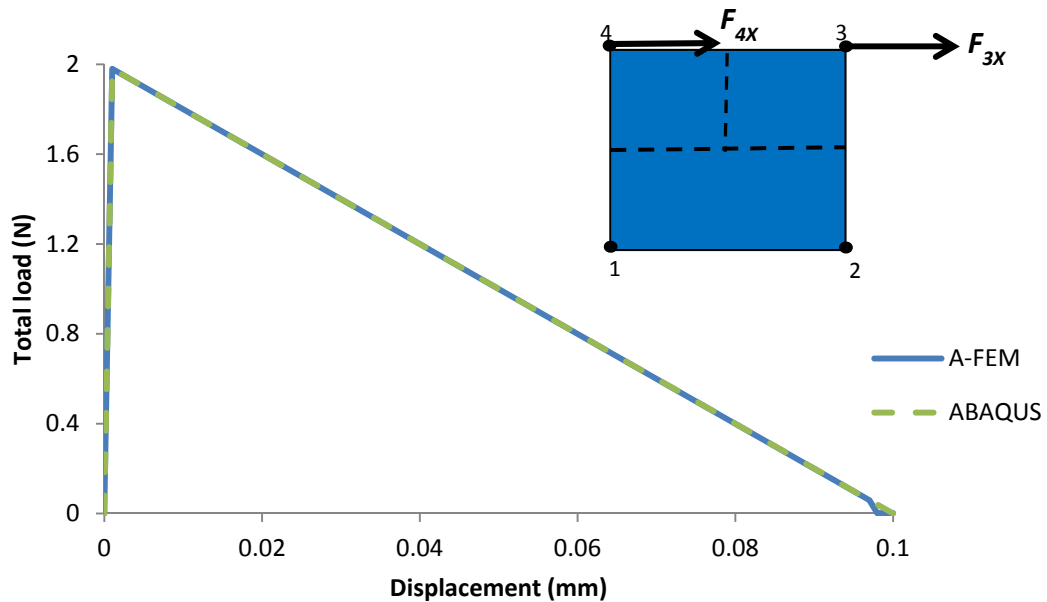


Figure 3-12 Single A-FE response with two cracks under mode II loading conditions for configuration 3

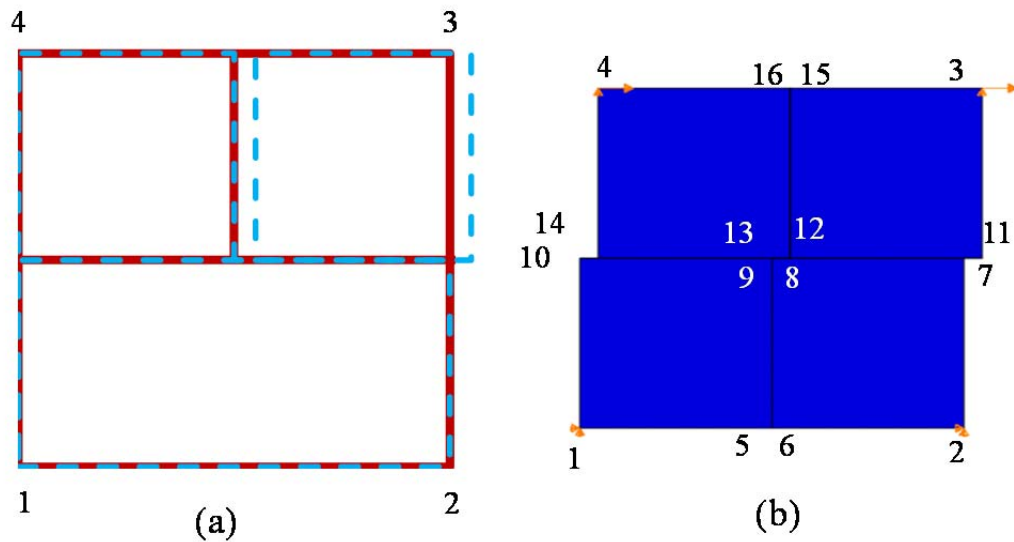


Figure 3-13 (a) Deformed shape from A-FEM, (b) Deformed shape from ABAQUS for configuration 3, mode II

3.7.5 Wedge Opening (configuration 3)

The last case in verifying two crack configurations can be the wedge opening problem. Assume that nodes 3 and 4 are displaced horizontally in opposite directions; the predicted load-displacement curves are shown in Figure 3-14.

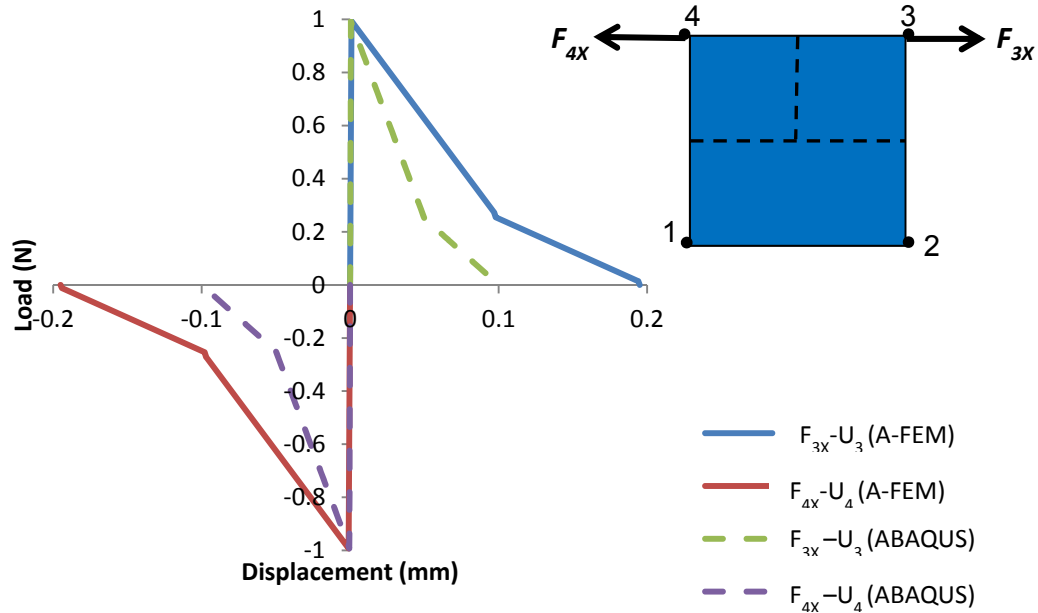


Figure 3-14 Single A-FE response with two cracks under wedge opening loading conditions for configuration 3

It can be seen from Figure 3-14 that the A-FEM and ABAQUS results are quite different. Both A-FEM and ABAQUS predict the correct peak load, and the results in elastic stage are identical. The difference in the post-peak response is due to the difference in cohesive stress integration schemes used in A-FEM and in ABAQUS. ABAQUS uses Newton-Cotes integration scheme, with elemental nodes being the integration points. Thus, nodal stresses are used for elemental stress integration. If one node is failed (for instance 15 or 16 in Figure 3-15(b)) and the other node is never failed (wedge opening as shown in Figure 3-15(a)), both nodes have zero stress. This leads to premature failure prediction. In the A-FEM, Gaussian quadrature integration scheme is used. Integration points are located between nodes so stresses at these integration points are not zero, even if the nodal stresses are zero. The Gaussian integration scheme is much more accurate in this case [261].

The predicted deformed shapes from A-FEM and ABAQUS are also shown in Figure 3-15. These are consistent to each other.

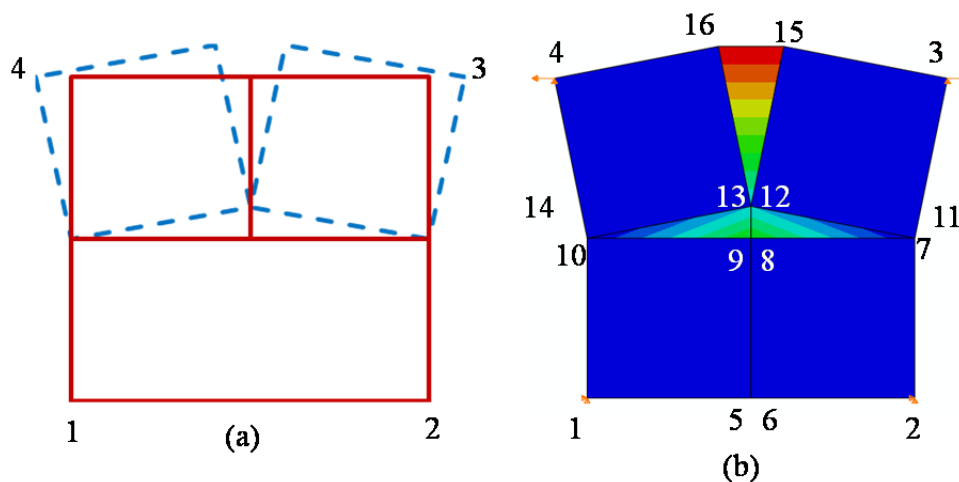


Figure 3-15 (a) Deformed shape from A-FEM, (b) Deformed shape from ABAQUS for configuration 3, wedge opening

3.7.6 Mode I (configuration 4)

After verifying configurations with two cracks, this section studies the response of the A-FEM with three cracks. We start by displacing nodes 2 and 3 in horizontal direction to test the configuration. As shown in Figure 3-16, ABAQUS and A-FEM predict similar peak loads but different post-peak behavior. ABAQUS predicts that all four crack segments are active, leading to a larger energy release rate, which is almost two times than that of A-FEM. The A-FEM predicts the opening of two vertical cracks. By simple load equilibrium it can be found that the predicted peak load is correct. The opening of two horizontal cracks predicted by ABAQUS is due to loading elements rotation. Recall that in the ABAQUS model, in addition to the external nodes 2 and 3, there are two more external nodes 7 and 11. If these external nodes are also loaded, the deformation and

load-displacement curve should conform to the A-FEM results. This is shown in Figure 3-18 and Figure 3-19. Consider that the total load on the right edge is plotted.

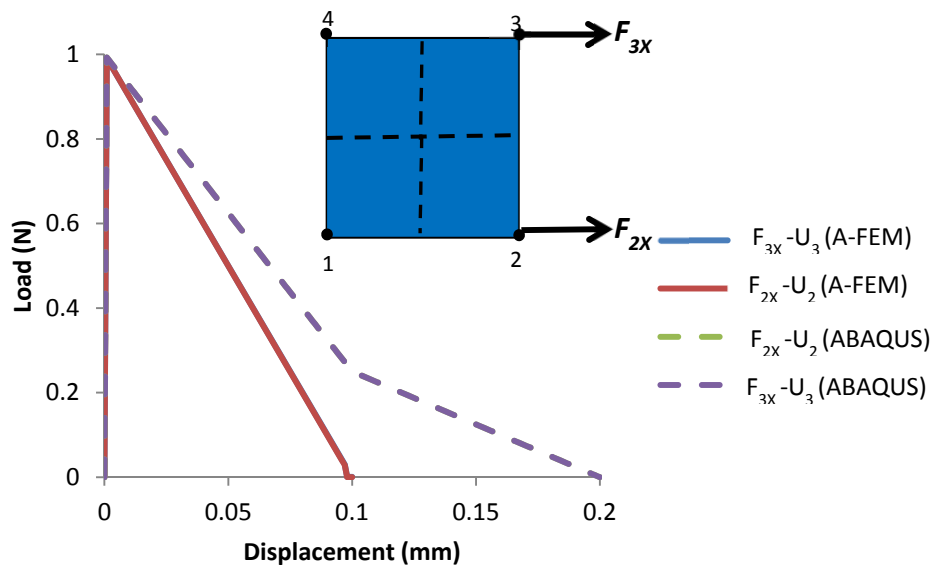


Figure 3-16 Single A-FE response with three cracks under mode I loading conditions for configuration 4

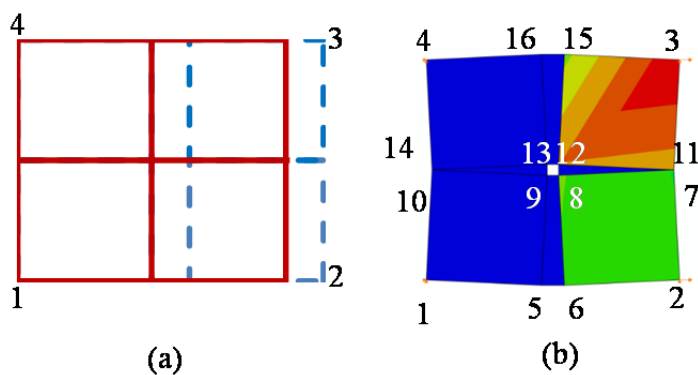


Figure 3-17 (a) Deformed shape from A-FEM, (b) Deformed shape from ABAQUS for configuration 4, mode I

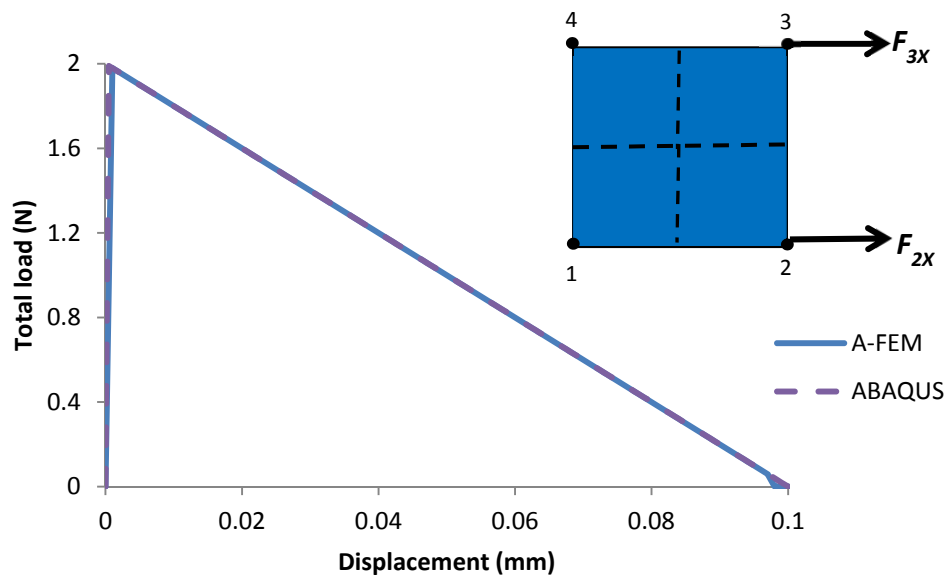


Figure 3-18 Single A-FE response with three cracks under mode I loading conditions for configuration 4 by displacing two middle nodes on the right edge

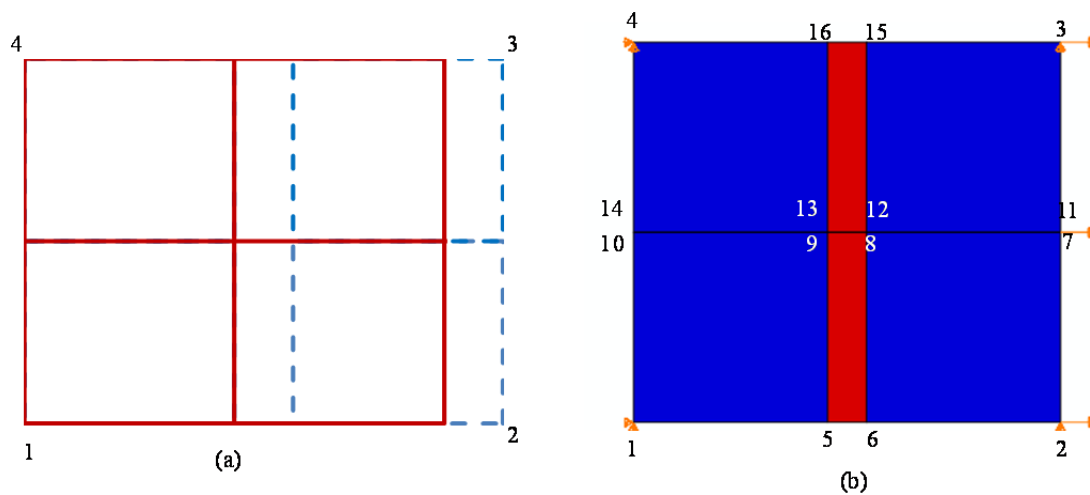


Figure 3-19 Deformed shape from A-FEM, (b) Deformed shape from ABAQUS for configuration 4, mode I by displacing four nodes in ABAQUS

3.7.7 Mode II (configuration 4)

By moving nodes 3 and 4 in horizontal and same direction we can test mode II displacement. As shown in Figure 3-20, ABAQUS and A-FEM predict identical load-

displacement curves. The peak loads from both methods are verified by FBD evaluation of the failed portion. The deformed shapes from ABAQUS and A-FEM are also seen in Figure 3-21.

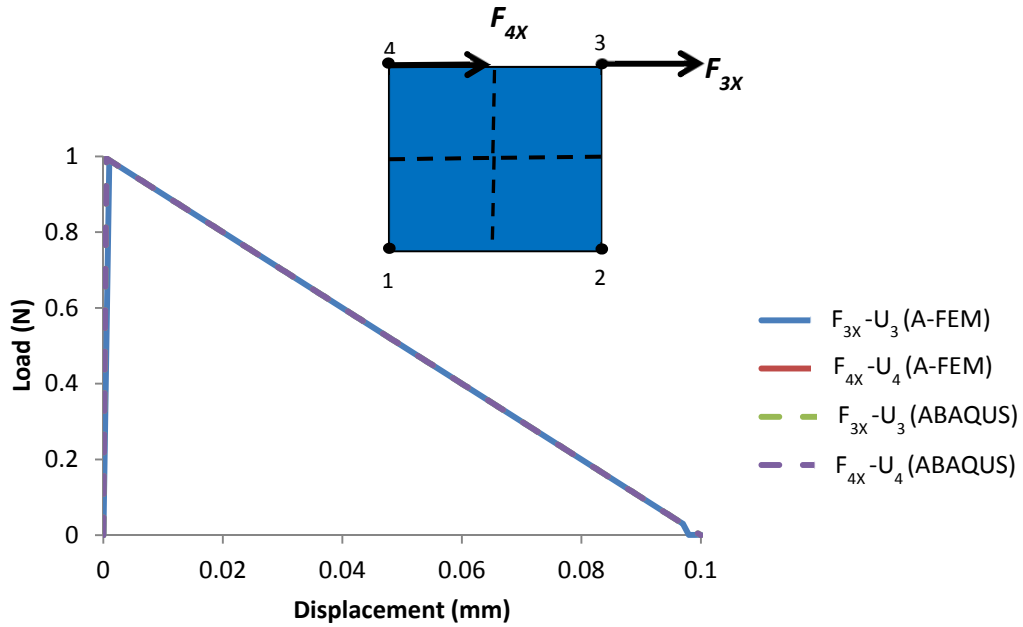


Figure 3-20 Single A-FE response with three cracks under mode II loading conditions for configuration 4

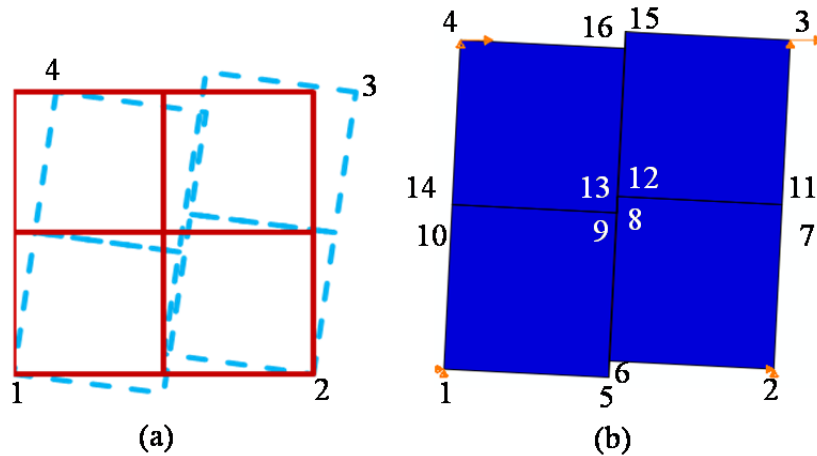


Figure 3-21 Deformed shape from A-FEM, (b) Deformed shape from ABAQUS for configuration 4 under mode II displacement

3.7.8 Wedge opening (configuration 4)

Such as in one and two crack configurations, wedge opening displacement is an important case that needs to be tested. Assume nodes 3 and 4 are displaced in horizontal and opposite directions, this can lead to wedge opening mode. Load-displacement curves in Figure 3-22 show that both methods predict the same elastic stage but ABAQUS predicts larger energy release rate. Such as previous cases we can compare the predicted deformed shapes from two methods in Figure 3-23.

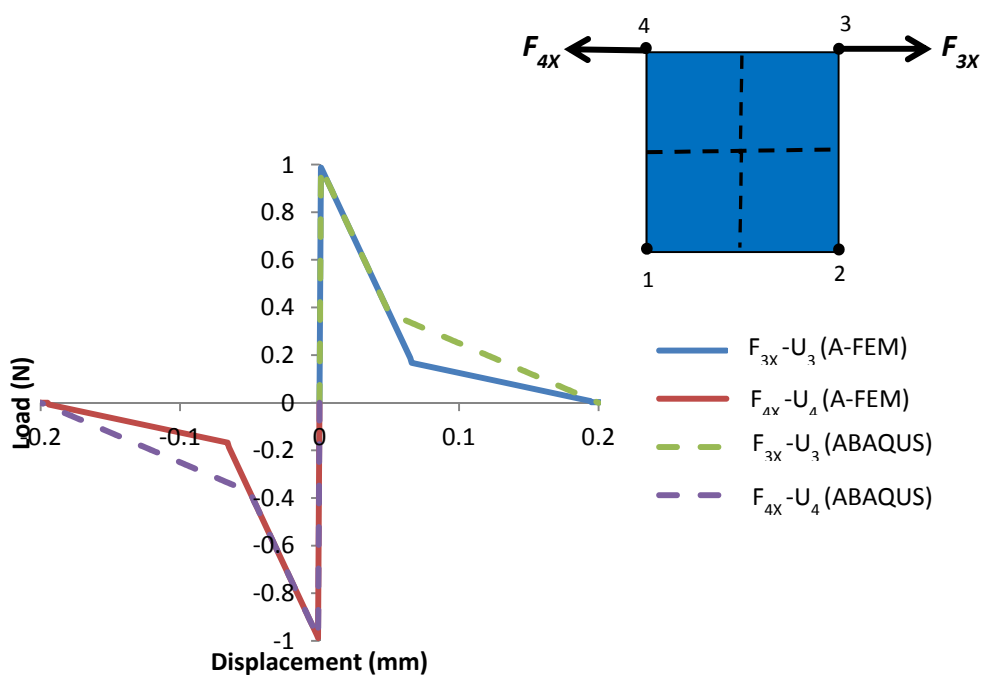


Figure 3-22 Single A-FE response with three cracks under wedge opening loading conditions for configuration 4

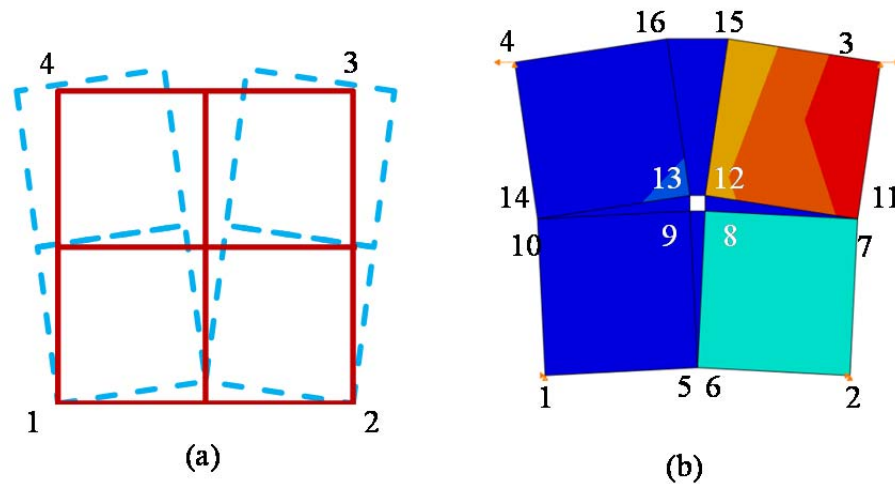


Figure 3-23 Deformed shape from A-FEM, (b) Deformed shape from ABAQUS for configuration 4 under wedge opening displacement

Figure 3-23 shows that in ABAQUS results, horizontal crack will slightly open while in reality in wedge opening mode it should not behave in this way, this is the reason why ABAQUS predicts larger energy release rate than A-FEM.

3.7.9 One corner loading (configuration 4)

As the last test, we study the behavior of an element with three cracks under one corner loading. By displacing node 3 in vertical direction, the top right domain will be separated from the other domains and the load-displacement curves from A-FEM and ABAQUS can be seen in Figure 3-24. ABAQUS could not finish the job and aborted shortly after the peak load is achieved. The A-FEM can model the problem to the final failure point. The peak load predicted from ABAQUS is also smaller than that of A-FEM. However, a FBD evaluation of the top right block shows that the A-FEM predicts peak load accurately.

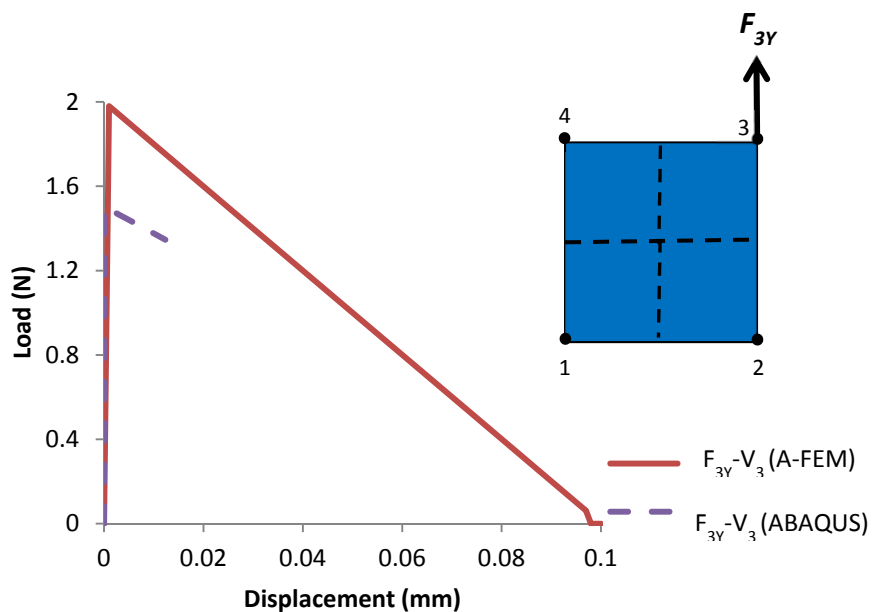


Figure 3-24 Single A-FE response with three cracks under one corner loading conditions for configuration 4

The predicted deformed shapes from ABAQUS and A-FEM also are seen in Figure 3-25.

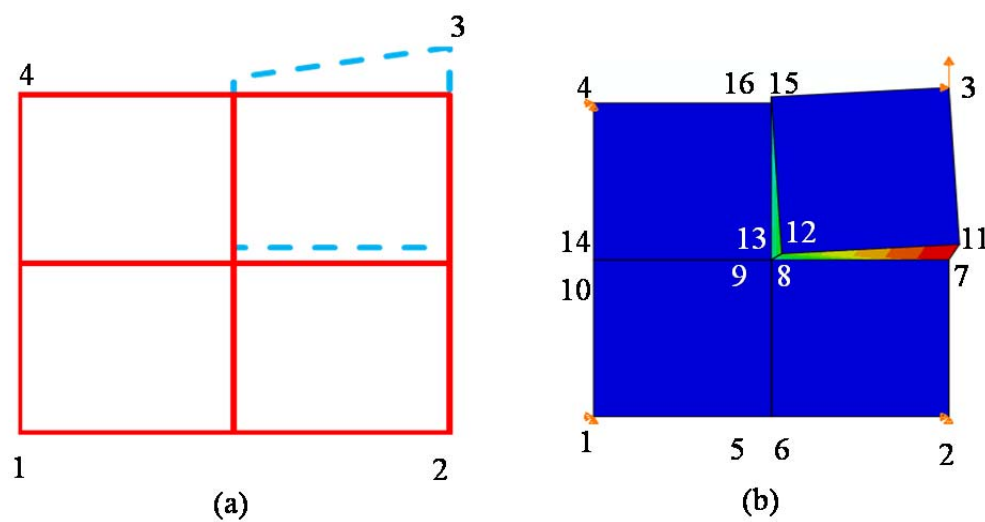


Figure 3-25 (a) Deformed shape from A-FEM, (b) Deformed shape from ABAQUS for configuration 4, one corner loading

3.8 Summary

In this chapter, after deriving the formulation and basic concepts of augmenting elements, the novel A-FEM has been developed to consider multiple crack cases. Demonstrated by the single crack case, the solution procedure includes addition of internal nodes to describe the displacement discontinuities. Then a condensation procedure is developed to delete the DoFs associated with the internal nodes. There is no need to know the crack path *a priori*. The A-FEM for multiple cracks has been implemented into a standard FEM package using the algorithm discussed in chapter 2. Single element validation tests were performed to verify the A-FEM for basic cases. All the validations showed that the A-FEM method with only one element and without any additional DoFs or nodes can predict the fracture behavior better than standard FEM performed with ABAQUS. Despite ABAQUS using more elements to simulate the single element fracture, in several cases it was not able to capture the correct response.

Chapter 4: Numerical Examples

4.1. Shear Test of a Precracked Short Beam

In this section, we test the A-FEM's capability in simulating the crack propagation in a widely used shear test, as shown in the below figure:

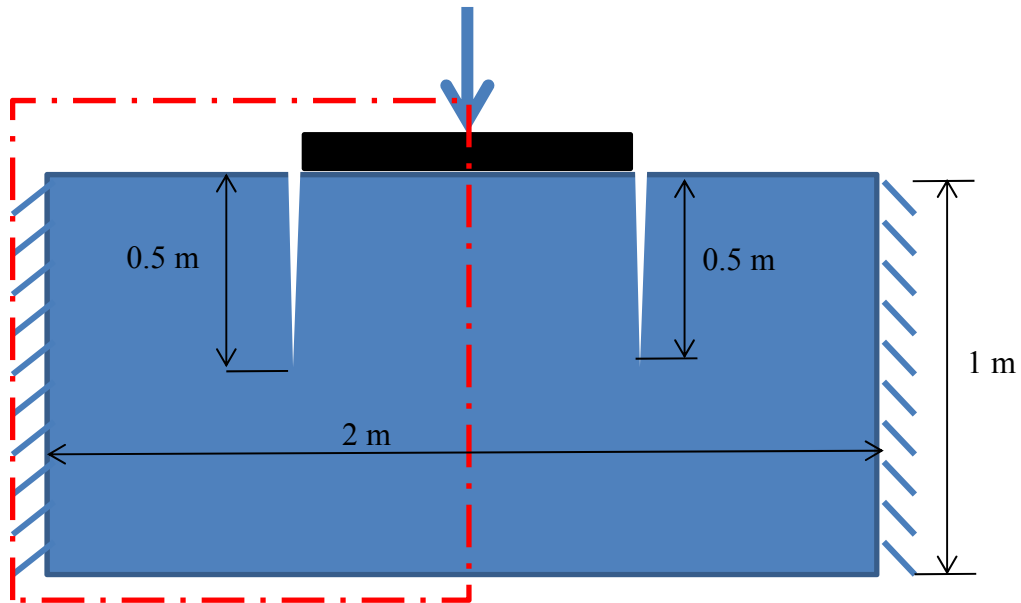


Figure 4-1 Precracked short beam

The short beam is 2 meters (2000 mm) long and 1 m (1000 mm) high and both ends are fixed. Two precracks, each of length 0.5 m, are located 0.5 m away from the respective fixed edges. The specimen is loaded with displacement-controlled transverse load in the center region. Due to symmetry, only half of the specimen shown in the dashed box in Figure 4-1 is modeled.

Maximum principal stress criterion is used for crack initiation. That is, crack initiation from a pristine elastic element occurs when the maximum principal stress averaged within the element ($\bar{\sigma}_{\max}$), reaches the mode I cohesive strength ($\hat{\sigma}$). The crack path is perpendicular to the maximum principal stress direction. The elastic material properties are $E = 30$ GPa, $\nu = 0.3$ and the cohesive law is a triangular one with the mode I cohesive fracture properties of $\Gamma_1 = 0.1$ N/mm (100 J/m²), and $\hat{\sigma} = 3.0$ MPa. These properties are typical of concretes.

4.1.1 Mesh Sensitivity

At first, the mesh sensitivity of the new A-FEM method will be tested. The simulation domain of 1000 mm \times 1000 mm is discretized into four different meshes (i) $11 \times 10 = 110$ elements (i.e., mesh size $h \sim 100$ mm); (ii) $21 \times 20 = 420$ elements ($h \sim 50$ mm); (iii) $51 \times 50 = 2550$ elements ($h \sim 20$ mm); and (iv) $101 \times 100 = 10,100$ elements ($h \sim 10$ mm). From mesh (i) to (iv) the mesh size decreases by a factor of 10.

The simulated load-displacement curves with the four meshes are plotted in Figure 4-2. For each case, the load linearly increases with displacement until crack initiation from the precrack tip, which occurs at an applied displacement of ~ 0.09 mm. After initiation the load-displacement curve becomes increasingly nonlinear due to crack growth. The peak load is reached at the displacement of about 0.15 mm. The peak load corresponds to the full establishment of the cohesive zone, which is about 150 mm ($\sim E\Gamma_1 / 2\hat{\sigma}^2$) in this test. A rapid decreasing phase following the peak load is seen for each case, which is due to fast crack growth (a near steady-state propagation) after the cohesive zone is fully

established. However, as the crack reaches the fixed boundary (left edge), the load increases again due to further bending of the severed domain below the crack trajectory.

The crack trajectories predicted by the four simulations are summarized in Figure 4-3.

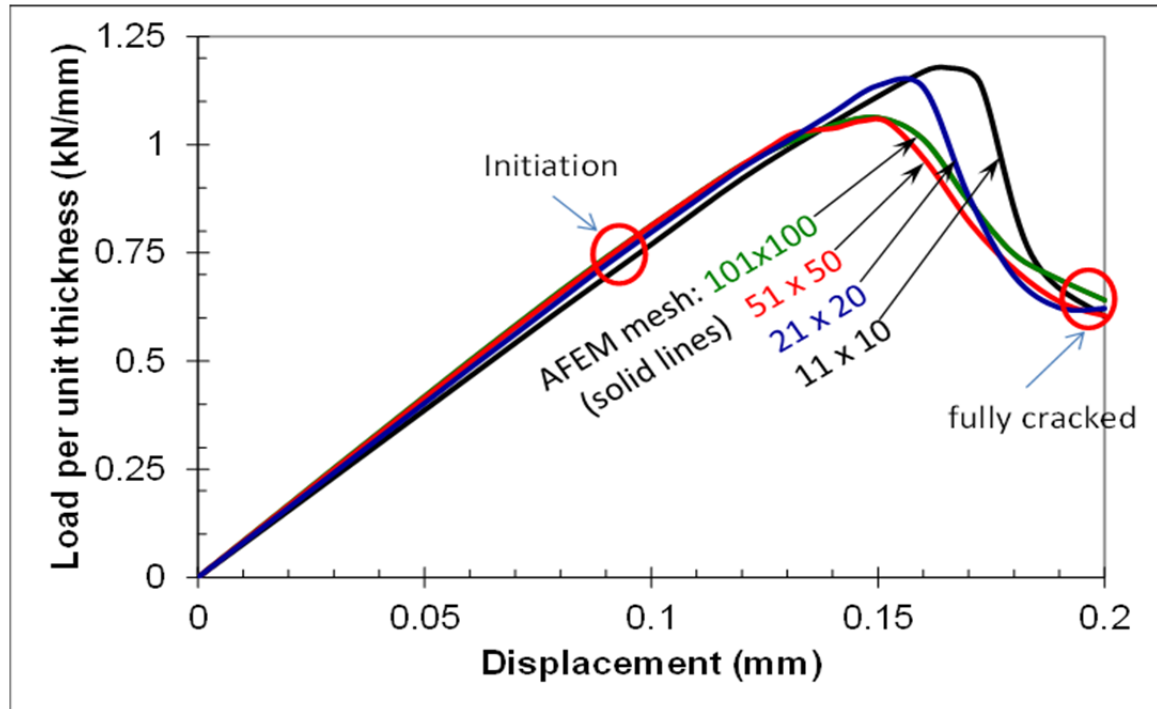


Figure 4-2 Simulated load-displacement curves for precracked short beam

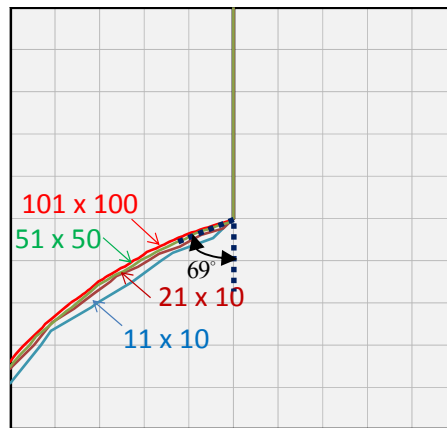


Figure 4-3 Crack trajectories for the shear test with four vastly different meshes

It is rather satisfactory that the paths are almost identical despite the fact that they are obtained with vastly different mesh sizes. The moderate difference in crack paths is largely attributed to the maximum kinking angle limit of ± 45 degree permitted by our numerical program. This is a standard numerical treatment to avoid the possible crack curve back (for example, in ABAQUS it is also set to be ± 45 degree). However, it is seen that even with this artificial limit, it takes no more than two or three sequential kinks for the trajectories to establish a steady kink angle of ~ 69 degree, which agrees extremely well with the well-known experimental value of 70 degree.

The crack trajectory for each mesh size can be seen in Figure 4-4.

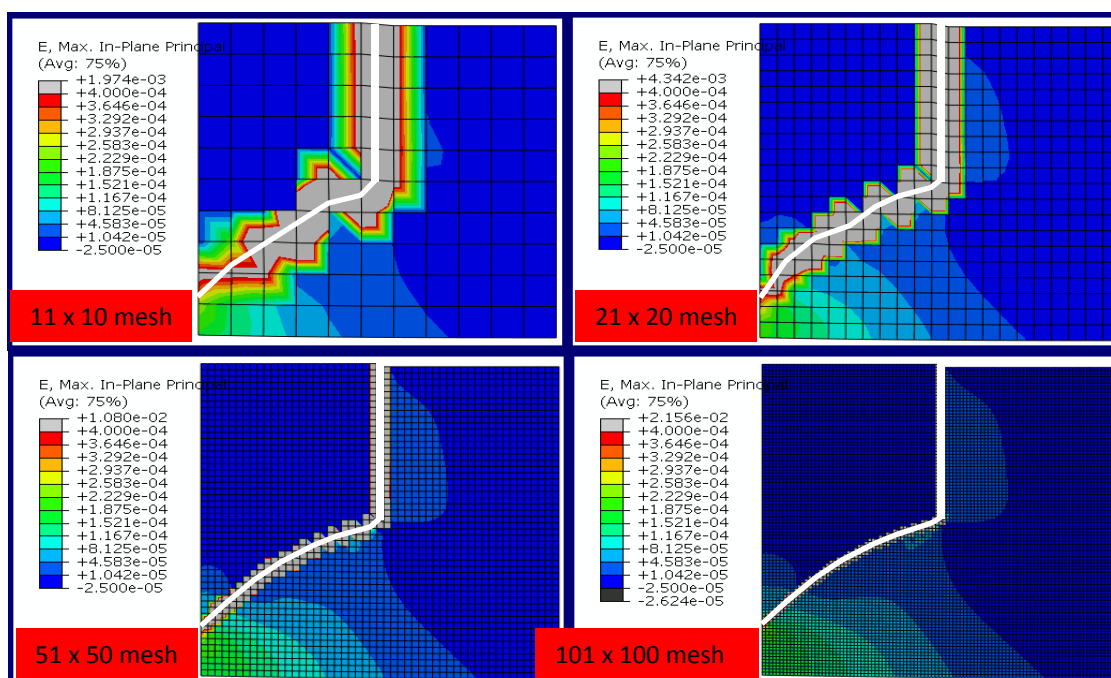


Figure 4-4 Crack trajectory for each mesh size

We emphasize that, despite the difference in mesh size by 10 times, all the predicted load-displacement curves and crack trajectories remain extremely consistent with each

other. This clearly demonstrates the mesh insensitivity of the new A-FEM. Furthermore, we shall mention that the largest mesh used here ($h \sim 100\text{mm}$) is as large as 70% of the cohesive zone size, while the mesh size used in literature for similar problems rarely exceeds 10% of the cohesive zone size (e.g., [183,235,236]). This is a direct benefit of the improved Gaussian method for elemental cohesive stress integration and the mathematical exactness of elemental equilibrium equation.

4.1.2 Numerical Efficiency and Stability as Compared to X-FEM

In this section, we compare the numerical accuracy, efficiency, and the stability of the new A-FEM against the X-FEM available in the commercial code ABAQUS (v6.10). ABAQUS CPS4 elements (i.e., four-node bilinear plane stress element with standard integration) were used. To compare more objectively with ABAQUS X-FEM results, we set the loading parameters to be identical with a maximum prescribed displacement of 0.2 mm, and suggested maximum incremental size is 10^{-9} that is necessary for ABAQUS X-FEM, but not for the present A-FEM (the minimum incremental size observed with the A-FEM simulations among all the cases is 0.0125, while for ABAQUS X-FEM is 6.0×10^{-8}). All simulations were run on a Dell precision M4600 ($\times 64$ bit) movable workstation with Intel Core i7-2860 QM central processing unit (CPU) at 2.5 GHz and with 8 GB of RAM.

We first ran the models without any solution enhancement techniques. The new A-FEM was able to complete all four cases without any numerical difficulty and results are already summarized in Figure 4-2 and Figure 4-3. However, the X-FEM could not complete the simulations with mesh (iii) and (iv); the simulations were aborted before the

cracks reached the left edge (fixed). Therefore, viscous damping coefficients of 1.0×10^{-4} and 4.54×10^{-4} were used for mesh (iii) and (iv), respectively. With such aid, the X-FEM was able to finish the cases and its predicted trajectories are not very different from the A-FEM results shown in Figure 4-3.

However, the X-FEM results show very severe mesh dependence in the load-displacement curves, which are shown in Figure 4-5 by the dashed lines with corresponding mesh clearly labeled. For comparison purposes, the A-FEM predicted curves are redrawn in this figure. For mesh (i) ($h \sim 100\text{mm}$, 110 elements), the X-FEM predicts a significantly delayed crack initiation at the displacement of 0.225 mm, and overestimates the peak load by more than 70%. The load-displacement response improves gradually as the mesh size decreases. Only with finer meshes of $h \sim 20\text{mm}$ (2550 elements) or $h \sim 10\text{mm}$ (10,100 elements), the X-FEM predicted load-displacement curves become sufficiently close to the A-FEM results. The X-FEM's difficulty in obtaining converged solutions is also evident in the load-displacement curves by the severe oscillations during the softening phases, while the A-FEM load-displacement curves remain very smooth even without the aid of numerical damping.

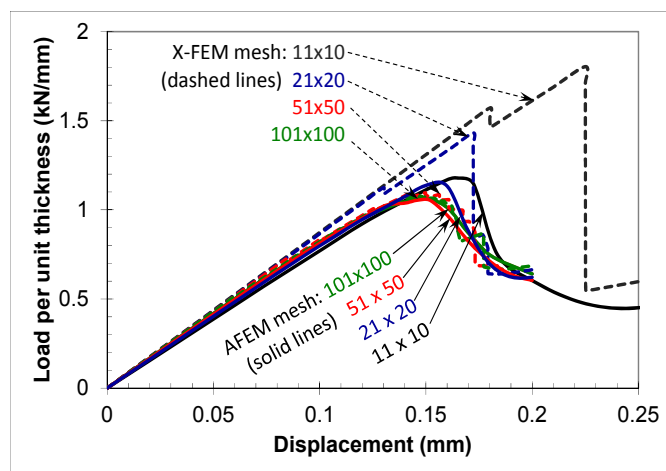


Figure 4-5 X-FEM predicted load-displacement curves compared with the A-FEM predictions

Figure 4-6 compares the CPU time (right vertical axis) and numerical discrepancy (left vertical axis) as function of the mesh size. For numerical discrepancy measure, the peak load (1.05 kN/mm) from the X-FEM converged solution of mesh 101×100 , which is also in good agreement with all of the A-FEM predicted peak loads, is used as a reference (1% error) for comparing the numerical discrepancies of other simulations. All of the A-FEM predicted peak loads are well within 10 % of this reference peak load. However, the numerical discrepancies associated with the X-FEM predictions increase with the mesh size and rapidly exceed 10%.

The computational cost in terms of CPU time of the A-FEM is also greatly reduced as compared to X-FEM. From Figure 4-6, for an identical mesh, the A-FEM is typically 5-8 times faster than the X-FEM. However the numerical discrepancies associated with the larger X-FEM meshes ($h=50, 100$ mm) are not at acceptable levels. If 10% of the numerical uncertainty is acceptable, the X-FEM converged solution achieved with mesh

size $h \sim 20$ mm (2550 elements) and a total CPU time of 161 s, can be easily obtained, with the same solution accuracy, using the A-FEM with a mesh size of $h \sim 100$ mm (110 elements) and a CPU time of merely 1.4 s.

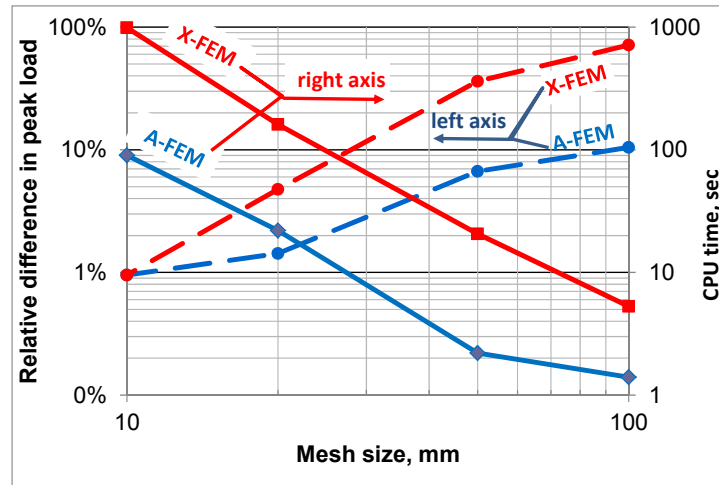


Figure 4-6 Comparison of CPU time (right vertical axis) and the numerical error (left axis) as function of mesh sizes

Thus, we demonstrated through this shear test that the A-FEM improves numerical efficiency by more than two orders of magnitude as compared to the X-FEM.

4.2 Four Point Shear Beam Test

In this section, another numerical example is proposed to evaluate the capabilities of the new A-FEM by simulating the crack propagation in a 4-point shear beam (4PSB) test reported in [262]. The problem has been simulated by Moes and Belytschko in [183] using X-FEM with a non-structured triangular mesh. The numerical model setup used in [183] is reproduced in Figure 4-7.

The geometry dimensions are:

$$b = 200 \text{ mm}; l/b = 4; a/b = 0.2; c/b = 0.4; l_1 = l_2 = 20 \text{ mm}; t = 100 \text{ mm}$$

The concrete material properties are:

$E = 28,000 \text{ N}/(\text{mm})^2$; $\nu = 0.1$; $\Gamma_1 = 145 \text{ N}/\text{mm}$; $\hat{\sigma} = 2.4 \text{ N}/(\text{mm})^2$. The cohesive law used is of triangular type with an initial slope of $\alpha_{n1} = 2.0 \times 10^4 \text{ N}/(\text{mm})^3$ and a softening slope of $\alpha_{n2} = -20 \text{ N}/(\text{mm})^3$.

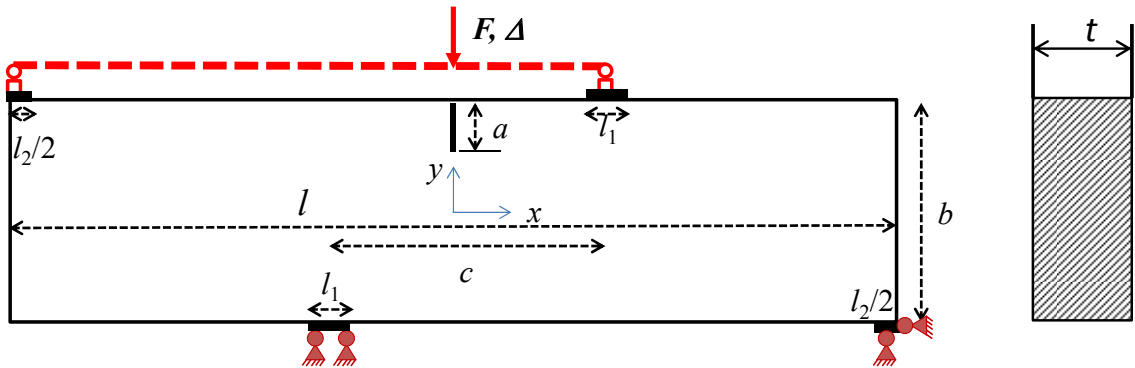


Figure 4-7 PSB Geometry, boundary and loading

As in [183], the maximum principal stress criterion was used for crack initiation. That is, crack initiation from a pristine elastic element occurs when the maximum principal stress averaged within an element ($\bar{\sigma}_{\max}$), reaches the mode I cohesive strength ($\hat{\sigma}$). The crack path is perpendicular to the maximum principal stress direction.

To investigate the mesh sensitivity of the present A-FEM, the problem was analyzed by five different structured meshes with characteristic mesh sizes of $h=2, 4, 8, 13.3,$ and 20 mm (the total elements are 10760, 2849, 1094, 640, and 410, respectively), and three

unstructured meshes with $h=4, 8,$ and 13 mm (total elements 4062, 1333, and 463, respectively). The two finer meshes ($h=2$ and 4 mm) are the typical of those used in literature [183,235,236,257], while the larger meshes ($8, 13.3$ and 20 mm) are used in this study to explore the mesh limit of the present A-FEM. The unstructured meshes of $\sim 4, 8,$ and 13 mm were intended to check the mesh sensitivity and the robustness of the new A-FEM. Five of the discretized models (structured $h=2, 8,$ and 20 mm meshes and unstructured $h\sim 8,$ and 13 mm meshes) under deformed states are shown in Figure 4-8 (a, b, c, d, e) with the crack trajectories roughly following the center lines of the white bands.

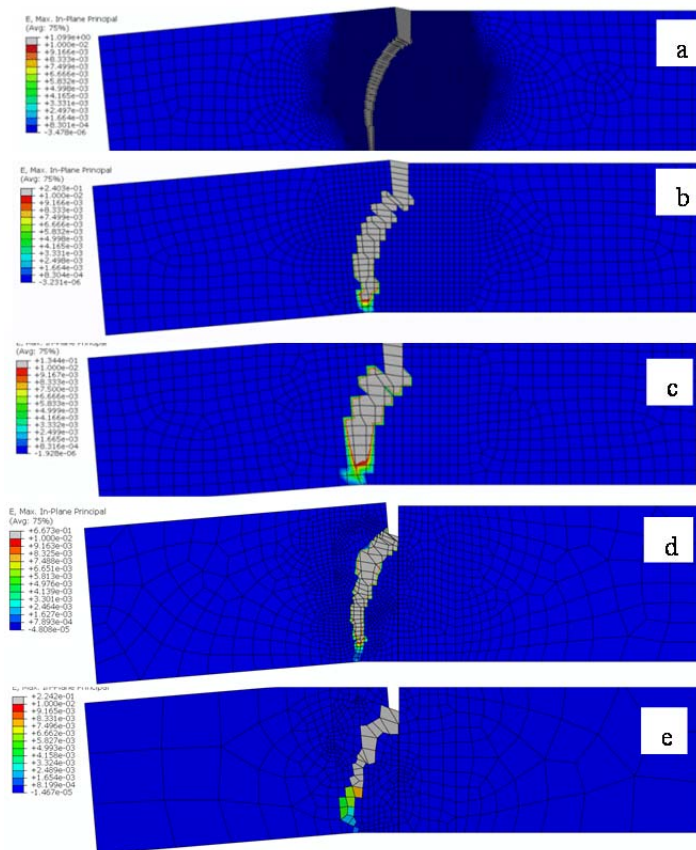


Figure 4-8 Simulated crack paths for structured 2mm (a), 8mm (b), and 20 mm (c) meshes, and unstructured 8mm (d) and 13 mm (e) meshes

4.2.1 Mesh sensitivity

The simulated load-displacement curves are plotted in Figure 4-9. The X-FEM prediction obtained by Moes and Belytschko [183], which used a triangular mesh of $h \sim 3$ mm, was superimposed on this plot for comparison (the dashed line). For each case, the load linearly increases with the applied displacement until crack initiation from the pre-crack tip, which occurs at an applied displacement of ~ 0.04 mm. After the initiation the load-displacement curve becomes increasingly nonlinear due to continuous crack growth. The peak load is reached at the displacement of about ~ 0.09 mm. After the peak load, all curves exhibit a strong snap-back behavior. In this study, the strong snap-back behavior was captured using the arc-length method available in ABAQUS (option RIKS).

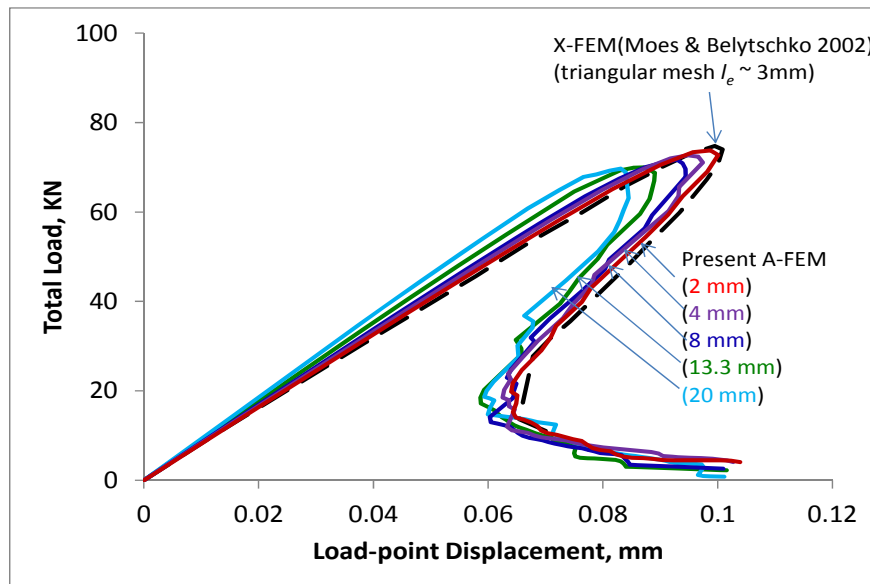


Figure 4-9 A-FEM simulated load-displacement curves with the five structured meshes as compared to the X-FEM results

The A-FEM computed load-displacement results are very consistent with the X-FEM results obtained in [183]. In particular, the load-displacement curves obtained with smaller mesh sizes (i.e., $h=2$ mm, 4 mm, and 8 mm) are almost identical with the X-FEM results. For the larger meshes, i.e., $h=13.3$ mm and 20 mm, the curves deviate mildly from the finer mesh curves due to increases in initial stiffness. The systematic increase of initial stiffness with the increase of mesh size is largely due to the inherent numerical inaccuracy associated with the 4-node plane elements (it is well-known that larger FE elements lead to overestimate of elemental stiffness). If the deviation of initial slope is discounted, the load-displacement curves obtained with larger meshes ($h= 13.3$ mm and $h= 20$ mm) remain very consistent with the X-FEM curve and the finer mesh results. This clearly demonstrates the mesh insensitivity of the present A-FEM.

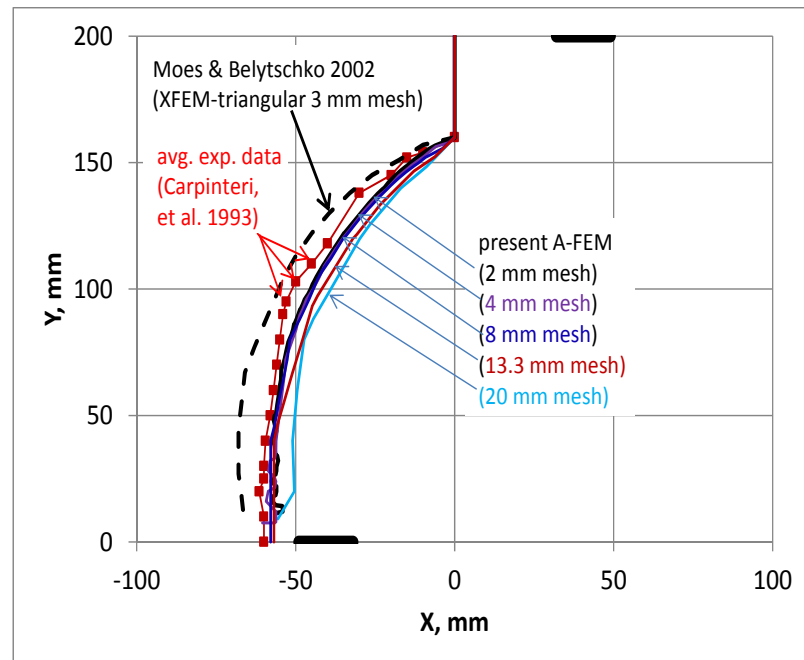


Figure 4-10 Crack trajectories with the five structured meshes as compared to the X-FEM results and experimental results

Figure 4-10 summarizes the crack trajectories predicted by the five simulations with structured meshes. The crack paths are all very consistent and close to the experimental curves, despite they were obtained with vastly different mesh sizes. The mild difference in crack paths with larger meshes is largely attributed to the maximum kinking angle limit of ± 45 degree permitted by our numerical program. It is seen that even with this artificial limit, it takes no more than 2 to 3 sequential kinks for the trajectories to establish a path that is very close to the experimental curve.

It should be mentioned that the mesh insensitivity in this example is expected because all the mesh sizes are considerably smaller than the cohesive zone size (or fracture process zone size). The cohesive zone size, estimated by $l_{coh} = E\Gamma_1 / 2\hat{\sigma}^2$ [71,100] is about $l_{coh} = 350$ mm. This is about twice the beam depth and more than 15 times the largest mesh size (20 mm). However, it has been demonstrated in section 4.2.1 that the A-FEM remains fairly accurate with mesh sizes up to 70% of the cohesive zone size, in which cases the X-FEM (ABAQUS) exhibited serious (unacceptable) mesh dependency [256].

4.2.2 Numerical Efficiency and Stability as Compared to X-FEM in ABAQUS

In this section, the numerical accuracy, efficiency, and stability of the new A-FEM are compared against the X-FEM results obtained with ABAQUS (v6.10). Comparisons were carried out for the structured meshes only because the X-FEM failed to obtain converged solutions for any of the unstructured meshes. The meshes and boundary conditions are exactly the same as those used in previous section. ABAQUS CPS4 elements (i.e., 4-node bilinear plane stress element with full integration) were used. To compare more objectively with the X-FEM, the loading parameters were to be identical with a

maximum prescribed displacement of 0.1 mm, and a suggested maximum incremental size of 0.002 mm. The minimum increment size was 10^{-8} mm, which was necessary for the X-FEM but not for the A-FEM. RIKS option (arc-length method) was invoked in attempt to capture the snap-back behavior. All simulations were run on a Dell precision M4600 (x64 bit) mobile workstation with Intel Core i7-2860 QM CPU @ 2.5 GHz and with 8 GB of RAM.

The X-FEM (ABAQUS) simulated load-displacement curves are plotted in Figure 4-11. The X-FEM had enormous difficulty in completing these simulations. For the 2 mm mesh, the simulation proceeded with such a small incremental size ($10^{-6} \sim 10^{-8}$ mm) that it had to be terminated at the displacement of 0.08 mm after 72 CPU hours of running. For the 4 mm mesh, a sudden strong snap back resulted from an incorrectly predicted crack path occurred at the displacement of 0.09 mm after the peak (Figure 4-11). For the 20 mm mesh, the simulation diverged at the displacement of 0.072 mm (after snap back). For the other cases (i.e., 8 mm and 13.3 mm mesh), the simulations were able to finish and the X-FEM curves captures the peak loads and snap back behavior reasonably well able to finish and they are close to the A-FEM results in Figure 4-9.

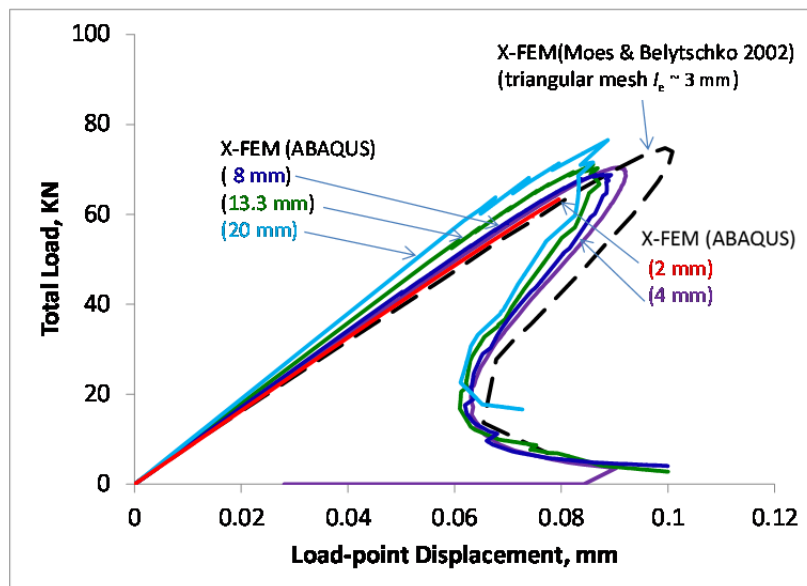


Figure 4-11 X-FEM predicted load-displacement curves

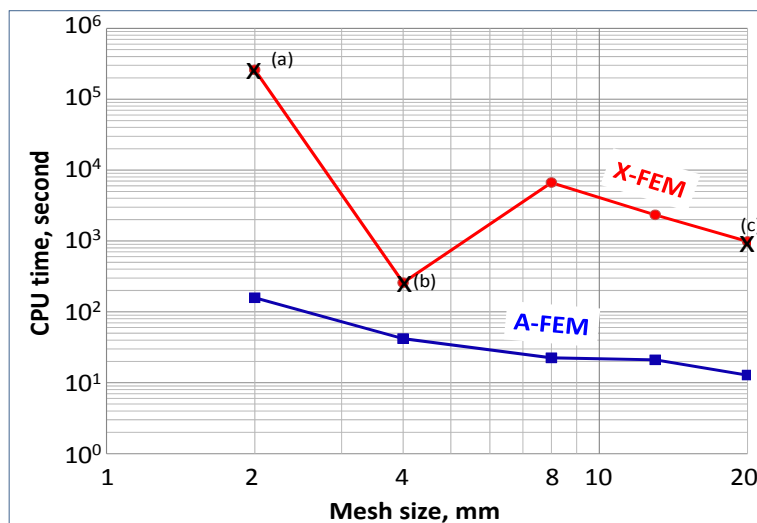


Figure 4-12 Comparison of the CPU time (right vertical axis), and the numerical error (left axis) as function of mesh sizes

Figure 4-12 compares the computational cost in terms of CPU time (in seconds) as functions of the mesh size. The CPU time corresponds to the point that when the

displacement reached 0.1 mm (after snap back). For the 2 mm, 4 mm, and 20 mm mesh, the X-FEM simulations were aborted due to the reasons discussed before. In these cases, the CPU times at the aborting points were taken and such data points were indicated by the X in Figure 4-12. From Figure 4-12, it is concluded that the present A-FEM empowered by the novel condensation procedure, is at least 2 orders of magnitude more efficient than the X-FEM.

4.3 Coupled Fiber- Matrix Interface Debonding and Kinking

We next demonstrate the capability of the A-FEM in dealing with multiple crack interactions. We chose to model a single fiber/matrix domain as shown in Figure 4-13. The entire domain is $1 \text{ mm} \times 1 \text{ mm}$ and the fiber diameter is 0.5 mm (i.e., fiber volume fraction 19.6%). Symmetric, displacement-controlled loading is imposed on both the left and right edges, while the top and bottom edges are stress free.

Two sets of meshes were used to simulate the problem: (a) a fine mesh as shown by the top graphs of Figure 4-13 with 2244 elements, and (b) a coarse mesh as shown in the bottom graphs of Figure 4-13 with 110 elements. In the fine mesh (a) the elements are arranged to conform to the circular fiber/matrix interface. In mesh (b) the coarse mesh is structured and not conforming to the fiber/matrix interface (shown by dashed circle in Figure 4-13). That is, the fiber-matrix interface is deliberately set to bisect the structured elements rather than along element boundaries. The elements traversed by the interface are initially augmented to account for intra-element material difference as well as possible interface debonding. In both meshes, secondary cracking in the matrix domain is also permitted to capture the possible crack kinking from the interface into the matrix

domain. Such a coupled cracking phenomenon has been observed experimentally but is still waiting for detailed calibration. The modulus and Poisson's ratio for the fiber and matrix are $E_f = 40 \text{ Gpa}$; $\nu_f = 0.33$; and $E_m = 4 \text{ Gpa}$; $\nu_m = 0.4$. A cohesive model with triangular traction-separation laws was used for interface debonding and matrix cracking. The cohesive parameters for matrix cracking and interface debonding are set to be identical: $\hat{\sigma} = \hat{\tau} = 50 \text{ Mpa}$; $\delta_{nc} = \delta_{sc} = 1 \times 10^{-2} \text{ mm}$; $\delta_{n1} = \delta_{s1} = 1 \times 10^{-6} \text{ mm}$

Therefore, the fracture toughnesses for modes I and II are $\Gamma_I = \Gamma_{II} = 0.25 \text{ N/mm}$. For matrix crack initiation and propagation, the maximum principal stress criterion is assumed.

The predicted curves of nominal stress versus nominal strain are shown in Figure 4-13. In both cases, the nominal stress-strain curves can be roughly categorized into three stages. The first stage is the elastic stage, wherein the interface remains well bonded and the response is linear. In stage 2 the nonlinearity caused by interface debonding starts to manifest, and as a result, stiffness is gradually reduced. But the stress continues to rise due to further stretching in matrix. The third stage begins immediately after the peak nominal stress is reached. The peak stress corresponds to the onset of crack kinking from the interface into the matrix. The kinking crack is unstable and accompanied by a sudden drop to zero, at which point the domain is completely separated. The entire debonding/kinking process is illustrated by the top and bottom maximum-strain contour plots in Figure 4-13 for respective meshes. It is seen that, despite the vast difference in mesh size and interface conformity, the predicted stress-strain curves remain very similar to each other.

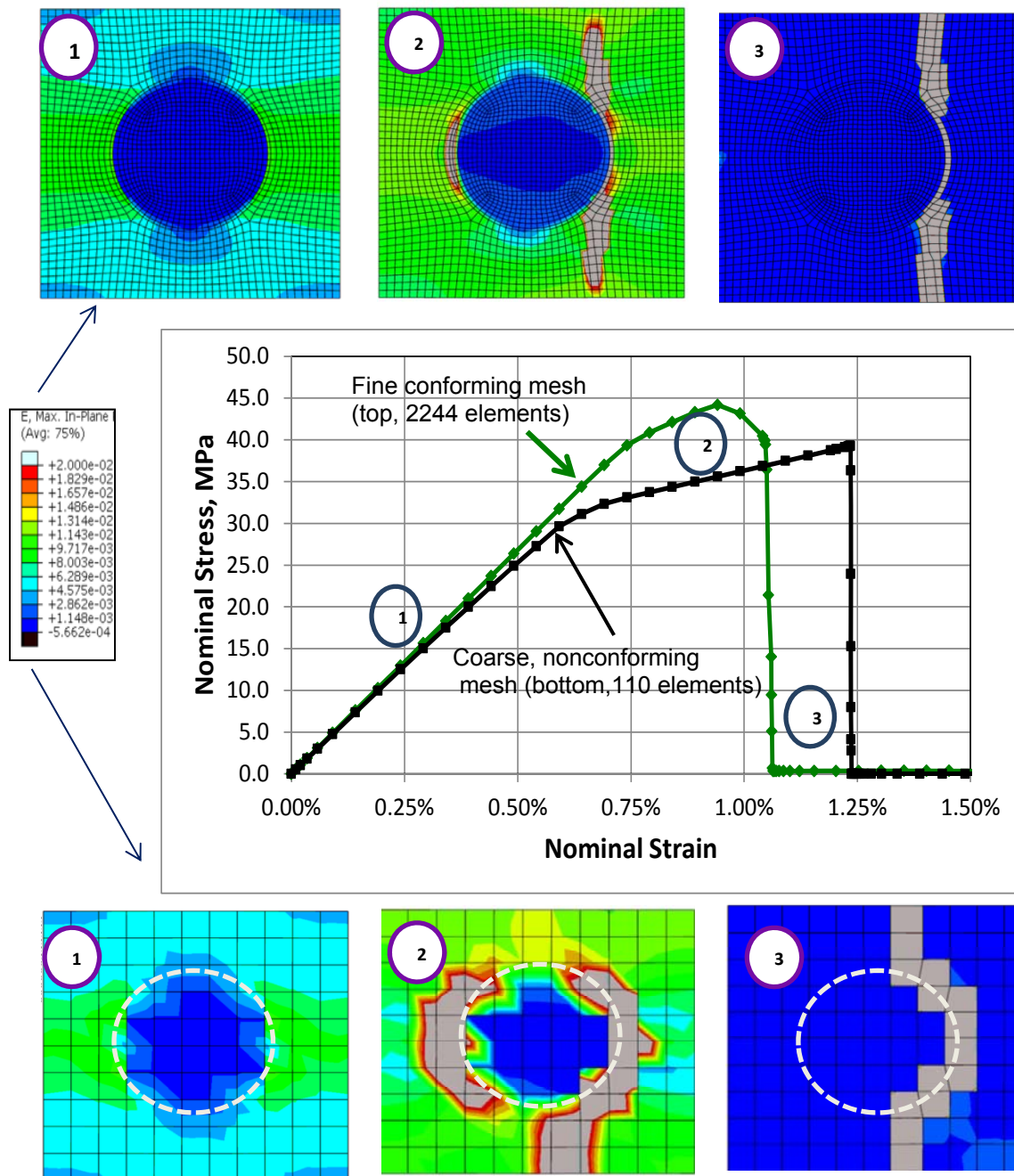


Figure 4-13 A-FEM Simulated nominal stress versus displacement for a single fiber/matrix domain under uniaxial tension. Crack development, including the initial fiber-matrix interface (dashed line), debonding crack and final kinking cracks in matrix are indicated

More quantitative comparisons of the predicted composite modulus, strength, and energy dissipation after complete fracture, are summarized in Table 4-1. The differences in predicted composite elastic modulus and energy dissipation are well within 5% (the predicted modulus values, 5.2 GPa for mesh (a) or 5.37 GPa for mesh (b), are mildly greater than the lower bound estimation of 4.86 GPa based on the rule-of-mixture, which is another proof that the current predictions are reasonable).

Finally, the 10% difference in predicted composite strengths by the two meshes is rather impressive given the large difference in mesh size and interface conformity.

We emphasize here that in above simulations, the tightly coupled cracking development processes, including the initiation and propagation of the interface cracks, the location of kinking initiation, as well as the kink crack paths, are all determined automatically by the program according to the computed local stresses and the predicted initiation and propagation criteria. Few existing methods can truly handle this complex fracture process with such high fidelity.

Table 4-1: Comparisons of predicted composite properties by mesh (a) and (b)

	Composite Modulus (Gpa)	Composite Strength (Gpa)	Energy Dissipation (N - mm)
Mesh a (fine & conforming)	5.37	44.21	0.290
Mesh b (coarse & nonconforming)	5.20	39.63	0.304
Difference	3.2%	10.3%	4.8%

4.4 Axisymmetric Tension Acting on a Fiber-Matrix Interface

The A-FEM's capability in handling intra-element material heterogeneity and the progressive debonding along the material interface is demonstrated in this section with a typical fiber/matrix unit cell under axisymmetric, displacement-controlled loading as shown in the inset of Figure 4-14. The outer radius is $b = 10 \times 10^{-3}$ mm and the embedded fiber radius is $a = 5 \times 10^{-3}$ mm .

The modulus and Poisson's ratio for the fiber and matrix, respectively, are $E_f = 300$ Gpa; $\nu_f = 0.33$, and $E_m = 4$ Gpa; $\nu_m = 0.4$. The interface cohesive parameters are: $\hat{\sigma} = \hat{\tau} = 100$ Mpa; $\delta_{nc} = \delta_{sc} = 0.12 \times 10^{-3}$ mm; $\delta_{n1} = \delta_{s1} = 0.001 \times 10^{-3}$ mm ;

Therefore, the fracture toughnesses for mode I and mode II are $\Gamma_I = \Gamma_{II} = 0.006$ N/mm .

An exact solution to this problem has been derived in [206] and it is plotted in Figure 4-14 by the dashed line. The analytical solution contains three distinct deformation stages characterized by three different slopes in the load-displacement curve.

The first stage reflects the deformation stage when the interface remains elastically bonded (weak discontinuity). Towards the end of stage one, the cohesive strength of the interface is reached. Interface debonding (strong discontinuity) starts after this point. The interface cohesive stress decreases linearly with further displacement increase and the interface tangential stiffness becomes negative. This leads to a sharp decrease of surface traction. Towards the end of this stage, the critical displacement of the cohesive law is reached and the matrix is completely separated from the fiber. Therefore, in stage 3 the slope is completely determined by the matrix stiffness.

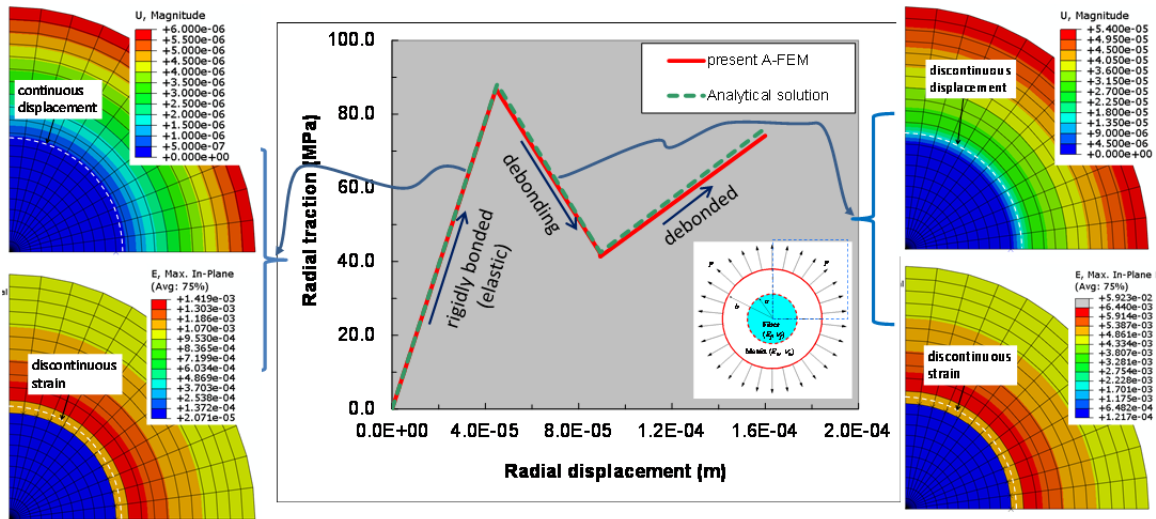


Figure 4-14 A-FEM simulated radial surface traction as a function of radial displacement for an axial symmetric single-fiber/matrix unit cell (center plot). The two contour micrographs to its left show the continuous displacement and discontinuous strain (maximum principal) during the elastic stage when the fiber and matrix are rigidly bonded (weak discontinuity). The two right contour graphs show that both the displacement and strain are discontinuous after interface debonding occurs (strong discontinuity)

In the A-FEM modeling, we chose to model one quarter of the domain with symmetrical conditions as shown in Figure 4-14. The domain was discretized into $12 \times 21 = 252$ elements. In order to test the capability of the A-FEM in handling intra-element material heterogeneity, the fiber-matrix interface (dashed line) was deliberately set to bisect the elements rather than along element boundaries. Since for this particular problem the location of the discontinuity is known *a priori*, we simply defined those elements traversed by the interface as augmented elements with intra-element bi-material domains and interfaces.

The numerically obtained radial surface traction as a function of radial displacement is plotted in Figure 4-14 (central plot) in direct comparison with the analytical solution. The

A-FEM predicted curve closely follows the analytical solution in all three stages. During the first elastic stage, as evidenced in contour micrographs of displacement and maximum principal strain to the left of the stress-displacement plot, the displacement is continuous across the interface but the strain is discontinuous. This demonstrates the present A-FEM can account for existing weak discontinuity accurately. The strong discontinuity across the fiber/matrix interface during stage 2 is also well captured. The two contour micrographs to the right of the load-displacement plot show that both the displacement and the strain across the interface are discontinuous. Thus, the A-FEM's capability in capturing the characteristics of a weak discontinuity and its smooth transition to a strong discontinuity has been demonstrated.

4.5 Three Point Bending Beam Test

In this section, another numerical example is proposed to examine the capabilities of the new A-FEM in initiating crack in a system with no initial crack. Three point bending test is a widely used method to characterize the fracture of engineering materials. Here the A-FEM is used to simulate the crack propagation in a concrete beam under 3-point bending. The numerical model set up in this chapter is reproduced in Figure 4-15. The geometry dimensions are $l=600$ mm and $b=150$ mm. The thickness normal to the plane can be considered as $t=150$ mm [263].

As in previous examples, the maximum principal stress criterion was used for crack initiation. The material properties are $E=36500$ MPa and $\nu=0.18$.

The cohesive law used is of triangular type with the parameters:

$$\hat{\sigma} = \hat{\tau} = 3.19 \text{ Mpa}; \delta_{nc} = \delta_{sc} = 0.0313 \text{ mm}; \delta_{n1} = \delta_{s1} = 0.0313 \times 10^{-4} \text{ mm}.$$

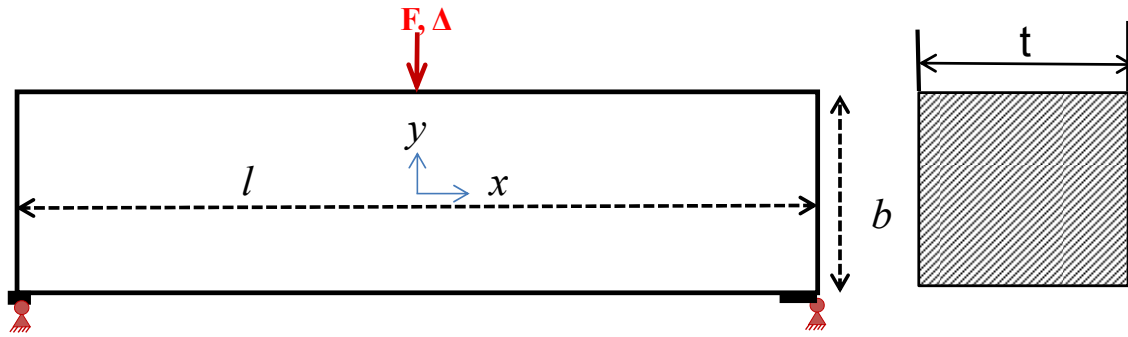


Figure 4-15 Three point beam bending specimen, boundary and loading

Abbas et al has simulated this problem using X-FEM method in [263] which in the case of high gradient enrichment functions, only the crack-tip element is enriched. The initial mesh is a 65×29 structured mesh. In the case of adaptive mesh refinement, the mesh is 5 times refined at the crack-tip in order to capture the high gradients.

By simulating the problem using the A-FEM with the same initial mesh size as in [263] and also with a coarser mesh, 37×15 , the results can be compared together. The load-displacement plot is scaled to have a dimensionless axis. As shown in Figure 4-16, load and displacement increase simultaneously in the elastic stage, while there may be a very short crack initiating from the midpoint of bottom surface. A sudden drop is due to a relatively fast crack growth which led to drop in the load. Although all the results are almost identical, X-FEM needs to enrich and refine some cracked elements while the A-FEM does not need enrichment for crack-tip elements. To obtain better results, the X-FEM has to refine the mesh near the enriched tip but the A-FEM is able to model the problem with uniform mesh within the whole domain.

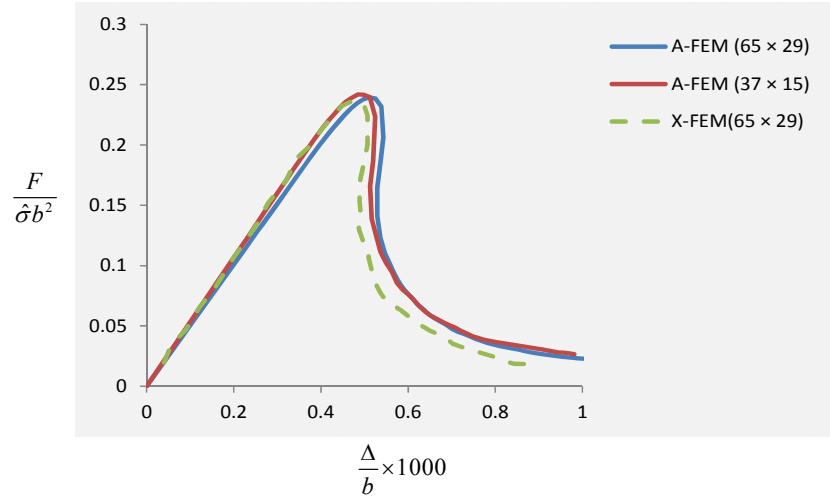


Figure 4-16 Simulated normalized load displacement plot for 3-point beam bending test

4.6 Multiple Crack Interaction in a Plate

In this section, we test the capability of the A-FEM in dealing with multiple initial cracks. Two initial cracks within an elastic domain are considered, one of which is parallel to the top edge and other is at an angle 47° to the top edge, so then the two initial cracks are not parallel. The geometry was a $25.4 \text{ mm} \times 88.9 \text{ mm}$ rectangular plate which the location and orientation of cracks, boundary conditions and displacement-controlled loading are shown in Figure 4-17.

Both top and bottom edges are under monotonically increasing displacement-controlled loading in the vertical direction and fixed in horizontal direction. The material properties are $E = 5000 \text{ MPa}$ and $\nu = 0.3$.

The cohesive law used is of triangular type with the parameters:

$$\hat{\sigma} = \hat{\tau} = 50 \text{ Mpa}; \delta_{nc} = \delta_{sc} = 0.07 \text{ mm}; \delta_{n1} = \delta_{s1} = 7 \times 10^{-6} \text{ mm}.$$

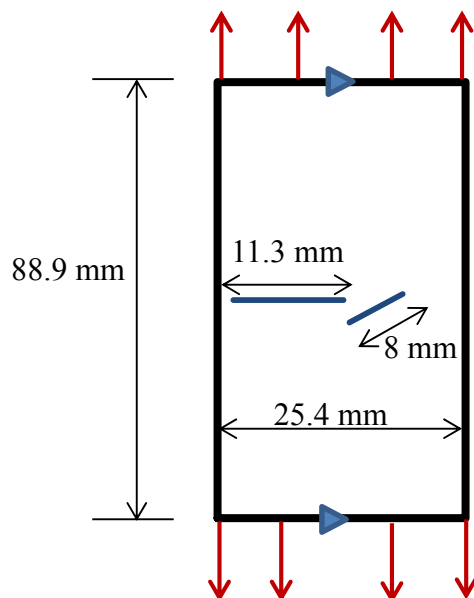


Figure 4-17 Two cracks within the plate

There is no available analytic solution for this problem. The A-FEM predicted the load-displacement curve is shown in Figure 4-18. The crack propagation stages are demonstrated in Figure 4-19.

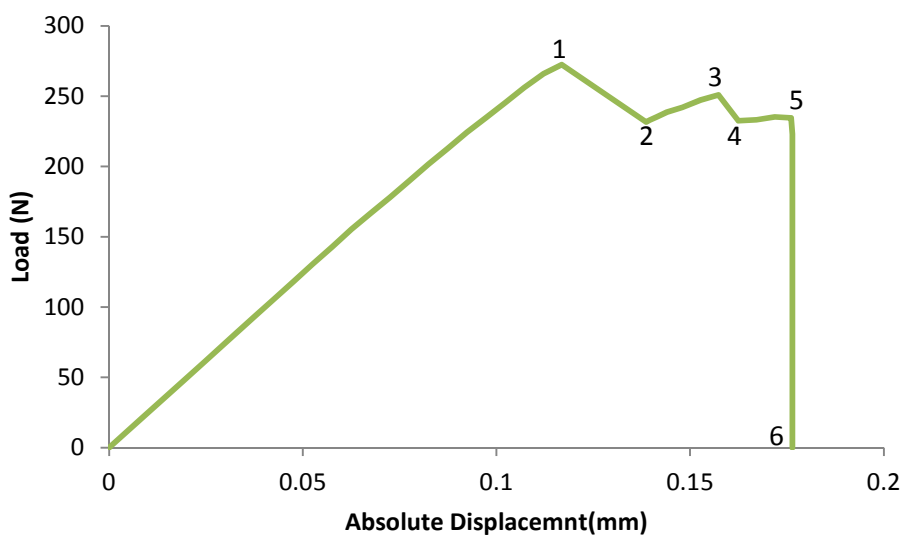


Figure 4-18 Load displacement curve for a plate with two far from edge cracks

At the beginning, which is the elastic stage, load and displacement increase and according to Figure 4-19, strain concentration is considerable around all crack tips. By increasing the displacement, the left tip of the horizontal crack first starts to grow immediately after the peak load is reached (point 1). The crack grows in an unstable manner until it reaches the left stress-free edge. The load drops from point 1 to point 2. After point 2, an increase in further loading is needed to drive the right tip of the horizontal crack to propagate to right (point 3), before it finally merges with the slant crack (point 4). After the two cracks merge, there is a sudden increase in displacement (from 4-5) but no increase in load. This is because the combined crack leads to a quick propagation of the top-tip of the slant crack toward the right stress-free edge. Beyond that, the specimen fails into two parts and load drops to zero (point 6).

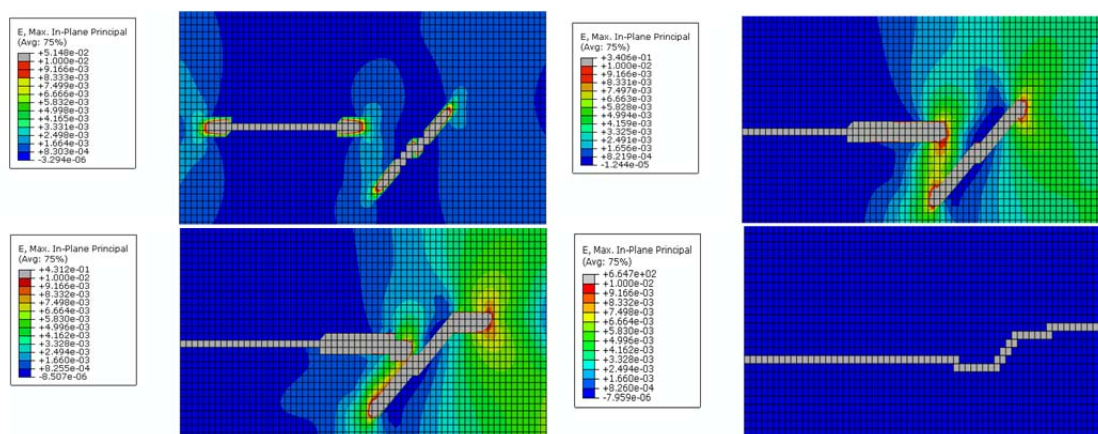


Figure 4-19 Crack propagation stages for a plate with two far from edge cracks

4.7 Summary

Throughout the numerical examples, we have demonstrated that the new A-FEM method, empowered by the new solving algorithm, achieved a significant improvement in numerical accuracy, stability and efficiency. In particular, through a rigorous comparison study on the shear test of a precracked short beam, we have demonstrated that the new A-FEM achieved a substantial improvement in numerical efficiency by two orders of magnitude as compared to the X-FEM.

Through modeling of coupled fiber-matrix interface debonding, the capability of the A-FEM in correctly accounting for the weak discontinuity, as well as in arbitrary crack bifurcation, has been demonstrated.

By modeling multiple cracks in a plate, crack merging and closing were successfully demonstrated by the A-FEM.

In the 4-point shear beam simulation, it has also been demonstrated that the A-FEM is a mesh insensitive method because different mesh sizes and loading schemes did not have much influence in final results.

Chapter 5: Conclusions and Future Study

5.1. General Conclusions

In this thesis, a very capable numerical platform based on Augmented Finite Element Method (A-FEM) has been developed. A new elemental augmentation procedure has been established to derive augmented finite elements that allows for prediction of crack initiation and propagation without need for *a priori* knowledge of crack path information and other traditional limits. This method can accurately account for arbitrary intra-element cracks and their interaction without the need for additional external DoFs as in X-FEM or extra nodes as in PNM (Phantom Node Method). It has been demonstrated that this makes it much easier in handling multiple crack interaction including crack coalescence or bifurcation because it does not require complex numerical algorithms to track the complex crack fronts.

The new A-FEM formulation does not need to assume deformation modes for elemental displacement enrichment as in the embedded discontinuity method either. Instead, it introduces internal node-pairs with regular displacements as internal DoFs, which are eventually condensed at elemental level. With this new formulation, the crack displacements become natural outcomes of the elemental equilibrium consideration. The biggest advantage of this new formulation is that it enables explicit derivation of elemental equilibrium equations in a mathematically rigorous fashion, which greatly improves the numerical stability and efficiency, as demonstrated in the 4-point shear beam test and other simulations.

Furthermore, we have demonstrated that the new formulation allows for repeated augmentation procedure to include multiple intra-element cracks, which is extremely powerful in dealing with multiple crack interaction problems, as demonstrated by the single fiber/matrix example.

Another capability proposed by A-FEM is its ability to initiate a new crack in a pristine elastic element. Maximum principal stress criterion is used for crack initiation; there is no need to define the crack path, the crack path is perpendicular to the maximum principal stress direction. This ability has been demonstrated in the point shear beam test simulation.

Mesh independency is another achievement of the new A-FEM which has been demonstrated in several numerical simulations in this thesis.

A novel companion algorithm that can rapidly solve the nonlinear equilibrium equation at elemental level has also been developed for cohesive cracks with piece-wise linear traction-separation laws. The novelty in this algorithm is that, instead of assuming trial displacements and searching for stiffness for element equilibrium such as in Newton-Raphson method, it starts with trial stiffness in the cohesive laws and finds the crack displacements through a simple consistency check. For piece-wise linear cohesive laws with only a small number of possible stiffness segments, this algorithm is extremely efficient. Further, we have proven that the crack displacements obtained in this way are mathematically exact. This enables the derivation of the explicit mathematically exact expressions for the elemental equilibrium equations.

Through the numerical examples, we have demonstrated that the new A-FEM method, empowered by the new solving algorithm, achieved drastic improvement in numerical accuracy, efficiency, and stability. Finally, the A-FEM's excellent capability in high fidelity simulation of interactive cohesive cracks in heterogeneous solids has been also demonstrated through ample numerical examples.

The A-FEM as a virtual testing tool looks very attractive, which enables partial replacement of many experimental tests by high fidelity simulations. The payoff in reduced cycle time and costs for designing and certifying different structures, especially composites, is very interesting. However, some challenges still remain. In this thesis, only 2D elements have been developed so far. To make it a more powerful method for more realistic problems, there is an urgent need to develop 3D A-FEM.

5.2 Future Study

To have an effective method that can simulate various and real structures under thermo-mechanical loadings, there is a need to develop the 3D A-FEs and also add temperature DoF to the A-FEM formulations.

The simplest 3D element is the tetrahedron element which includes four nodes and four surfaces. There are two possible configurations if a tetrahedral element is cut by a planar crack. Similar to 2D formulations, we can introduce internal nodes and by solving the nonlinear system of equations, the instantaneous element stiffness matrix and external force array (RHS) can be established in order to implement into an existing FE program.

Figure 5-1 shows the two possible configurations for a tetrahedral element cut by a crack.

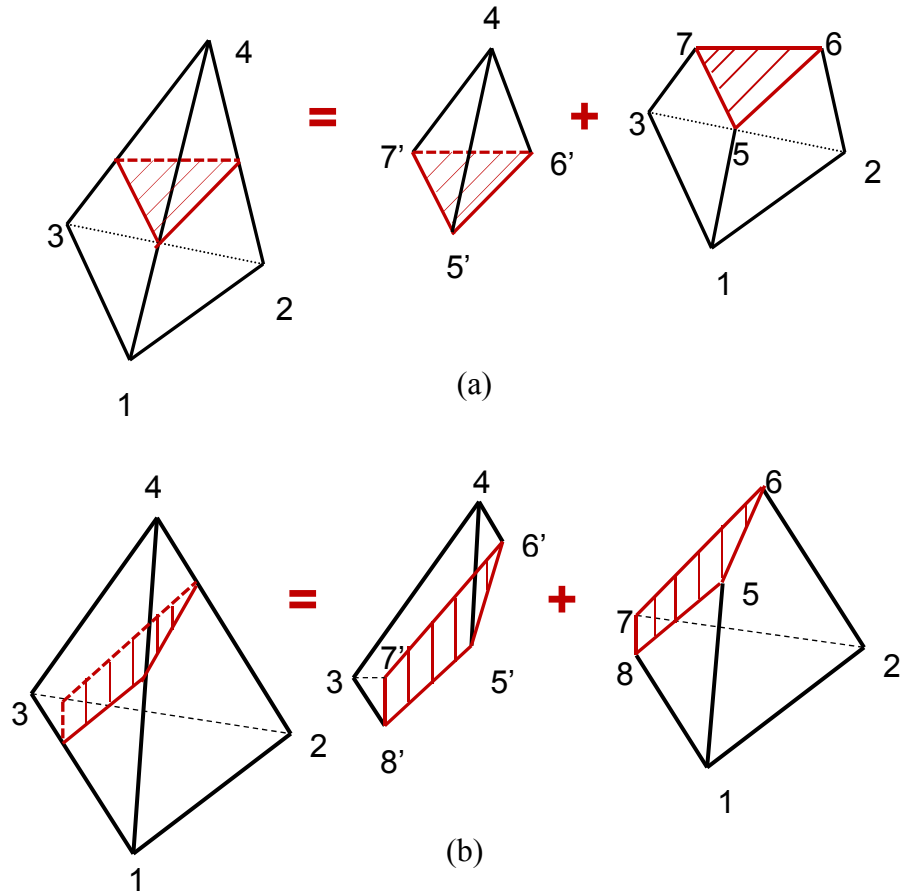


Figure 5-1 possible configurations for a tetrahedral element cut by a crack

As shown in Figure 5-1, depending on the crack direction, a tetrahedral element can be cut into (a) a tetrahedral and a wedge subdomain, or (b) two wedge subdomains. Configurations can be treated in a similar way of the 2D cases, and implemented in a FEM package.

For each subdomain, the equilibrium equation can be derived. The internal nodal DoFs can be condensed similarly as in the 2D problem.

However, it is expected that the 3D problem is much more complicated than 2D problem.

The most important factor is that in 2D, a crack is a 1D line which is much easier to deal

with than the planar crack surface in 3D. Computing equivalent nodal forces from nodal stresses, or Gaussian point stresses, is much more complicated than that in 2D.

To see a simple 3D single element A-FEM response, assume that a single tetrahedron element is under mode I loading. All the DoFs are fixed except the one that shows with the arrow. A crack plane is considered a plane parallel to the tetrahedron base. By displacing the above node normal to that crack plane, mode I displacement loading can be achieved. The load-displacement plot from A-FEM and ABAQUS are shown in Figure 5-2.

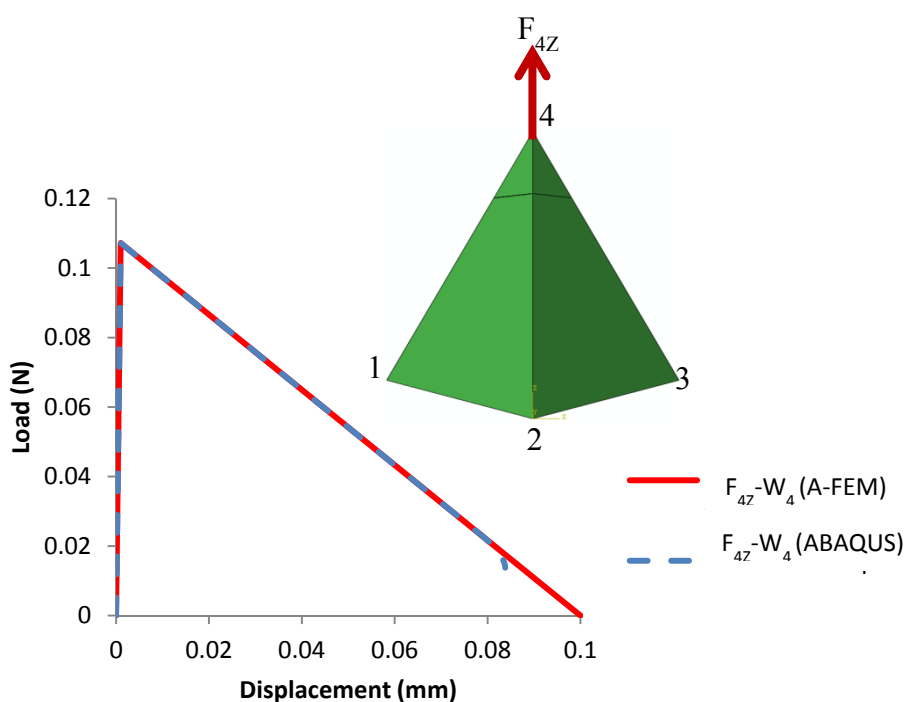


Figure 5-2 Load-displacement curve from A-FEM and ABAQUS for a tetrahedron element

As shown in Figure 5-2, the A-FEM result is initially identical to ABAQUS result. The post-peak behavior is almost identical but ABAQUS is not able to finish the job to reach complete failure. The 3D A-FEM finishes the failure process smoothly. Similar to the 2D case, ABAQUS needs to use more than one element to simulate the crack problem. Because all the elements are 3D, by increasing number of elements, computational time also increases substantially. By using A-FEM, the crack in a tetrahedral element can be simulated by just using one element. It is expected that the same order of magnitude improvement in numerical efficiency as 2D may be achieved.

The accomplishment of 2D A-FEM serves a strong base to develop the 3D A-FEM. By implementing 3D A-FEs in FEM package, it will be possible to analyze more realistic 3D problems. Such capabilities are in high demand in composite and heterogeneous material research.

References

1. **Jones, Robert M.** *Mechanics of Composite Material*. 2nd. Blacksburg : Taylor & Francis, 1999.
2. **Melro, Antonio Rui.** Analytical and Numerical Modeling of Damage and Fracture of Advanced Composites. *Doctorate Thesis*. s.l. : University of Porto, February 2011.
3. **Herakovic, Carl T.** *Mechanics of Fibrous Composites*. s.l. : John Wiley & Sons, 1998.
4. **Strong, A. B.** *History of Composite Materials- Opportunities and Necessities*. s.l. : Brigham Young University.
5. **Bensaude-Vincent, Tim Palucka and Bernadette.** Composite Overview. *Materials Research Activities*. [Online] Caltech, October 19, 2002.
http://authors.library.caltech.edu/5456/1/hrst.mit.edu/hrs/materials/public/composites/Composites_Overview.htm.
6. Polymer Matrix Composite Applications. [Online]
<http://www.rapra.net/composites/introduction/polymer-matrix-composite-applications.asp>.
7. *Inorganic Fibers- A Literature Review*. **Cooke, T. R.** 1991, Journal of the American Ceramic Society, Vol. 74, pp. 2959-2978.
8. **Zhou, Zhiqiang.** Multiple- Scale Numerical Analysis of Composites Based on Augmented Finite Element Method. *Doctorate Thesis*. Coral Gabels, Florida : University of Miami, August 2010.
9. **Kasturi, Krishna Kumar.** Microcracking Fracture Toughness for Graphite Epoxy Composite Laminates Using Finite Fracture Mechanics. *MS Thesis*. s.l. : University of New Orleans, 2006.
10. **Joffe, R.** Damage Accumulation and Stiffness Degradation in Composite Laminates. *Doctoral Thesis*. s.l. : Lulea University of Technology, 1999.
11. **Jaap H. Heida, Derk J. Platenkamp.** Evaluation of Non-Destructive Inspection Methods for Composite Aerospace Structures. *International Workshop of NDT Experts, Prague, 10-12 Oct 2011*.
12. **Case, S. W., Reifsnider, K. L.** *MRLife 12 Theory Manual--Composite Materials*. s.l. : Materials Respnose Group, Virginia Polytechnical Institute and State University, 1999.

13. *Fatigue Damage Mechanics of Composite Materials. II: A Damage Growth Model.* **Spearing, S. M., Beaumont, P. W. R.** s.l. : Composite Science and Technology, 1992, Vol. 44, pp. 169-177.
14. *Continuum Damage Mechanics, Anisotropy and Damage Deactivation for Brittle Materials like Concrete and Ceramic Composites.* **Chaboche, J. L., Lesne, P. M., & Maire, J.F.** 1, 1995, International Journal of Damage Mechanics, Vol. 4, pp. 5-22.
15. *Damage Tolerance of Laminated Composites Containing an Open Hole and Subjected to Tensile Loadings.* **Chang, K. Y., Liu, S., & Chang, F. K.** 1991, Journal of Composite Materials, Vol. 25, pp. 274-301.
16. *Physically Based Damage Models for Laminated Composites.* **McCartney, L. N.** 3, 2003, Journal of Materials: Designs and Applications, Vol. 217, pp. 163-199.
17. *A Micromechanical Modeling Approach to the Mechanical Properties of Textile Elastomeric Composites.* **Huang, Z. M., Ramakrishna, S., & Tay, A. A. O.** 1999, Materials Science Research International, Vol. 5, pp. 189-194.
18. *The Physics and Mechanics of Fiber- Reinforced Brittle Matrix Composites.* **Evans. A. G., & Zok, F. W.** 1994, Journal of Material Science, Vol. 29, pp. 3857-3896.
19. *A Direct Micromechanics Method for Analysis of Failure Initiation of Plain Weave Textile Composites.* **Karkkainen, R. L., & Sankar, B. V.** 2006, Composite Science and Technology, Vol. 66, pp. 137-150.
20. *Modeling Stiffness and Strength of 3D Textile Structural Composites.* **Pochiraju, K., Chou, T. W., Shah, B. M.** 1996. Collection of Technical Papers- AIAA/ASME/ASCE/AHS/ASC Structures, Structural Dynamics & Materials Conference. Vol. 4, pp. 2294-2304.
21. *General Techniques for Exploiting Periodicity and Symmetries in Micromechanics Analysis of Textile Composites.* **Tang, X. D., Whitcomb, J.D.** 2003, Journal of Composite Materials, Vol. 37, pp. 1167-1189.
22. *Virtual Textile Composite Software Wiseex: Integration with Micromechanical, Permeability and Structural Analysis.* **Verpoest, I., & Lomov, S. V.** 2005, Composite Science and Technology, Vol. 65, pp. 2563-2574.
23. *3D Analysis of Stress Transfer in the Micromechanics of Fiber Reinforced Composites by Using and Eigen-Function Expansion Method.* **Wu. Z. J., Ye, J. Q., & Cabrera, J. G.** 5, 2000, Journal of Mechanics and Physics of Solids, Vol. 48, pp. 1037-1063.

24. **Mohammadi, Soehil.** *Extended Finite Element Method for Fracture Analysis of Structures*. s.l. : Blackwell Publishing Ltd, 2008.
25. **Mirzaei, Majid.** *Fracture Mechanics, Theory and Applications*. Tehran : s.n.
26. *In Quest of Virtual Tests for Structural Composites*. **Brian Cox, Qingda Yang.** 5802, November 17, 2006, Science Journal, Vol. 314, pp. 1102-1107.
27. *A Stiffness Derivative Finite Element Technique for Delamination of Crack Tip Stress Intensity Factors*. **Parks, D. M.** 4, 1974, International Journal of Fracture, Vol. 10, pp. 487-502.
28. *Computation of Energy Release Rates for Kinking Cracks Based on Virtual Crack Closure Technique*. **De Xie, Anthony M. Waas, Khaled W. Shahvan, Jessica A. Schroeder, raymond G. Boeman.** 6, 2004, CMES, Vol. 6, pp. 515-524.
29. *A Finite Element Calculation of Stress Intensity Factors by a Modified Crack Closure Integral*. **Kanninen, E. F. Rybicki & M. F.** 1977, Engineering Fracture Mechanics, Vol. 9, pp. 931-938.
30. *A Virtual Crack-Closure Technique for Calculating Stress Intensity Factors for Cracked Three Dimensional Bodies*. **Shivakumar, K. N., Tan, P.W. & Newman, Jr. J. C.** 1988, International Journal of Fracture, Vol. 36, pp. R43-R50.
31. **Krueger, Ronald.** *The Virtual Crack Closure Technique: History, Approach and Applications*. Hampton, Virginia : Nasa Langely Research Center, 2002. ICASE.
32. *Strain Energy Release Rate Calculation for a Moving Delamination Front of Arbitrary Shape Based on Virtual Crack Closure Technique*. **Xie, D. & Biggers, Jr. S. B.** 6, 2006, Engineering Fracture Mechanics, Vol. 37, pp. 771-785.
33. *A Finite Element Analysis of Stress Intensity Factors for Combined Tensile and Shear Loading by only a Virtual Crack Extension*. **Ishikawa, H.** 5, 1980, International Journal of Fracture, Vol. 16, pp. R243-R246.
34. *Weight Function Calculations for Mixed Mode Fracture problems with the Virtual Crack Extension Technique*. **Sha, G. T & Yang, C. T.** 1985, Engineering Fracture Mechanics, Vol. 21, pp. 1119-1149.
35. *Calculation of Strain-Energy Release Rates with Higher Order and Singular Finite Elements*. **Raju, I. S.** 1987, Engineering Fracture Mechanics, Vol. 28, pp. 251-274.
36. *An Equivalent Domain Integral Method for Three Dimensional Mixed Mode Fracture Problems*. **Shivakumar, K. N. & Raju, I. S.** 1992, Engineering Fracture Mechanics, Vol. 42, pp. 935-959.

37. *Path Independent Integrals, Energy Release Rates, and General Solutions of Near-Tip Fields in Mixed Mode Dynamic Fracture Mechanics.* **Nishioka, T. & Atluri, S. N.** 1983, Engineering Fracture Mechanics, Vol. 18, pp. 1-22.
38. *On the Computation of Mixed Mode K-Factors for a Dynamically Propagating Crack, Using Path Independent Integrals.* **Nishioka, T. & Atluri, S. N.** 1984, Engineering Fracture Mechanics, Vol. 20, pp. 193-208.
39. *Numerical Analysis of Directionally Unstable Crack Propagation in Adhesively Bonded Joints.* **Chen, B. & Dillard, D. A.** 2001, International Journal of Solids and Structures, Vol. 38, pp. 6907-6924.
40. *Energy-Release Rate and Crack Kinking.* **Hayashi, K. & Nemat- Naser, S.** 1981, International Journal of Solids and Structures, Vol. 17, pp. 107-114.
41. *Energy-Release Rate and Crack Kinking in Anisotropic Brittle Solids.* **Azhdari, A. & Nemat- Naser, S.** 6, 1996, Journal of the Mechanics and Physics of Solids, Vol. 44, pp. 929-951.
42. *Kinking of a Crack Out of an Interface: Role Of In- Plane Stress.* **He, M. Y & Hutchinson, J. W.** 1991, Journal of Amer. Ceram. Soc, Vol. 74, pp. 767-771.
43. *On the Problem of Crack Extension in Brittle Solids Under General Loading.* **Palaniswamy, K. & Knauss, W. G.** 1978, Mechanics Today, Vol. 4.
44. *Finite Crack Kinking and T-Stresses in Functionally Graded Materials.* **Becker, Jr. T. L., Cannon, R. M & Ritchie, R. O.** 2001, International Journal of Solids and Structures, Vol. 38, pp. 5545-5563.
45. *Delamination- A Damage Mode in Composite Structures.* **Garg, A. C.** 1988, Engineering Fracture Mechanics, Vol. 29, pp. 557-584.
46. *Delaminations in Composite Structures: its Origin, Buckling, Growth and Stability.* **Bolotin, V. V.** 1996, Composites Part B : Engineering, Vol. 27B, pp. 129-145.
47. *Delaminations of Polymer Matrix Composites: Problems and Assessment.* **Schoeppner, N. J. Pagano & G. A.** [ed.] Elsevier Science. 2000, In Comprehensive Composite Materials, Vol. 2, pp. 433-528.
48. *Characterization of Delamination Onset and Growth in a Composite Laminate.* **O'Brien, T. K.** 1982, Damage in Composite Materials , pp. 140-167.
49. *Interlaminar Fracture Toughness: The Long and Winding Road to Standardization.* **O'Brien, T. K.** 1998, Composites Part B, Vol. 29, pp. 57-62.

50. *Incorporating Interlaminar Fracture Mechanics into Design*. **Martin, R. H.** London, UK : s.n., 1998. International Conference on Designing Cost- Effective Composites: IMech Conference Transaction. pp. 83-92.
51. *Round Robin Testing for Mode I Interlaminar Fracture Toughness of Composite Materials*. **Martin, T. K. O'Brien & R. H.** 1993, Journal of Composite Technology and Research, pp. 269-281.
52. *Composite Interlaminar Shear Fracture Toughness: Shear Measurement or Shear Myth?* **O'Brien, T. K.** 1998, Composite Materials: Fatigue and Fracture, Vol. 7, pp. 3-18.
53. *Mixed Mode Bending Method for Delamination Testing*. **Crews, J. R. Reeder & J. H.** 1990, AIAA, Vol. 28, pp. 1270-1276.
54. *Redesign of the Mixed Mode Bending Delamination Test to Reduce Nonlinear Effects*. **Crews, J. R. Reeder & J. H.** 1, 1992, Journal of Composites, Vol. 14, pp. 12-19.
55. *A Bilinear Failure Criterion for Mixed Mode Delamination*. **Reeder, J. R.** 1993, Composite Materials: Testing and Design, Vol. 11th, pp. 303-322.
56. *2D and 3D Applications of the Improved and Generalized Modified Crack Closure Integral Method*. **F. G. Buchholz, H. Grebner, K. H. Dreyer & H. Krome.** [ed.] S. N. Atluri & G. Yagawa. 1988, Computational Mechanics.
57. *Finite Element Estimates of Strain Energy Release Rate Components at the Tip of an Interface Crack under Mode I Loading*. **Dattaguru, B., Venkatesha K. S., Ramamurthy, T. S., & K. Vijayakumar. K.** 1994, Engineering Fracture Mechanics, Vol. 49, pp. 451-463.
58. *Convergence of Strain- Energy Release Rate Components for Edge Delaminated Composite Laminates*. **Raju, I. S., Crews, J. H. & Aminpour, M. A.** 1988, Engineering Fracture Mechanics, Vol. 30, pp. 383-396.
59. *Characterization and Analysis of Delamination Fracture in Composites: An Overview of Developments from 1990 to 2001*. **T.E, Tay.** 1, 2003, Applied Mechanics Review, Vol. 56, pp. 1-32.
60. *Nodal Constraint, Shear Deformation and Continuity Effects Related to the Modeling of Debonding of Laminates Using Plate Elements*. **Glasessgen, E. H., Riddell, W. T., & Raju, I. S.** 1, 2002, Computer Modeling in Engineering and Sciences, Vol. 3, pp. 103-116.
61. *Cohesive Zone Model for Cracks Terminating at a Bimaterial Interface*. **Romeo A, Ballarini R. A.** 1997, International Journal of Solids and Structures, Vol. 34, pp. 1307-1326.

62. *Mixed Mode Cracking in Layered Materials*. **Hutchinson, JW & Suo Z.** 1992, Journal of Advanced Applied Mechanics, Vol. 29, pp. 63-191.
63. *Crack Growth Across a Strength Mismatched Bimaterial Interface*. **Wappling D, Gunnars J, Stahle P.** 1998, International Journal of Fracture, Vol. 89, pp. 223-243.
64. *Comparison of Cohesive Zone Model and Linear Elastic Fracture Mechanics for a Mode I Crack Near a Compliant/ Stiff Interface*. **Chang- Rong Chen, Yiu-Wing Mai.** 2010, Engineering Fracture Mechanics, Vol. 77, pp. 3408-3417.
65. *A Path Independent Integral and Approximate Analysis of Strain Concentration by Notches and Cracks*. **Rice, J. R.** 1968, ASME Journal . Appl. Mech, Vol. 35, pp. 379-386.
66. *Analysis of Energy Balance when Using Cohesive Zone Models to Simulate Fracture Process*. **Shet, C. & Chandra, N.** s.l. : Journal of Engineering Materials and Technology, 2002, Journal of Engineering Materials and Technology, Vol. 124, pp. 440-450.
67. *Stress Singularities and Fracture Mechanics*. **Atkinson, C. 2,** 1979, Applied Mechanics, Vol. 32, pp. 123-135.
68. *The Formation of Equilibrium Cracks During Brittle Fracture, General Ideas and Hypothesis*. **Barenblatt, G. I.** 1959, PMM, Vol. 23, pp. 434-444.
69. *The Mathematical Theory of Equilibrium Cracks Formed in Brittle Fracture*. **Barenblatt, G. I.** 1962, Advances in Applied Mechanics, pp. 55-125.
70. *Yielding of Steel Sheets Containing Slits*. **Dugdale, D. S.** 1960, Journal of Mech, Phys, Solids, Vol. 8, pp. 100-104.
71. *Cohesive Zone Models for Damage Evolution in Laminated Composites*. **Yang, Q. D., & Cox, B. N.** 2, 2005, International Journal of Fracture, Vol. 133, pp. 107-137.
72. **Bower, Allan F.** Constitutive Models-Relations between Stress and Strain. *Applied Mechanics of Solids*. s.l. : CRC Press, 2009.
73. *A Continuum Model for Void Nucleation by Inclusion Debonding*. **Needleman, A.** 1987, ASME Journal of Appl. Mech, Vol. 54, pp. 525-531.
74. *Embirttlement of Interfaces by Solute Segregation*. **Rice, J. R. & Jian-Sheng, Wang.** 1989, Material Science Engineering, Vol. 107, pp. 23-40.
75. *An Analysis of Decohesion Along an Imperfect Interface*. **Needleman, A.** 1990, International Journal of Fracture, Vol. 42, pp. 21-40.

76. *Numerical Simulation of Fast Crack Growth in Brittle Solids*. **Xu, X. P., & Needleman, A.** 9, 1994, *Journal of the Mechanics and Physics of Solids*, Vol. 42, pp. 1397-1434.
77. *Void Nucleation by Inclusion Debonding in a Crystal Matrix*. **Xu, X. P., & Needleman, A.** 1993, *Model. Simul. Mater. Sci. Eng.*, Vol. 1, pp. 111-132.
78. *The Relation between Crack Growth Resistance and Fracture Process Parameters in Elastic-Plastic Solids*. **Tvergaard, V., & Hutchinson, J. W.** 1992, *Journal of Mech. Phys, Solids*, Vol. 40, pp. 1377-1397.
79. *Numerical Simulation of Adhesively-Bonded Beams Failing with Extensive Plastic Deformation*. **Yang, Q. D. M. D. Thouless, and S. M. Ward.** 1999, *Journal of Mechanics and Physics of Solids*, Vol. 47, pp. 1337-1353.
80. *Mixed Mode Fracture of Plastically-Deforming Adhesive Joints*. **Yang, Q and M.D Thouless.** 2001, *International Journal of Fracture*, Vol. 110, pp. 175-187.
81. *Effect of Fiber Debonding in a Whisker-Reinforced Metal*. **Tvrgaard, V.** 1990, *Mater. Sci. Eng.*, Vol. A125, pp. 203-215.
82. *Computational Modeling of Impact Damage in Brittle Materials*. **Camacho, G. T., & Ortiz, M.** 1996, *International Journal of Solids and Structures*, Vol. 33, pp. 2899-2938.
83. *The Impact-Induced Delamination of Laminated Composites: A 2D Simulation*. **Geubelle, P. H., & Baylor, J.** 1998, *Composites, part B*, Vol. 29B, pp. 589-602.
84. *Cohesive Element Modeling of Viscoelastic Fracture*. **Rahulkumar, P., Jagota, A., Bennison, S. J., & Saigal, S.** 2000, *International Journal of Solids and Structures*, Vol. 37, pp. 1873-1897.
85. *Cohesive Zone Modeling of Crack Nucleation at Bimaterial Corners*. **Mohammed, I. & Liechti, K. M.** 2000, *Journal of Mech. Phys, Solids*, Vol. 48, pp. 735-764.
86. *Mechanics of Materials: Top-Down Approach to Fracture*. **Hutchinson, J. W. & Evans, A. G.** 2000, *Acta Materials*, Vol. 48, pp. 125-135.
87. *A Numerical Study on the Correlation between the Work of Separation and the Dissipation Rate in Ductile Fracture*. **Siegmund, T. & Brocks, W.** 2000, *Engineering Fracture Mechanics*, Vol. 67, pp. 139-154.
88. *Formulation of a Three- Dimensional Cohesive Zone Model for Application to Finite Element Algorithm*. **Fouk, J. W., Allen, D. H & Helms, K. L. E.** 2000, *Comput. Methods Appl. Mech. Eng.*, Vol. 183, pp. 51-66.

89. *Modeling Impact Induced Delamination of Woven Fiber Reinforced Composites with Contact/ Cohesive Laws*. **Espinosa, H. D., Dwivedi, S., Lu, H. C.** 2000, *Comput. Methods Appl. Mech. Eng.*, Vol. 183, pp. 259-290.
90. *A Cohesive Zone Model for Fatigue Crack Growth in Quasibrittle Materials*. **Yang, B., Mall, S. & Ravi-Chander, K.** 22-23, 2001, *International Journal of Solid Structures*, Vol. 38, pp. 3927-3944.
91. **Thouless, M. D., & Yang, Q. D.** *Measurement and Analysis of Fracture Properties of Adhesive Joints*. s.l. : Elsevier, 2001. pp. 235-271. Vol. 1.
92. *Interface Strength, Work of Adhesion and Plasticity in the Peel Test*. **Wei, Y., & Hutchinson, J. W.** 1997, *International Journal of Fracture*, Vol. 93, pp. 315-333.
93. *Simulating DCB, ENF and MMB Experiments Using Shell Elements and a Cohesive Zone Model*. **Borg, R., Nilsson, L., & Simonsson, K.** 2, 2004, *Composite Science and Technology*, Vol. 64, pp. 269–278.
94. *Numerical Simulation of Mixed-Mode Progressive Delamination in Composite Materials*. **Camanho, P. P., Davila, C. G., & De Moura, M. F.** 2003, *Journal of Composite Materials*, Vol. 37, pp. 1415-1438.
95. *Formulation, Identification and Use of Interface Models in the Numerical Analysis of Composite Delamination*. **Corigliano, A.** 1993, *International Journal of Solids and Structures*, Vol. 30, pp. 2779-2811.
96. *The Energy Absorption Potential of Chain Composites*. **Cox, B. N., Davis, J. B., Sridhar, N., Zok, F., & Gong, X.-Y.** 2000, *Acta Materialia*, Vol. 48, pp. 755-766.
97. *Effective Simulation of Delamination in Aeronautical Structures Using Shells and Cohesive Elements*. **Davila, C. G., Camanho, P. P., & Turon, A.** 2008, *Journal of Aircraft*, Vol. 45, pp. 663-672.
98. *Numerical Investigation of Progressive Damage and the Effect of Layup in Notched Tensile Tests*. **Hallett, S., & Wisnom, M. R.** 2006, *Journal of Composite Materials*, Vol. 40, pp. 1229-1245.
99. *Nonlinear Fracture Analysis of Delamination Crack Jumps in Laminated Composites*. **Ling, D. S., Fang, X. J., Cox, B. N., & Yang, Q. D.** 2, 2011, *Journal of Aerospace Engineering*, Vol. 24, pp. 181-188.
100. *A Damage Model for the Simulation of Delamination in Advanced Composites Under Variable-Mode Loading*. **Turon, A., Camanho, P. P., Costa, J., & Davila, C. G.** 2006, *Mechanics of Materials*, Vol. 38, pp. 1072-1089.

101. *The Evolution of a Transverse Intra-Ply Crack Coupled to Delamination Cracks.* **Zhou, Z. Q., Fang, X. J., Cox, B. N., & Yang, Q. D.** 1, 2010, International Journal of Fracture, Vol. 165, pp. 77-92.
102. *Crack Propagation in a Nonlinearly Viscoelastic Solid with Relevance to Adhesive Bond Failure.* **Knauss WG, Losi GU.** 1993, ASME J Appl, Vol. 60, pp. 793-801.
103. *Polymer Interfacial Fracture Simulations Using Cohesive Elements.* **Rahul-Kumar P, Jagota A, Bennison SJ, Saigal S, Muralidhar S.** 15, 1999, Acta Mater, Vol. 47, pp. 4161-4169.
104. *A Micromechanical Model for a Viscoelastic Cohesive Zone.* **Allen DH, Searcy CR.** 2001, International Journal of Fracture, Vol. 107, pp. 159-176.
105. *Cohesive Crack Model with Rate-dependent Opening and Viscoelasticity: I. Mathematical Model and Scaling.* **Bazant ZP, Li Y-N.** 1997, International Journal of Fracture, Vol. 86, pp. 247-265.
106. *Rate-Dependent Crack Growth in Adhesives: I. Modeling Approach.* **Xu C, Siegmund T, Ramani K.** 1, 2003, International Journal of Adhesions, Vol. 23, pp. 9-13.
107. *A Bilinear Cohesive Zone Model Tailored for Fracture of Asphalt Concrete Considering Viscoelastic Bulk Material.* **Seong Hyeok Song, Glaucio H. Paulino, William G. Buttlar.** s.l. : Engineering Fracture Mechanics, 2006, Vol. 73.
108. *Crack Growth with a Part-through Process Zone in Thin Plates.* **Shiva, B. Yang · S.** 2011, International Journal of Fracture, Vol. 168, pp. 145-158.
109. *Modeling and Validation of Coupled Evolution of Nonlinear Fracture Processes in Laminated Composites.* **Fang, X. J., Zhou, Z. Q., Cox, B. N., & Yang, Q. D.** Continua, Materials and Computers.
110. *Computational Analysis of Progressive Failure in a Notched Laminate Including Shear Nonlinearity and Fiber Failure.* **Van de Meer, F. P., Oliver, C., & Sluys, L. J.** 2010, Composite Science and Technology, Vol. 70, pp. 692-700.
111. *Fracture and Length Scales in Human Cortical Bone: The Necessity of Nonlinear Fracture Models.* **Yang, Q. D. , Cox, B. N., Nalla, R. K., & Ritchie, R. O.** 2006, Biomaterials, Vol. 27, pp. 2095-2113.
112. *Re-evaluating the Toughness of Human Cortical Bone.* **Yang, Q. D. , Cox, B. N., Nalla, R. K., & Ritchie, R. O.** 6, 2006, Bones, Vol. 38, pp. 878-887.
113. *Failure Criteria for FPR Laminates.* **Davila, C. G., Camanho, P. P., & Rose, C. A.** 2005, Journal of Composite Materials, Vol. 39, pp. 323-345.

114. *Impact-Induced Delamination of Composites: A 2D Simulation*. **Geubelle PH, Baylor JS**. 1998, Compos Part B, Vol. 29B, pp. 589-602.
115. *A Grain Level Model for the Study of Failure Initiation and Evolution in Polycrystalline Brittle Materials*. **Espinosa HD, Zavattieri PD**. 2003, Mech Mater, Vol. 35, pp. 333-364.
116. *Non-Self Similar Decohesion Along a Finite Interface of Unilaterally Constrained Delaminations*. **Shahwan, K. W., & Waas, A. M.** 1997. Proceedings of Royal Society of London.
117. *Modeling of Splitting and Delamination in Notched Cross-Ply Laminates*. **Wisnom, M. R., & Chang, F.-K.** 2000, Composite Science and Technology, Vol. 60, pp. 2849-2856.
118. *Fracture Assesment in Concrete Structures*. **Carpinteri, A., & Ferro, G.** Concrete Structure Integrity, Vol. 7.
119. *In Quest of Virtual Tests for Structural Composites*. **Cox, B. N., & Yang, Q. D.** 2006, Science, Vol. 314, pp. 1102-1107.
120. **Rao, Singiresu S.** *The Finite Element Method in Engineering*. Miami : Elsevier, 2004.
121. *Stiffness and Deflection Analysis of Complex Structures*. **M.J. Turner, R.W. Clough, H.C. Martin, and L.J. Topp:** 1956, Journal of Aeronautical Sciences, Vol. 23, pp. 805-824.
122. *Energy Theorems and Structural Analysis*. **Kelsey, J.H. Argyris and S.** 1955, Aircraft Engineering, Vol. 26 and 27.
123. *The Finite Element Method in Plane Stress Analysis*. **Clough, R.W.** Pittsburgh, PA : s.n., 1960. Second ASCE Conference on Electronic Computation.
124. *Variational Methods for the Solution of Problems of Equilibrium and Vibration*. **Courant, R.** 1942, Transaction of the American Mathematical Society, Vol. 49, pp. 1-23.
125. *Variational Methods for the Solution of Problems of Equilibrium and Vibrations*. **Courant, R.** 1943, Bulletin of American Mathematical Society, Vol. 49, pp. 1-23.
126. **Przemieniecki, J.S.** *Theory of Matrix Structural Analysis*. New York : McGraw-Hill, 1968.
127. **Cheung, C. Zienkiewicz and Y.K.** *The Finite Element Method in Structural and Continuum Mechanics*. London : McGraw-Hill, 1967.

128. *A Brief History of the Beginning of the Finite Element Method*. **Meek, K.K. Gupta and J.L.** 1996, International Journal for Numerical Methods in Engineering, Vol. 39, pp. 3761-3774.
129. *An Efficient Augmented Finite Element Method (A-FEM) for Arbitrary Cracking and Crack Interaction in Solids*. **W. Liu, Q. D. Yang, S. Mohammadzadeh, and X. Y. Su.** in press, 2013, International Journal of Numerical Methods.
130. *Une Theorie Statistique Du Corps Fargile Quasi-Homogene*. **J, Murzewski.** Bruxells : s.n., 1957. Proc. IUTAM 9th Congress.
131. *Nonlinear Behaviour of Ductile Quasi-Homogeneous Solids*. **JW, Murzewski.** 2006, International Journal of Damage Mechanics, Vol. 15.
132. *Introduction to Continuum Damage Mechanics*. **M, Kachanov L.** 1968.
133. **Rabotnov Y, N.** *Creep Problems in Structural Members*. s.l. : North-Holland Pub. Co, 1969.
134. *Some Aspects of Creep Rupture*. **J, Odqvist F K G and Hult.** 1961, Arkiv for Fysik.
135. *Damage Parameter in Continuum Damage Mechanics*. **Chrzanowski, M.** 1978, *Mechanika, Teoretyczna i Stosowana*.
136. *Continuous Damage Mechanics. A Tool to Describe Phenomena before Crack Initiation*. **Chaboche J, L.** 2, 1981, Nuclear Engineering and Design, Vol. 64, pp. 233-247.
137. **Krajcinovic, D.** *Continuum Damage Mechanics*. s.l. : Springer-Verlag Kg, 1987.
138. *How to Use Damage Mechanics*. **Lemaitre, J.** 1984, Nuclear Engineering and Design, Vol. 80, pp. 233-245.
139. **Ambroziak, Andrzej & Klosowski, Pawel.** *Survey of Modern Trends in Analysis of Continuum Damage Mechanics*. Gdansk, Poland : s.n., 2006.
140. *Continuum Damage Mechanics Model for Void Growth and Micro Crack Initiation*. **Dhar S, Sethuraman R and Dixit P M.** 1996, Engineering Fracture Mechanics.
141. *Continuum Damage Mechanics Treatment of Constraint in Ductile Fracture*. **Z-B, Fashang M and Kuang.** 4, 1995, Engineering Fracture Mechanics, Vol. 51, pp. 615-628.
142. *Large-Scale Simulation of Crack Propagation Based on Continuum Damage Mechanics and Two-Step Mesh Partitioning*. **Chung S W, Lee C S and Kim S J.** 2006, *Mech. Mater.*

143. *Prediction of Stable Crack Growth Using Continuum Damage Mechanics.* **Moyer E T, McCoy H and Sarkani S.** 1997, International Journal of Fracture, Vol. 86, pp. 375-384.
144. *Simplified Analysis of Steady-State Crack Growth of Piezoelectric Ceramics Based on the Continuum Damage Mechanics.* **Y, Mizuno M and Honda.** 2005, Acta Mech.
145. *Modeling of Particle Fracture by Repeated Impacts Using Continuum Damage Mechanics.* **P, Tavares L M and King R.** 2002, Powder Technology.
146. *Numerical Stress Analysis in Rotor Blade of Helicopter after Combat Damage.* **Leski, A.** 2003, Zagadnienia Eksploatacji Maszyn.
147. *Rotating Crack Model with Transition to Scalar Damage.* **Jirásek, M., & Zimmermann, T.** 3, 1998, Journal of Engineering Mechanics, Vol. 123, pp. 277-284.
148. *A Finite Element with Embedded Localization Zones.* **Belytschko, T., Fish, J., & Englemann, B. E.** 1, 1998, Computer Methods in Applied Mechanics and Engineering, Vol. 70, pp. 59-89.
149. *Finite Element with Displacement Interpolated Embedded Localization Lines Insensitive to Mesh Size and Distortions.* **Dvorkin, E. N., Cuitiño, A. M., & Gioia, G.** 3, 1990, International Journal for Numerical Methods in Engineering, Vol. 30, pp. 541-564.
150. *A Finite Element Method for Localized Failure Analysis.* **Ortiz, M., Leroy, Y., & Needleman, A.** 2, 1987, Computer Methods in Applied Mechanics and Engineering, Vol. 61, pp. 189-214.
151. *Continuum Models for the Analysis of Progressive Failure in Composite Laminates.* **Van de Meer, F. P., & Sluys, L. J.** 2, 2009, Journal of Composite Materials, Vol. 3, pp. 2131-2156.
152. *Theoretical and Experimental Investigation of Stress Redistribution in Open-Hole Composite Laminates Due to Damage Accumulation.* **Iarve, E. V., Mollenhauer, D., & Kim, R.** 2005, Composites, part A, Vol. 36, pp. 163-171.
153. *Special Finite Element Methods for a Class of Second Order Elliptic Problems with Rough Coefficients.* **Babuska, I., Caloz, G., & Osborn, J. E.** 4, 1994, SIAM Journal on Numerical Analysis, Vol. 31, pp. 945-981.
154. *The Partition of Unity Method.* **Babuška, I., & Melenk, J. M.** 1997, International Journal for Numerical Methods in Engineering, Vol. 40, pp. 727-758.

155. *The Partition of Unity Finite Element Method: Basic Theory and Applications*. **Melenk, J. M., & Babuška, I.** 1996, Computer Methods in Applied Mechanics and Engineering, Vol. 139, pp. 289-314.
156. *Generalized Finite Element Methods: Main Ideas, Results, and Perspective*. **Osborn, Ivo Babuška . Uday Banerjee . John E.** 67, 2004, International Journal of Computational Methods, Vol. 01.
157. *Generalized Finite Element Method for Second-Order Elliptic Operators with Dirichlet Boundary Conditions*. **Babuska, I., Nistor, V., & Tarfulea, N.** 2008, Journal of Computational and Applied Mechanics, Vol. 218, pp. 175-183.
158. **Duarte, C.A. and Oden, J.T.** *Hp Clouds – a Meshless Method to Solve Boundary-Value*. s.l. : TICAM Report, 1995.
159. *Elastic Crack Growth in Finite Elements with Minimal Remeshing*. **Belytschko, T. and Black, T.** 1999, International Journal of Fracture Mechanics, Vol. 45, pp. 601-620.
160. *A Finite Element Method for Crack Growth without Remeshing*. **Moës, N., Dolbow, J. and Belytschko, T.** 1999, International Journal for Numerical Methods in Engineering, Vol. 46, pp. 131-150.
161. **Dolbow, J.E.** *An Extended Finite Element Method with Discontinuous Enrichment for Applied Mechanics*. s.l. : Northwestern University, 1999.
162. *Discontinuous Enrichment in Finite Elements with a Partition Unity Method*. **Dolbow, J., Moës, N. and Belytschko, T.** 2000, Finite Elements in Analysis and Design, Vol. 36, pp. 235-260.
163. *Modeling Fracture in Mindlin–Reissner Plates with the Extended Finite Element Method*. **Dolbow, J., Moës, N. and Belytschko, T.** 2000, International Journal of Solids and Structures, Vol. 37, pp. 7161–7183.
164. *An Extended Finite Element Method for Modeling Crack Growth with Frictional Contact*. **Dolbow, J., Moës, N. and Belytschko, T.** 3, 2000, Finite Elements in Analysis and Design, Vol. 36 , pp. 235–260.
165. *Arbitrary Branched and Intersecting Cracks with the Extended Finite Element Method*. **Daux, C., Moës, N., Dolbow, J., Sukumark, N. and Belytschko, T.** 2000, International Journal for Numerical Methods in Engineering, Vol. 48, pp. 1741–1760.
166. *Extended Finite Element Method for Three Dimensional Crack Modeling*. **Sukumar, N., Moës, N., Moran, B. and Belytschko, T.** 2000, International Journal for Numerical Methods in Engineering, Vol. 48, pp. 1549–1570.

167. *Modelling Crack Growth by Level Set in the Extended Finite Element Method*. **Stolarska, M., Chopp, D.L., Moës, N. and Belytschko, T.** 2001, International Journal for Numerical Methods in Engineering, Vol. 51, pp. 943–960.
168. *Arbitrary Discontinuities in Finite Elements*. **Belytschko, T., Moës, N., Usui, S. and Parimik, C.** 2001, International Journal for Numerical Methods in Engineering, Vol. 50, pp. 993–1013.
169. *Modeling Holes and Inclusions by Level Sets in the Extended Finite-Element Method*. **Sukumar, N., Chopp, D.L., Moës, N. and Belytschko, T.** 2001, Computer Methods in Applied Mechanics and Engineering, Vol. 190, pp. 6183–6200.
170. *Non-planar 3D Crack Growth by the Extended Finite Element and Level Sets—Part I: Mechanical Model*. **Moës, N., Gravouil, A. and Belytschko, T.** 2002, International Journal for Numerical Methods in Engineering, Vol. 53, pp. 2549–2568.
171. *Non-planar 3D Crack Growth by the Extended Finite Element and Level Sets—Part II: Level Set Update*. **Gravouil, A., Moës, N. and Belytschko, T.** 2002, International Journal for Numerical Methods in Engineering, Vol. 53, pp. 2569–2586.
172. *Vector Level Sets for Description of Propagating Cracks in Finite Elements*. **Ventura, G., Budyn, E. and Belytschko, T.** 2003, International Journal for Numerical Methods in Engineering, Vol. 58, pp. 1571–1592.
173. *A Method for Growing Multiple Cracks without Remeshing and its Application to Fatigue Crack Growth*. **Zi, G., Song, J.H., Budyn, E., Lee, S.H. and Belytschko, T.** 2004, Modeling and Simulations for Material Science and Engineering, Vol. 12, pp. 901–915.
174. *A Method for Multiple Crack Growth in Brittle Materials without Remeshing*. **Budyn, E., Zi, G., Moës, N. and Belytschko, T.** 2004, International Journal for Numerical Methods in Engineering, Vol. 61, pp. 1741–1770.
175. *Enriched Finite Elements and Level Sets for Damage Tolerance Assessment of Complex Structures*. **Bordas, S. and Moran, B.** 2006, Engineering Fracture Mechanics, Vol. 73, pp. 1176–1201.
176. *Modeling Thermal Fatigue Cracking in Integrated Circuits by Level Sets and the Extended Finite Element Method*. **Stolarska, M. and Chopp, D.L.** 2003, International Journal of Engineering Science, Vol. 41, pp. 2381–2410.
177. *Embedded Crack Model. Part I: Basic Formulation*. **Jirásek, M. and Zimmermann, T.** 2001, International Journal for Numerical Methods in Engineering, Vol. 50, pp. 1269–1290.

178. *Embedded Crack Model. Part II: Combination with Smeared Crack*. **Jirásek, M. and Zimmermann, T.** 2001, International Journal for Numerical Methods in Engineering, Vol. 50, pp. 1291–1305.
179. *Brittle Fracture in Polycrystalline Microstructures with the Extended Finite Element Method*. **Sukumar, N., Srolovitz, D.J., Baker, T.J. and Prevost, J.H.** 2003, International Journal for Numerical Methods in Engineering, Vol. 56, pp. 2015–2037.
180. *Finite Element Modelling of Cracks Based on the Partition of Unity Method*. **Dumstorff, P. and Meschke, G.** 2003. Proceedings of Applied Mathematics and Mechanics (PAMM).
181. *Process Zone Resolution by Extended Finite Elements*. **Patzak, B. and Jirásek, M.** 2003, Engineering Fracture Mechanics, Vol. 70, pp. 957–977.
182. *Dislocations by Partition of Unity*. **Ventura, G., Moran, B. and Belytschko, T.** 2005, International Journal for Numerical Methods in Engineering, Vol. 62, pp. 1463–1487.
183. *Extended Finite Element Method for Cohesive Crack Growth*. **Moës, N. and Belytschko, T.** 2002, Engineering Fracture Mechanics, Vol. 69, pp. 813–833.
184. *New Crack-Tip Elements for XFEM and Applications to Cohesive Cracks*. **Zi, G. and Belytschko, T.** 2003, International Journal for Numerical Methods in Engineering, Vol. 57, pp. 2221–2240.
185. *Extended Finite Element Method for Quasi-brittle Fracture*. **Mariani, S. and Perego, U.** 2003, International Journal for Numerical Methods in Engineering, Vol. 58, pp. 103–126.
186. *A Finite Element Method for the Computational Modeling of Cohesive Cracks*. **Mergheim, J., Kuh, E. and Steinmann, P.** 2005, International Journal for Numerical Methods in Engineering, Vol. 63, pp. 276–289.
187. *Computational Aspects of Cohesive-Zone Models*. **De Borst, R., Remmers, J.J.C. and Needleman, A.** Sweden : s.n., 2004. Fifteenth European Conference of Fracture.
188. *Cohesive Zone Models, Higher-order Continuum Theories and Reliability Methods for Computational Failure Analysis*. **De Borst, R., Gutiérrez, M.A., Wells, G.N., Remmers, J.J.C. and Askes, H.** 2004, International Journal for Numerical Methods in Engineering, , Vol. 60, pp. 289–315.
189. *Discrete vs Smeared Crack Models for Concrete Fracture: Bridging the Gap*. **De Borst, R., Remmers, J.J.C., Needleman A. and Abellan, M.A.** 2004, International Journal for Numerical and Analytical Methods in Geomechanics, Vol. 28, pp. 583–607.

190. *Continuum–Discontinuum Modelling of Shear Bands*. **Samaniego, E. and Belytschko, T.** 2005, International Journal for Numerical Methods in Engineering, Vol. 62, pp. 1857–1872.
191. *Two-scale Shear Band Evolution by Local Partition of Unity*. **Areias, P.M.A. and Belytschko, T.** 2006, International Journal for Numerical Methods in Engineering, Vol. 66, pp. 878–910.
192. *A Method for Dynamic Crack and Shear Band Propagation with Phantom Nodes*. **Song, J.H., Areias, P.M.A. and Belytschko, T.** 2006, International Journal for Numerical Methods in Engineering, Vol. 67, pp. 868–893.
193. *Appropriate Extended Functions for X-FEM Simulation of Plastic Fracture Mechanics*. **Elguedj, T., Gravouil, A. and Combescure, A.** 2006, Computer Methods in Applied Mechanics and Engineering, Vol. 195, pp. 501–515.
194. *On the Use of Effective Properties for the Fracture Analysis of Microstructured Materials*. **Dolbow, J.E. and Nadeau, J.C.** 2006, Engineering Fracture Mechanics, Vol. 69, pp. 1607–1634.
195. *On the Computation of Mixed-Mode Stress Intensity Factors in Functionally Graded Materials*. **Dolbow, J.E. and Gosz, M.** 2002, International Journal of Solids and Structures, Vol. 39, pp. 2557–2574.
196. *A Solid-like Shell Element Allowing for Arbitrary Delaminations*. **Remmers, J.J.C., Wells, G.N. and de Borst, R.** 2003, International Journal for Numerical Methods in Engineering, Vol. 58, pp. 2013–2040.
197. *Partition of Unity Enrichment for Bimaterial Interface Cracks*. **Sukumar, N., Huang, Z., Prevost, J.H. and Suo, Z.** 2004, International Journal for Numerical Methods in Engineering, Vol. 59, pp. 1075–1102.
198. *Stress Intensity Factor Analysis of Interface Cracks Using X-FEM*. **Nagashima, T., Omoto, Y. and Tani, S.** 2003, International Journal for Numerical Methods in Engineering, Vol. 56, pp. 1151–1173.
199. *Application of Extended Finite Element Method to Fracture of Composite Materials*. **Nagashima, T. and Suemasu, H.** Jyväskylä, Finland : s.n., 2004. European Congress on Computational Methods in Applied Sciences and Engineering (ECCOMAS).
200. *Modeling Crack in Orthotropic Media Using a Coupled Finite Element and Partition of Unity Methods*. **Asadpoure, A., Mohammadi, S. and Vafai, A.** 13, 2006, Finite Elements in Analysis and Design, Vol. 42, pp. 1165–1175.

201. *A New Approach to Simulate the Crack with the Extended Finite Element Method in Orthotropic Media*. **Asadpoure, A. and Mohammadi, S.** 2007, International Journal for Numerical Methods in Engineering, Vol. 69, pp. 2150–2172.
202. *On the Construction of Blending Elements for Local Partitioning of Unity Enriched Finite Elements*. **Chessa, J., Wang, H., & Belytschko, T.** 2003, International Journal for Numerical Methods in Engineering, Vol. 57, pp. 1015-1038.
203. *An Augmented Cohesive Zone Element for Arbitrary Crack Coalescence and Bifurcation in Heterogeneous Materials*. **X. J. Fang, Q. D. Yang, B. N. Cox and Z. Q. Zhou.** 9, 2011, International Journal for Numerical Methods in Engineering , Vol. 88, pp. 841-861.
204. *A Method for Dynamic Crack and Shear Band Propagation with Phantom Nodes*. **Song JH, Areias PMA, Belytschko T.** 2006, International Journal for Numerical Methods in Engineering, Vol. 67, pp. 868–893.
205. *A Finite Element Method for the Simulation of Strong and Weak Discontinuities in Solid Mechanics*. **Hansbo A, Hansbo P.** 2004, Computational methods in Applied Mechanics and Engineering, Vol. 193, pp. 3523–3540.
206. *An Augmented Finite Element Method for Modeling Arbitrary Discontinuities in Composite Materials*. **Ling DS, Yang QD, Cox BN.** 2009, International Journal of Fracture, Vol. 156, pp. 53-73.
207. *High-fidelity Simulations of Multiple Fracture Processes in a Laminated Composite in Tension*. **X.J. Fang, Z.Q.Zhou , B.N.Cox , Q.D.Yang.** 7, 2011, Journal of the Mechanics and Physics of Solids, Vol. 59, pp. 1355–1373.
208. *On Local Tracking Algorithms for the Simulation of Three-Dimensional Discontinuities*. **Jager P, Steinmann P, Kuhl E.** 2008, Computational Mechanics 2008, Vol. 42, pp. 395–406.
209. *Towards the Algorithmic Treatment of 3D Strong Discontinuities*. **Mergheim J, Kuhl E, Steinmann P.** 2007, Communications in Numerical Methods in Engineering, Vol. 23, pp. 97–108.
210. **JC., Remmers.** *Discontinuities in Materials and Structures—A Unifying Computational Approach*. s.l. : Delft University, 2006.
211. *Mesh-Independent Discrete Numerical Representations of Cohesive-Zone Models*. **De Borst R, Remmers JJC, Needleman A.** 2, 2006, Engineering Fracture Mechanics, Vol. 73, pp. 160–177.

212. *A Phantom Node Formulation with Mixed Mode Cohesive Law for Splitting in Laminates.* **Van de Meer FP, Sluys LJ.** 2009, International Journal of Fracture, Vol. 158, pp. 107–124.
213. **Budyn, E.R.L.** *Multiple Crack Growth by the Extended Finite Element Method.* Evanston, Illinois : Northwestern University, 2004.
214. *An Adaptive Multiscale Method for Crack Propagation and Crack Coalescence.* **Holl, M., S. Loehnert, and P. Wriggers.** 2012, Inter. J. Numer. Meth.
215. **Borden, M.J., et al.,** *A Phase-field Description of Dynamic Brittle Fracture.* The University of Texas at Austin : The Institute for Computational Engineering and Sciences, 2011.
216. *A Phase Field Model for Rate-independent Crack Propagation: Robust Algorithmic Implementation Based on Operator Splits.* **Miehe, C., M. Hofacker, and W. F.** 2010, Computer Methods in Applied Mechanics and Engineering, Vol. 199, pp. 2765–2778.
217. *The Variational Approach to Fracture.* **Bourdin, B., G.A. Francfort, and J.J. Marigo.** 2008, Journal of Elasticity, Vol. 91, pp. 5-148.
218. *The Variational Approach to Fracture.* **B. Bourdin, G. A. Francfort, and J. J. Marigo.** 1-3, 2008, Journal of Elasticity, Vol. 91, pp. 5–148.
219. *Optimal Approximations by Piecewise Smooth Functions and Associated Variational Problems.* **Shah, D. Mumford and J.** 5, 1989, Communications on Pure and Applied Mathematics, Vol. 42, pp. 577–685.
220. *Approximation of Functional Depending on Jumps by Elliptic Functional via Gamma Convergence.* **Tortorelli, L. Ambrosio and V. M.** 8, 1990, Communications on Pure and Applied Mathematics, Vol. 43, pp. 999–1036.
221. *A Time-discrete Model for Dynamic Fracture Based on Crack Regularization.* **B. Bourdin, C. Larsen, and C. Richardson.** 2, 2011, International Journal of Fracture, Vol. 168, pp. 133–143.
222. *Existence of Solutions to a Regularized Model of Dynamic Fracture.* **C. J. Larsen, C. Ortner, and E. Suli.** 7, 2010, Mathematical Methods and Models in Applied Sciences, Vol. 20, pp. 1021–1048.
223. *Models for Dynamic Fracture Based on Griffith's Criterion.* **Larsen, C. J.** 2010. IUTAM Symposium on Variational Concepts with Applications to the Mechanics of Materials.

224. *A Phase Field Model for Rate-independent Crack Propagation: Robust Algorithmic Implementation Based on Operator Splits*. **C. Miehe, M. Hofacker, and F. Welschinger**. 2010, *Computer Methods in Applied Mechanics and Engineering*, Vol. 199, pp. 2765–2778.
225. *Thermodynamically Consistent Phase-field Models of Fracture: Variational Principles and Multi-field FE Implementations*. **C. Miehe, F. Welschinger, and M. Hofacker**. 10, 2010, *International Journal for Numerical Methods in Engineering*, Vol. 83, pp. 1273–1311.
226. **A. Karma, D. A. Kessler, and H. Levine**. Phase-Field Model of Mode III Dynamic Fracture. s.l. : *Physical Review letters*, 2001.
227. *Finite Elements with Displacement Interpolated Embedded Localization Lines Insensitive to Mesh Size and Distortions*. **Dvorkin, E.N., A.M. Cuitiño, and G. Gioia**. 3, 1990, *International Journal for Numerical Methods in Engineering*, Vol. 30, pp. 541-564.
228. *A Class of Mixed Assumed Strain Methods and the Method of Incompatible Modes*. **Simo, J.C. and M.S. Rifai**. 1990, *International Journal for Numerical Methods in Engineering*, Vol. 29, pp. 1595-1638.
229. *On Enhanced Strain Methods for Small and Finite Deformation of Solids*. **Wriggers, P. and J. Korelc**. 1996, *Computational Mechanics*, Vol. 18, pp. 413-428.
230. *On the Variational Foundations of Assumed Strain Methods*. **Simo, J.C. and T.J.R. Hughes**. 1986, *Journal of Applied Mechanics*, Vol. 53, pp. 51-54.
231. *On the Use of Embedded Discontinuity Elements with Crack Path Continuity for Mode-I and Mixed-Mode Fracture*. **Alfaiate, J., G.N. Wells, and L.J. Sluys**. 2002, *Engineering Fracture Mechanics*, Vol. 69, pp. 661-686.
232. *Embedded Discontinuity Finite Element Method for Modeling of Localized Failure in Heterogeneous Materials with Structured Mesh: An Alternative to Extended Finite Element Method*. **Ibrahimbegovic, A. and S. Melnyk**. 1, 2007, *Computational Mechanics*, Vol. 40, pp. 149-155.
233. *Discontinuous Failure Analysis for Mode-I and Mode-II Localization Problems*. **Sluys, L.J. and A.H. Berends**. 1998, *International Journal of Solids and Structures*, Vol. 35, pp. 4257–4274.
234. *Finite Elements with Embedded Branching*. **Linder, C. and F. Armero**. 4, 2009, *Finite Elements in Analysis and Design*, Vol. 45, pp. 280-293.

235. *Finite Elements with Embedded Strong Discontinuities for Modeling of Failure in Solids*. **Linder, C. and F. Armero**. 2007, International Journal for Numerical Methods in Engineering, Vol. 72, pp. 1391-1433.
236. *Towards a Generalization of a Discrete Strong Discontinuity Approach*. **Dias-da-Costa, D., et al.** 2009, Computational Methods in Applied Mechanics and Engineering, Vol. 198, pp. 3670-3681.
237. *In-plane Fracture of Laminated Fiber Reinforced Composites with Varying Fracture Resistance: Experimental Observations and Numerical Crack Propagation Simulations*. **Rudraraju, S., et al.** 2010, International Journal of Solids and Structures, Vol. 47, pp. 901-911.
238. *Comparative Study on Finite Elements with Embedded Discontinuities*. **Jirásek, M.** 2000, Computer Methods in Applied Mechanics and Engineering, Vol. 188, pp. 307-330.
239. *An Analysis of Strong Discontinuities in Multiplicative Finite Strain Plasticity and their Relation with the Numerical Simulation of Strain Localization in Solids*. **Armero, F. and K. Garikipati**. 1996, International Journal of Solids & Structures, Vol. 33, pp. 2863-2885.
240. *An Analysis of Strong Discontinuities Induced by Softening Solutions in Rate-independent Solids*. **Simo, J.C., J. Oliver, and F. Armero**. 1993, Journal of Computational Mechanics, Vol. 12, pp. 277-296.
241. *Experimental Investigation of Progressive Damage and the Effect of Layup in Notched Tensile Tests*. **Hallet, S., & Winsom, M. R.** s.l. : Journal of Composite Materials, 2006, Journal of Composite Materials, Vol. 40, pp. 119-141.
242. *Practical Challenges in Formulating Virtual Tests for Structural Composites*. **Cox, B. N., Spearing, S. M.,** 2008, Computational Methods in Applied Sciences, Vol. 10, pp. 57-75.
243. *Failure Mechanisms of 3D Woven Composites in Tension, Compression, and Bending*. **Cox, B. N., Dadkhah, M. S., et al.** 1994, Acta Metallurgica et Materialia, Vol. 42, pp. 3967-3984.
244. *Delamination of Polymer Matrix Composites: Problems and Assessments*. **Pagano, N. J., Schoeppner, G. A.,** 2000, Comprehensive Composite Materials, pp. 433-528.
245. *Discrete Cohesive Zone Model to Simulate Static Fracture in 2D Tri-axially Braided Carbon Fiber Composites*. **Xie, D., Amit, G., et al.** 2006, Journal of Composite Materials, Vol. 40, pp. 2025-2046.

246. *Progressive Damage Modeling in Fiber-Reinforced Materials*. **Lapczyk, I., Hurtado, J.** 11, 2007, Composites Part A: Applied Science and Manufacturing, Vol. 38, pp. 2333-2341.
247. *A Multi-scale Progressive Failure Approach for Composite Laminates Based on Thermodynamical Viscoelastic and Damage Models*. **Laurin, F., Carrere, N. et al.** 2007, Composites part A, Vol. A38, pp. 198-209.
248. *A Continuum Damage Model for Composite Laminates*. **Maimi, P., Camanho, P. P., et al.,** 10, 2007, Mechanics of Materials, Vol. 39, pp. 909-919.
249. *A Model for Predicting Damage in Graphite/ Epoxy Laminated Composites Resulting from Low Velocity Point Impact*. **Choi, H. Y., Chang, F. K.** 1992, Journal of Composite Materials, Vol. 26, pp. 2134-2169.
250. *Multiscale Modeling in Damage Mechanics of Composite Materials*. **Talerja, R.** 2006, Journal of Material Science, Vol. 41, pp. 6800-6812.
251. *Multiscale Modeling of Fracture in Fiber-Reinforced Composites*. **Gonzalez, C., LLorca, J.,** 2006, Acta Materialia, Vol. 54, pp. 4171-4181.
252. *The Intrinsic XFEM: A Method for Arbitrary Discontinuities without Additional Unknowns*. **Fries, T. P., Belytschko, T.,** 2006, International Journal of Numerical Methods in Engineering, Vol. 68, pp. 1358-1385.
253. *Numerical Aspects of Cohesive Zone Models*. **De Borst, R.,** 2003, Engineering Fracture Mechanics, Vol. 70, pp. 1743-1757.
254. *Generalized Gaussian Quadrature Rules on Arbitrary Polygons*. **Mousavi, S. E., H. Xiao, and N. Sukumar.** 2010, International Journal for Numerical Methods in Engineering, Vol. 82, pp. 99-113.
255. *A Critical Evaluation of Cohesive Zone Models of Dynamic Fracture*. **Falk, M. L., A. Needleman, et al.** 2001, Journal de Physique IV, Vol. 11, pp. 43-50.
256. *An Accurate and Efficient Augmented Finite Element Method for Arbitrary Crack Interaction*. **Liu, Yang, Mohammadizadeh, Su & Ling.** 4, 2013, Journal of Applied Mechanics, Vol. 80.
257. *An Embedded Formulation with Conforming Finite Elements to Capture Strong Discontinuities*. **Dias-da-Costa, D., et al.,** 2012, International Journal for Numerical Methods.
258. **De Borst, R., et al.,** *Nonlinear Finite Element Analysis of Solids and Structures*. s.l. : John Wiley & Sons., 2012.

259. *Mixed Stabilized Finite Element Methods in Nonlinear Solid Mechanics part II: Strain Localization.* **Cervera, M., M. Chiumenti, and R. Codina.,** 2010, Computer Methods in Applied Mechanics and Engineering, Vol. 199, pp. 2571-2589.
260. *An Improved Cohesive Element for Shell Delamination Analysis.* **Yang, Q. D et al.** 5, 2010, International Journal for Numerical Methods in Engineering, Vol. 83, pp. 611-641.
261. *Improved Cohesive Integration Schemes for Cohesive Zone Elements.* **B. C. Do, W. Liu, Q. D. Yang, X. Y. Su.** s.l. : Engineering Fracture Mechanics, July 2013, Vol. 107, pp. 14-28.
262. *Is Mode II Fracture Energy a Real Material Property?* **Carpinteri, A., et al.** 3, s.l. : Computers and Structures, 1993, Vol. 48, pp. 397-413.
263. *Model-independent Approaches for the XFEM in Fracture Mechanics.* **Sadaf Abbas, Alaskar Alizada, Thomas-Peter Fries.** 10, Aachen : International Journal of Numerical Methods in Engineering, 2010, Vol. 1.
264. *Experimental Determination of Interfacial Toughness Using Brazil-nut Sandwich.* **Wang, J. S, Z. Suo.** 1990, Acta Metallurgica, Vol. 38, pp. 1279-1290.
265. *The Effects of Cohesive Strength and Toughness on Mixed-Mode Delamination of Beam-like Geometries.* **Parmigiani, J. and M.D. Thouless.** 2007, Engineering Fracture Mechanics, Vol. 74, pp. 2675-2699.
266. *Augmented Cohesive Elements for Efficient Delamination Analysis of Composite Laminates.* **Qiao.H, Chem, W. Q., Yang, Q. D., Lua,J.** 2011, Engineering Materials and Technology, Vol. 13.

Appendix A: A Piece-Wise Linear Constitutive Law for Cohesive Cracks

In this study, a mixed-mode cohesive law with piece-wise linear traction-separation relations for normal and shear fracture modes as shown in Figure A1 was used. In this figure, δ_{nc} and δ_{sc} are critical normal and shear crack displacements under pure modes beyond which the cohesive stresses become zero, indicating complete fracture. ($\hat{\sigma}_1$ and $\hat{\sigma}_2$), and ($\hat{\tau}_1$ and $\hat{\tau}_2$) are critical normal and shear cohesive stresses at which sudden changes of cohesive stiffness occur, respectively. Together with the critical normal and shear crack displacements, (δ_{n1} and δ_{n2} for mode-I, and δ_{s1} and δ_{s2} for mode-II), they dictate the shapes of the traction-separation laws. All these stresses and displacements are defined in the local coordinates with s along the crack plane and n perpendicular to the crack plan as indicated in Figures 2-7, 3-2 and others.

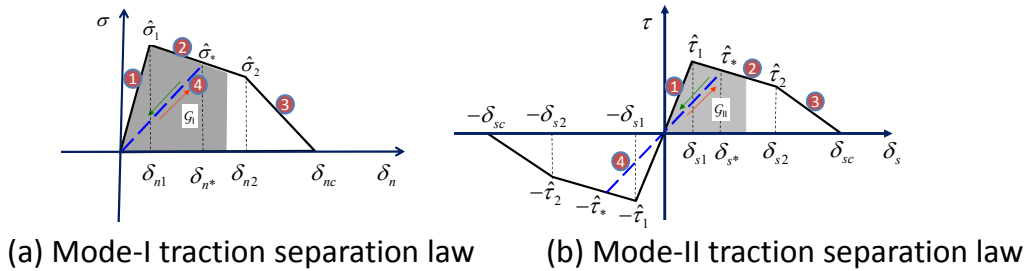


Figure A1 The piece-wise linear, mixed-mode cohesive zone model used in this study. The circled numbers indicate the respective segment numbers.

Any other types of cohesive models can be linearized like the above one. For the piece-wise linearized models, it is advantageous to index the traction-separation laws by cohesive segment numbers as labeled in Figure A1 by the circled numbers. Each segment is characterized by a critical stress ($\hat{\tau}^{(i)}$ or $\hat{\sigma}^{(j)}$), a corresponding crack displacement (δ_{s1} or δ_{n1}), and a corresponding critical crack displacement (δ_{sc} or δ_{nc}).

$\delta_s^{(i)}$ or $\delta_n^{(j)}$), and a constant stiffness ($\alpha_s^{(i)}$ or $\alpha_n^{(j)}$). Here the free superscripts (i) and (j) ($i, j=1, 2, \text{ and } 3$) are free indices for the cohesive segments. For cohesive model shown in Figure A1:

$$\hat{\sigma}^{(1)} = \hat{\sigma}_1; \hat{\sigma}^{(2)} = \hat{\sigma}_2; \hat{\sigma}^{(3)} = 0; \hat{\tau}^{(1)} = \hat{\tau}_1; \hat{\tau}^{(2)} = \hat{\tau}_2; \hat{\tau}^{(3)} = 0. \quad (\text{A1})$$

$$\delta_n^{(1)} = \delta_{n1}; \delta_n^{(2)} = \hat{\sigma}_{n2}; \delta_n^{(3)} = \delta_{nc}; \delta_s^{(1)} = \delta_{s1}; \delta_s^{(2)} = \delta_{s2}; \delta_s^{(3)} = \delta_{sc}. \quad (\text{A2})$$

And the constant cohesive slopes for any segments are:

$$\alpha_s^{(i)} = (\hat{\tau}^{(i)} - \hat{\tau}^{(i-1)}) / (\delta_s^{(i)} - \delta_s^{(i-1)}); \quad \alpha_n^{(j)} = (\hat{\sigma}^{(j)} - \hat{\sigma}^{(j-1)}) / (\delta_n^{(j)} - \delta_n^{(j-1)}) \quad (i, j = 1, 2, 3) \quad (\text{A3})$$

Where $\hat{\sigma}^{(0)} = \hat{\tau}^{(0)} = 0$ and $\delta_n^{(0)} = \delta_s^{(0)} = 0$. Further, the crack displacement ranges consistent with the cohesive segments are indexed with:

$$\Delta\delta_s^{(i)} = (\delta_s^{(i-1)}, \delta_s^{(i)}]; \quad \Delta\delta_n^{(j)} = (\delta_n^{(j-1)}, \delta_n^{(j)}] \quad (i, j = 1, 2, 3) \quad (\text{A4})$$

Thus the linearized relation between the cohesive stresses, $\sigma(\delta_n)$ and $\tau(\delta_s)$, and the crack displacements, δ_n and δ_s , for any segments may be written as:

$$\begin{aligned} \tau(\delta_s) &= \text{sgn}(\delta_s) \left[\hat{\tau}^{(i-1)} + \alpha_s^{(i)} (|\delta_s| - \delta_s^{(i-1)}) \right] && (\text{for } |\delta_s| \in \Delta\delta_s^{(i)} \ \&\& \ |\delta_s| > \delta_s^*) \\ \sigma(\delta_n) &= \hat{\sigma}^{(j-1)} + \alpha_n^{(j)} (\delta_n - \delta_n^{(j-1)}) && (\text{for } \delta_n \in \Delta\delta_n^{(j)} \ \&\& \ \delta_n > \delta_n^*) \end{aligned} \quad (\text{A5})$$

Where the sign function, $\text{sgn}(\bullet)$, is defined as $\text{sgn}(\bullet) = \begin{cases} 1 & \text{if } \bullet > 0 \\ 0 & \text{if } \bullet = 0 \\ -1 & \text{if } \bullet < 0 \end{cases}$. $|\bullet|$ denotes taking

the absolute value of the argument. δ_s^* and δ_n^* are two solution-dependent variables related to the irreversibility of the cohesive model, as discussed below.

The irreversibility of the cohesive model was explicitly considered by an additional unloading segment in each traction-separation law (segment 4 in Figure A1). In this study, the maximum crack displacements ever reached, δ_n^* for mode I and δ_s^* for mode II as shown in Figure A1, were used as the historical (or, solution-dependent) variables to facilitate the distinguishing of loading and unloading path (unloading occurs when the current crack displacement is smaller than the respective historical displacements). The corresponding historical cohesive stresses, $\hat{\sigma}_*$ and $\hat{\tau}_*$, were computed from these historical crack displacements using Eqn (A5). Thus for segment i or $j = 4$, the cohesive stress – crack displacement relation is

$$\begin{aligned} \tau(\delta_s) &= \text{sgn}(\delta_s) \alpha_s^{(4)} |\delta_s|; & (\text{for } |\delta_s| \in \Delta\delta_s^{(4)}) \\ \sigma(\delta_n) &= \alpha_n^{(4)} \delta_n & (\text{for } \delta_n \in \Delta\delta_n^{(4)}) \end{aligned} \quad (\text{A6})$$

The cohesive slopes and the displacements ranges are

$$\begin{aligned} \alpha_s^{(4)} &= (\hat{\tau}_* / \delta_s^*); & \alpha_n^{(4)} &= (\hat{\sigma}_* / \delta_n^*) \\ \Delta\delta_s^{(4)} &= [0, \delta_s^*]; & \Delta\delta_n^{(4)} &= [-\infty, \delta_n^*] \end{aligned} \quad (\text{A7})$$

For other cohesive laws such cohesive segments may be constructed similarly after piecewise linearization.

The mixed-mode cohesive model is constructed by recognizing that the total energy dissipated during fracture, \mathcal{G} , can be separated into the opening (mode-I) and shear (mode-II) components, \mathcal{G}_I and \mathcal{G}_{II} , so that,

$$\mathcal{G} = \mathcal{G}_I + \mathcal{G}_{II} \quad (\text{A8})$$

The two separate components can be calculated by integration of the mode-I and mode-II traction-separation curves (Figure A1):

$$\mathcal{G}_I = \int_0^{\delta_n} \sigma(\delta) d\delta; \quad \mathcal{G}_{II} = \int_0^{\delta_s} \tau(\delta) d\delta \quad (\text{A9})$$

Note that δ_n and δ_s are not independent parameters; they evolve together as a natural result of the interplay between the deformation of two joined domains and the details of the two traction-separation laws. A failure criterion is required to determine the critical values of \mathcal{G}_I^* and \mathcal{G}_{II}^* (shaded areas in Figure A1), at which complete fracture of the cohesive zone occurs. The criterion used in this study is a simple one [264]:

$$\mathcal{G}_I^* / \Gamma_I + \mathcal{G}_{II}^* / \Gamma_{II} = 1 \quad (\text{A10})$$

where Γ_I and Γ_{II} are the total areas under the pure opening and pure shear traction-separation laws. They are the mode-I and mode-II fracture toughnesses in linear elastic fracture mechanics (LEFM) context.

A more detailed account of this mixed-mode cohesive zone model can be found in [71, 79, 80]. The major advantage of this cohesive law is that there is no need to specify the

mode mixture *a priori*. The mode mixture and the mixed-mode toughness ($G^* = G_I^* + G_{II}^*$) evolve as numerical outcomes of the local equilibrium of stresses. More importantly, this law guarantees correct mode mixedness when LEFM conditions are satisfied [260, 265].

Finally it is emphasized here that, to index the cohesive laws by respective cohesive segment number is quite novel and it is one of the center pieces of the efficient elemental condensation process in this study. It enables one to assume a cohesive segment (i or j) (i.e., a linear cohesive stress-crack displacement relation), rather than the cohesive displacements, to formulate and solve the nonlinear equations associated with an embedded cohesive discontinuity. As seen next, this is of great advantage, because, once a cohesive segment is assumed the cohesive traction-displacement relation becomes linear. The local equilibrium equation with the embedded cohesive discontinuity becomes linear too and can be solved analytically. Whether the obtained solution is true or not is then determined by a consistency check: A solution is true if the solved cohesive displacements are all consistent with the respective ranges of the assumed segments.

Appendix B: Equilibrium Equations for First 2D Configuration

In the case that the element is cut into two rectangular domains, the equilibrium equation can be readily derived from Eqn (2-34). Note that in standard FEM formulation, the stiffness matrix follows counterclockwise nodal numbering sequence. But here we have to put the nodal displacements in crack in same position for the top and bottom elements for easy mathematical manipulation. For instance, if v_6 (the opening displacement at node 6 for the bottom element) is in sixth row for the bottom nodal displacement vector, $v_{6'}$ should be at the sixth row of the nodal displacement vector for the top element. This needs some rows and column changes in the stiffness matrix. From this point on we assume that the stiffness matrices are the new matrices built by shifting rows and columns.

$$\begin{bmatrix}
 k_{11}^+ & k_{12}^+ & k_{13}^+ & k_{14}^+ & k_{15}^+ & k_{16}^+ & k_{17}^+ & k_{18}^+ \\
 k_{12}^+ & k_{22}^+ & k_{23}^+ & k_{24}^+ & k_{25}^+ & k_{26}^+ & k_{27}^+ & k_{28}^+ \\
 k_{13}^+ & \dots\dots & & & & & & k_{38}^+ \\
 \cdot & & & & & & & \\
 \cdot & & & & & & & \\
 \cdot & & & & & & & \\
 \cdot & & & & & & & \\
 k_{18}^+ & k_{28}^+ & \dots\dots & & & & & k_{88}^+
 \end{bmatrix}
 \begin{Bmatrix}
 u_3 \\
 v_3 \\
 u_4 \\
 v_4 \\
 u_{6'} \\
 v_{6'} \\
 u_{5'} \\
 v_{5'}
 \end{Bmatrix}
 =
 \begin{Bmatrix}
 F_{x3} \\
 F_{y3} \\
 F_{x4} \\
 F_{y4} \\
 F_{x6'} \\
 F_{y6'} \\
 F_{x5'} \\
 F_{y5'}
 \end{Bmatrix}
 \quad (\Omega^+)$$

$$\begin{bmatrix}
 k_{11}^- & k_{12}^- & k_{13}^- & k_{14}^- & k_{15}^- & k_{16}^- & k_{17}^- & k_{18}^- \\
 k_{12}^- & k_{22}^- & k_{23}^- & k_{24}^- & k_{25}^- & k_{26}^- & k_{27}^- & k_{28}^- \\
 k_{13}^- & \dots\dots & & & & & & k_{38}^- \\
 \cdot & & & & & & & \\
 \cdot & & & & & & & \\
 \cdot & & & & & & & \\
 \cdot & & & & & & & \\
 k_{18}^- & k_{28}^- & \dots\dots & & & & & k_{88}^-
 \end{bmatrix}
 \begin{Bmatrix}
 u_1 \\
 v_1 \\
 u_2 \\
 v_2 \\
 u_6 \\
 v_6 \\
 u_5 \\
 v_5
 \end{Bmatrix}
 =
 \begin{Bmatrix}
 F_{x1} \\
 F_{y1} \\
 F_{x2} \\
 F_{y2} \\
 F_{x6} \\
 F_{y6} \\
 F_{x5} \\
 F_{y5}
 \end{Bmatrix}
 \quad (\Omega^-)$$

Appendix C: Stiffness Matrix for Pentagonal Subdomains

In the case that an A-FE is cut into a triangular and a pentagonal sub-domain, the stiffness matrix for the pentagonal sub-domain cannot be computed with standard FE approach. There are two methods in the literature to compute the stiffness matrix: 1) the triangulization method used by [168, 183], and 2) the polygon FEM recently developed by Mousavi and colleagues [254]. In this study, the polygon FEM was used and it is briefly summarized below.

For a physical convex polygon as shown in Figure C1 (a), a one-to-one mapping between the physical polygon and the reference (perfect) pentagon in Figure C1 (b) exists. Denote the natural coordinates within the reference element as ξ and η as shown in Figure C1 (b) so that the corner nodes are:

$$\xi_i = \cos(2\pi i / 5), \quad \eta_i = \sin(2\pi i / 5) \quad (i = 1, 2, \dots, 5) \quad (C1)$$

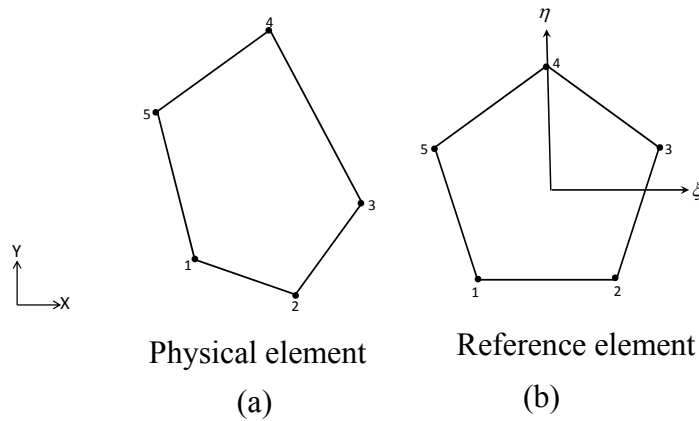


Figure C1 (a) an arbitrary physical pentagonal element and (b) its reference element

According to [254], the shape functions for the pentagonal reference element are defined

$$\text{as } N_i(\xi) = a_i(\xi, \eta) / b(\xi, \eta) \quad (i = 1, 2, \dots, 5) \quad (\text{C2})$$

Where

$$\begin{aligned} b(\xi, \eta) &= 87.05 - 12.7004\xi^2 - 2.7004\eta^2 \\ a_1(\xi, \eta) &= -0.092937(3.23607 + 4\xi)(-3.80423 + 3.80423\xi - 2.76393\eta) \\ &\quad (15.2169 + 5.81234\xi + 17.8885\eta) \\ a_2(\xi, \eta) &= -0.0790569(3.80423 - 3.80423\xi - 2.76393\eta) \\ &\quad (-3.80423 + 3.80423\xi - 2.76393\eta)(15.2169 + 5.81234\xi + 17.8885\eta) \\ a_3(\xi, \eta) &= -0.0790569(15.2169 + 5.81234\xi - 17.8885\eta) \\ &\quad (3.80423 - 3.80423\xi - 2.76393\eta)(-3.80423 + 3.80423\xi - 2.76393\eta), \\ a_4(\xi, \eta) &= 0.092937(3.23607 + 4\xi_1)(15.2169 + 5.81234\xi_1 - 17.8885\eta) \\ &\quad (3.80423 - 3.80423\xi_1 - 2.76393\eta) \\ a_5(\xi, \eta) &= 0.0232343(3.23607 + 4\xi_1)(15.2169 + 5.81234\xi_1 - 17.8885\eta) \\ &\quad (15.2169 + 5.81234\xi_1 + 17.8885\eta) \end{aligned} \quad (\text{C3})$$

With the shape functions known, the location of any point $\mathbf{x} = (x, y)$ within the pentagon

and its displacements $\mathbf{u} = (u, v)$ can be interpolated from the nodal coordinates, i.e. ,

$$\{x, y\}^T = \begin{bmatrix} N_1 & 0 & \dots & N_5 & 0 \\ 0 & N_1 & \dots & N_5 & 0 \end{bmatrix} \{x_1, y_1, \dots, x_5, y_5\}^T \quad (\text{C4})$$

$$\{u, v\}^T = \begin{bmatrix} N_1 & 0 & \dots & N_5 & 0 \\ 0 & N_1 & \dots & N_5 & 0 \end{bmatrix} \{u_1, v_1, \dots, u_5, v_5\}^T \quad (\text{C5})$$

Form Eqn (C5) the strain matrix (also called B-matrix) can be derived

$$\begin{bmatrix} \varepsilon_x \\ \varepsilon_y \\ \gamma_{xy} \end{bmatrix} = \begin{bmatrix} \partial u / \partial x \\ \partial v / \partial y \\ \partial u / \partial y + \partial v / \partial x \end{bmatrix} = \underbrace{\begin{bmatrix} \partial N_1 / \partial x & 0 & \dots & \partial N_5 / \partial x & 0 \\ 0 & \partial N_1 / \partial y & \dots & 0 & \partial N_5 / \partial y \\ \partial N_1 / \partial y & \partial N_1 / \partial x & \dots & \partial N_5 / \partial y & \partial N_5 / \partial x \end{bmatrix}}_{B\text{-matrix}(3 \times 10)} \begin{bmatrix} u_1 \\ v_1 \\ \vdots \\ u_5 \\ v_5 \end{bmatrix} \quad (\text{C6})$$

The elements in the B- matrix $(\partial N_i / \partial x)$ can be obtained explicitly using the chain rule in derivation, i. e.,

$$\begin{Bmatrix} \partial N_i / \partial x \\ \partial N_i / \partial y \end{Bmatrix} = \begin{bmatrix} \partial x / \partial \xi & \partial x / \partial \eta \\ \partial y / \partial \xi & \partial y / \partial \eta \end{bmatrix}^{-1} \begin{Bmatrix} \partial N_i / \partial \xi \\ \partial N_i / \partial \eta \end{Bmatrix} = \mathbf{J}^{-1} \begin{Bmatrix} \partial N_i / \partial \xi \\ \partial N_i / \partial \eta \end{Bmatrix} \quad (\text{C7})$$

where the matrix \mathbf{J} is the Jacobian matrix, i.e.

$$\mathbf{J} = \begin{bmatrix} \partial x / \partial \xi & \partial y / \partial \xi \\ \partial x / \partial \eta & \partial y / \partial \eta \end{bmatrix} = \begin{bmatrix} \sum_{i=1}^5 x_i \frac{\partial N_i}{\partial \xi} & \sum_{i=1}^5 y_i \frac{\partial N_i}{\partial \xi} \\ \sum_{i=1}^5 x_i \frac{\partial N_i}{\partial \eta} & \sum_{i=1}^5 y_i \frac{\partial N_i}{\partial \eta} \end{bmatrix} \quad (\text{C8})$$

By substituting Eqns (C7) into (C6), the explicit B-matrix can be established. The sub-domain stiffness matrix is then obtained by numerically integrating

$$\mathbf{L}^\alpha = \iint_{\Omega^\alpha} |\mathbf{J}| \mathbf{B}^T \mathbf{D} \mathbf{B} d\xi d\eta. \text{ According to [254], six Gaussian points are needed to integrate}$$

the stiffness matrix with sufficient numerical accuracy. The quadrature points for the six Gaussian points and their weight factors are given in table C1. The integrated elemental stiffness matrix for the pentagon can thus be written as

$$\mathbf{L}^\alpha = \sum_{j=1}^6 w_j \left| \mathbf{J}(\xi_j, \eta_j) \right| \mathbf{B}^T(\xi_j, \eta_j) \mathbf{D} \mathbf{B}(\xi_j, \eta_j) \quad (\text{C9})$$

Table C1: Gaussian Quadrature Points and Corresponding Weight Factors

Quadrature points(j)	w_j	ξ_j	η_j
1	0.3888911512256	-0.6384668826471	0.275553846540691
2	0.3888911512256	0.381135494755148	-0.58575440679964
3	0.422990789220551	-0.4373628915568	-0.5193915726330
4	0.676403174782686	0.12399251372737	0.136333638364358
5	0.251029512898982	0.0600583693601523	0.7940563773360
6	0.243640520985923	0.779135301079186	0.193675422668734

Appendix D: Integration and Interpolation Matrices for Various Integration Schemes

In local coordinates, the cohesive forces integrated from the cohesive stresses along the crack plane can be written in the following general form which we wrote them in the expanded form:

$$\begin{Bmatrix} F_{x6} \\ F_{y6} \\ F_{x5} \\ F_{y5} \end{Bmatrix} = - \begin{Bmatrix} F_{x6'} \\ F_{y6'} \\ F_{x5'} \\ F_{y5'} \end{Bmatrix} = l_e [\mathbf{T}_{coh}]^T \{\boldsymbol{\sigma}_0\} + l_e [\mathbf{T}_{coh}]^T [\mathbf{a}_0] [\mathbf{N}_{coh}] \begin{Bmatrix} \Delta u_{66'} \\ \Delta v_{66'} \\ \Delta u_{55'} \\ \Delta v_{55'} \end{Bmatrix} \quad (\text{D1})$$

D.1 Newton-Cotes Integration (Trapezoidal Integration) Method

Consider the cohesive law as shown in Figure A1. This integration method assumes linear stress distribution between the two node pairs 5-5' and 6-6'.

$$\begin{Bmatrix} F_{x6} \\ F_{y6} \\ F_{x5} \\ F_{y5} \end{Bmatrix} = - \begin{Bmatrix} F_{x6'} \\ F_{y6'} \\ F_{x5'} \\ F_{y5'} \end{Bmatrix} = l_e [\mathbf{T}_{NC}]^T \{\boldsymbol{\sigma}_0\} + l_e [\mathbf{T}_{NC}]^T [\mathbf{a}_0] \begin{Bmatrix} \Delta u_{66'} \\ \Delta v_{66'} \\ \Delta u_{55'} \\ \Delta v_{55'} \end{Bmatrix} \quad (\text{D2})$$

Where

$$[\mathbf{T}_{NC}] = \begin{bmatrix} 1/3 & 0 & 1/6 & 0 \\ 0 & 1/3 & 0 & 1/6 \\ 1/6 & 0 & 1/3 & 0 \\ 0 & 1/6 & 0 & 1/3 \end{bmatrix}; \{\boldsymbol{\sigma}_0\} = \begin{Bmatrix} \hat{\tau}^{(m)} - \alpha_t^{(m)} \delta_t^{(m)} \\ \hat{\sigma}^{(n)} - \alpha_n^{(n)} \delta_n^{(n)} \\ \hat{\tau}^{(k)} - \alpha_t^{(k)} \delta_t^{(k)} \\ \hat{\sigma}^{(l)} - \alpha_n^{(l)} \delta_n^{(l)} \end{Bmatrix}; [\mathbf{a}_0] = \begin{bmatrix} \alpha_t^{(m)} & 0 & 0 & 0 \\ 0 & \alpha_n^{(n)} & 0 & 0 \\ 0 & 0 & \alpha_t^{(k)} & 0 \\ 0 & 0 & 0 & \alpha_n^{(l)} \end{bmatrix} \quad (\text{D3})$$

Thus for NC integration method,

$$[\mathbf{T}_{coh}] = [\mathbf{T}_{NC}]; \quad [\mathbf{N}_{coh}] = [\mathbf{I}] \quad (\text{D4})$$

This method is effective when the element is very small compared to the cohesive zone. However, the numerical accuracy deteriorates very quickly as element size approaches about 1/3 of the cohesive zone size. A detailed analysis can be found in [266].

D.2 Gaussian Integration Method

Here we adopt the first order (linear) Gaussian integration method. This method uses stresses at the two Gaussian points to compute the resultant forces at the two node pair.

The integration matrix is derived as follows.

To obtain the Gaussian point stresses, we first need to interpolate the crack displacements at Gaussian points. The locations of the Gaussian points are shown in Figure D1. Point 1 is $\xi_1 l_e$ away from $6'$ and point 2 is $\xi_2 l_e$ away from $6'$; and $\xi_1 = (1 - 1/\sqrt{3})/2$
 $\xi_2 = (1 + 1/\sqrt{3})/2$.

It is straightforward to derive that the crack displacements at Gaussian points:

$$\begin{Bmatrix} \Delta u_1 \\ \Delta v_1 \\ \Delta u_2 \\ \Delta v_2 \end{Bmatrix} = [\mathbf{T}_{GS}] \begin{Bmatrix} \Delta u_{66'} \\ \Delta v_{66'} \\ \Delta u_{55'} \\ \Delta v_{55'} \end{Bmatrix} \quad (\text{D5})$$

where

$$[\mathbf{T}_{GS}] = \begin{bmatrix} \xi_2 & 0 & \xi_1 & 0 \\ 0 & \xi_2 & 0 & \xi_1 \\ \xi_1 & 0 & \xi_2 & 0 \\ 0 & \xi_1 & 0 & \xi_2 \end{bmatrix} \quad (\text{D6})$$

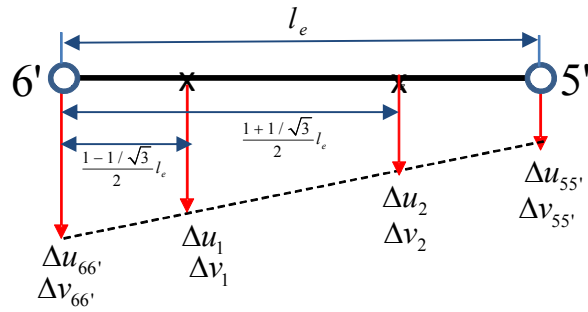


Figure D1 Displacement interpolation with Gaussian Integration method

is the Gaussian interpolation matrix.

The cohesive stresses at the Gaussian points are:

$$\begin{Bmatrix} \tau_1^{(m)} \\ \sigma_1^{(n)} \\ \tau_2^{(k)} \\ \sigma_2^{(l)} \end{Bmatrix} = \{\boldsymbol{\sigma}_0\} + [\mathbf{a}_0][\mathbf{T}_{GS}] \begin{Bmatrix} \Delta u_{66'} \\ \Delta v_{66'} \\ \Delta u_{55'} \\ \Delta v_{55'} \end{Bmatrix} \quad (\text{D7})$$

The resultant node-pair forces can be obtained from equilibrium analysis similar to the Newton-Cotes analysis except that the two equivalent forces are now acting at the Gaussian points.

$$\begin{Bmatrix} -F_{x6'} = F_{6x} \\ -F_{y6'} = F_{6y} \\ -F_{x5'} = F_{5x} \\ -F_{y5'} = F_{5y} \end{Bmatrix} = l_e [\mathbf{T}_{GS}]^T \begin{Bmatrix} \tau_1^{(m)} \\ \sigma_1^{(n)} \\ \tau_2^{(k)} \\ \sigma_2^{(l)} \end{Bmatrix} = l_e [\mathbf{T}_{GS}]^T \{\boldsymbol{\sigma}_0\} + l_e [\mathbf{T}_{GS}]^T [\mathbf{a}_0][\mathbf{T}_{GS}] \begin{Bmatrix} \Delta u_{66'} \\ \Delta v_{66'} \\ \Delta u_{55'} \\ \Delta v_{55'} \end{Bmatrix} \quad (\text{D8})$$

$$[\mathbf{T}_{GS}]^T [\mathbf{a}_0][\mathbf{T}_{GS}] = \begin{bmatrix} \alpha_t^{(m)} \xi_2^2 + \alpha_t^{(k)} \xi_1^2 & 0 & (\alpha_t^{(m)} + \alpha_t^{(k)}) \xi_1 \xi_2 & 0 \\ 0 & \alpha_n^{(n)} \xi_2^2 + \alpha_n^{(l)} \xi_1^2 & 0 & (\alpha_n^{(n)} + \alpha_n^{(l)}) \xi_1 \xi_2 \\ (\alpha_t^{(m)} + \alpha_t^{(k)}) \xi_1 \xi_2 & 0 & \alpha_t^{(m)} \xi_1^2 + \alpha_t^{(k)} \xi_2^2 & 0 \\ 0 & (\alpha_n^{(n)} + \alpha_n^{(l)}) \xi_1 \xi_2 & 0 & \alpha_n^{(n)} \xi_1^2 + \alpha_n^{(l)} \xi_2^2 \end{bmatrix}$$

Thus for Gaussian Integration method, the integration matrices are:

$$[\mathbf{T}_{coh}] = [\mathbf{T}_{GS}]^T; \quad [\mathbf{N}_{coh}] = [\mathbf{T}_{GS}] \quad (D9)$$

D.3 Improved Gaussian Integration Method

The above Gaussian integration is widely used in cohesive element formulation. However, the numerical accuracy still deteriorates as the elemental size becomes comparable to the cohesive zone size. The reason has been illustrated in [266]. In that paper, a mixed Gaussian and subdomain integration method has been proposed and been shown very effective even as the elemental size is 1.5 times the cohesive zone size. Here we adopted a similar approach, but, instead of using subdomain integration when an element is partially cracked, we shall use Gaussian integration. The formulation is given in the following:

Consider the case shown in Figure D-2 where the crack-tip is located within the cohesive element l_e . With a distance $(1-\gamma)l_e$ away from the left node pair (6-6'), i.e., the remaining active zone is γl_e .

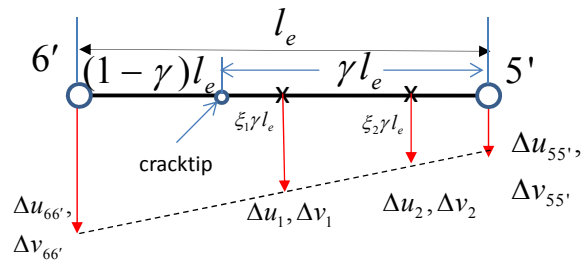


Figure D2 Displacement interpolation with improved Gaussian Integration method in the case the node-pair 66' is completely failed while node pair 55' remains active

Now the crack displacements interpolated from node pair 5-5' and 6-6' are

$$\begin{Bmatrix} \Delta u_1 \\ \Delta v_1 \\ \Delta u_2 \\ \Delta v_2 \end{Bmatrix} = \begin{bmatrix} \gamma\xi_2 & 0 & (1-\gamma+\gamma\xi_1) & 0 \\ 0 & \gamma\xi_2 & 0 & (1-\gamma+\gamma\xi_1) \\ \gamma\xi_1 & 0 & (1-\gamma+\gamma\xi_2) & 0 \\ 0 & \gamma\xi_1 & 0 & (1-\gamma+\gamma\xi_2) \end{bmatrix} \begin{Bmatrix} \Delta u_{66'} \\ \Delta v_{66'} \\ \Delta u_{55'} \\ \Delta v_{55'} \end{Bmatrix} = [\mathbf{T}_{GSI}] \begin{Bmatrix} \Delta u_{66'} \\ \Delta v_{66'} \\ \Delta u_{55'} \\ \Delta v_{55'} \end{Bmatrix} \quad (\text{D10})$$

where

$$[\mathbf{T}_{GSI}] = \begin{bmatrix} \gamma\xi_2 & 0 & (1-\gamma+\gamma\xi_1) & 0 \\ 0 & \gamma\xi_2 & 0 & (1-\gamma+\gamma\xi_1) \\ \gamma\xi_1 & 0 & (1-\gamma+\gamma\xi_2) & 0 \\ 0 & \gamma\xi_1 & 0 & (1-\gamma+\gamma\xi_2) \end{bmatrix} \quad (\text{D11})$$

is the modified integration matrix. It reduces to standard integration matrix Eqn (D6) as

$\gamma \rightarrow 1$. The stresses at these integration points are

$$\begin{Bmatrix} \tau_1^{(m)} \\ \sigma_1^{(n)} \\ \tau_2^{(k)} \\ \sigma_2^{(l)} \end{Bmatrix} = \{\boldsymbol{\sigma}_0\} + [\mathbf{a}_0][\mathbf{T}_{GSI}] \begin{Bmatrix} \Delta u_{66'} \\ \Delta v_{66'} \\ \Delta u_{55'} \\ \Delta v_{55'} \end{Bmatrix} \quad (\text{D12})$$

Equilibrium consideration leads to

$$\begin{Bmatrix} F_{x6} \\ F_{y6} \\ F_{x5} \\ F_{y5} \end{Bmatrix} = \begin{Bmatrix} -F_{x6'} \\ -F_{y6'} \\ -F_{x5'} \\ -F_{y5'} \end{Bmatrix} = l_e [\mathbf{T}_{GSI}]^T \begin{Bmatrix} \tau_1^{(m)} \\ \sigma_1^{(n)} \\ \tau_2^{(k)} \\ \sigma_2^{(l)} \end{Bmatrix} = l_e [\mathbf{T}_{GSI}]^T \{\boldsymbol{\sigma}_0\} + l_e [\mathbf{T}_{GSI}]^T [\mathbf{a}_0][\mathbf{T}_{GSI}] \begin{Bmatrix} \Delta u_{66'} \\ \Delta v_{66'} \\ \Delta u_{55'} \\ \Delta v_{55'} \end{Bmatrix} \quad (\text{D13})$$

Therefore in this case,

$$[\mathbf{T}_{coh}] = [\mathbf{T}_{GSI}]^T; \quad [\mathbf{N}_{coh}] = [\mathbf{T}_{GSI}] \quad (\text{D14})$$

In case that node pair 55' is completely failed while node 66' remains active, as shown in

Figure D3, the derivation of integration matrix are similarly straightforward.

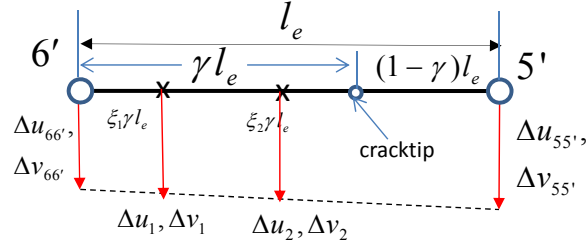


Figure D3 Displacement interpolation with improved Gaussian Integration method in the case the node-pair 55' is completely failed while node pair 66' remains active

$$\begin{Bmatrix} \Delta u_1 \\ \Delta v_1 \\ \Delta u_2 \\ \Delta v_2 \end{Bmatrix} = \begin{bmatrix} 1-\gamma+\gamma\xi_2 & 0 & \gamma\xi_1 & 0 \\ 0 & 1-\gamma+\gamma\xi_2 & 0 & \gamma\xi_1 \\ 1-\gamma+\gamma\xi_1 & 0 & \gamma\xi_2 & 0 \\ 0 & 1-\gamma+\gamma\xi_1 & 0 & \gamma\xi_2 \end{bmatrix} \begin{Bmatrix} \Delta u_{66'} \\ \Delta v_{66'} \\ \Delta u_{55'} \\ \Delta v_{55'} \end{Bmatrix} = [\mathbf{T}_{GSII}] \begin{Bmatrix} \Delta u_{66'} \\ \Delta v_{66'} \\ \Delta u_{55'} \\ \Delta v_{55'} \end{Bmatrix} \quad (\text{D15})$$

where

$$[\mathbf{T}_{GSII}] = \begin{bmatrix} 1-\gamma+\gamma\xi_2 & 0 & \gamma\xi_1 & 0 \\ 0 & 1-\gamma+\gamma\xi_2 & 0 & \gamma\xi_1 \\ 1-\gamma+\gamma\xi_1 & 0 & \gamma\xi_2 & 0 \\ 0 & 1-\gamma+\gamma\xi_1 & 0 & \gamma\xi_2 \end{bmatrix} \quad (\text{D16})$$

is the integration matrix for this case.

Following the same procedure, the resultant node pair cohesive forces are:

$$\begin{Bmatrix} -F_{x6'} = F_{6x} \\ -F_{y6'} = F_{6y} \\ -F_{x5'} = F_{5x} \\ -F_{y5'} = F_{5y} \end{Bmatrix} = l_e [\mathbf{T}_{GSII}]^T \begin{Bmatrix} \tau_1^{(m)} \\ \sigma_1^{(n)} \\ \tau_2^{(k)} \\ \sigma_2^{(l)} \end{Bmatrix} = l_e [\mathbf{T}_{GSII}]^T \{\boldsymbol{\sigma}_0\} + l_e [\mathbf{T}_{GSII}]^T [\boldsymbol{\alpha}_0] [\mathbf{T}_{GSII}] \begin{Bmatrix} \Delta u_{66'} \\ \Delta v_{66'} \\ \Delta u_{55'} \\ \Delta v_{55'} \end{Bmatrix} \quad (\text{D17})$$

Therefore in this case,

$$[\mathbf{T}_{coh}] = [\mathbf{T}_{GSII}]^T; \quad [\mathbf{N}_{coh}] = [\mathbf{T}_{GSII}] \quad (\text{D18})$$

D.4 Mixed Newton-Cotes and Subdomain Integration (Mixed NCI and SDI)

Following the similar procedure to that in the improved Gaussian method, we could derive an improved NCI method too. However, we found that this will lead to significant underprediction of equivalent nodal forces. Instead, mixed NCI and SDI formulation is recommended. This method assumes a constant cohesive stress within the remaining bonded area after one of the node-pairs failed, and the cohesive stress is evaluated from the midpoint of the bonded area. The interpolation and integration matrix after an element is partially cracked is

$$[\mathbf{N}_{\text{NCI-SDI}}] = \begin{bmatrix} 3\gamma/4 & 0 & 1-3\gamma/4 & 0 \\ 0 & 3\gamma/4 & 0 & 1-3\gamma/4 \\ \gamma/4 & 0 & 1-\gamma/4 & 0 \\ 0 & \gamma/4 & 0 & 1-\gamma/4 \end{bmatrix} \quad (\text{D19})$$

$$[\mathbf{T}_{\text{NCI-SDI}}] = \frac{\gamma}{2} [\mathbf{N}_{\text{NCI-SDI}}]^T \quad (\text{D20})$$

VITA

Seyedreza Mohammadizadeh was born in Shiraz, Iran, on September 20, 1983. His parents are Mohammadsadegh and Soehila. He received his high school diploma at Alavi School. In September 2001 he entered the Shiraz University (the former Pahlavi University) from which he was graduated with the B.S. degree in September 2005. In September 2006 he entered Tarbiat Modares University from which he was graduated with the M.S. degree in July 2009. In January 2011 he was admitted to the Graduate School of the University of Miami, where he was granted a PhD degree in December 2013.

Permanent Address: No.1, Sarv Apartment, Banafshe Ave, Mahalati St., Ghodoosi Gharbi, Shiraz, Iran